Melting curve and liquid-liquid transition in phosphorus

Hermann Muhammad

Sorbonne Université

The European Synchrotron Radiation Facility

Ecole doctorale 397

IMPMC / PHYSIX

Melting curve and liquid-liquid transition in phosphorus

Par Hermann MUHAMMAD

Thèse de doctorat de Physique

Dirigée par Frédéric DATCHI et Mohamed MEZOUAR

Présentée et soutenue publiquement le [20 / 10 / 2023]

Devant un jury composé de :

Mme Vittoria PISCHEDDA	Professeure, Université de Lyon 1	Présidente du jury
M. Roman MARTONAK	Professeur, Université de Comenius	Rapporteur
M. Guillaume MORARD	Chargé de recherches, Université Grenoble Alpes	Examinateur
M. Volodymyr SVITLYK	Scientifique de ligne, HZDR Rossendorf	Examinateur
M. Frédéric DATCHI	Directeur de Recherche, Université Paris 6	Directeur de thèse
M. Mohamed MEZOUAR	Responsable ligne de lumière, ESRF	Co-directeur

Table of Content

Introduction

In standard textbooks, the liquid state is usually described as a disordered and isotropic assembly of particles, which responds to a pressure (P) or temperature (T) change by a continuous variation of its density. This picture has been drastically altered at the start of the millennium with the discovery[1-11] of first-order transitions separating two liquid phases of the same single-component substance, a phenomenon referred as liquid-liquid transition (LLT). As a matter of fact, the possibility of having more than one liquid phase of the same substance, i.e. liquid polymorphism, has been discussed since the 1970's, and emerged from computer simulations of model systems[12]. The interest was strongly boosted in 1992 when Poole et al.[13] suggested, again from computer simulations, the existence of two alternative forms of molecular arrangements in supercooled water, the so-called low-density (LDL) and high-density (HDL) liquids, which may coexist along a line of LLT. Moreover, it was postulated that this line ends at a critical point, called second or liquid-liquid critical point (LLCP), in a similar fashion as the vapor-liquid transition line. Unfortunately, despite intense experimental efforts, the LLT and LLCP in bulk water have not been evidenced by experiment so far because, at their presumed location, water is unstable and spontaneously crystallizes.

Apart from water, LLTs have been predicted or reported in a number of diverse compounds, including (but not limited to) carbon[1], silicon[2], hydrogen[3], carbon dioxide[4], nitrogen[5], boron oxide[6], sodium[7], Y_2O_3-Al_2O_3 mixtures[8], triphenyl phosphite[9], phosphorus[10-11] and sulfur[14]. This shows that this phenomenon is not restricted to specific systems but has a more general scope. So far, theoretical attempts to rationalize liquid polymorphism have mainly relied on the "two-state" phenomenological model and the concept of "locally-favored structures"[15,16]. Another recurrent pattern in the literature is that liquid polymorphism mirrors that of the crystal. However, our understanding remains relatively primitive, and there is no theory at present able to predict whether a given system will exhibit a LLT. This is why the experimental realizations reported so far remain scarce and have been made rather accidentally. Moreover, most cases of LLT have been strongly disputed, in particular those observed in metastable, supercooled liquids, as they occur simultaneously with crystallization, making it difficult to separate the two phenomena. There is thus a need to find and study LLTs in thermodynamically stable liquids, of which only two examples are known to date, phosphorus and sulfur.

The experimental observation of the LLT in phosphorus in 2000 stands as a landmark in the field as it provided the first direct, in-situ and unambiguous observation of a LLT in a stable liquid. This first-order transition was initially detected by Katayama et al[10-11] at about 0.9 GPa and 1300 K, revealing two liquid forms of phosphorus differing in density by as much as 40 %. The LLT was later confirmed by experiments made at ESRF who determined the transition line to about 2500 K[17]. This discovery gathered a large attention and paved the way to several theoretical studies of LLTs in other systems under high pressure such as in nitrogen[5], carbon dioxide[6], hydrogen[3] and sodium[7]. Since then, only one more experimental confirmation of a liquid-liquid transition has been observed, this time in elemental sulfur by L. Henry and collaborators[14].

At the start of this thesis, considerable discrepancies persisted in the determination of the phase diagram of phosphorus, manifesting as significant disparities among various reports in the scientific literature, particularly concerning its melting curve[18-21]. Furthermore, numerous questions persisted regarding the nature and origin of liquid-liquid transitions, as well as their relationship with the process of melting. Key aspects of LLTs, such as the associated order parameter, latent heat, entropy and internal energy remain unresolved. Additionally, the existence or absence of a liquid-liquid critical point (LLCP) within the phase diagram of phosphorus, and the manner in which the LLT thermodynamics correlate with the melting phenomenon, remain open areas of investigation.

This thesis addresses these issues by conducting a comprehensive investigation of both the solid and liquid state of phosphorus using x-ray-based techniques, aiming to illuminate its controversial and intriguing phase diagram. The manuscript is organized as follows:

Chapter 1 provides an overview of the current knowledge of the polymorphism in solid and liquid phosphorus within the relevant pressure-temperature (P-T) domain for this thesis work. We describe the main allotropes of phosphorus as well as experimental and theoretical investigations of these forms, and we raise the fundamental questions that remain unsolved.

Chapter 2 presents the experimental methods that we employed to reach the high pressure and high temperature conditions in our experiments. The two main devices, the diamond anvil cell and the Paris-Edinburgh press, are described as well as the means to determine P and T for each of them.

Chapter 3 is devoted to the characterization methods employed in this research. We review various state-of-the-art techniques used to characterize the solid and liquid states of phosphorus in the context of this thesis. This includes examining the local structure of both the liquid and solid phases using X-ray diffraction. We also assess macroscopic properties of the liquid, such as density and viscosity, to define the boundaries of different liquid domains and gain insights into the nature of these liquids.

Chapter 4 presents the experimental findings related to the directional thermal equation of state (EOS) of hexagonal boron nitride (hBN) and black phosphorus (bP) using in situ high-resolution synchrotron x-ray diffraction. Besides providing an accurate description of the effects of pressure and temperature on the lattice parameters and volume of these two materials, our findings allow to highlight a new pressure-temperature metrology based on the exceptional anisotropic properties of bP, which can be simultaneously used as pressure and temperature sensor during XRD experiments in an extended P-T domain.

Chapter 5 presents accurate melting points measurements up to 5 GPa and 1700 K using in situ synchrotron X-ray diffraction and the original P-T metrology presented in Chapter 4. Moreover, we present our experimental findings on the reversible behavior of the transformation in the whole P-T domain of interest. Lastly, we report combined in situ X-ray diffraction and density measurements that provide direct evidence for a colossal density discontinuity at melting in phosphorus and discuss the thermodynamics of the transformation.

Chapter 6 focusses on the liquid-liquid transition of phosphorus. We present results from combined in situ X-ray diffraction and absorption experiments that allowed us to extract crucial information on the position of the transition, its slope, and on the variation of the density variation along the transition line in an extended temperature range up to 2500 K. We discuss the thermodynamics of the LLT and how it compares with that of melting. Lastly, we present and discuss the results of viscosity measurements performed in the LDL and HDL stability fields that provide invaluable insights on the structural nature of the liquid phases.

References

1. J. N. Glosli and F. H. Ree, Liquid-Liquid Phase Transformation in Carbon. *Phys Rev. Lett.*, 1999, **82**, 4659-4662.
2. S. Sastry and C. A. Angell, Liquid-liquid phase transition in supercooled silicon. *Nat. Mater.*, 2003, **2**, 739-743.
3. M. A. Morales, C. Pierleoni, E. Schwegler and D. M. Ceperley, Evidence for a first-order liquid-liquid transition in high-pressure hydrogen from ab initio simulations. *Proc. Natl. Acad. Sci. USA*, 2010, **107**, 12799-12803.
4. B. Boates, A. M. Teweldeberhan and S. A. Bonev, Stability of dense liquid carbon dioxide. *PNAS*, 2012, **109**, 14808-14812.
5. B. Boates and S. A. Bonev, First-order liquid-liquid phase transition in compressed nitrogen. *Phys. Rev. Lett.*, 2009, **102**, 015701.
6. V. V. Brazhkin, I. Farnan, K. Funakoshi, M. Kanzaki, Y. Katayama, A. G. Lyapin and H. Saitoh, Structural Transformations and Anomalous Viscosity in the B_2O_3 Melt under High Pressure. *Phys. Rev. Lett.*, 2010, **105**, 115701.
7. J. -Y. Raty, E. Schwegler and S. A. Bonev, Electronic and structural transitions in dense liquid sodium. *Nature*, 2007, **449**, 448-451.
8. S. Aasland and P. F. McMillan, Density-driven liquid-liquid phase separation in the system Al_2O_3-Y_2O_3. *Nature*, 1994, **369**, 633-636.
9. H. Tanaka, R. Kurita and H. Mataki, Liquid-Liquid Transition in the Molecular Liquid Triphenyl Phosphite, *Phys. Rev. Lett.*, 2004, **92**, 025701.
10. Y. Katayama, T. Mizutani, W. Utsumi, O. Shimomura, M. Yamakata and K. Funakoshi, A first-order liquid-liquid phase transition in phosphorus. *Nature*, 2000, **403**, 170-173.
11. Y. Katayama, Y. Inamura, T. Mizutani, M. Yamakata, W. Utsumi, O. Shimomura, Macroscopic separation of dense fluid phase and liquid phase of phosphorus. *Science*, 2004, **306**, 848-851.
12. P. C. Hemmer and C. Stell, Fluids with several phase transitions. *Phys. Rev. Lett.*, 1970, **24**, 1284-1287.
13. P. H. Poole, F. Sciortino, U. Essmann and H. E. Stanley, Phase behavior of metastable water. *Nature*, 1992, **360**, 324-328.
14. L. Henry, M. Mezouar, G. Garbarino, D. Sifré, G. Weck and F. Datchi, Liquid-liquid transition and critical point in sulfur. *Nature*, 2020, **584**, 382-386.

15. M. A. Anisimov, M. Duška, F. Caupin, L. E. Amrhein, A. Rosenbaum and R. J. Sadus, Thermodynamics of Fluid Polyamorphism. *Phys. Rev. X*, 2018, **8**, 011004.
16. H. Tanaka, Liquid-liquid transition and polyamorphism. *J. Chem. Phys.*, 2020, **153**, 130901.
17. G. Monaco, S. Falconi, W. Crichton and M. Mezouar, Nature of the first-order phase transition in fluid phosphorus at high temperature and pressure, *Phys. Rev. Lett.*, 2003, **90**, 2557011-2557014.
18. Y. Akahama, W. Utsumi, S. Endo, T. Kikegawa, H. Iwasaki, O. Shimomura, T. Yagi and S. Akimoto, Melting curve of black phosphorus. *Phys. Lett. A*, 1987, **122**, 129-131.
19. T. Mizutani, Y. Katayama, W. Utsumi, K. Funakoshi, M. Yamakata and O. Shimomura, Anomaly in the melting curve of black phosphorus associated with a liquid-liquid transition. *Science Technol. High Press. (Proceedings of AIRAPT-17),* 2000, 525-528.
20. V. L. Solozhenko and V. Turkevich, P-T phase diagram of phosphorus revisited. *J. Phys. Chem. C*, 2023, **127**, 12, 6088-6092.
21. G. B. Guarise and A. Marani, Fusione del fosforo nero fino a 16.000 atm. *Chim. Ind.*, 1968, **50**, 663665.

Chapter 1:
Polymorphism of solid and liquid phosphorus: state of the art

1. Introduction

Polymorphism, derived from the Greek word meaning "many shapes", refers to the remarkable ability of an object to exist in multiple forms or configurations. Within crystallography, polymorphism represents a common attribute of various materials, and almost all elements and compounds possess several distinct structural forms. When referring to a pure element, these forms are termed polymorphs or allotropes, and they are defined as solid phases that differ in both their crystal structure and diffraction pattern from other polymorphs of the same element or compound. This concept can also be extended to liquids and amorphous materials, which are likewise characterized by their unique diffraction patterns.

Polymorphism arises in a given system due to its response to external perturbations, such as variations in the thermodynamic conditions. The structural transformations within the system occur as a result of the system's endeavor to minimize its Gibbs energy. The investigation of the various forms a substance can take is crucial for comprehending the connections between its structure and properties.

Within the liquid state, the examination of first-order phase transitions, which occur between two liquid phases of a homogeneous and isotropic material, has garnered significant attention and research efforts in recent years[1-14]. Approximately two decades ago, Y. Katayama and colleagues made a significant discovery regarding a liquid-liquid transition in elemental phosphorus[8]. This discovery had a profound impact on the scientific community as it challenged the longstanding paradigm that any structural or thermodynamic changes in a fluid due to variations in pressure and temperature should only occur continuously. Moreover, it emphasized the incomplete nature of our understanding of this fundamental state of matter. Since then, additional experimental evidence has emerged supporting the existence of liquid-liquid transitions in some supercooled liquids[9-13], and more recently in compressed liquid sulfur[14]. Sulfur stands out as the unique case where a liquid-liquid critical point (LLCP) terminating the liquid-liquid transition line was experimentally evidenced. The existence of

LLCPs has been a subject of intense debate and research in water, where it could potentially explain numerous thermodynamic anomalies[1,2,10,11,13] and in phosphorus[68,74,78], but no definite experimental evidence has been found in these two cases so far.

This chapter provides an overview of the current understanding of polymorphism in solid and liquid phosphorus within the relevant pressure-temperature (P-T) domain for this thesis work.

2. Phosphorus

Phosphorus, represented by the chemical symbol P, possesses the atomic number 15 and an atomic weight of 30.974. It is categorized as a non-metallic p-block element belonging to group VA (group 15) of the periodic table. This group comprises nitrogen, phosphorus, arsenic, antimony, and bismuth, which are occasionally referred to as pnicogens, pnictogens, or pnictides. The phase diagram of phosphorus is presented in Figure 1.1. In this section, we will successively introduce the distinct solid and liquid polymorphs of phosphorus and their structural relations.

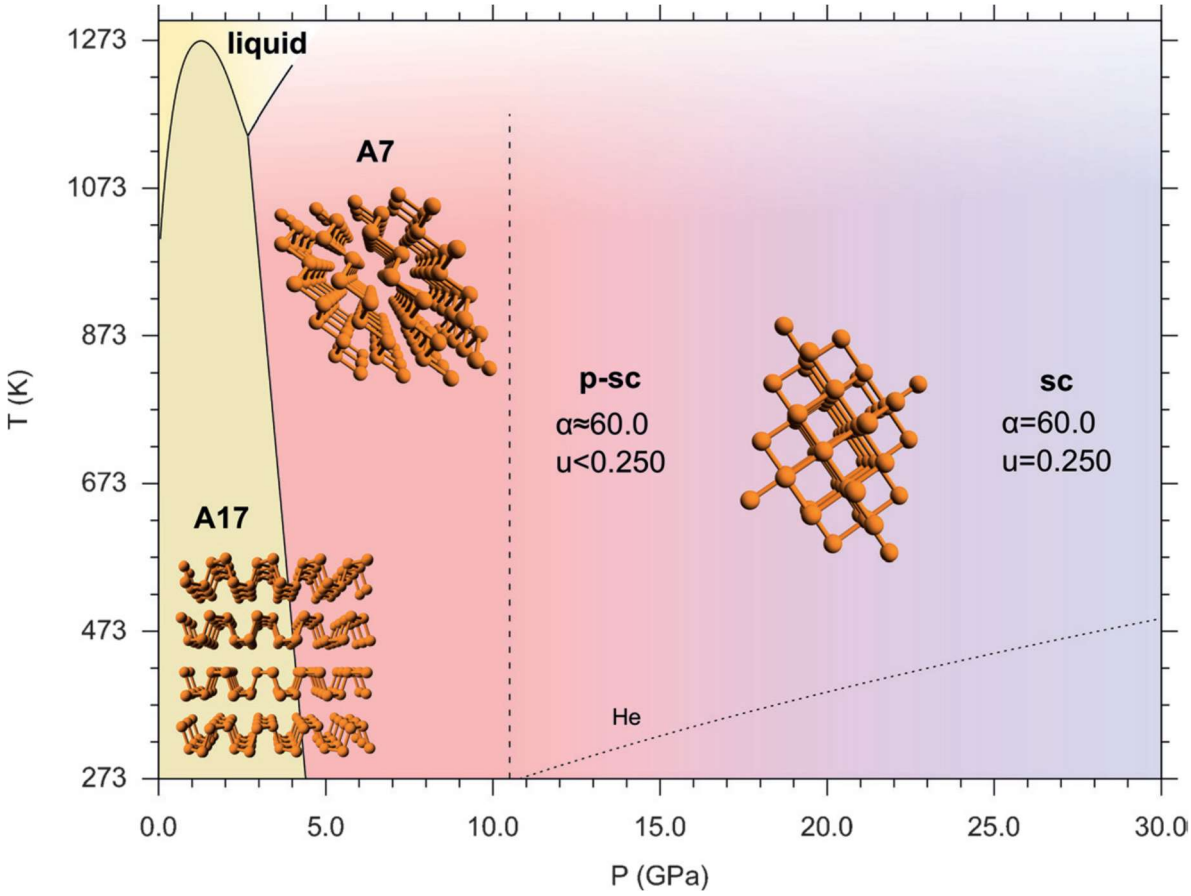

Figure 1.1. Thermodynamic phase diagram of phosphorus from ref[54].

2.1. Solid polymorphism

Approximately a century ago, three major allotropic modifications of elemental phosphorus had been generally acknowledged: white (or yellow when impure), red and black. These allotropes, capable of conversion between each other, represent successively denser and chemically less reactive forms. Moreover, the existence of gaseous and liquid states, as well as several additional solid forms of the element, has been discovered, although the majority of these can be considered as subcategories of the three main allotropes.

White phosphorus corresponds to the original pyrophoric form of the element prepared by H. Brand in 1669[16]. The red allotrope was first obtained by A. Von Schrotter in 1847[17], and the black variety by P. W. Bridgman in 1914[18].

As shown in Figure 1.2., the solid polymorphism of phosphorus exhibits a diverse range of forms, and considerable research has been devoted to studying the structures and physico-chemical properties of these various allotropes. In this section, we will begin by providing an

overview of the two most prevalent forms of phosphorus that exist under ambient conditions. Subsequently, we will present information regarding its phase diagram under high pressure and high temperature conditions relevant to this work.

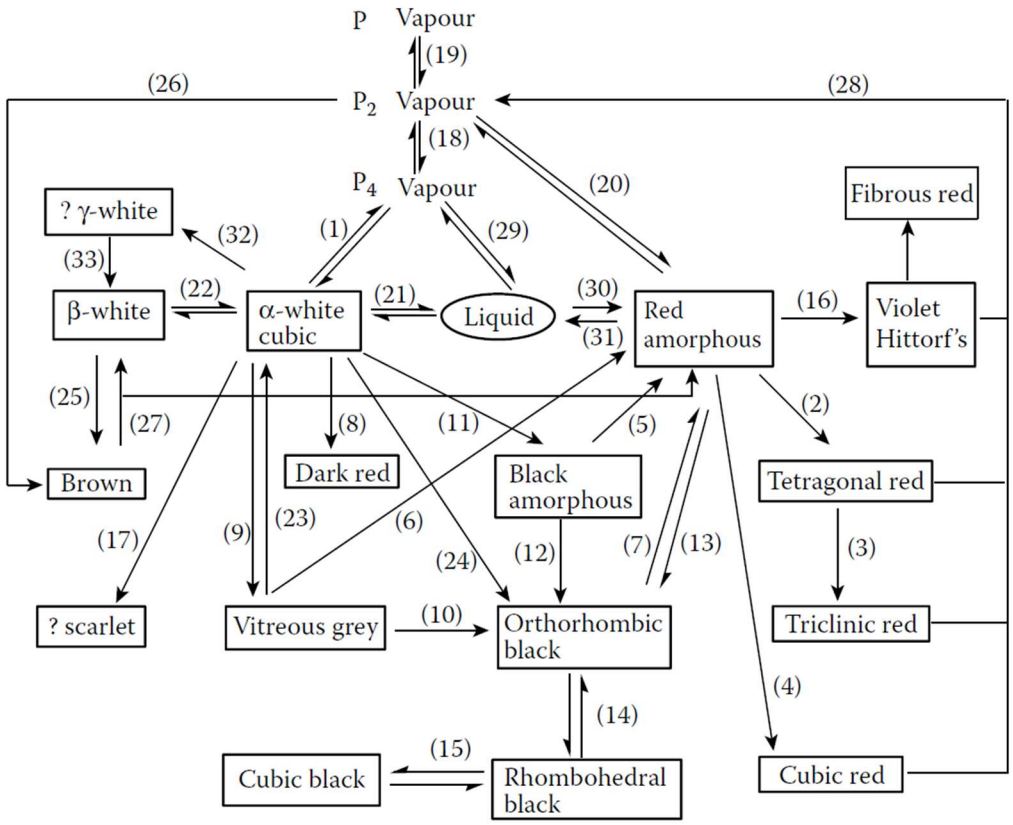

Figure 1.2. Some relationships between reported allotropes of phosphorus. (1) High vapour pressure at room temperatures. (2) heat at 540°C, (3) heat at 550°C, (4) heat at 600°C, (5) heat at 125°C, (6) heat at 400°C, (7) heat at 550°C, (8) heat at 330°Cand 8000 atm, (9) heat at 380°C with Hg, or above 250°C and 12 kb, (10) heat at 400°Cwith Hg for some days, (11) heat at 200°C and 12000 atm, (12) heat at 200°Cand 15000 atm, (13) heat at 200°C and 12000 atm, (14) reversible transition at 50-100 kb, (15) reversible transition at 110 kb, (16) recrystallize from molten Pb, (17) heat a PBr3 solution, (18) reversible transition at 900°C, (19) reversible transition at 1700°C, (20) reversible transition at low pressure, (21) reversible transition at 44.1°C but can supercool, (22) reversible transition at -77°C or +64°C and 1200 atm, (23) sublime under vacuum, (24) heat at 220°C and 12 kb, (25) irradiate with UV at 180°C, (26) condense P2 vapour at -196°C, (27) heat above -100°C, (28) heat at low pressure, (29) boils at 280°C, (30) heat at 300°C or expose to visible light or x-rays, (31) melt about 600°C, (32) low temperature supercool, (33) warm up.[28,46]

2.1.1. White phosphorus

The credit for the discovery of phosphorus is commonly attributed to Hennig Brand of Hamburg, who, in 1669, isolated it through urine distillation[16]. The resulting substance exhibited phosphorescent properties and ignited upon exposure to air. Consequently, it was named 'phosphorus', denoting its light emitting nature. It is possible that Arabian alchemists had discovered the element earlier, but the term 'phosphorus' was often used to describe various light-emitting substances that did not contain the element. Examples include 'Bologna phosphorus', a luminescent barium sulphide, and 'Baldwin's phosphorus', a luminescent calcium nitrate.

Following the discovery of elemental (white) phosphorus, subsequent investigations led to the identification of its combustion byproduct, phosphorus pentoxide[19]. In 1694, R. Boyle successfully synthesized phosphoric acid by dissolving phosphorus pentoxide in water. The presence of phosphorus in plants was first observed by B. Albino in 1688, while J. T. Hensing detected the element in human brain tissue in 1719[20].

White phosphorus, the most abundant form of phosphorus, exhibits high volatility and reactivity compared to other solid forms. It shares close structural similarities with the liquid and vapour phases of the element into which it readily transforms. While white phosphorus is soft and waxy and readily soluble in organic solvents, its solubility in water is practically non-existent. Its molecular structure consists of tetra-atomic phosphorus, with the P_4 molecule arranged in a tetrahedral configuration (see below).

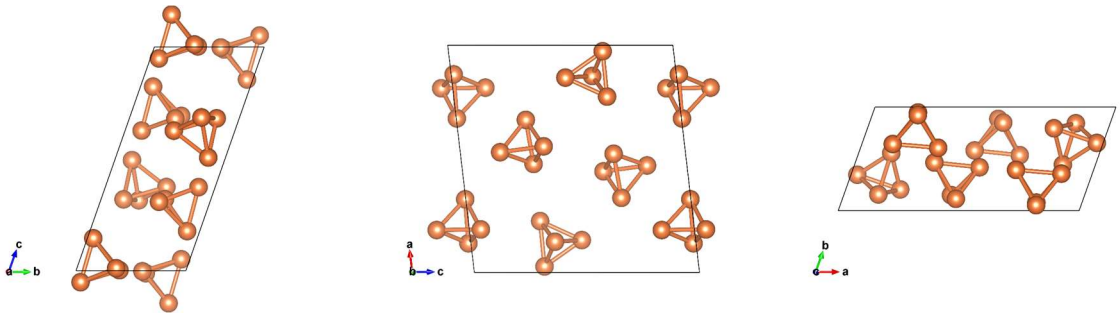

Figure 1.3. Triclinic-structure of white β-P with different orientations. Figure created with VESTA. Structural information from ICSD[22].

Under ambient conditions, white phosphorus crystallizes in two main metastable forms[21]. The first form is referred to as α-P, with a cubic crystalline structure belonging to the

I-43m space group with a lattice parameter of a = 18.51 Å. α-P has a density of 1.83 g.cm^{-3} at 20°C, a melting point of 44.1°C, a boiling point of 280°C, and a vapor pressure of 0.033 mbar. α-P transits to the triclinic β form (space group P-1) at -77°C at ambient P or 0.78 GPa at ambient T. β-P has a density of 1.88 g.cm^{3}.[22] Additionally, the existence of a metastable low-temperature monoclinic γ form, with a density of 1.94 g.cm^{-3}, has been reported[23-24,26]. In both α-P and β-P, the P-P bond length is 2.21 Å in the P_4 tetrahedron.

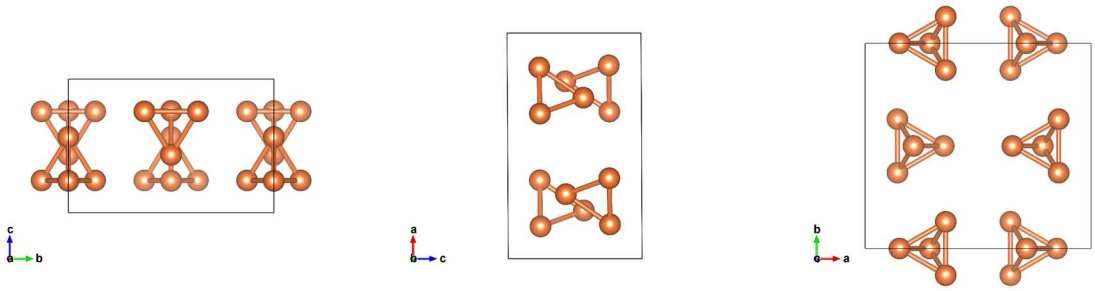

Figure 1.4. Crystal structures of bulk γ white phosphorus ($C2/m$) with different orientations. Black lines represent the conventional unit cell. Figure created with VESTA. Structural information from ICSD[26].

2.1.2. Red phosphorus

Amorphous red phosphorus (a-red P) is the second most abundant allotrope of phosphorus found in nature, following white phosphorus (white-P). Red P can be made from other allotropes, by heating white P at 260°C, or amorphous black P at 125°C (see Figure 1.2.). The term "red phosphorus" encompasses various forms, either amorphous or crystalline, all exhibiting a red color[15,27-29]. They display densities ranging from approximately 2.0 to 2.4 g.cm^{-3}. In terms of stability and reactivity, the red forms lie between the white and black forms, though they bear closer resemblance to the black form. There have only been few studies on the red forms of phosphorus and, up to now, only two crystalline phases, monoclinic and triclinic respectively, have been structurally characterized[34,38-39], although many more phases have been predicted, including hexagonal and tetragonal red phosphorus[29]. Raman spectra of several allotropes of red-P are shown in Figure 1.5., although only the monoclinic phase, known as Hittorf's or violet phosphorus, was identified.

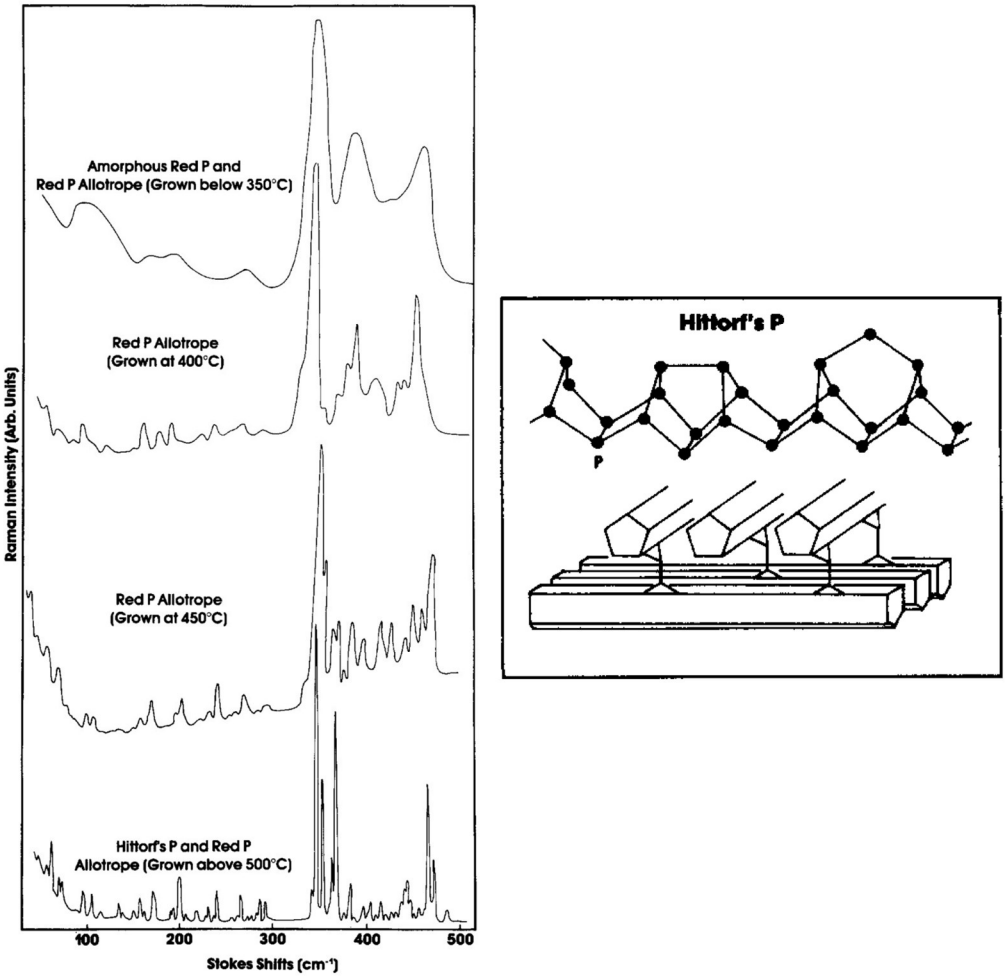

Figure 1.5. (Left) Raman spectra evolution of red phosphorus for different temperature of synthesis: (from top to bottom) Bulk amorphous red P, red P allotropes and Monoclinic Hittorf's structure. (Right) Representation of the Hittorf's monoclinic structure of red phosphorus. Figures from ref[35].

Hittorf's phosphorus, also known as violet phosphorus[37], has been the first allotrope of red phosphorus fully characterized[38-39]. It was originally obtained through the recrystallisation of the element from molten lead[38], who reported a space group *P*2*/n* and more recently through chemical vapor transport (CVT) method using amorphous red phosphorus as phosphorus source and Sn + SnI_4 as transport agents with fine control over the temperature[39], who reported a space group *P*2*/c*. Hittorf's violet phosphorus is a complex three-dimensional polymer, where each phosphorus atom adopts a pyramidal arrangement connected to three neighboring phosphorus atoms. It is composed of –[P2][P8][P2][P9]- tubular strands (Figure 1.7.). Layered structures are obtained when the tubular strands are covalently linked through [P9]. This arrangement forms a network of interconnected tubes, as depicted in Figure 1.6. These tubes, which have a

repeating unit of 21 phosphorus atoms and possess a pentagonal cross-section, are aligned parallel to each other, forming double layers. Notably, the tubes in one layer are packed perpendicular to those in the adjacent layer[38].

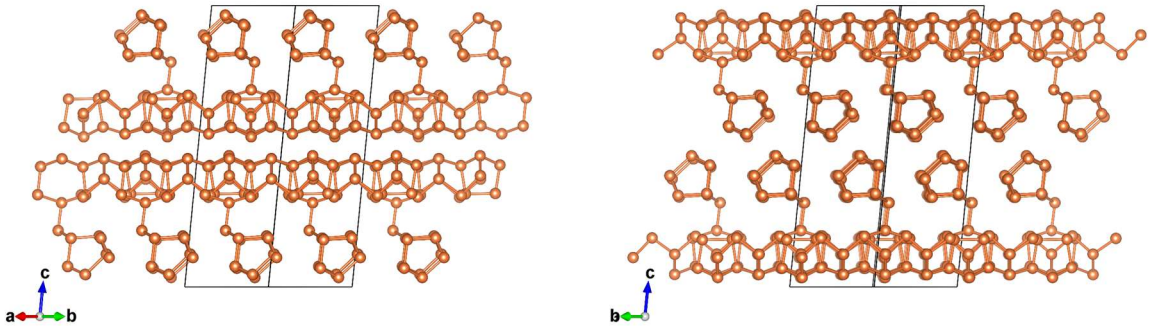

Figure 1.6. Crystal structures of bulk Hittorf's phosphorus ($P2/c$) with different orientations. Black lines represent the conventional unit cell. Figure created with VESTA. Structural information from ICSD[39].

Fibrous red phosphorus, the triclinic phase of red phosphorus, was the second and last structurally characterized variation of crystalline red phosphorus[34]. They synthesized the allotrope through iodine-catalyzed recrystallization of red phosphorus in small temperature gradients. Ruck and collaborators indicated that Hittorf's phosphorus was also produced at the same time[34]. The two structures have been predicted to be energetically equivalent. It was shown that the crystal structure of the fibrous type of crystalline red phosphorus is closely related to the structure of Hittorf's phosphorus. The fibrous one also consists of tubes with pentagonal cross section, with the same building unit (Figure 1.7.). The subunits are cages of eight or nine phosphorus atoms, and dumbbells of two phosphorus atoms in both allotropes.

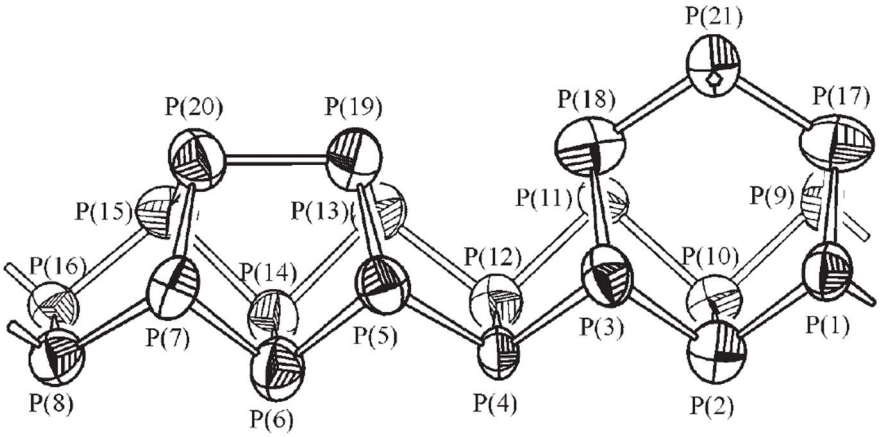

Figure 1.7. Repeating unit of the tubes in fibrous and in Hittorf's phosphorus. Thermal ellipsoids enclose the probability for atomic displacement.[34]

In contrast to Hittorf's phosphorus, the arrangement of tubes in fibrous red phosphorus are linked to parallel double tubes. The doubles tubes are stacked in the a direction and the space group symmetry is $P\bar{1}$. The packing density of the tubes in Hittorf's and fibrous phosphorus is very similar, although the arrangements of the tubes differs considerably.

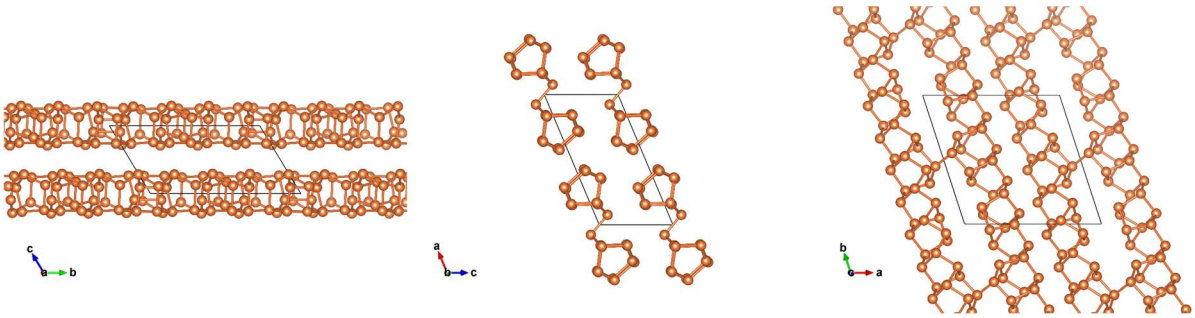

Figure 1.8. Crystal structures of bulk fibrous red phosphorus ($P\bar{1}$) with different orientations. Black lines represent the conventional unit cell. Figure created with VESTA. Structural information from ICSD[34]

Amorphous red phosphorus is also important in the framework of this thesis as it has been proposed that the high-density liquid (HDL) of phosphorus has a similar local atomic arrangement[8,32-33]. The molecular units of this structurally disordered form of phosphorus can be seen as a polymeric P_n network. The structure of amorphous red phosphorus has been investigated using neutron diffraction, x-ray diffraction, and simulations[40-46]. A principal discovery of those experiments is that amorphous red phosphorus comprises P_3 triangles and P_4 pyramidal subunit structures linked by chains of P atoms[43]. Analysis of the S(Q) profile, as

depicted in Figure 1.9., reveals diffraction peaks in amorphous red phosphorus located at 1 $Å^{-1}$, 2.2 $Å^{-1}$, and 3.75 $Å^{-1}$, followed by a series of subsidiary peaks at longer wavevectors. Notably, significant changes in the intensity ratio between the first and second peaks are observed under varying temperature and pressure conditions. Additionally, the pair distribution function (PDF) of amorphous red phosphorus, shown in Figure 1.9., exhibits two sharp peaks located at 2.22 Å and 3.49 Å, accompanied by subsidiary peaks at larger distances. The impact of pressure on the position of these two peaks has also been investigated: the displacement of the first- and second nearest neighbor PDF peaks is found to be -0.010 Å and -0.170 Å at 6.30 GPa. The coordination number of the nearest neighbors was found to remain virtually unaffected by compression[43], and pressure has minimal influence on the correlation lengths of short-range-order, such that the structure at 6.30 GPa exhibits no significant deformation.

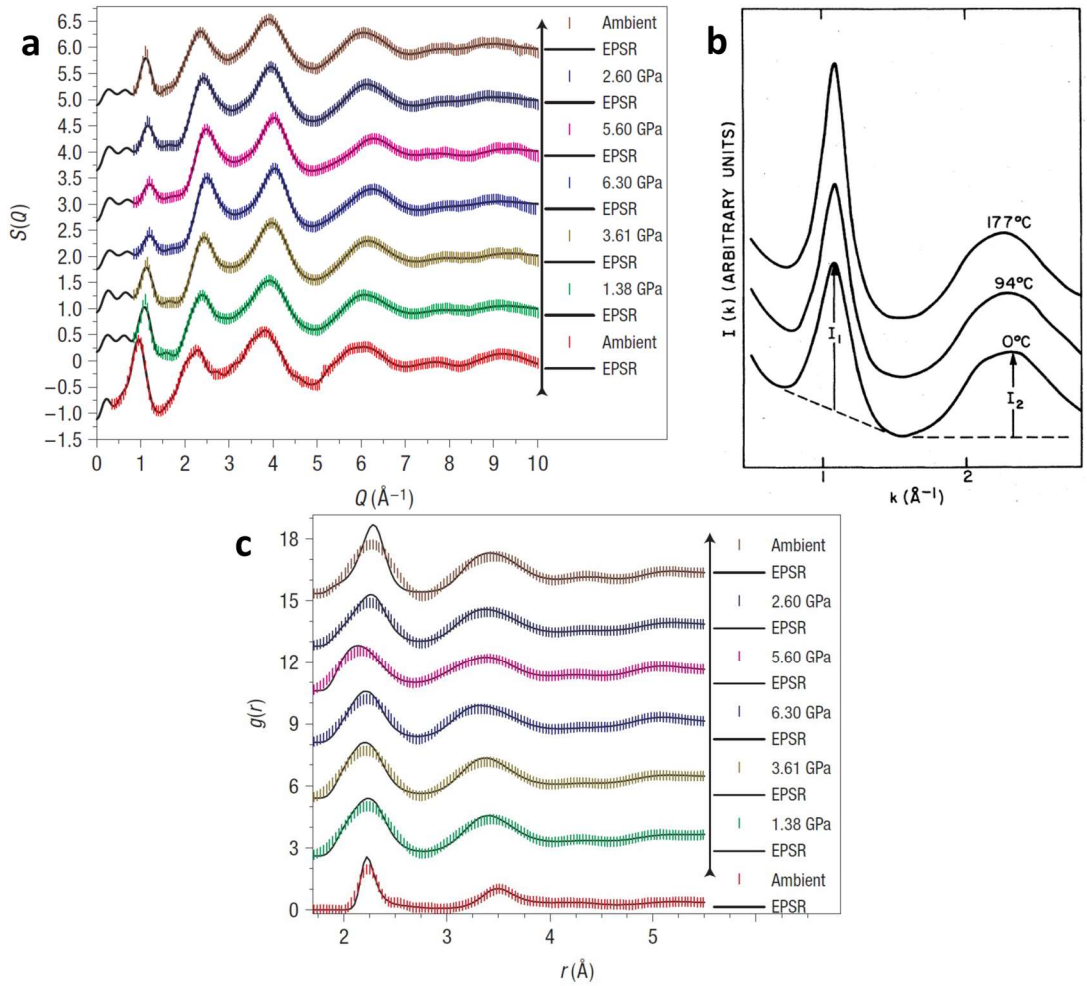

Figure 1.9. (a) Pressure evolution of modelled structure factors S(Q) results (solid black lines) compared against experimental S(Q) data from X-ray diffraction experiments[43]. (b) Temperature evolution of the relative intensity between the first two peaks of the diffraction pattern of amorphous red-P[40]. (c) Pressure evolution of modelled PDF results (solid black lines) compared against Fourier-transformed experimental S(Q) data of amorphous red-P[43].

2.1.3. Black phosphorus

Black phosphorus is the thermodynamically most stable form of the element[46], and it exists in three known crystalline structures as well as an amorphous form. It was first synthesized from white phosphorus by P. W. Bridgman[18] in 1914 under high pressure (P > 1.2 GPa) and high temperature (T > 500 K). Unlike white phosphorus, the black form is highly insoluble, practically non-inflammable, and exhibit relatively low vapor pressures. At ambient conditions, black phosphorus adopts an orthorhombic structure (space group *Cmce*), denoted A17 and consisting of stacked puckered layers. In this structure, each phosphorus atom forms three bonds with a length of 2.23 Å, arranged pyramidally at mutual angles of 100°. The

material exhibits strong covalent bonds within the layers and weak van der Waals forces between the layers, which allows to produce single-layer material known as Phosphorene through exfoliation techniques[47-48]. Orthorhombic black phosphorus is a semiconductor and shares flakiness characteristics similar to mica and graphite layer structures. Following the long-lasting prediction of P. W. Bridgman of high temperature decomposition of black phosphorus, recent studies have demonstrated that it actually undergoes thermal decomposition above 600 K[49-50].

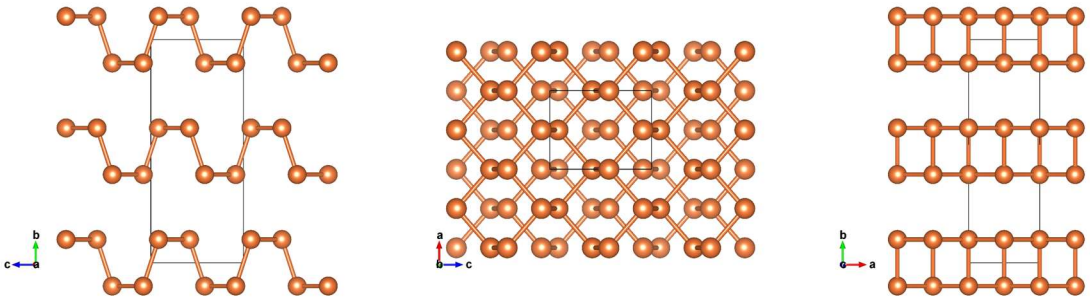

Figure 1.10. Crystal structures of bulk orthorhombic black phosphorus (*Cmce*) with different orientations. Black lines represent the conventional unit cell. Figure created with VESTA. Structural information from ICSD[51].

Under high pressures, the orthorhombic black phosphorus (bP) undergoes reversible transitions, leading to the formation of more densely packed rhombohedral and cubic forms[52], like other elements of the group VB[53]. At ambient temperature, A17 black phosphorus maintains its orthorhombic structure up to 4.8 GPa[54]. Beyond this pressure, black phosphorus transforms into a rhombohedral structure with the space group $R\text{-}3m$, known as A7[53]. The A7 structure corresponds to a lamellar compound, with its single layer known as blue phosphorene. In the rhombohedral form, the hexagonal layers are less folded compared to the orthorhombic form. The puckered sheets in the rhombohedral form can be linked to the flat hexagonal sheets of carbon atoms in graphite, commonly known as 'graphene' sheets.

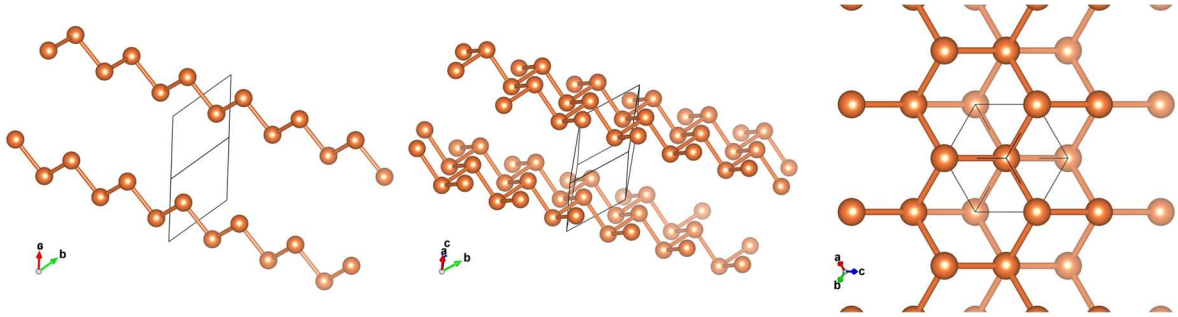

Figure 1.11. Crystal structures of bulk rhombohedral black phosphorus (R-3m) with different orientations. Black lines represent the conventional unit cell. Figure created with VESTA. Structural information from ICSD[54]

Phosphorus retains its rhombohedral structure until 10.5 GPa where it undergoes a first-order structural transformation to the pseudo-simple cubic (p-sc) phase adopting still a rhombohedral cell[53]. The later remains stable up to 100 GPa at which point it undergoes a further transformation into a metallic, nonlayered simple cubic structure (sc) with the space group $Pm3m$ (Z =1). The cubic form of black phosphorus can be derived from the rhombohedral form by reducing the interbond angles from 100° to 90° and bringing the layers closer together. In the cubic form, each atom assumes an octahedral environment. In the present thesis work, all experimental work has been carried out at pressures below 6 GPa. Therefore, we will mainly consider the A17 and A7 phases of black phosphorus.

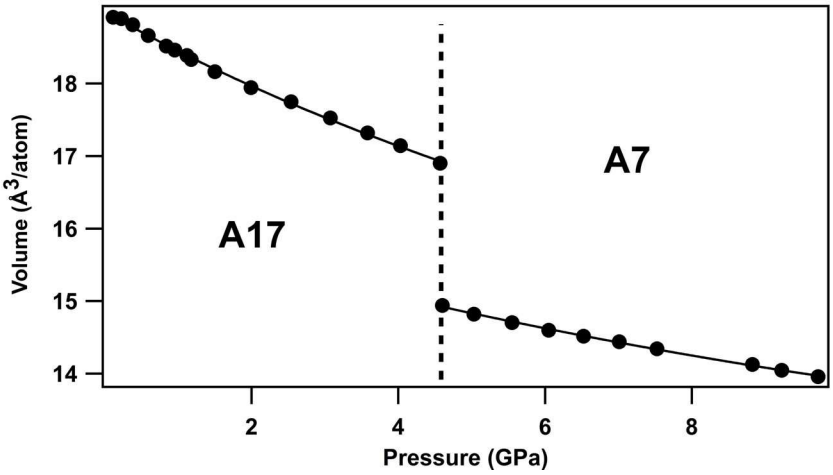

Figure 1.12. Equation of state of black phosphorus at ambient temperature. A phase transition between orthorhombic $Cmce$ (A17) and rhombohedral R-3m (A7) is observed at 4.8 GPa.[53]

Due to its double-layered structure, with strong covalent intralayer bonds with sp^3 hybridization and weak van der Waals interlayers forces, orthorhombic black phosphorus exhibits very contrasting directional thermo-elastic properties (or thermal equations of state EoS). The precise determination of the EoS parameters of orthorhombic black phosphorus is made very difficult due to the weak pressure and temperature variations of the intra-plane inter-atomic distances. Indeed, the intra-plane compressibility is 1 to 2 orders of magnitude lower than the inter-plane ones[53,55-58]. Additionally, nonlinear pressure and temperature effects have also been reported, although not yet precisely quantified[59-62].

2.2. Melting curve of black phosphorus

Figure 1.13. illustrates the significant discrepancies existing between the various literature determination of the melting line of black phosphorus. Some researchers, namely Akahama et al.[63], Mizutani et al.[64], and Solozhenko et al.[65], have suggested that there is a maximum at the triple point, where black phosphorus, the low-density liquid (LDL), and the high-density liquid (HDL) coexist. However, Guarise et al.[66] have argued for a continuous increase of the melting curve.

Akahama's work[63], conducted using X-ray diffraction in a large volume press, is considered the reference melting curve for black phosphorus. It contradicts Marani and Guarise's earlier work[66] which reported a continuously increasing melting curve. Solozhenko et al.[65] also observed a maximum point in the melting curve, although the location of that maximum differs from the one reported by Akahama and collaborators[63]. However, Solozhenko et al.[65] only reported three melting points in the 0-3 GPa pressure range, making it challenging to confirm the presence of such a maximum. Akahama's results imply that the HDL is denser than solid orthorhombic black phosphorus below the melting point, explaining the decrease in melting temperature (Tm) with pressure in the 1 – 2.7 GPa pressure range. At approximately 2.7 GPa and 1150 K, the triple point of the orthorhombic, rhombohedral, and liquid phase is reached, and beyond this pressure, the melting curve shows a positive slope. Lastly, Mizutani et al.[64] latest work, using the same methodology as Akahama et al.[63], have provided evidence of a break in the melting curve, indicating the presence of a triple point. The authors have argued that the previously reported maximum point in the melting curve from Akahama[63] was due to limited statistical data above 1 GPa.

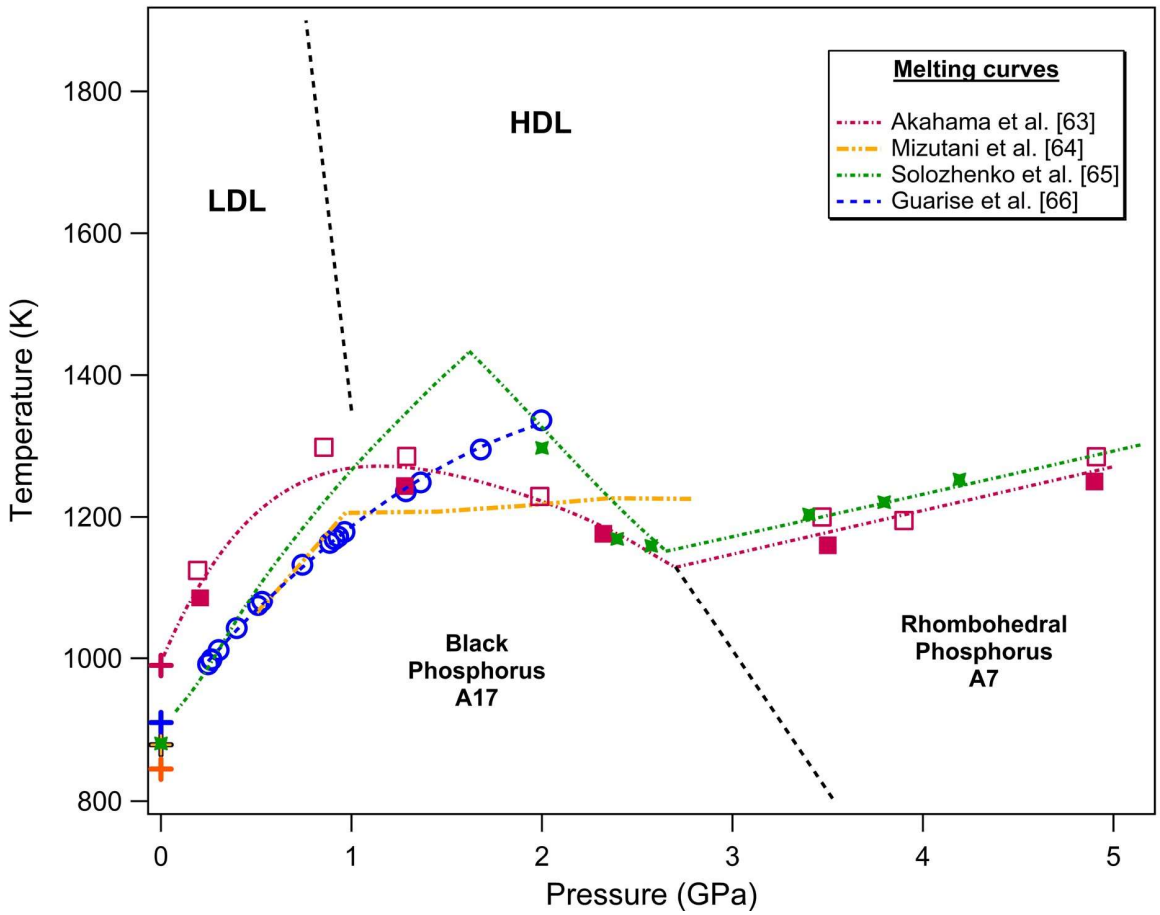

Figure 1.13. Phase diagram of black phosphorus with several melting curves from the literature: Akahama[63] and Solozhenko[65] have reported the existence of a maximum in the melting curve, although not at the same pressure, Guarise[66] has reported a monotonous increase of the melting temperature with respect to the pressure, and finally, Mizutani has shown that the melting curve presents a break concomitant to the intersection of the liquid-liquid transition line.

2.3. Molten white P

At ambient P, white-P melts at a temperature of 317 K. We will refer to this liquid as molten white-P. This liquid was investigated in the stable (T=323 K) and supercooled regime (283-303 K) by neutron diffraction[67]. Figure 1.14. depicts the diffraction patterns and the intermolecular contribution to the structure factor $D_M(Q)$ of molten white phosphorus at 323 K. The diffraction data is consistent with a liquid composed of P_4 molecules with a P-P bond length of 2.21 Å as in the solid white-P and the vapour phase. It is also characterized by the presence of a first sharp diffraction peak (FSDP) occurring around 1.3 $Å^{-1}$, indicating the existence of medium-range orientational ordering of the P_4 tetrahedra. The local structure of molten white phosphorus closely resembles that of solid white phosphorus. In the liquid state, P atoms exhibit

three-fold coordination, which arises from their electronic configuration, with P-P distances similar to those observed in solid white phosphorus. At greater distances, the pair distribution function (PDF) exhibits weak oscillations attributable to the feeble intermolecular interactions[67]. The density of molten white phosphorus at 323 K is measured to be 1.74 g.cm^{-3}, a value close to that of solid white phosphorus after correcting for thermal expansion effects.

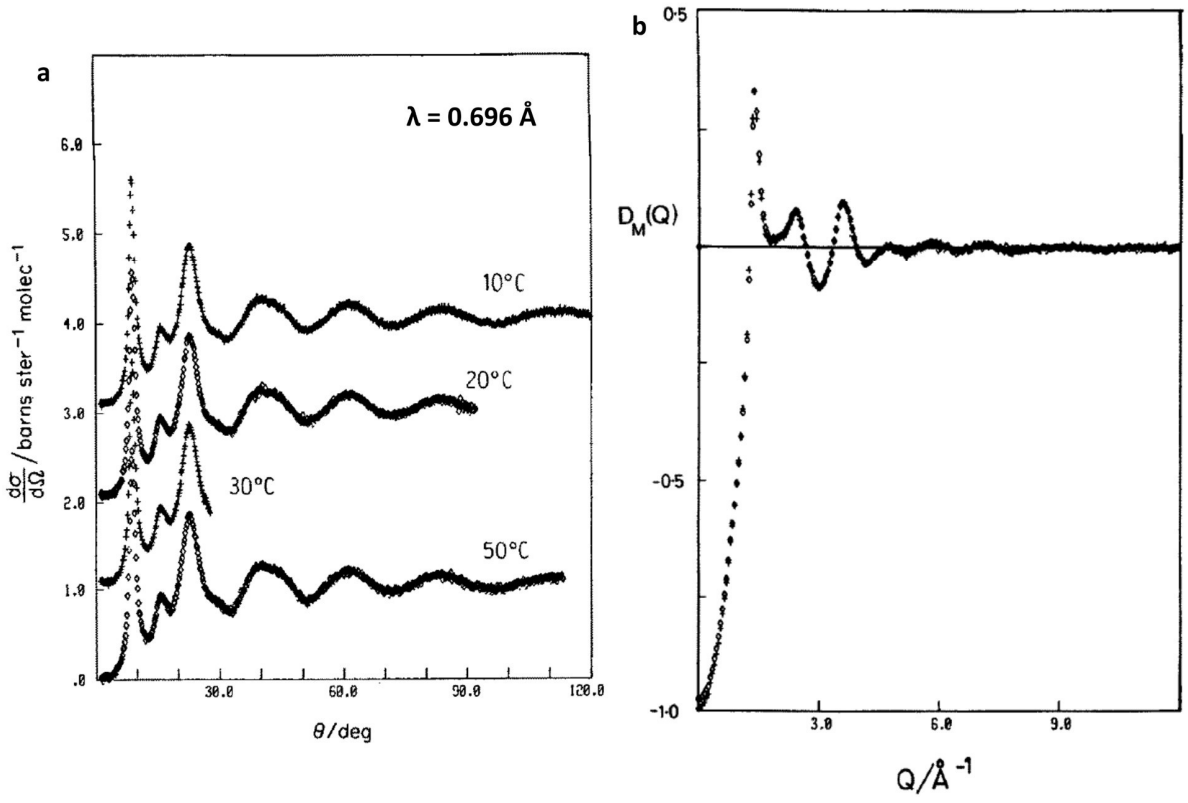

Figure 1.14. (a) Neutron diffraction patterns for white phosphorus in the normal and supercooled liquid phases. (b) Intermolecular contribution to the structure factor $D_M(Q)$ (S(Q) = f(Q) + $D_M(Q)$) where f(Q) is the molecular form factor of the P_4 molecule and S(Q) is the structure factor of molten white phosphorus. From ref[67].

Liquid white phosphorus holds significant importance within the context of this thesis. It is recognized that the low-density liquid (LDL) phase of black phosphorus shares similarities with liquid white phosphorus in terms of their molecular composition, both consisting of P_4 molecules.

2.4. The liquid-liquid phase transition of phosphorus

In 2000, Y. Katayama and collaborators[8] reported the existence of a first-order liquid-liquid phase transition in phosphorus. This discovery is of considerable scientific significance as it presents the first conclusive evidence supporting the occurrence of transitions between two distinct liquid phases, characterized by differing density and entropy. This section aims to provide crucial structural details about the low- and high-density liquids, while also delving into the thermodynamics of the transformation process using existing theoretical models documented in the scientific literature.

2.4.1. Microscopic and macroscopic changes in liquid phosphorus

Hohl[32], through molecular dynamics (MD) simulations, initially predicted the occurrence of an ambient pressure high-temperature phase transition in the liquid state of phosphorus. In his study, the transformation is conceptualized as a polymerization process induced by defects, wherein the opening of P_4 tetrahedra initiates a chain reaction that spreads throughout the sample, resulting in the formation of a liquid resembling amorphous red phosphorus. However, experimentally, the transformation from solid white P to red P is a very slow process, requiring typically several days at temperatures between 500 K and 600 K. This presents an onerous issue for MD simulations, where accessible time scales are orders of magnitude shorter. Hence, Hohl[32] accelerated the polymerization process in his simulations by using temperatures that are much above the melting point. As a result, he successfully simulated the phase transition in the range of 3000 to 3500 K.

In 2000, Katayama and collaborators[8] provided the first experimental evidence of an unambiguous first order phase transition between two liquid states of phosphorus, distinguished by their distinct density and entropy, and this work was subsequently re-examined by Monaco et al[68]. Using in situ energy dispersive X-ray diffraction in a multi-anvil apparatus, Katayama et al. investigated this liquid structure factors along an isothermal pathway at approximately 1300 K, as depicted in Figure 1.15.

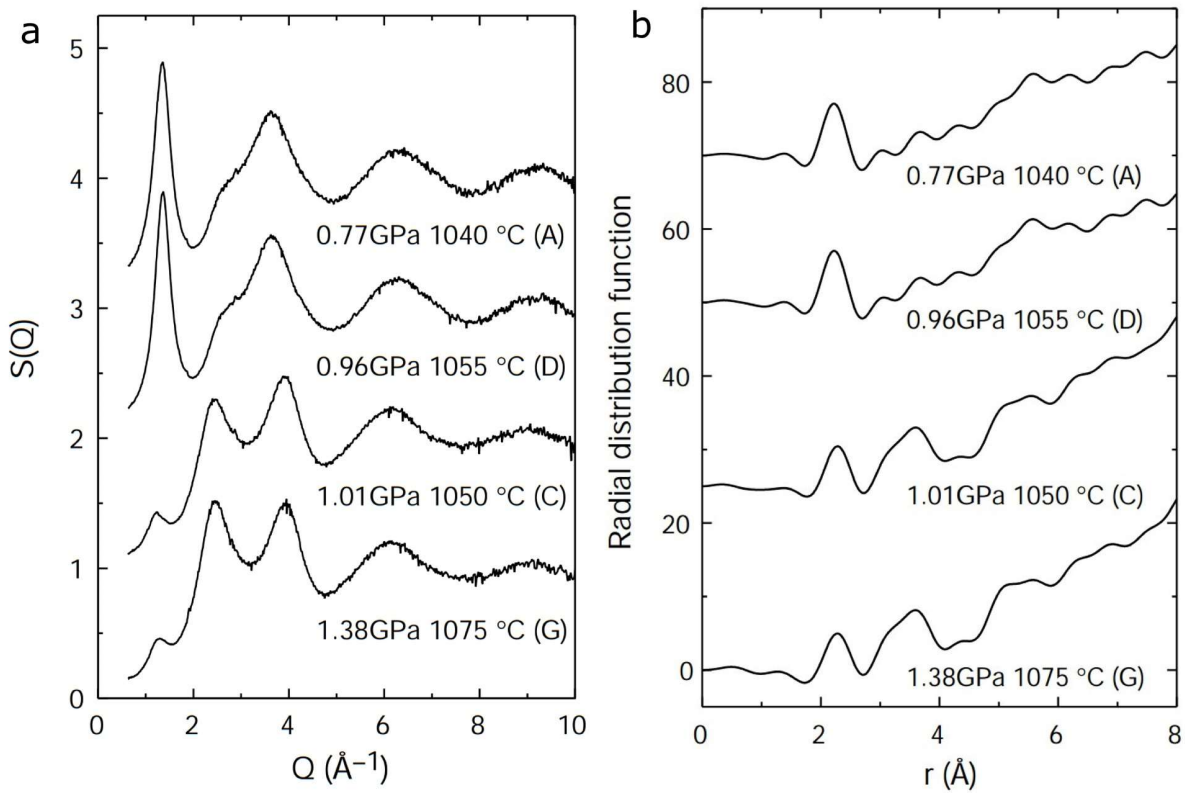

Figure 1.15. (a) Structure factors S(Q) of liquid phosphorus at selected pressures on isothermal compression around 1300 K. (b) Associated radial distribution function RDF. From Katayama et al.[8]

In the low-pressure region below 0.96 GPa, the liquid phosphorus structure factor closely resembles that of the molten white phosphorus. Notably, it exhibits a characteristic first sharp diffraction peak (FSDP) at 1.4 $Å^{-1}$, indicative of intermediate-range order correlations among the tetrahedral P_4 units present in the liquid state at low pressure. In their study, the abrupt disappearance of the FSDP upon pressurization served as the primary criterion to establish the first-order nature of the liquid-liquid transition. As shown in Figure 1.15., the FSDP collapses within a narrow pressure range ($\Delta P < 0.05$ GPa), accompanied by the emergence of two broad peaks at 2.5 $Å^{-1}$ and 4.0 $Å^{-1}$ in the structure factor.

Significant modifications are also observed in the corresponding radial distribution functions. Firstly, the distance between first-neighbor atoms increases from 2.22 Å to 2.28 Å. Secondly, a distinct second peak appears at 3.5 Å. These pronounced correlations at distances beyond the first neighbor shell support the notion of a polymeric liquid. Drawing an analogy between the structure factor of the high-pressure liquid and that of amorphous red phosphorus,

the researchers postulated that these two forms share similar local atomic arrangements with polymer-like characteristics.

In a subsequent publication, Katayama and collaborators[25] presented additional macroscopic evidence supporting the existence of the liquid-liquid transition. Illustrated in Figure 1.16., their findings highlight a significant density discontinuity exceeding 40% across the transition. Furthermore, they provided a x-ray radiographic image showcasing the coexistence of the two distinct liquid phases. Upon compression of the low-pressure fluid, the radiographic image revealed the emergence of dark spherical "object". X-ray diffraction measurements corroborated that these entities corresponded to the high-pressure liquid phase. Over time, these droplets expanded and gradually occupied the entire sample volume. Conversely, the reverse process was observed upon decompression.

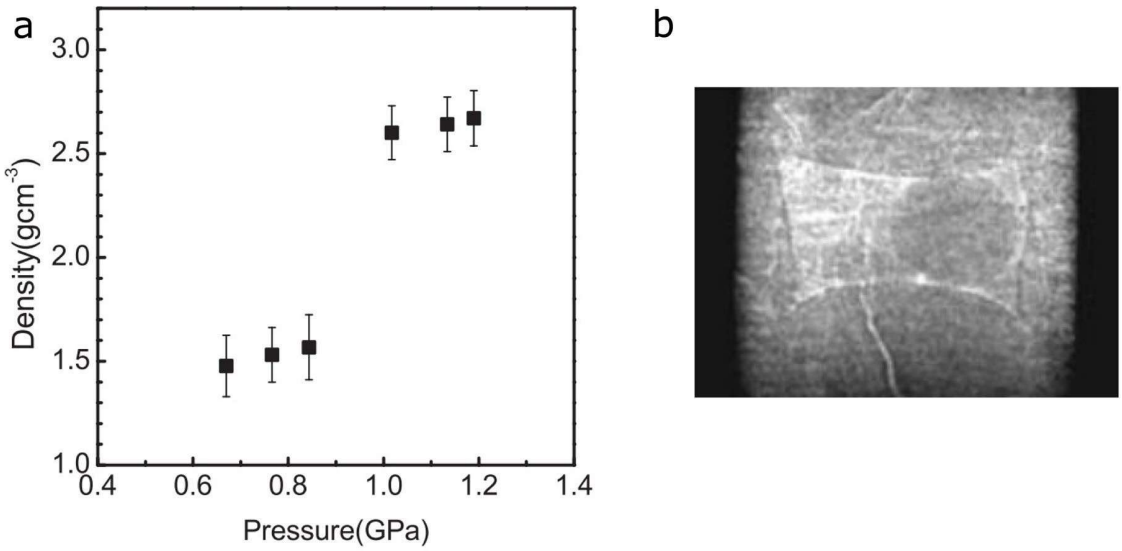

Figure 1.16. (a) Pressure dependence of the density of liquid phosphorus at 1300 K showing a density jump of about 40% of the high-density liquid around 1 GPa. (b) Snapshot of droplet of high-density liquid (dark round object in the image) inside the low-density liquid during the transition. From ref[25].

The groundbreaking research conducted by Y. Katayama et al.[8,25] has spurred numerous and theoretical investigations. G. Monaco and colleagues[68] have further explored the liquid state of phosphorus in a wider range of pressure and temperature (P-T) conditions. In their study, they utilized *in situ* X-ray diffraction within the Paris-Edinburgh press to determine the position of the liquid-liquid transition line. They employed the same criteria as Katayama et

al.[8], where the transformation is identified by the disappearance of the FSDP (First Sharp Diffraction Peak) in the liquid structure factor. As shown in Figure 1.17., they measured the liquid-liquid transition line across an expanded temperature range, reaching up to 2300 K. Their findings revealed a negative slope of the liquid-liquid transition in the P-T phase diagram, and employing the Clapeyron equation, they estimated the latent heat associated with the transformation. By incorporating this transition line into the established phase diagram of P_4, they proposed a first-order transition between a dense molecular fluid and a polymeric liquid, referring to it as a fluid-liquid phase transition (FLPT). This conclusion was based on the hypothetical location of the critical point that terminates the boiling line of white-P, located at 968 K and 8.2 MPa in the metastable phase diagram, as shown in Figure 1.17. They concluded that the transformation occurs between a dense molecular fluid and a polymeric liquid. However, the existence and precise location of the liquid-gas critical point was never directly measured. Thus, one objective of this thesis is to verify the existence of the sublimation of black P and validate or not the fluid nature of the low-density melt.

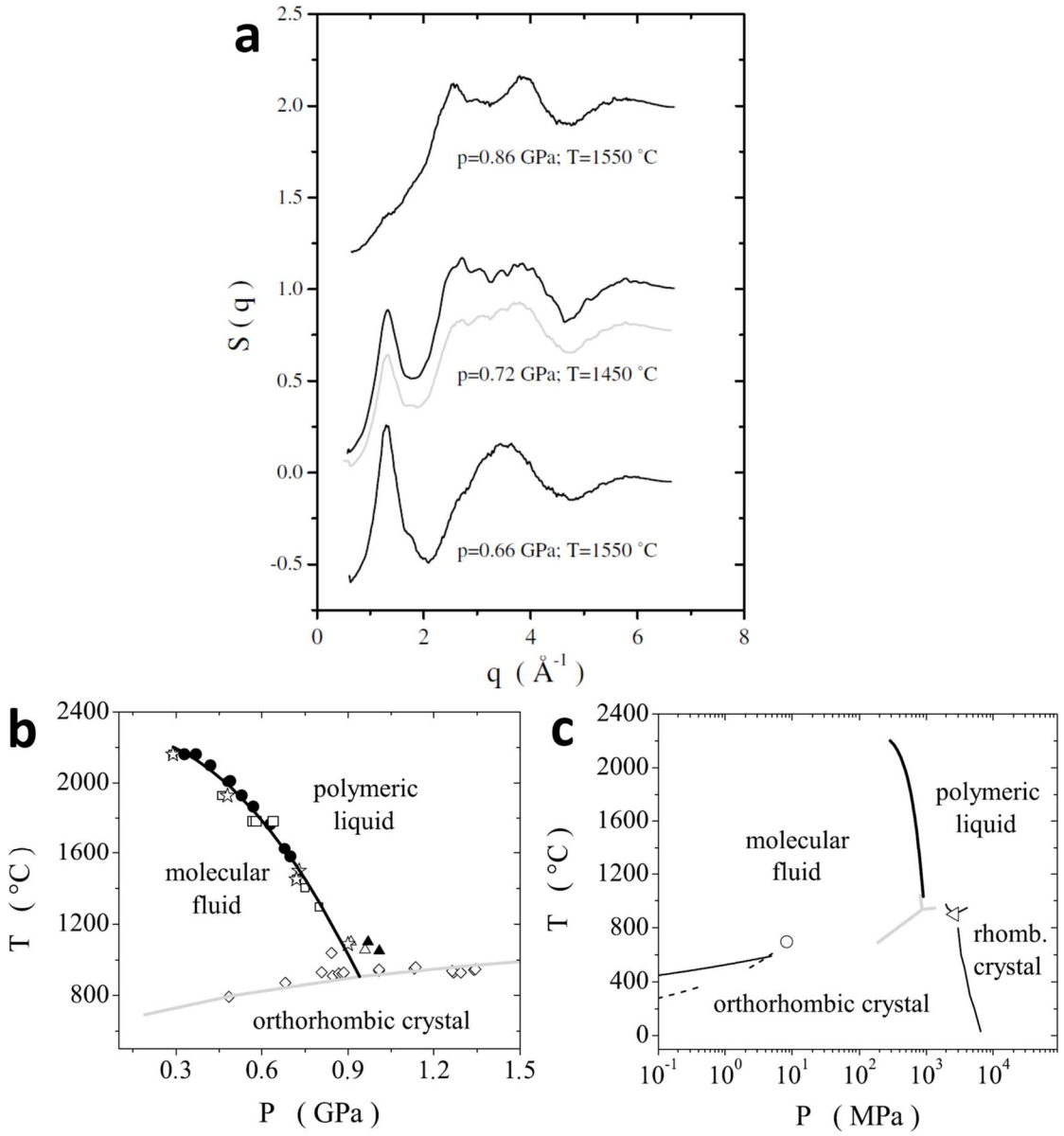

Figure 1.17. (a) Structure factor S(Q) corresponding to the coexistence point on the transition line at 0.72 GPa and 1450°C compared with a pattern in the molecular phase (lower plot) and one in the polymeric phase (upper plot). (b) The high-pressure high temperature phase diagram of phosphorus in the region where the first-order phase transition occurs, as constructed by Monaco et al.[68] (c) Simplified version of the phase diagram of phosphorus in semilog scale: the black circle corresponds to the calculated liquid-gas critical point (LGCP). From ref[68].

The composition of the low-density fluid (LDF), or low-density liquid (LDL), has been accepted as consisting of P_4 tetrahedral units. However, there has been ongoing debate regarding the structure of the high-density liquid (HDL) for the past two decades. Notably, Senda and collaborators[33] conducted an extensive investigation of the HDL through *ab-initio*

molecular dynamics simulations, providing valuable insights. Figure 1.18. illustrates their ability to accurately replicate the first-order liquid-liquid transition and structure factors of the two liquids by manipulating the density. For densities below 2 g.cm^{-3}, they confirmed the presence of highly stable P_4 molecules in the liquid, as evidenced by a distinct and sharp first peak in the pair distribution function g(r). Based on the similarities observed in the distribution of bond angles, Senda et al.[33] proposed that the local structure of the HDL likely resembles that of amorphous red phosphorus and black phosphorus.

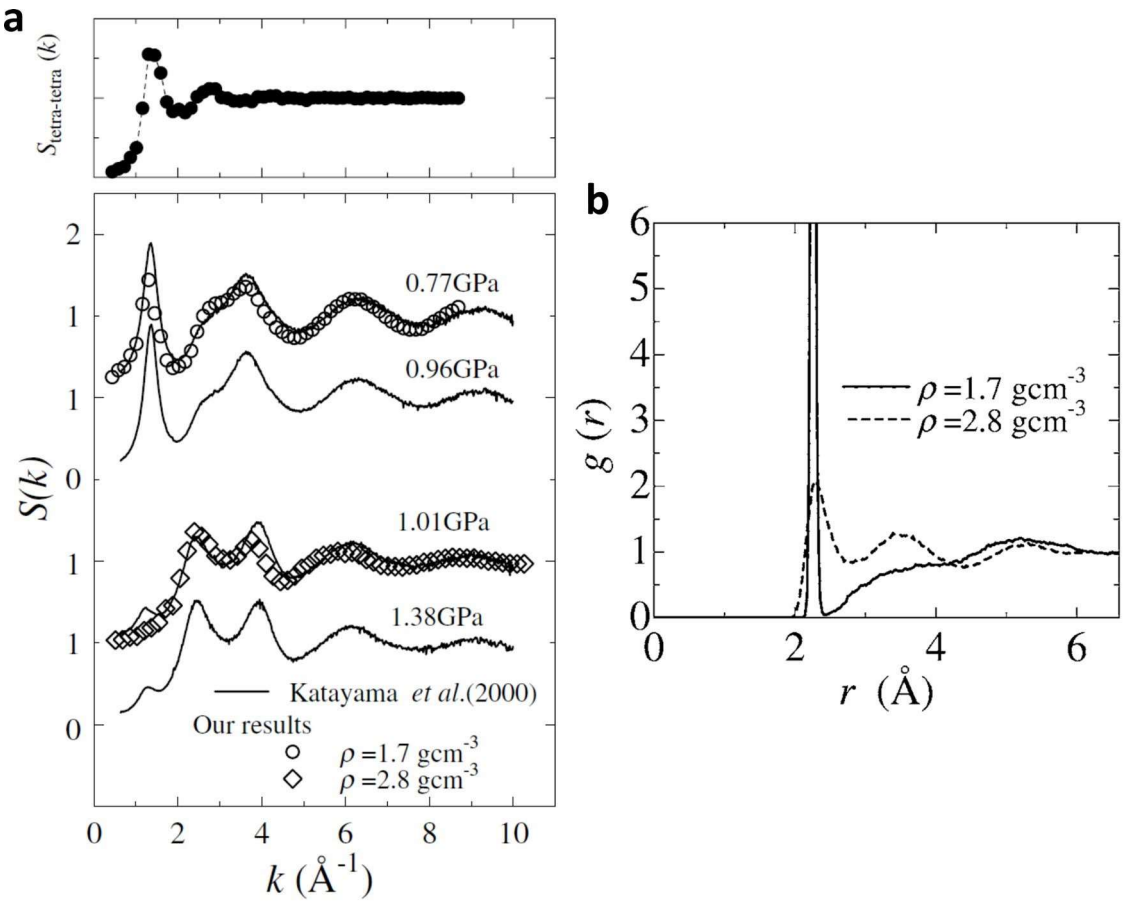

Figure 1.18. (a) The bottom panel shows the structure factor for liquid P at low and high-density generated by ab-initio molecular dynamics compared with the experimental ones. The upper panel shows the pair correlation function between the centers of mass of the P_4 tetrahedral molecules for the low-density liquid. (b) The g(r) for liquid P with the low- and high- density. From ref[33].

Figure 1.19. illustrates the distribution function P(n), which represents the probability of a P ion having n neighboring P ions within its first coordination shell at a distance of r of 2.28 Å from the central atom, which corresponds to the distance of the first-neighbor given by

the g(r) function. In the low-density liquid, P(n) is strictly equal to 3, indicating a consistent and uniform coordination environment. On the other hand, in the high-density phosphorus liquid, P(n) can adopt various values ranging from 1 to 5. This observation suggests that chemical bonds undergo breaking and rearrangements within the high-density liquid, leading to a more intricate local structure. Snapshots of the ionic configurations of the high- and low-density liquids are presented in Figure 19 to visually demonstrate these distinctions.

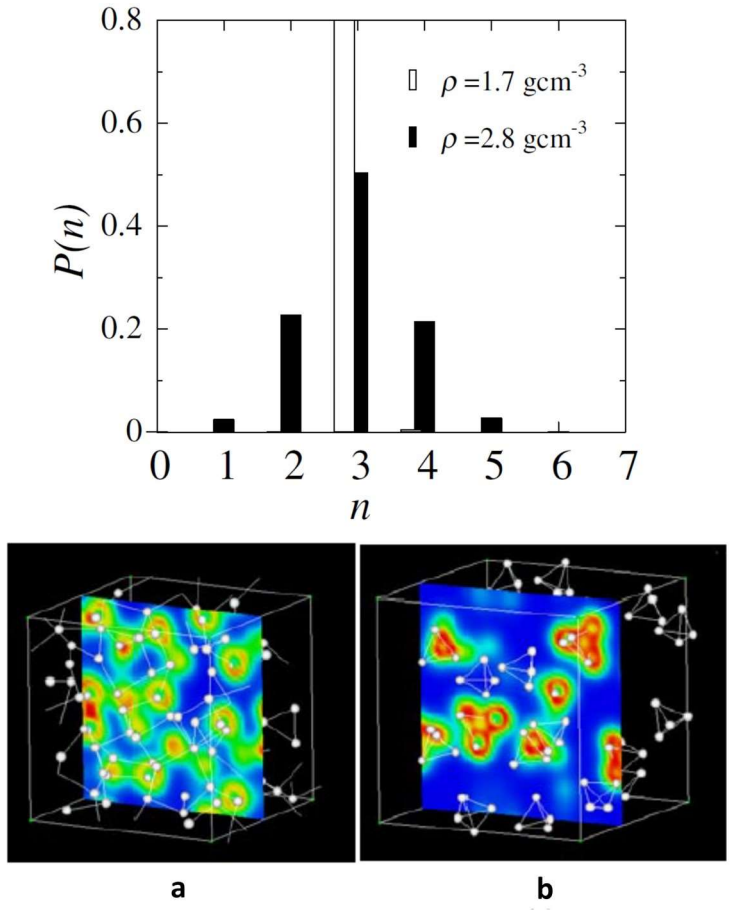

Figure 1.19. Upper plot shows the distribution function P(n) for the coordination number of P ions in liquid P. Lower plots shows snapshots of ionic configurations and the electron density distribution for liquid P with (a) the high-density and (b) the low-density forms. From ref[33].

2.4.2. Thermodynamics of the liquid-liquid phase transition in phosphorus and the liquid-liquid critical point

In the preceding discussion, we have observed a transition occurring in liquid phosphorus, characterized by a conversion from a low-density molecular liquid to a high-density polymeric liquid[8,68]. This transformation is distinguished by substantial structural

modifications and a sudden increase in density exceeding 40%[25], indicative of a first-order phase transition. Various models have been developed to comprehend the thermodynamic nature of such liquid-liquid transitions (LLT) in general.

Murata and Tanaka[69] proposed a two-order parameters model that incorporates density and a bond-order parameter to account for locally favored structures and explain the existence of liquid-liquid transitions. In the case of water, the putative LLT has been attributed to an entropy-driven process, employing a model that considers water as an "athermal solution" with two molecular structures possessing distinct entropies and densities[70]. Another model, the two-liquid model[71], suggests that the liquid state comprises a mixture of two phases, with their relative concentrations dependent on external parameters. Additionally, explanations for LLTs encompass considerations of an anisotropic potential[71-74], while it has also been proposed that LLTs can emerge even with an isotropic pair interaction potential possessing two characteristic lengths[73]. Despite multiple attempts to describe the thermodynamic nature of LLT, a consensus model has not yet been achieved.

Recently, Zhao et al.[74] conducted ab-initio computer simulations to investigate the thermodynamics of phosphorus. Figure 1.20. demonstrates that Zhao et al.[74] successfully replicated the LLT and associated structure factors with high precision.

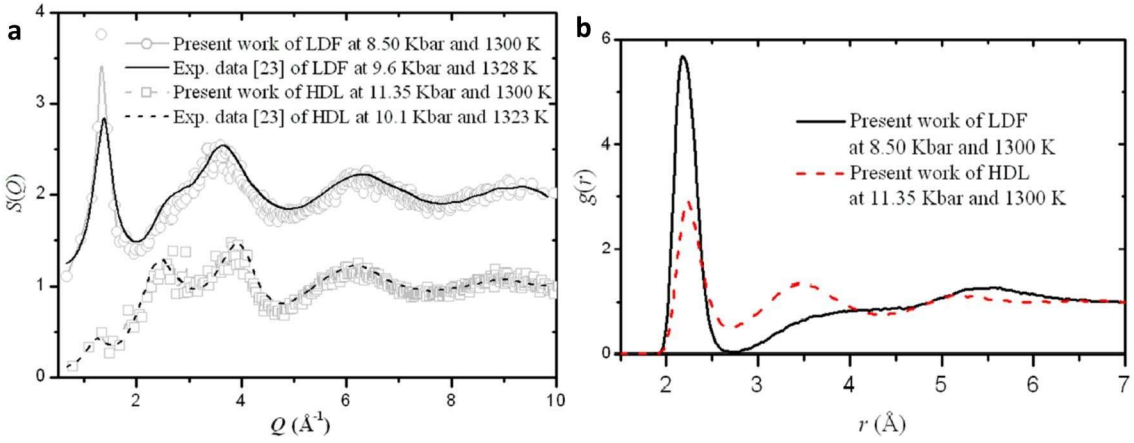

Figure 1.20. (a) Zhao's calculated structure factors S(Q) of the HDL and LDF[74], in good agreement with experimental data of Y. Katayama[8]. (b) Corresponding pair correlation functions g(r) of the HDL and LDF. From ref[74].

Figure 1.21. presents a significant outcome of this study, revealing a notable observation regarding the density jump's temperature dependence during the liquid-liquid transition (LLT).

It is observed that as the temperature decreases from 3500 K, the density jump initially rises from zero, reaches a maximum value, and subsequently declines. This behavior stands in contrast to the monotonic increase in density observed during liquid-gas transitions (LGT).

This non-monotonic variation suggests that the order parameter characterizing the LLT encompasses contributions from both density and entropy. Particularly, at lower temperatures, entropy appears to govern the transition rather than density. This finding contradicts the case of LGT, where density solely acts as the order parameter.

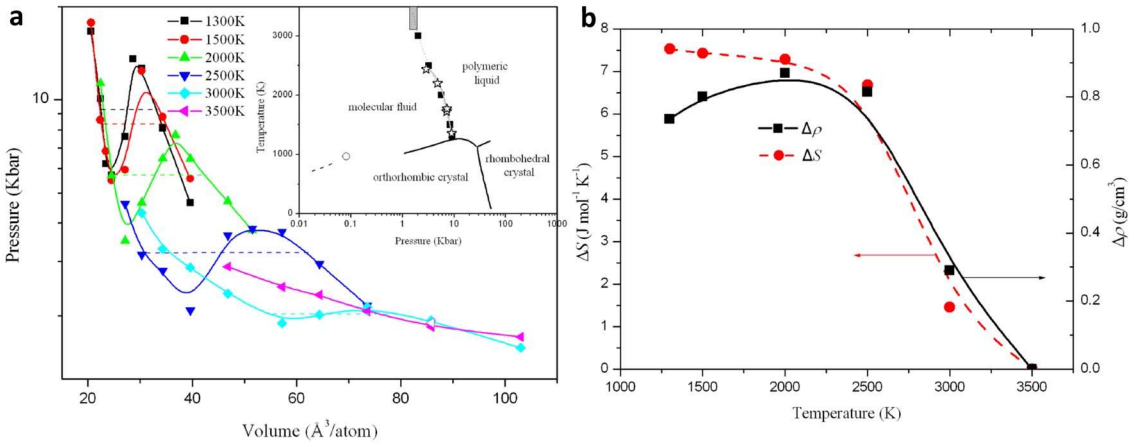

Figure 1.21. (a) Calculated expansion isotherms between 1300 K and 3500 K. (b) Calculated density difference and entropy difference between two coexisting phases along the transition line as a function of temperature. From ref[74].

This study also predicted the presence of a liquid-liquid critical point (LLCP) marking the termination of the liquid-liquid transition at a pressure of approximately 0.2 GPa and a temperature of around 3500 K, where the volume variation becomes zero. The experimental confirmation of such an LLCP associated with LLTs remains elusive and continues to be a subject of intense scientific debates and ongoing investigations within the scientific community.

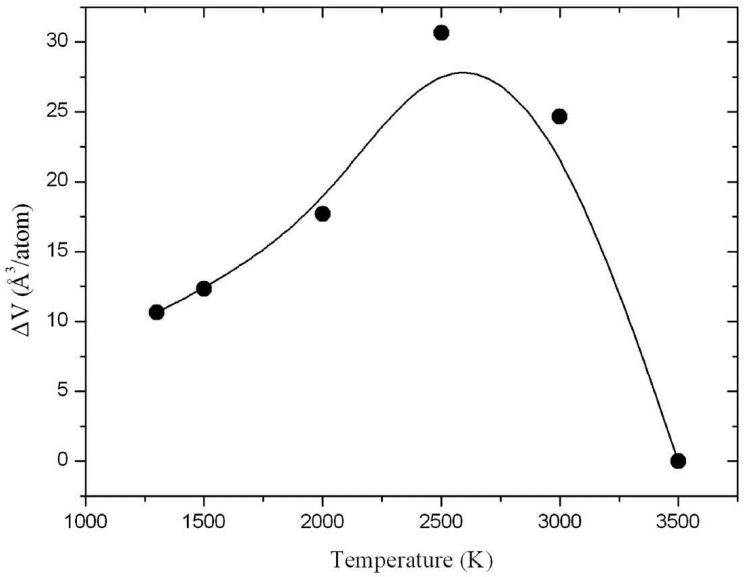

Figure 1.22. Calculated volume difference (ΔV) between two coexisting phases along the fluid-liquid transition line. A non-monotonic dependence of ΔV on temperature and an obvious maximum at about 2500 K are observed.

This subject holds significant relevance, particularly in the case of water, where multiple proposals have been put forth to understand the density anomalies observed in its supercooled regime[75]. These proposals encompass the potential existence of an LLCP[1], as well as more general thermodynamic constraints without any singularities[76], and the possibility of a transition occurring without a critical point[77].

In a more recent study, Yang and colleagues[78] employed high-quality ab-initio molecular dynamics simulations to investigate the liquid-liquid transition and explore a substantial portion of the phosphorus phase diagram's liquid regime. They successfully constructed the liquid-liquid coexistence curve across a wide temperature range and determined that it terminates at a second-order critical point. However, the critical point was found to occur at different conditions than previously suggested, specifically at 2750 K and 0.2 GPa. Notably, in close proximity to the critical point, the simulations revealed significant fluctuations in both structural and electronic properties. The observations of Yang et al.[78] align with the experimental findings, particularly the negative slope observed for the coexistence line.

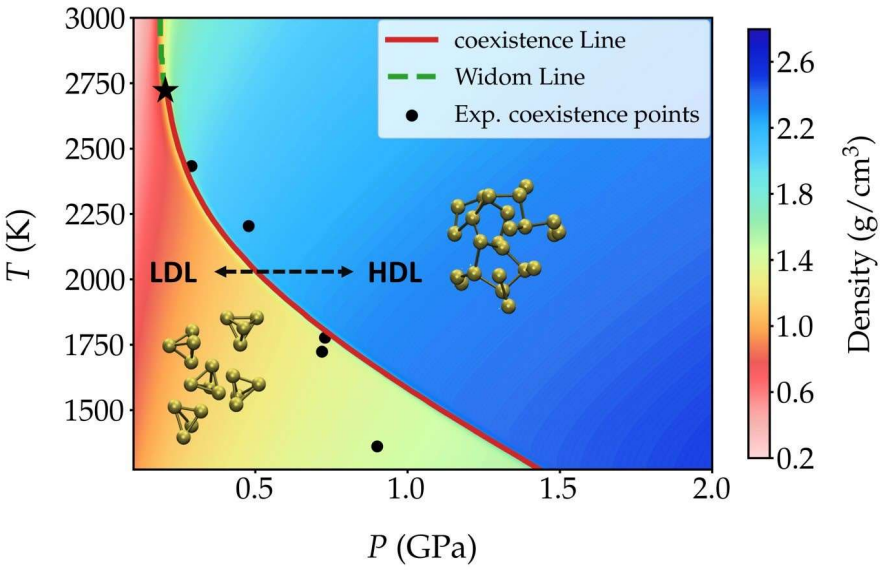

Figure 1.23. Liquid phosphorus phase diagram : the value of the density as a function of T and P is also plotted. Black points denote the experimental coexistence points. The calculated liquid-liquid critical point is indicated by the black star.

Furthermore, they conducted simulations to examine the structural evolution of the system within the critical region. Figure 1.24. portrays the extensive density fluctuations characteristic of a system in its critical state, where one phase undergoes permanent transformation into another and vice versa. The figure also illustrates the typical density evolution as the system transforms from the polymeric to the molecular phase. This density change accompanies the transformation from a metallic to a non-metallic phase, as evidenced by the density of states (DOS). Additionally, the structural evolution from the polymeric phase to the molecular phase through various intermediate states is depicted.

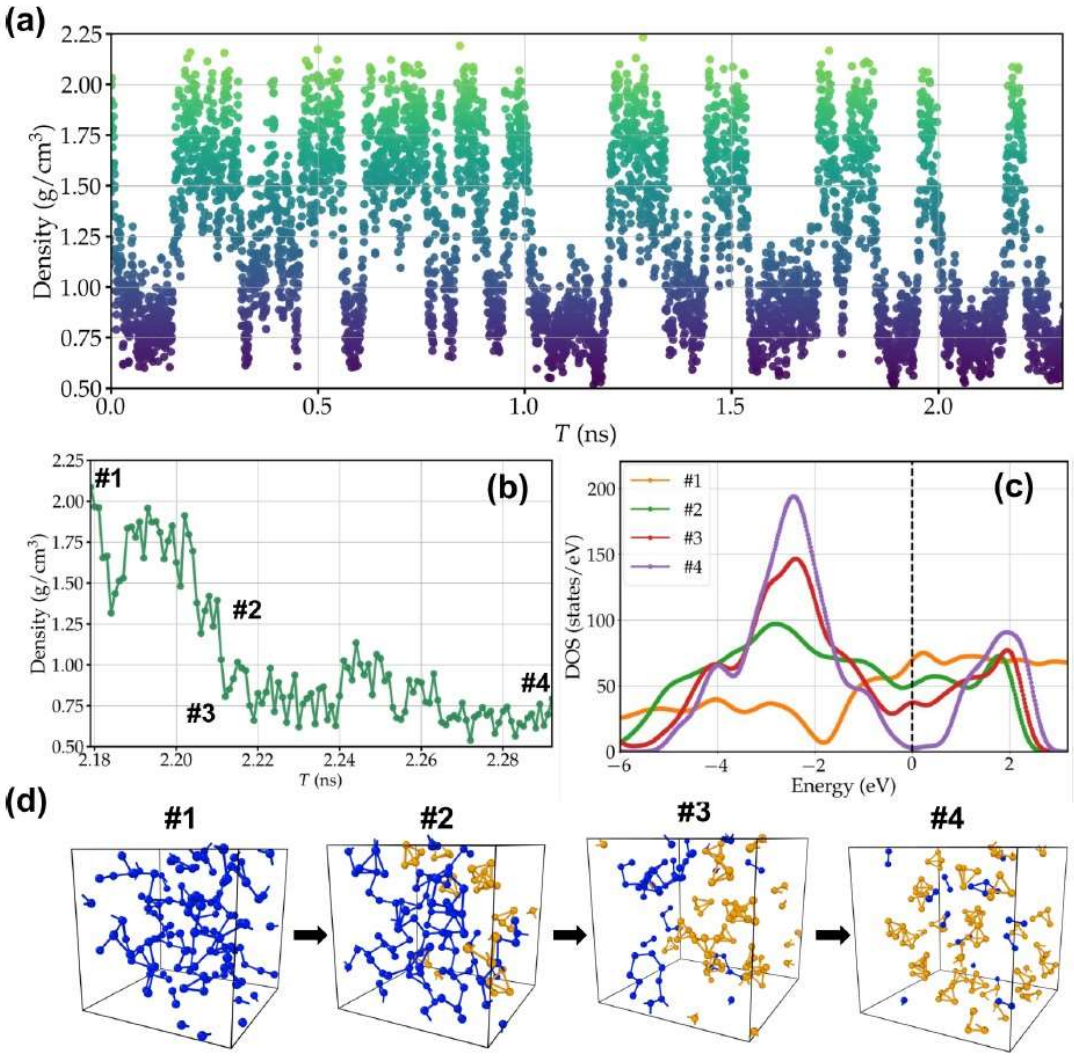

Figure 1.24. (a) Density as a function of the simulation time at T = 2700 K and P = 0.2 GPa. The evolution of (b) density, (c) DOS, and (d) structures as the system transits from the polymeric to the molecular phase. Atoms belonging to polymers are shown in blue while those belonging to the P_4 units are displayed in orange. From ref[78] SI.

Conclusion

In summary, despite extensive experimental and theoretical investigations conducted on phosphorus, numerous fundamental questions remain unresolved. Substantial disparities exist among the various phase diagrams documented in the literature, particularly regarding the precise location and shape of the liquid-liquid transition and the melting line. Only one density measurement has been conducted across the LLT, and it was at relatively low temperature. Furthermore, no density data is available for the melting of black phosphorus. The evolution of

the density variation across these two first-order phase transitions under varying pressure and temperature conditions remains unknown. Theoretical studies have suggested the possible existence of a liquid-liquid critical point marking the termination of the LLT line, but this theoretical prediction awaits experimental validation. Additionally, the existence of a low-pressure gas-liquid critical point remains an open question. Lastly, the driving forces behind the LDL-HDL transition and the microscopic characteristics of the liquids continue to be subjects of debate.

In Chapters 5 and 6, we will try to address these questions through the application of the experimental techniques detailed in Chapters 2 and 3.

References

1. P. H. Poole, F. Sciortino, U. Essmann and H. E. Stanley, Phase behavior of metastable water. *Nature*, 1992, **360**, 324-328.
2. S. Harrington, R. Zhang, P. H. Poole, F. Sciortino and H. E. Stanley, Liquid-liquid phase transition: evidence from simulations. *Phys. Rev. Lett.*, 1997, **78**, 2409-2412.
3. S. Sastry and C. A. Angell, Liquid-liquid phase transition in supercooled silicon. *Nat. Mater.*, 2003, **2**, 739-743.
4. B. Boates, A. M. Teweldeberhan and S. Bonev, Stability of dense liquid carbon dioxide. *Proc. Natl. Acad. Sci. USA*, 2012, **109**, 14808-14812.
5. J. N. Glosli and F. H. Ree, Liquid-liquid phase transformation in carbon. *Phys. Rev. Lett.*, 1999, **82**, 4659-4662.
6. M. A. Morales, C. Pierleoni, E. Schwegler and D. M. Ceperley, Evidence for a first-order liquidliquid transition in high-pressure hydrogen from *ab initio* simulations. *Proc. Natl. Acad. Sci. USA*, 2010, **107**, 12799-12803.
7. B. Boates and S. Bonev, First-order liquid-liquid phase transition in compressed nitrogen. *Phys. Rev. Lett.*, 2009, **102**, 015701.
8. Y. Katayama, T. Mizutani, W. Utsumi, O. Shimomura, M. Yamakata and K. Funakoshi, A first-order liquid-liquid phase transition in phosphorus. *Nature*, 2000, **403**, 170-173.
9. S. Aasland and P. F. McMillan, Density-driven liquid-liquid phase separation in the system $Al_2O_3Y_2O_3$. *Nature*, 1994, **369**, 633-636.
10. O. Mishima and H. E. Stanley, The relationship between liquid, supercooled and glassy water. *Nature*, 1998, **396**, 329-335.
11. S. Woutersen, B. Ensing, M. Hilbers, Z. Zhao and C. A. Angell, A liquid-liquid transition in supercooled aqueous solution related to the HDA-LDA transition. *Science*, 2018, **359**, 1127-1131.
12. H. Tanaka, R. Kurita and H. Mataki, Liquid-liquid transition in the molecular liquid triphenyl phosphite. *Phys. Rev. Lett.*, 2004, **92**, 025701-025704.
13. R. Kurita and H. Tanaka, On the abundance and general nature of the liquid-liquid phase transition in molecular systems. *J. Phys. Condens. Matter*, 2005, **17**, 293-302.
14. L. Henry, M. Mezouar, G. Garbarino, D. Sifre, G. Weck and F. Datchi, Liquid-liquid transition and critical point in sulfur, *Nature*, 2020, **584**, 382-386.

15. J. W. Mellor, A Comprehensive Treatise on Inorganic and Theoretical Chemistry, 1922, **Vol. VIII**, 729-1080.

16. H. Peters, *Arch. Geschichte Naturw*, 1912, **4**, 206.

17. A. Schrötter, *Sitzber. Akad. Wien*, 1848, **1**, 25, 310.

18. P. W. Bridgman, Two new modifications of phosphorus. *J. Am. Chem. Soc.*, 1914, **36**, 7, 1344-1363.

19. R. Boyle, *Phil. Trans.*, 1680, **13**, 196, 428.

20. J. Emsley, The shocking history of phosphorus. *Macmillan*, 2000, London.

21. D. Corbridge and E. Lowe, Structure of white phosphorus: Single crystal X-ray examination. *Nature*, 1952, **170**, 629.

22. A. Simon, H. Borrmann and H. Craubner, Crystal structure of Ordered White Phosphorus (β-P). *Sulfur Relat. Elem.*, 1987, **30**, 1-2, 507-510.

23. A. Simon, H. Borrmann and J. Horakh, On the polymorphism of white phosphorus. *Chem. BerRecl.*, 1997, **130**, 9, 1235-1240.

24. H. W. Spiess, R. Grosescu and H. Haeberlen, Molecular motion studied by NMR powder spectra. II. Experimental results for solid P_4 and solid $Fe(CO)_5$. *Chem. Phys.*, 1974, **6**, 2, 226-234.

25. Y. Katayama, Y. Inamura, T. Mizutani, M. Yamakata, W. Utsumi, O. Shimomura, Macroscopic separation of dense fluid phase and liquid phase of phosphorus. *Science*, 2004, **306**, 848-851.

26. H. Okudera, R. E. Dinnebier, and A. Simon, The crystal structure of γ-P_4, a low temperature modification of white phosphorus. *Z. Kristallogr.*, 2005, **220**, 259-264.

27. A. D. F. Toy, Phosphorus compounds, in *Comprehensive Inorganic Chemistry*. 1973, **Vol. 2**, Pergamon.

28. D. E. C. Corbridge, The Structural Chemistry of Phosphorus. *Elsevier Scientific Pub. Co.*, 1974, Amsterdam.

29. W. L. Roth, T. W. DeWitt and A. J. Smith, Polymorphism of red phosphorus. *J. Am. Chem. Soc.*, 1947, **69**, 11, 2881-2885.

30. H. W. Melville and S. C. Gray, The vapour pressure of red phosphorus. *Trans. Faraday Soc.*, 1936, **32**, 1026-1030.

31. R. A. L. Winchester, M. Whitby and M. S. P. Shaffer, Synthesis of pure phosphorus nanostructures. Angew. *Chem. Int. Ed.*, 2009, **48**, 3616-3621.

32. D. Hohl and R. O. Jones, Polymerization in liquid phosphorus: Simulation of a phase transition. *Phys. Rev. B*, 1994, **50**, 17047-17053.
33. Y. Senda, F. Shimojo and K. Hoshino, The metal-nonmetal transition of liquid phosphorus by *ab initio* molecular-dynamics simulations. *J. Phys.: Condens. Matter*, 2002, **14**, 3715-3723.
34. M. Ruck, D. Hoppe, B. Wahl, P. Simon, Y. Wang and G. Seifert, Fibrous red phosphorus. *Angew. Chem. Int. Ed.*, 2005, **44**, 7616-7619.
35. D. J. Olego, J. A. Baumann, M. A. Kuck, R. Schachter, C. G. Michel and P. M. Raccah, The microscopic structure of bulk amorphous red phosphorus: A Raman scattering investigation. *Solid State Commun.*, 1984, **52**, 311-314.
36. J. R. Durig and J. M. Casper, On the vibrational spectra and structure of red phosphorus. *J. Mol. Struct.*, 1970, **5**, 351-358.
37. W. Hittorf, Zur kenntnifs des phosphors. *Ann. Phys. Chem.*, 1865, **126**, 193-228.
38. H. Thurn and H. Krebs, Über struktur und Eigenschaften der halbmetalle. XXII. Die kristallstruktur des Hittorfschen phosphors. *Acta Crystallogr. Sec. B*, 1969, **25**, 125-135.
39. L. Zhang, H. Huang, B. Zhang, M. Gu, D. Zhao, X. Zhao, L. Li, J. Zhou, K. Wu, Y. Cheng and J. Zhang, Structure and properties of violet phosphorus and its phosphorene exfoliation. *Angew. Chem. Int. Ed.*, 2020, **59**, 1074-1080.
40. B. V. Shanabrook and J. S. Lannin, Structural and vibrational properties of amorphous phosphorus. *Phys. Rev. B*, 1981, **24**, 4771-4780.
41. S. Elliott, J. Dore and E. Marseglia, The structure of amorphous phosphorus. *J. Phys. Colloques*, 1985, **46**, C8349-C8353.
42. P. Jóvári and L. Pusztai, On the structure of amorphous red phosphorus. *Appl. Phys. A*, 2002, **74**, S1092-S1094.
43. J. M. Zaug, A. K. Soper and S. M. Clark, Pressure-dependent structures of amorphous red phosphorus and the origin of the first sharp diffraction peaks. *Nat. Mater.*, 2008, **7**, 890-899.
44. E. N. Rissi, E. Soignard, K. A. McKiernan, C. J. Benmore and J. L. Yarger, Pressure-induced crystallization of amorphous red phosphorus. *Solid State Comm.*, 2012, **152**, 390-394.
45. Y. Zhou, W. Kirkpatrick and V. L. Deringer, Cluster fragments in amorphous phosphorus and their evolution under pressure. *Adv. Mater.*, 2022, **34**, 2107515.

46. D. E. C. Corbridge, Phosphorus: Chemistry, biochemistry and technology. *CRC Press*, 2016, 6th Edition.
47. L. Li, G. J. Ye, Q. Ge, X. Ou, H. Wu, D. Feng, X. H. Chen and Y. Zhang, Black phosphorus field-effect transistors. *Nat. Nanotech.*, 2014, **9**, 372-377.
48. M. Serrano-Ruiz, M. Caporali, A. Ienco, V. Piazza, S. Heun and M. Peruzzini, The role of water in the preparation and stabilization of high-quality Phosphorene flakes. *Adv. Mater. Interfaces*, 2016, **3**, 1500441.
49. W. Luo, R. Yang, J. Liu, Y. Zhao, W. Zhu and G. M. Xia, Thermal sublimation: a scalable and controllable thinning method for the fabrication of few-layer black phosphorus. *Nanotechnology*, 2017, **28**, 285301.
50. L. Henry, V. Svitlyk, M. Mezouar, D. Sifré, G. Garbarino, M. Ceppatelli, M. Serrano-Ruiz, M. Peruzzini and F. Datchi, Anisotropic thermal expansion of black phosphorus from nanoscale dynamics of Phosphorene layers. *Nanoscale*, 2020, **12**, 4491-4497.
51. W. Crichton, M. Mezouar and G. Monaco, Phosphorus: New in situ powder data from largevolume apparatus. *Cambridge Univ. Press. Power Diffr.*, 2003, **18**, 155-158.
52. J. C. Jamieson, Crystal structures adopted by black phosphorus at high pressures, *Science*, 1963, **139**, 1291-1292.
53. D. Scelta, A. Baldassarre, M. Serrano-Ruiz, K. Dziubek, A. B. Cairns, M. Peruzzini, R. Bini and M. Ceppatelli, The p-sc structure in phosphorus: bringing order to the high pressure phases of group 15 elements, *Chem. Commun.*, 2018, **54**, 10554-10557.
54. D. Scelta, A. Baldassarre, M. Serrano-Ruiz, K. Dziubek, A. B. Cairns, M. Peruzzini, R. Bini and M. Ceppatelli, Interlayer bond formation in black phosphorus at high pressure. *Angew. Chem. Int. Ed.*, 2017, **56**, 14135-14140.
55. T. Kikegawa and H. Iwasaki, An X-ray diffraction study of lattice compression and phase transition of crystalline phosphorus. *Acta Cryst.*, 1983, B**39**, 158-164.
56. Y. Akahama, M. Miyakawa, T. Taniguchi, A. Sano-Furukawa, S. Machida and T. Hattori, Structure refinement of black phosphorus under high pressure. *J. Chem. Phys.*, 2020, **153**, 014704.
57. L. Cartz, S. R. Srinivasa, R. J. Riedner, J. D. Jorgensen and T. G. Worlton, Effect of pressure on bonding in black phosphorus. *J. Chem. Phys.*, 1979, **71**, 1718.
58. S. Appalakondaiah, G. Vaitheeswaran, S. Lebègue, N. E. Christensen and A. Savane, Effect of van der Waals interactions on the structural and elastic properties of black phosphorus. *Phys. Rev. B*, 2012, **86**, 035105.

59. J. E. F. S. Rodrigues, J. Gainza, F. Serrano-Sánchez, C. López, O. J. Dura, N. Nemes, J. L. Martinez, Y. Huttel, F. Fauth, M. T. Fernández-Diaz, N. Biškup and J. A. Alonso, Structural features, anisotropic thermal expansion, and thermoelectric performance in bulk black phosphorus synthesized under high pressure. *Inorg. Chem.,* 2020, **59**, 20, 14932-14943.
60. R. Riedner, S. R. Srinivasa, L. Cartz, T. G. Worlton, R. Klinger and R. Beyerlein, Anisotropic thermal expansion and compressibility of black phosphorus. *AIP Conf. Proc.*, 1974, **17**, 8-20.
61. R. W. Keyes, The Electrical properties of black phosphorus, *Phys. Rev.*, 1953, **92** ,580.
62. G. Sansone, A. J. Karttunen, D. Usvyat, M. Schütz, J. G. Brandenburg and L. Maschio, On the exfoliation and anisotropic thermal expansion of black phosphorus, *Chem. Commun.*, 2018, **54**, 70, 9793-9796.
63. Y. Akahama, W. Utsumi, S. Endo, T. Kikegawa, H. Iwasaki, O. Shimomura, T. Yagi and S. Akimoto, Melting curve of black phosphorus. *Phys. Lett. A*, 1987, **122**, 129-131.
64. T. Mizutani, Y. Katayama, W. Utsumi, K. Funakoshi, M. Yamakata and O. Shimomura, Anomaly in the melting curve of black phosphorus associated with a liquid-liquid transition. *Science Technol. High Press. (Proceedings of AIRAPT-17),* 2000, 525-528.
65. V. L. Solozhenko and V. Turkevich, P-T phase diagram of phosphorus revisited. *J. Phys. Chem. C*, 2023, **127**, 12, 6088-6092.
66. G. B. Guarise and A. Marani, Fusione del fosforo nero fino a 16.000 atm. *Chim. Ind.*, 1968, **50**, 663665.
67. J. Granada and J. Dore, Neutron diffraction studies of phosphorus: II. The super-cooled liquid and plastic crystal phases. *Molecular Physics*, 1982, **46**, 757-768.
68. G. Monaco, S. Falconi, W. Crichton and M. Mezouar, Nature of the first-order phase transition in fluid phosphorus at high temperature and pressure, *Phys. Rev. Lett.*, 2003, **90**, 2557011-2557014.
69. K. Murata and H. Tanaka, Liquid-liquid transition without macroscopic phase separation in a water-glycerol mixture. *Nature Materials*, 2012, **11**, 436-443.
70. V. Holten and M. A. Anisimov, Entropy-driven liquid-liquid separation in supercooled water. *Scientific Reports*, 2012, **2**, 713.
71. W. Klement, A. Jayaraman and G. C. Kennedy, Phase diagrams of arsenic, antimony, and bismuth at pressures up to 70 kbars. *Phys. Rev.*, 1963, **131**, 632-637.

72. V. V. Brazhkin, S. V. Popova and R. N. Voloshin, High-pressure transformations in simple melts. *High Pressure Research*, 1997, **15**, 267-305.
73. G. Franzese, G. Malescio, A. Skibinsky, S. V. Buldyrev and H. E. Stanley, Generic mechanism for generating a liquid-liquid phase transition. *Nature*, 2001, **409**, 692-695.
74. G. Zhao, H. Wang, D. M. Hu, M. C. Ding, X. G. Zhao and J. L. Yan, Anomalous phase behavior of first-order fluid-liquid phase transition in phosphorus. *J. Chem. Phys.*, 2017, **147**, 204501.
75. P. Gallo, K. Amann-Winkel, C. A. Angell, M. A. Anisimov, F. Caupin, C. Chakravrty, E. Lascaris, T. Loerting, A. Z. Panagiotopoulos, J. Russo, J. A. Sellberg, H. E. Stanley, H. Tanaka, C. Vega, L. Xu and L. G. M. Pettersson, Water: A tale of two liquids. *Chem. Rev.*, 2016, **116**, 13, 7463-7500.
76. S. Sastry, P. G. Debenedetti, F. Sciortino and H. E. Stanley, Singularity-free interpretation of the thermodynamics of supercooled water. *Phys. Rev. E*, 1996, **53**, 6144-6154.
77. P. H. Poole, F. Sciortino, T. Grande, H. E. Stanley and C. A. Angell, Effect of hydrogen bonds on the thermodynamic behavior of liquid water. *Phys. Rev. Lett.*, 1994, **73**, 1632-1635.
78. M. Yang, T. Karmakar and M. Parrinello, Liquid-liquid critical point in phosphorus. Phys. Rev. Lett., 2021, 127, 080603.

Chapter 2:

High pressure – high temperature experimental methods

1. Introduction

This thesis deals with the experimental investigation of the phase diagram of phosphorus across an extended range of pressure and temperature conditions, and thus requires the use of experimental methods to reach the high pressure and temperature conditions. In this chapter, we present the devices employed for creating these specific conditions, elucidate diverse techniques for determining both pressure and temperature, and discuss the precision and fidelity associated with each of these methods.

2. High Pressure and high temperature generation devices

A general principle used in many high-pressure devices is that, when pressure is applied at the base of an anvil, a higher pressure is generated at the tip if its area is much smaller than the area of the base. The resulting generated pressure will be proportional to the base to tip area ratio and will depend on the mechanical properties of the anvil material. Devices based on this principle include hydro-thermal devices for low-pressure generation, as well as multi-anvil and opposed-anvil devices for high-pressure generation. Opposed-anvil devices have been subject to many evolutions over the years, among them the basic Bridgman anvil design[1], the supported anvil Drickamer cell[2], the Troitsk toroid cell[3], the Paris-Edinburgh press (PEP)[4-6] and the diamond anvil cell (DAC)[7-9].

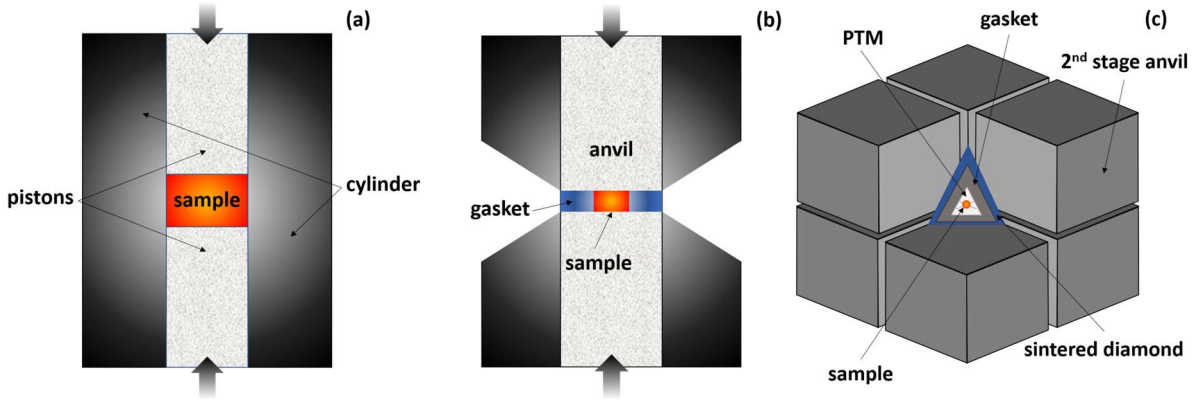

Figure 2.1. Main type of high-pressure devices in historical order of invention: a) piston-cylinder, b) opposed anvil apparatus, c) multianvil cell.

Percy Bridgman was one of the pioneers of high-pressure science. He developed the first design of high-pressure apparatus in the early 1900 that was initially using a carbide tungsten press, generating pressures up to several hundreds of bars at that time, and was later improved into a new apparatus allowing to reach dozens of kbars[1].

It is only in 1959 with the works of Weir et al.[7] that the first diamond anvil cells (DAC) were developed. Figure 2.2. shows a picture of the original DAC built by Weir and al. in 1958.

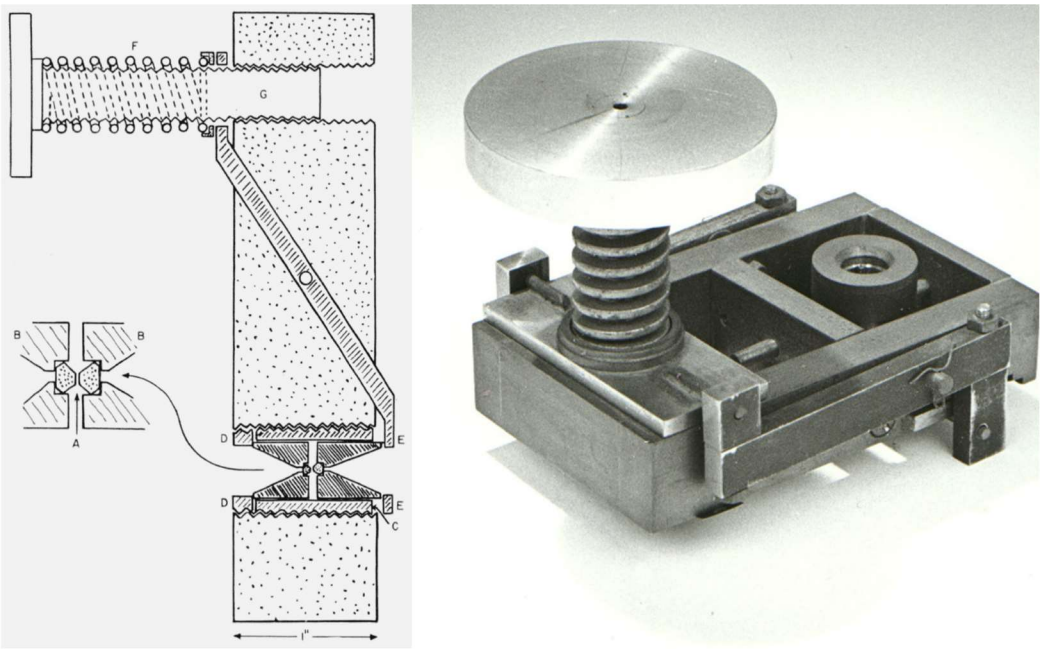

Figure 2.2. The first diamond anvil cell from Weir et al. (1959), on display at the National Institute of Standards and Technology (NIST) Museum in Gaithersburg.

Various materials have been used as anvils, such as steel, tungsten carbide, boron carbide, sapphire, cubic zirconia, sintered diamond or single crystal diamond. The use of a given material as an anvil for a specific technique and pressure range depends on its strength, size and shape, optical properties, x-ray transmission, as well as many other mechanical, thermoelectric and magnetic properties. Anvils sharing identical anvil shape but made of different materials will give access to different pressure regimes. For instance, considering an anvil base-to-top area ratio of 100, tungsten carbide Bridgman anvils can reach pressures up to 30 GPa[2], while single crystal diamond anvils can reach 400 GPa[10].

The choice of the pressure device strictly depends on the measurement to carry out: many macroscopic diagnostic techniques require sample sizes beyond those provided by DACs. In these cases, large volume pressure devices, such as the Paris-Edinburgh press, are preferred.

2.1. Membrane-type diamond anvil cell

Diamond anvil cells are devices typically used to generate static pressures in the range 1 GPa to 300 GPa, although pressures up to 1 TPa have been recently claimed to be achieved [11-12]. They are traditionally used in chemistry and physics to study phase transitions[13-14], physico-chemical properties of solids and liquids[15-16], as well as magnetic and electric properties[17-19]. These high-pressure devices are also used in geosciences, as DACs enable to generate pressures and temperatures similar to those present in the deep interior of Earth[15,20-22]. They are the most common device employed for generating very high static pressures.

DACs belong to the opposed-anvil setups. Their principle is simple: the two diamond anvils, made out of diamond single crystals, face each other and squeeze a sample between the two diamond culets, as shown in Figure 2.3. The pressure being defined as the ratio of the force F exerted on a surface S, $P = \frac{F}{S}$, the higher the force applied and the smaller the surfaces are, the higher the pressure is. The culet diameter are generally shaped between 1000 and 25 µm, depending on the desired maximum pressure, typically from 5 to 300 GPa respectively.

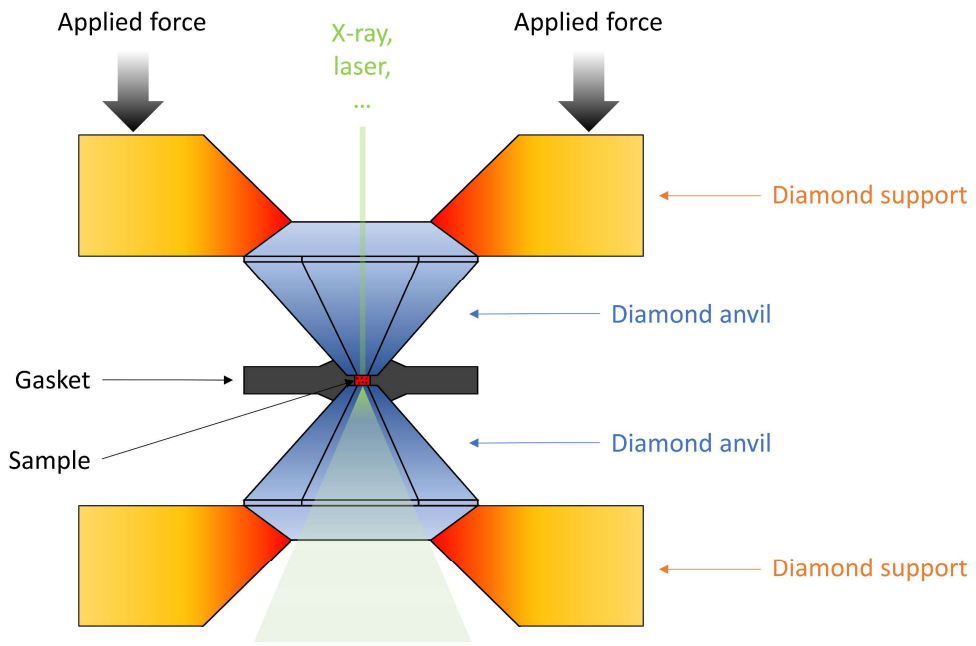

Figure 2.3. Drawing of the inner part of the DAC.

2.1.1. The diamond anvils

Diamond is a remarkable material and particularly interesting for high-pressure experiments because of its physico-chemical properties[23-27]:

- it is the hardest known material in nature, which makes it possible to compress the sample to extremely high pressure without breaking the anvils;
- it is a stable material under pressure and up to 1000 K. Above 800 K, diamond becomes susceptible to oxidation;
- it presents a very high thermal conductivity;
- it is transparent over a large range of energy except from the UV (~5 eV) to the soft x-ray (~ 5 keV). This property allows the use of diamonds in many analytical techniques such as spectroscopy or x-ray diffraction.

Both natural or synthetic diamonds can be used. Natural diamonds can present defects and impurities such as nitrogen, which alter their properties. Diamonds of type Ia, containing $\sim 2 \cdot 10^3$ ppm of nitrogen, represents around 98% of the diamonds. Its color varies from yellow to transparent. The nitrogen impurity leads to a non-negligible absorption in the 1100-1500 cm^{-1} range. This category of diamond is compatible with many experiments (such

as visible spectroscopy, photoluminescence, x-ray diffraction and spectroscopy, electrical, magnetic and Mössbauer spectroscopy measurement) but are usually not used in infrared spectroscopy due to the nitrogen absorption band.

Type II diamonds contain much lower level (~1 ppm) of impurities but are much less abundant in nature. Anvils of this type are thus mostly made nowadays from synthetic diamond, either grown by chemical vapor deposition (type IIac), or synthesized by a high-pressure and high-temperature process (type IIas). Type IIas diamond present the best transparency (they only exhibit the 2000 cm-1 absorption band) and have very low luminescence, this is why they are preferred in infrared and Raman spectroscopy experiments.

There exist several designs of anvils, the two most commonly used ones are the "Drukker" and the "Almax-Boehler" designs[28] (Figure 2.4.). These two designs mostly differ in the way they are supported on the diamond seat: in the Drukker design, the anvil seats flat on its support, while in the Almax-Boehler design, the bottom of the anvil is shaped as a cone which fits into the conical aperture of the seat. The Almax-Boehler design enables a larger angular access to the sample and is thus preferred nowadays in most experiment, in particular for x-ray diffraction. In both cases, the diamond culet is either polished flat or with bevels depending on the pressure range of operation[10]. More sophisticated shapes of culets have recently appeared, in particular the toroidal shape[12] which allow to reach higher pressures in the range of 0.5-0.6 TPa. The TPa range has been also reached recently by using secondary anvils made of nanodiamond shaped as hemisphere which are put on the culet of the diamond anvils[11].

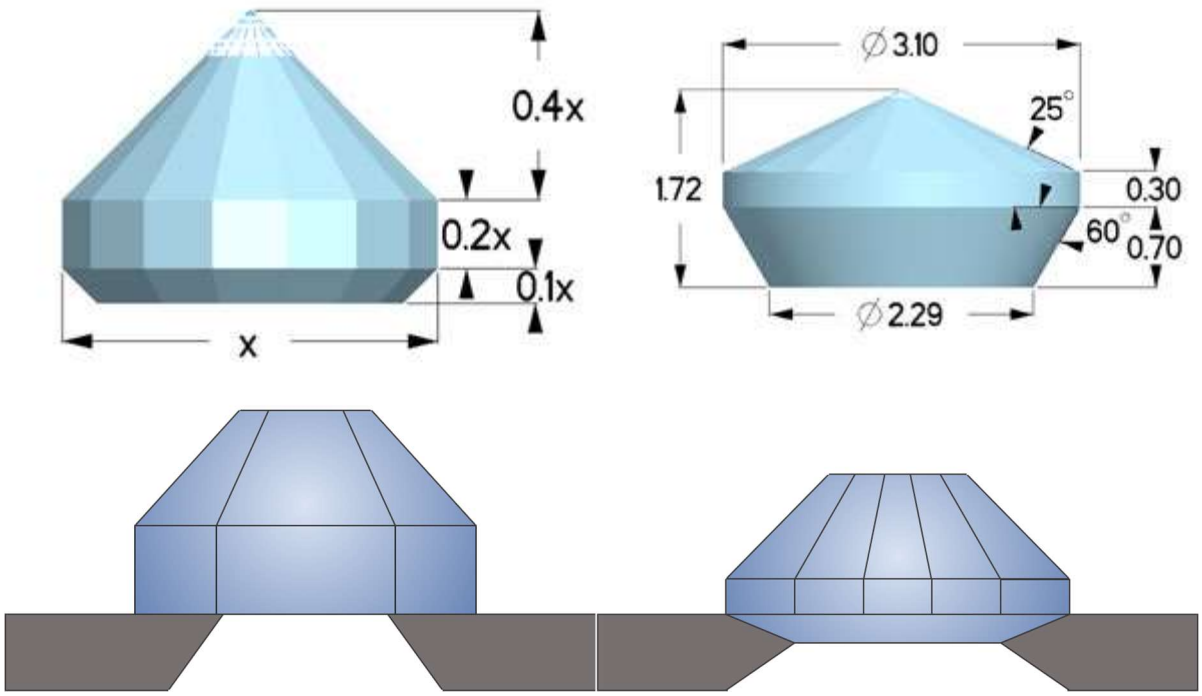

Figure 2.4. Drukker (left) and Almax-Boehler (right) design of diamond anvils. The Almax-Boehler diamonds have a conical seat, enabling a larger optical aperture while keeping a sufficient contact surface with the backing seat.

2.1.2. Membrane-type diamond anvil cell

In order to generate high pressures between the diamond anvils, only a few kN force is necessary on the piston of the cell. Over the past years, many devices were developed. Among them some of the most commonly used are the Merrill & Bassett DAC[29] and Le Toullec DAC [30]. In the former, the force is generated by rotation of three Allen screws, which push the upper plate. The main issue with this type of cell is the lack of a precise control of pressure increment. Each DAC requires a specific fraction of turns of the Allen keys to roughly reproduce the pressure. Moreover, manual pressure alterations require dismounting the DAC from the experimental stage each time pressure needs to be changed. While it seems not too troubling in the case of diffraction experiments which are several hours long on a commercial diffractometer, it is problematic for experiments at non-ambient temperature, and can also severely affect the productivity during time-limited synchrotron beamlines.

A membrane-driven (Le Toullec) DAC can serve as an alternative to the Merrill-Bassett DAC, when small pressure increments are required. In this case, a metallic doughnut-shaped membrane dilates upon injection of a pressurized inert gas (usually up to 100-150 bars).

Membrane presses onto the upper plate, pressurizing the sample confined in the cell. The gas pressure inside the membrane can be controlled by a digital and automatic controller (Figure 2.5.), so the pressurization/decompression rate can be precisely adjusted, without the need of dismounting the DAC from the experimental stage. The membrane gas is usually helium, fully compatible with low temperature experiments as well. In the framework of this thesis, we have used membrane-type diamond anvil cell similar to the ones developed by Le Toullec et al.[30].

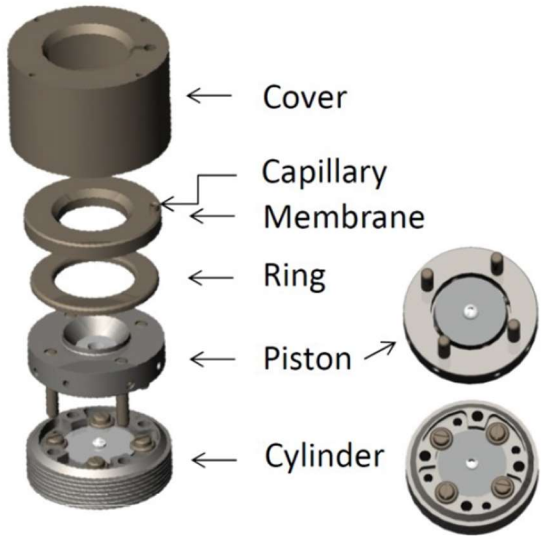

Figure 2.5. Membrane-driven DAC; (left) Main components of a cell; (right) Automatic pressure controller used during the synchrotron experiments.

2.1.3. Experimental chamber and gasket

Gaskets create the space for the experimental chamber and prevent the diamonds from crushing against each other. The experimental chamber is defined as the space confined between the two diamonds and the metallic gasket. Usually metal gaskets made of stainless steel are used. For special applications, the following gaskets might be used:

- Rhenium, tungsten and Inconel may be used for pressures above 20 GPa, as well as at high temperature. Stainless steel can be used for low-pressure experiments as well.
- Amorphous boron[31] or BN composite gaskets can be used at high temperature, since they maintain a superior mechanical support than metallic gaskets.
- Copper-Beryllium gaskets can be used for magnetic measurements.

- If the material of the gasket reacts with the sample or electrical insulation is needed, as in the case of electrical measurements, the gasket can be covered with cBN, MgO, alumina, or mixtures of these substances with epoxy resin. Instead of a full coating, in the case of gasket reaction, the sample can be insulated from the gasket using a ring made of another material, at the interface between the gasket and the sample, inert with both.
- If the radial access is needed, gaskets made of beryllium or diamond powder may be used.

Metal gaskets are initially cut out from a foil with a thickness of 100-250 μm. Hardening of the gasket is achieved via precompression ("preindentation") down to the desired thickness (30 – 100 μm). This will define the initial height of the sample chamber. Preindentation marks the anvil shape on the metallic foil, which serves as a guide for drilling the sample chamber. Depending on the gasket material, the hole can be drilled with a micro driller, spark-erosion technique, or with a laser drilling system. The typical radius of a cylindrical hole is about half of the culet diameter. Care is taken to drill the hole as circular and concentric with the culet as possible, otherwise it may flow and expand during the pressurization and ultimately lead to the gasket rupture. If the metallic gasket is thin and the hole well-centered, the hole extrudes inwards and ensure the sealing and the stability of the pressure chamber.

2.1.4. High temperature generation in DACs

DACs enable the coupling between high pressures and high temperatures to study a sample. This is of particular interest in the case of geophysics and planetology. We can generate, in a very small experimental volume, the pressure and temperature conditions expected in the planet deep interiors. Therefore, it is possible to study the structures of the planetary compounds, as well as their stability and physico-chemical properties. Two main solutions are employed in the case of static compression to generate high temperatures: resistive heating, used to generate temperature up to 1500 K and laser heating to reach temperatures above 1000 K up to 5000 K. In the framework of the thesis, only resistive heating was used, as, below 1000 K, temperatures are difficult to measure by spectroradiometry.

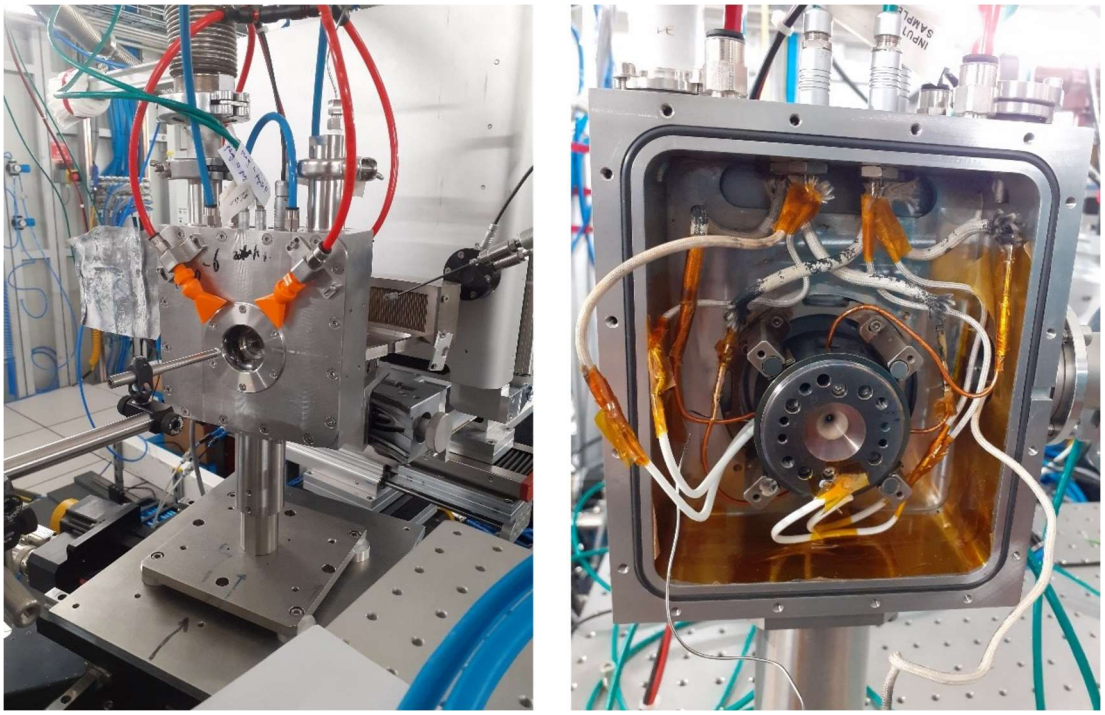

Figure 2.6. Resistive furnace inside vacuum chamber used on the ID27 beamline. The DAC is placed inside the vacuum chamber.

Resistive heating can be divided into two sub techniques:

- The internally resistively heated DAC in which two graphite furnaces are placed around the two diamonds to generate high temperatures up to 1500 K. This device is relatively complex to set-up and is shown in the Figure 2.6. above.
- The externally resistively heated DAC which can generate homogeneous temperatures up to 1000 K. It consists in a cylindrical heater placed around the DAC. The heat is generated by Joule effect and transmitted to the whole DAC including the diamonds, directly in contact with the sample. The temperature is electronically regulated with the use of a K-type thermocouple. Another K-type thermocouple is place on the body of the cell as close as possible from the anvils. Despite diamonds having an important thermal conductivity, a systematic thermal loss is observed. In order to avoid the oxidation of the metallic body of the DAC, the set-up is either placed under vacuum or under argon atmosphere.

2.2.The Paris-Edinburgh Press (PEP)

The Paris-Edinburgh press is a popular large volume device, with two opposed anvils acting to generate the desired pressure. It is a piston-cylinder type large volume device which was initially designed for high pressure neutron diffraction studies[32] that later was adapted to synchrotron x-ray diffraction experiments[33]. The press is relatively compact and its weight does not exceed 50-60 kgs, which makes it portable between laboratories.

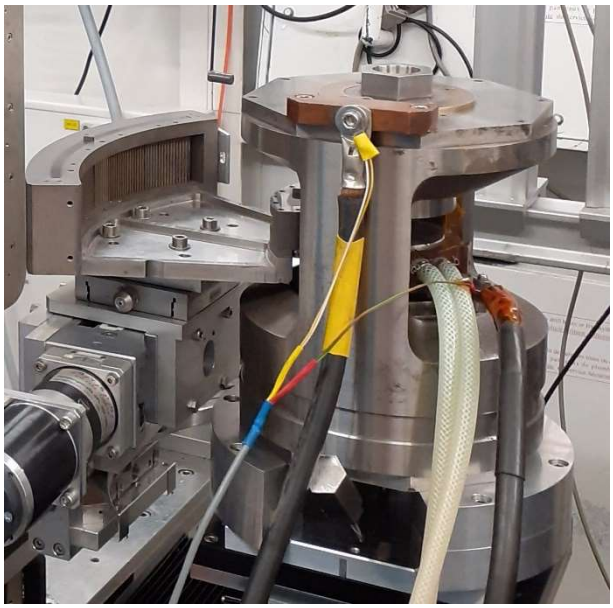

Figure 2.7. Two column Paris-Edinburgh Press VX5 model used at ID27 beamline. With its large opening angle of 120 degrees in the horizontal plane, the VX5 model is particularly well adapted to in situ x-ray diffraction experiments.

2.2.1. The anvils

One of the most crucial components of the PEP are the anvils. Their choice is determinant for the pressure range that is targeted. The VX5 model employs an opposed anvil design which enables a sample volume of several mm^3. The anvils have a conoidal shape to ensure good hydrostatic conditions and minimize the gasket extrusion and therefore any deformation of the sample assembly. The outer rim of the anvils is made of hardened steel, while the core is usually made of tungsten carbide WC, boron nitride BN or sintered diamond, a hard material which ensures good mechanical stability to the system under extremes conditions. The anvils consist of a special cavity in the center, where the sample assembly is placed.

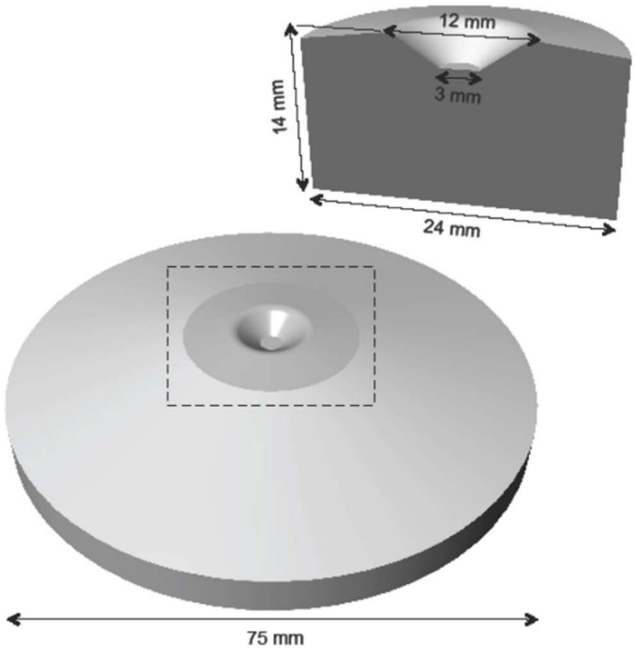

Figure 2.8. Tungsten carbide anvil along with a cross-section view showing typical dimension. The sample is placed at the center of the anvil[34].

2.2.2. Pressure and temperature generation in the PEP

The pressure is generated by a hydraulic oil pressure generator connected to the piston of the PEP and controlled by a motorized pump from the company Nova Swiss. The system can generate forces up to 600 kN. That force is transmitted to the WC anvils, and the maximum reachable pressure depends on the dimensions of the conoidal profile. The calibration curves of the pressure inside the cell assembly versus the force applied on the anvils are plotted on Figure 2.11. for different values of conoidal outer diameter[6]. In the framework of this thesis, most of the experiments were performed using WC anvils having a conoidal diameter of 7 mm. This configuration enables reaching a maximum pressure of 8 GPa.

The temperature is generated by two DC power supplies connected in series. Their combination enables providing a current up to 400 A and a voltage of 10 V, resulting in a maximum power of 4 kW. The current delivered in the PEP is finely regulated using a Eurotherm controller with a precision of ± 0.01 A.

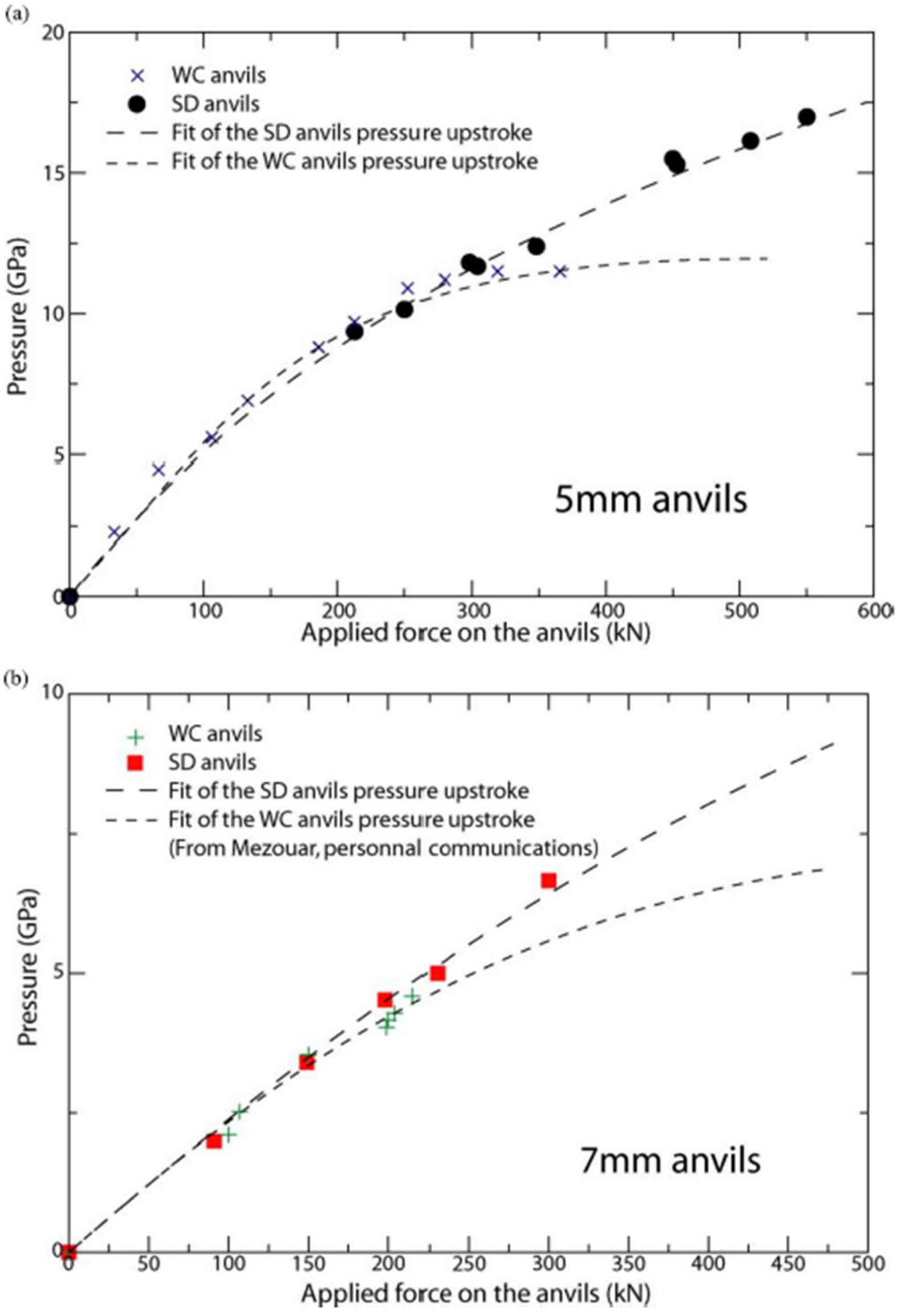

Figure 2.9. Calibration curves of the pressure inside the cell assembly versus the force applied on two types of anvils for two values of the conoidal outer diameter: 5 mm and 7 mm[6].

Figure 2.10. Photographs of the pressure generator (left) and the power supply with the PEP (right).

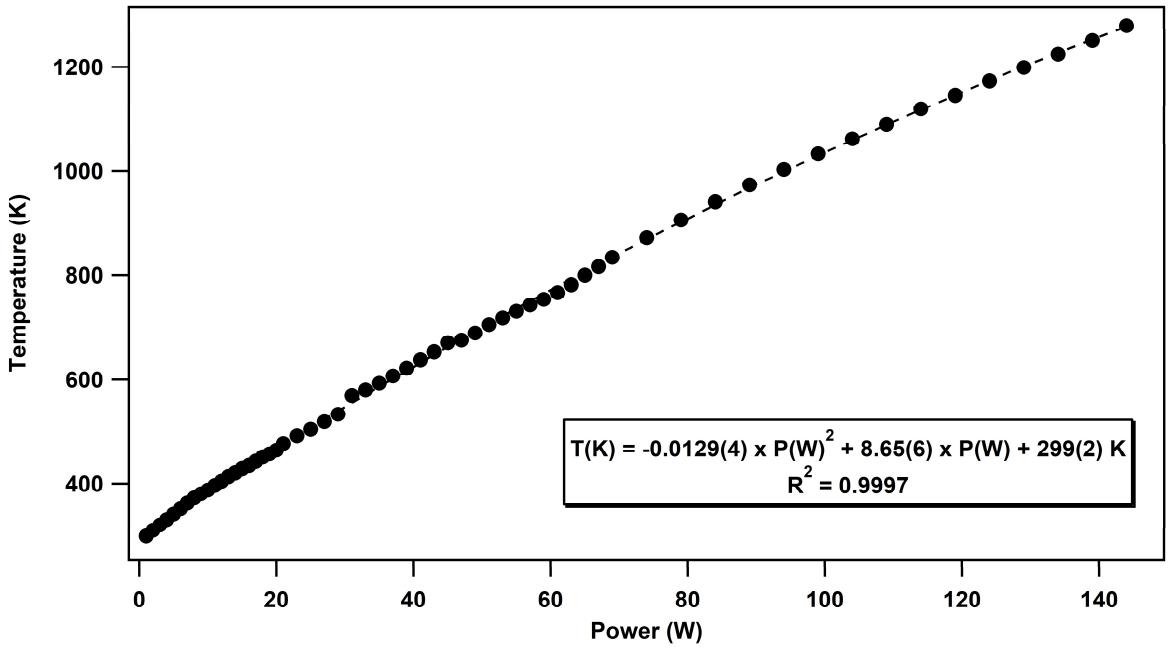

Figure 2.11. Power-temperature calibration curve in the PEP showing a polynomial variation of the temperature as a function of applied power.

2.2.3. Sample assembly

The sample assembly usually consists of a gasket, heater, sample capsule and electrical connection material. The gasket assembly for the experiments performed in the framework of this thesis is illustrated on Figure 2.12.

The gasket is made of boron-epoxy (5:1 in mass) mixture, which is transparent to x-ray, as its low Z value does not interfere heavily with the signal strength of the sample during x-ray diffraction. The gasket is used to transmit the pressure generated by the PEP through the two opposing tungsten carbide anvils. Teflon or PEEK rings are often used around the gasket to maintain its form during compression.

The sample is confined in a diamond cylinder which is encapsulated in a container composed of hexagonal boron nitride sealed with two caps made of hexagonal boron nitride as well. This acts as the sample capsule. The primary purpose of the sample capsule is to prevent direct contact between the sample and the furnace, and thus, it prevents undesirable chemical reactions between them. hBN has a melting point much higher[35] than the maximum obtainable temperature in PEP (~ 2500 K) and does not react with phosphorus. hBN is also a good thermal conductor and good electrical insulator[36-39], which are important pre-requisites for the capsule material.

The sample capsule is then placed inside a high resistivity graphite heater that generates the high temperatures. A maximum temperature of 2500 K can be obtained with this type of graphite furnace. The graphite heater is covered as the two vertical ends with molybdenum discs to enable good electrical conduction. Finally, magnesium oxide powder inside steel rings were placed over the molybdenum discs to increase the stability of the assembly and to ensure thermal insulation of the anvils.

A slightly different assembly uses a thermocouple to measure the sample temperature. To do so, a hole has to be drilled through the gasket and close to the sample. The thermocouple cable is surrounded by a protective ceramic sheath in order to be isolated. This implies that the diameter of the gasket hole has to be relatively large, which gives rise to numerous problems. Non-negligible quantities of gasket and sample must be removed, thus defects are introduced in the furnace and the capsule materials. This leads to a reduced mechanical performance of the gasket around the drill, to an increase of the risk of furnace rupture, and to the possibility of

non-uniform thermal gradients. Some samples are incompatible with the thermocouple setup, for example liquids or high reactive samples; the first one because the sample would escape from the sample capsule through the hole; the second one because they would react with the material of the thermocouple, leading to contamination of the sample environment. This setup also may affect the extent of thermal insulation and reduce the ability to reach high pressures, due to the outside diameter of the thermocouple insulating sheath, which diameter is of the same order of the gap between the anvils.

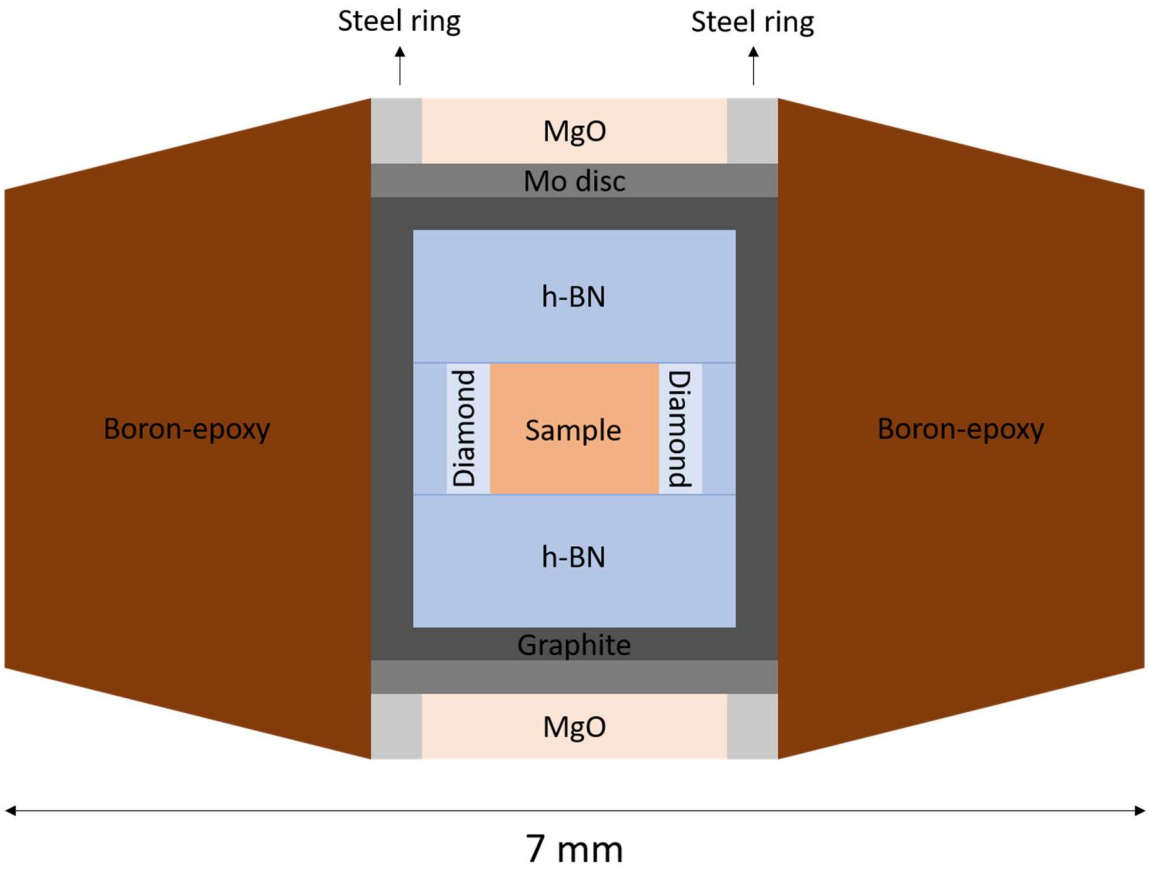

Figure 2.12. Scheme of full assembly used in the PEP setup. It shows the Boron-epoxy gasket, the graphite heater, the sample container consisting of h-BN and diamond, and the sample inside it. The heater is covered by molybdenum rings and steel rings filled with MgO. The Teflon ring is not represented in this figure.

3. Pressure and temperature measurements

The *in-situ* determination of the pressure and temperature conditions is a fundamental issue in high pressure science as it conditions the reliability of the experimental results. The

simple application of the relation $P = \frac{F}{S}$ is not reliable due to frictions and deformations of the press components. To accurately determine pressure and temperature, *in-situ* pressure sensors have to be used. In this section, we describe the different P-T metrologies used for the diamond anvil cell and Paris-Edinburgh press experiments.

3.1.Luminescence sensors

One effective way of measuring the pressure is the use of a luminescent material placed inside the experimental chamber. Because of its ease, accuracy and rapidity, this technique has become standard in high pressure DAC experiments. Luminescence sensors are however not appropriate for PEP experiments as the sample assembly is opaque. In this subsection, we will present the two luminescent materials used in the framework of this thesis, the ruby (Al_2O_3 :Cr^{3+}) and the samarium doped strontium tetraborate (SrB_4O_7 :Sm^{2+}).

3.1.1. Ruby luminescence

In 1972, Forman and co-workers[40] proposed for the first time the use of ruby as a pressure sensor in the diamond anvil cell. Ruby exhibits two intense luminescent peaks, R_1 and R_2 at 694.248 and 692.70 nm respectively, when excited by a light of frequency higher than the emission lines. Increasing the pressure on ruby results in a displacement of those two peaks towards higher wavelengths. Figure 2.13. shows the ruby spectrum and its behavior with respect to pressure and temperature. The displacement of the most intense peak has been the subject of numerous studies and calibrations: Barnett et al.[41] and Piermarini et al.[42] have calibrated the ruby using the equation of state of NaCl of Decker[43] up to 19.5 GPa. Later Mao et al.[44] revisited the ruby calibration up to 80 GPa and proposed to calculate the pressure from the displacement of the R_1 peak using the following empirical expression:

$$P = \frac{A}{B}\left[\left(\frac{\lambda_{R_1}(P) - \lambda_{R_1}(P=0)}{\lambda_{R_1}(P=0)}\right)^B - 1\right]$$

where $A = 1904$ GPa with $\lambda_{R_1}(P=0)$ the wavelength of the R_1 peak of ruby at ambient pressure. B is a parameter related to the degree of hydrostaticity on the sample: $B = 5$ for non-hydrostatic conditions and $B = 7.665$ for quasi-hydrostatic conditions. In the early 2000's, this calibration was shown to underestimate the pressure, as suggested by Dewaele and co-workers[45-46]. They found new values for the two coefficients: $A = 1920$ GPa and $B = 9.21$.

More recently, in 2017, a task group was formed to work on an International Practical Pressure Scale (IPPS) ruby gauge[47]. They selected three different approaches to establish the relation between the pressure and the ruby R_1 peak shift with three groups of optimal reference materials for applying these approaches. Using a polynomial form of the second order, the resulting recommended ruby gauge (referred as Ruby2020) is expressed as followed:

$$P[GPa] = 1.87(\pm 0.01) \times 10^3 \left(\frac{\Delta\lambda}{\lambda_0}\right)\left[1 + 5.63(\pm 0.03)\left(\frac{\Delta\lambda}{\lambda_0}\right)\right]$$

where λ_0 is the wavelength of the R_1 line at ambient conditions. The executive committee of AIRAPT endorsed the Ruby2020 gauge in June 2020. The two previous equations don't consider the effect of temperature. Indeed, the R_1 and R_2 peaks also shift with temperature and this contribution adds to the pressure shift. Datchi and co-workers[48] studied the effect of temperature on the displacement of the R_1 peak, and showed that its behavior could be expressed as a third-order polynomial equation, valid between 300 and 900 K:

$$\Delta\lambda_{R_1}(T) = 0.00746(4)\Delta T - 3.01(25) \times 10^{-6}\Delta T^2 + 8.76(33) \times 10^{-9}\Delta T^3$$

The luminescent peaks become weaker and broaden with temperature to a point where they eventually become unresolved, around 600 K. This makes the pressure reading less easy and precise. To overcome that limitation, an option is to use the samarium doped strontium tetraborate ($SrB_4O_7:Sm^{2+}$) pressure sensor instead of ruby.

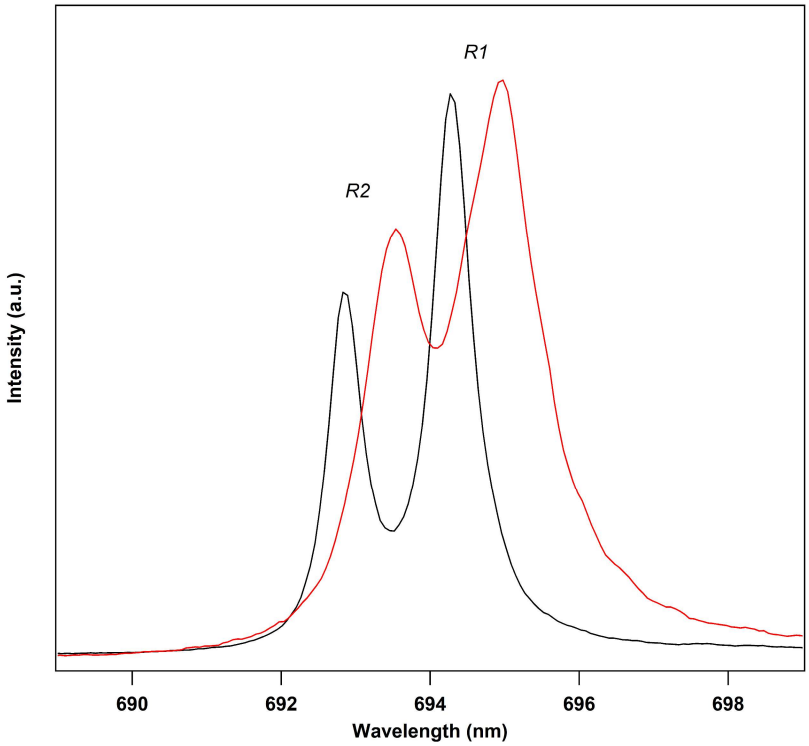

Figure 2.13. Ruby luminescence spectrum at room conditions (black) and at 360 K with as estimated pressure of 0.45 GPa.

3.1.2. Samarium doped strontium tetraborate luminescence

The first studies of $SrB_4O_7:Sm^{2+}$ (referred hereafter as SrBO:Sm) as a pressure sensor date back to the late eighties by Lacam and co-workers[49], and Leger and co-workers[50]. SrBO:Sm exhibits a luminescence line that is a non-degenerated $^5D_0$ - $^7F_0$ singlet (denoted 0 – 0) at 685.41 nm at ambient pressure. Figure 2.14. shows a typical spectrum. The 0 – 0 line is more intense and narrower than the line of ruby. It's also isolated from the other luminescence lines, so there is no issue of overlapping like in the case of ruby. The effect of temperature is also almost negligible. Datchi and co-workers calibrated this gauge using helium as pressure transmitting medium, to insure quasi-hydrostatic conditions, up to 124 GPa[51]. Ruby was used as reference for pressure, and the function to describe the pressure evolution was expressed as:

$$P = A\Delta\lambda\left(\frac{1 + B\Delta\lambda}{1 + C\Delta\Delta}\right)$$

where P is the pressure in GPa and $\Delta\lambda = \lambda_{0-0}(P) - \lambda_{0-0}(P = 0)$ in nm. Using the Ruby2020 calibration for ruby, one obtains: $A = 3.960(6)$ GPa.nm^{-1}, $B = 6.8(3) \times 10^{-3}$ nm^{-1}, $C = 1.63(5) \times 10^{-2}$ nm^{-1}. The temperature shift is negligible

below 500 K. Above that temperature, the small non-linear variation of the wavelength with temperature at ambient P is given by the following equation:

$$\Delta\lambda_{0-0}(T > 500) = 1.06 \times 10^{-4}(T - 500) + 1.5 \times 10^{-7}(T - 500)^2$$

with $\Delta\lambda_{0-0}(T)$ in nm and T in K. The overall shift from room temperature to 900 K is only about 0.06 nm, which is two orders of magnitude inferior to that of the ruby R_1 line. Therefore, SrBO:Sm is more adapted to high temperatures experiments than ruby. However, the luminescence intensity rapidly decreases above 500 K: at 700 and 900 K the intensity is respectively reduced by a factor of about 10^3 and 10^5 with respect to its value at 300 K, thus requiring longer acquisition times. SrBO:Sm can also be more easily attacked by corrosive media than ruby. During the framework of this thesis, whenever luminescent sensors were used, we employed both ruby and SrBO:Sm whenever it was possible, to measure the pressure inside the experimental chamber at high temperature and high pressure.

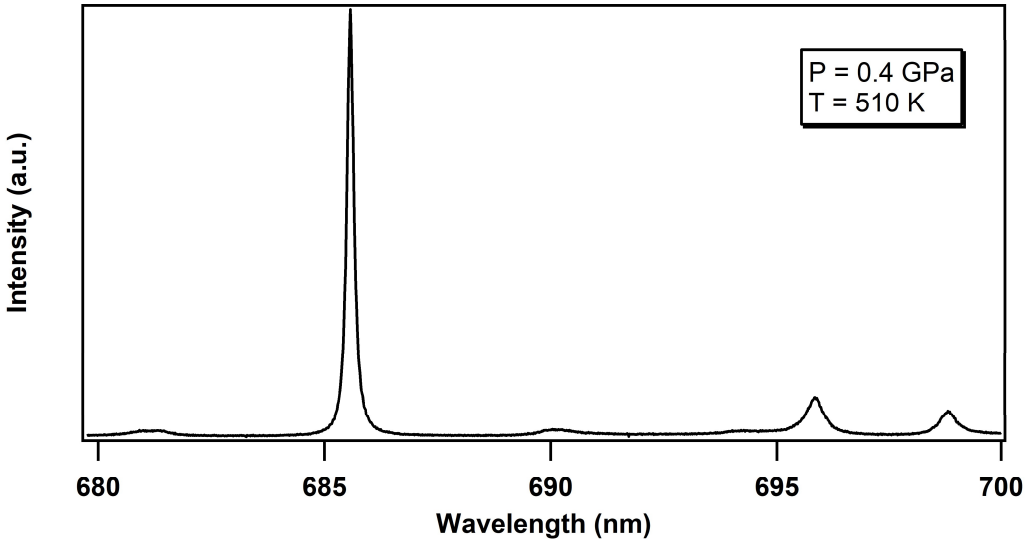

Figure 2.14. Luminescence spectrum of SrB_4O_7 :Sm^{2+} at 0.4 GPa and 510 K.

3.2.P-T determination by in situ x-ray diffraction measurements

It is possible to determine the pressure or the temperature using a compound whose equation of state (EoS) is well known, by calculating the variation of the unit cell dimensions from a diffraction pattern. Four important requisites must be respected:

- The EoS (P,V,T) of the material must be well determined in the thermodynamic regime of interest;
- The compound has to be compressible enough to allow a precise determination of the pressure;
- No phase transitions must take place in the P-T range in which the experiment is carried on;
- The material must be chemically inert with the sample;

It is also preferable that the chosen material has a relatively simple diffraction pattern (high symmetry, small cell), and different from the sample, so that it will not interfere with the diffraction from the sample.

Semi-empirical EoS have been developed. The most common are the Birch-Murnaghan[52] and Vinet[53] equations:

$$P_{BM} = \frac{3}{2}K_0(T)\left[\left(\frac{V(T)}{V_0(T)}\right)^{-\frac{7}{3}} - \left(\frac{V(T)}{V_0(T)}\right)^{-\frac{5}{3}}\right]\left[1 + \frac{3}{4}(K_0'(T) - 4)\left[\left(\frac{V(T)}{V_0(T)}\right)^{-\frac{2}{3}} - 1\right]\right]$$

$$P_{Vinet} = 3K_0(T)\left(\frac{1 - \left(\frac{V(T)}{V_0(T)}\right)^{\frac{1}{3}}}{\left(\frac{V(T)}{V_0(T)}\right)^{\frac{2}{3}}}\right) exp\left[\frac{3}{2}(K_0'(T) - 1)\left[1 - \left(\frac{V(T)}{V_0(T)}\right)^{\frac{1}{3}}\right]\right]$$

with:

$$V_0(T) = V_0 exp\left(\int \alpha_0(T)dT\right)$$

$$K_0(T) = K_0(298) + a(T - 298)$$

$$K_0'(T) = K_0'(298) + b(T - 298)$$

where V_0 is the volume at ambient conditions, $K_{0,298K} = -V(\partial P/\partial V)_{P=0}$ is the compressibility, also known as bulk modulus, at ambient conditions, $K'_{0,298K} = (\partial K/\partial P)_{P=0}$ is the first pressure-derivative of the bulk modulus as room pressure and temperature, and α_0 is the volumetric thermal expansion of the material.

These pressure gauge can either be metals, like platinum[54], gold[55] or rhenium[56], but also salts such as sodium chloride[54], or even oxides such as magnesium oxide[54].

This method is particularly powerful in combination with a luminescence sensor, as the pressure is directly given by ruby or samarium, and the temperature is given by a reference material, such as gold. The sample environment is opaque in the Paris-Edinburgh press, so the ruby and samarium method cannot be used. Because of the many inconveniences and physical limitations in the use of thermocouples in the PEP as previously discussed, a non-invasive method has been developed for the dual determination of pressure and temperature[57]. It consists in measuring the volume variations of two internal calibrants, whose EoS are well known. Ideally the chosen materials have well-determined and contrasting thermoelastic properties. A good choice is to combine the use of a metal and a salt or ceramic, as they have very contrasting response to pressure and temperature. Examples are Au/NaCl or hBN/Pt couples. It is also important to choose materials whose Bragg peaks used for the determination of the volume do not overlap and are easy to identify.

References

1 P. W. Bridgman, The Technique of High Pressure Experimenting. *Proc. Am. Acad. Arts Sci.*, 1914, **49**, 11, 627-643.

2 A. S. Balchan, H. G. Drickamer, High Pressure Electrical Resistance Cell, and Calibration Points above 100 Kilobars, *Rev. Sci. Instrum.*, 1961, **32**, 308-313.

3 L. G. Khvostantsev, L. F. Vereshchagin, A. P. Novikov, Device of toroid type for high pressure generation, *High Temp.-High Pres.*, 1977, **9**, 637-639.

4 J. M. Besson, G. Hamel, P. Grima, R. J. Nelmes, J. S. Loveday, S. Hull and D. Haüsermann, A Large Vokume Pressure Cell for High Temperatures. *High Press. Res.*, 1992, **8**, 625.

5 S. Klotz, Th. Strässle, G. Rousse, G. Hamel and V. Pomjakushin, Angle-dispersive neutron diffraction under high pressure to 10 GPa. *Appl. Phys Lett.*, 2005, **86**, 031917.

6 G. Morard, M. Mezouar, N. Rey, R. Poloni, A. Merlen, S. Le Floch, P. Toulemonde, S. Pascarelli, A. San Miguel, C. Sanloup and G. Fiquet, Optimization of Paris-Edinburgh press cell assemblies for *in situ* monochromatic X-ray diffraction and X-ray absorption. *High Press. Res.*, 2007, **27**, 223.

7 C. E. Weir, E. R. Lippincott, A. Van Valkenburg and E. N. Bunting, Infrared studies in the 1- to 15-micron region to 30,000 atmospheres. *J. Res. Natl. Bur. Stand. Sect. A Phys. Chem.*, 1959, **63A**, 55-62.

8 L. Merrill and W. A. Bassett, Miniature diamond anvil pressure cell for single crystal x-ray diffraction studies, *Rev. Sci. Instrum.*, 1974, **45**, 290-294.

9 R. Boehler and K. De Hantsetters, New anvil designs in diamond-cells, *High Press. Res.*, 2004, **24**, 391-396.

10 B. Li, C. Ji, W. Yang, J. Wang, K. Yang, R. Xu, W. Liu, Z. Cai, J. Chen and H. Mao, Diamond anvil cell behavior up to 4 Mbar. *Proc. Natl. Acad. Sci. U. S. A.*, 2018, **115**, 1713-1717.

11 N. Dubrovinskaia, L. Dubrovinsky, N. A. Solopova, A. Abakumov, S. Turner, M. Hanfland, E. Bykova, M. Bykov, C. Prescher, V. B. Prakapenka, S. Petitgirard, I. Chuvashova, B. Gasharova, Y.-L. Mathis, P. Ershov, I. Snigireva and A. Snigirev, Terapascal static pressure generation with ultrahigh yield strength nanodiamond. *Sci. Adv.*, 2016, **2**, e1600341.

12 A. Dewaele, P. Loubeyre, F. Occelli, O. Marie and M. Mezouar, Toroidal diamond anvil cell for detailed measurements under extreme static pressures. *Nat. Commun.*, 2018, **9**, 2913.

13 S. Anzellini, D. Alfé, M. Pozzo and D. Errandonea, Melting line of calcium characterized by in situ LH-DAC XRD and first-principles calculations. *Sci. Rep.*, 2021, **11**, 15025.

14 A. Dewaele, M. Mezouar, N. Guignot and P. Loubeyre, Melting of lead under high pressure studied using second-scale time resolved X-ray diffraction. *Phys. Rev. B*, 2007, **76**, 144106.

15 M. Krstulović, A. D. Rosa, N. Biedermann, T. Irifune and M. Wilke, Structural changes in aluminosilicate glasses up to 164 GPa and the role of alkali, alkaline earth cations and alumina in the densification mechanism. *Chem. Geol.*, 2021, **560**, 119980.

16 A. J. Anderson, H. Yan, R. A. Mayanovic, G. Solferino and C. J. Benmore, High-energy X-ray diffraction of a hydrous silicate liquid under conditions of high pressure and temperature in a modified hydrothermal diamond anvil cell. *High Press. Res.*, 2014, **34**, 100-109.

17 D. D. Jackson, C. Aracne-Ruddle, V. Malba, S. T. Weir, S. A. Catledge and Y. K. Vohra, Magnetic susceptibility measurements at high pressure using designer diamond anvils. *Rev. Sci. Instrum.*, 2003, **74**, 2467-2471.

18 L. Zhang, Y. Tang, A. R. Khan, M. M. Hasan, P. Wang, H. Yan, T. Yildirim, J. F. Torres, G. P. Neupane, Y. Zhang, Q. Li and Y. Lu, 2D Materials and Heterostructures at Extreme Pressure. *Adv. Sci.*, 2020, **7**, 2002697.

19 A. P. Nayak, Z. Yuan, B. Cao, J. Liu, J. Wu, S. T. Moran, T. Li, D. Akinwande, C. Jin and J.-F Lin, Pressure-Modulated Conductivity, Carrier Density, and Mobility of Multilayered Tungsten Disulfide. *ACS Nano*, 2015, **9**, 9, 9117-9123.

20 G. Morard, D. Andrault, D. Antonangeli and J. Bouchet, Properties of iron alloys under the Earth's core conditions. *C. R. Geoscience*, 2014, **346**, 130-139.

21 G. Morard, D. Andrault, D. Antonangeli, Y. Nakajima, A. L. Auzende, E. Boulard, S. Cervera, A. Clark, O. T. Lord, J. Siebert, V. Svitlyk, G. Garbarino and M. Mezouar, Fe-FeO and Fe-Fe_3C melting relations at Earth's core-mantle boundary conditions: Implications for a volatile-rich or oxygen-rich core. *E. P. Sci. Lett.*, 2017, **473**, 94-103.

22 S. Anzellini, A. Dewaele, M. Mezouar, P. Loubeyre and G. Morard, Melting of Iron at Earth's Inner Core Boundary Based on Fast X-ray Diffraction. *Science*, 2013, **340**, 464-466.

23 R. Boehler, Diamond cells and new materials. *Materialstoday*, 2005, **8**, 34-42.

24 H. Sumiya, N. Toda and S. Satoh, Mechanical properties of synthetic type IIa diamond crystal. *Dia. Rel. Materials*, 1997, **6**, 1841-1846.

25 J. E. Field, The mechanical and strength properties of diamond. *Rep. Prog. Phys.*, 2012, **75**, 126505.

26 A. V. Sukhadolau, E. V. Ivakin, V. G. Ralchenko, A. V. Khomich, A. V. Vlasov and A. F. Popovich, Thermal conductivity of CVD diamond at elevated temperatures. *Dia. Rel. Materials*, 2005, **14**, 589-593.

27 J. M. Wheeler, R. A. Oliver and T. W. Clyne, AFM observation of diamond indenters after oxidation at elevated temperatures. *Dia. Rel. Materials*, 2010, **19**, 1348-1353.

28 R. Boehler and K. De Hantsetters, New anvil designs in diamond-cells. *High Press. Res.*, 2004, **24**, 391-396.

29 L. Merrill and W. A. Bassett, Miniature diamond anvil pressure cell for single crystal x-ray diffraction studies. *Rev. Sci. Instrum.*, 1974, **45**, 290-294.

30 R. Letoullec, J.-P Pinceaux and P. Loubeyre, The membrane diamond anvil cell: A new device for generating continuous pressure and temperature variations. *High Press. Res.*, 1988, **1**, 77-90.

31 J. -F. Lin, J. Shu, H. Mao, R. J. Hemley and G. Shen, Amorphous boron gasket in diamond anvil cell research. *Rev. Sci. Instrum.*, 2003, **74**, 4732-4736.

32 J. Besson and R. Nelmes, New developments in neutron-scattering methods under high pressure with the Paris-Edinburgh cells. *Physica B: Condensed Matter*, 1995, **213**, 31-36.

33 M. Mezouar, T. Le Bihan, H. Libotte, Y. Le Godec and D. Häusermann, Paris-Edinburgh large-volume cell coupled with a fast imaging-plate system for structural investigation at high pressure and high temperature. *J. Synchrotron Radiat.*, 1999, **6**, 1115.

34 G. Shen and Y. Wang, High-pressure apparatus integrated with synchrotron radiation. *Reviews in Mineralogy and Geochemistry*, 2014, **78**, 745-777.

35 V. L. Solozhenko, V. Z. Turkevich and W. B. Holzapfel, Refined Phase Diagram of Boron Nitride. *J. Phys. Chem. B*, 1999, **103**, 15, 2903-2905.

36 C. Yuan, J. Li, L. Linday, D. Cherns, J. W. Pomeroy, S. Liu, J. H. Edgar and M. Kuball, Modulating the thermal conductivity in hexagonal boron nitride via controlled boron isotope concentration. *Comm. Phys.*, 2019, **2**, 43.

37 B. Håkansson and P. Andersson, Thermal conductivity and heat capacity of solid NaCl and NaI under pressure. *J. Phys. Chem. Solids*, 1986, **47**, 4, 355-365.

38 A. Pierret, D. Mele, H. Graef, J. Palomo, T. Taniguchi, K. Watanabe, Y. Li, B. Toury, C. Journet, P. Steyer, V. Garnier, A. Loiseau, J. -M Berroir, E. Bocquillon, G. Fève, C. Voisin, E. Baudin, M. Rosticher and B. Plaçais, Dielectric permittivity, conductivity and breakdown field of hexagonal boron nitride. *Mater. Res. Express*, 2022, **9**, 065901.

39 K. V. Rao, Electrical Conductivity and Dielectric Properties of NaCl, KCl, and KBr Single Crystals near Their Melting Temperatures. *Phys. Stat. Sol.*, 1975, **30**, 391-395.

40 R. A. Forman, G. J. Piermarini, J. D. Barnett and S. Block, Pressure measurement made by the utilization of ruby sharp-line luminescence. *Science*, 1972, **176**, 284-285.

41 J. D. Barnett, S. Block and G. J. Piermarini, An Optical Fluorescence System for Quantitative Pressure Measurement in the Diamond-Anvil Cell. *Rev. Sci. Instrum.*, 1973, **44**, 1-9.

42 G. J. Piermarini, S. Block, J. D. Barnett and R. A. Forman, Calibration of the pressure dependence of the R_1 ruby fluorescence line to 195 kbar. *J. Appl. Phys.*, 1975, **46**, 2774-2780.

43 D. L. Decker, High-Pressure Equation of State for NaCl, KCl and CsCl. *J. Appl. Phys.*, 1971, **42**, 3239-3244.

44 H. K. Mao, J. Xu and P. M. Bell, Calibration of the Ruby Pressure Gauge to 800 kbar Under Quasi-Hydrostatic Conditions. *J. Geophys. Res.*, 1986, **91**, 4673-4676.

45 A. Dewaele, P. Loubeyre and M. Mezouar, Equations of state of six metals above 94 GPa. *Phys. Rev. B*, 2004, **70**, 1-8.

46 A. Dewaele, M. Torrent, P. Loubeyre and M. Mezouar, Compression curves of transition metals in the Mbar range : Experiments and projector augmented-wave calculations. *Phys. Rev. B*, 2008, **78**, 10, 1-13.

47 G. Shen, Y. Wang, A. Dewaele, C. Wu, D. E. Frantanduono, J. Eggert, S. Klotz, K. F. Dziubek, P. Loubeyre, O. V. Fat'yanov, P. D. Asimov, T. Mashimo, R. M. M. Wentzcovitch and other members of the IPPS task group, Toward an international practical pressure scale: A proposal for an IPPS ruby gauge (IPPS-Ruby2020). *High Press. Res.*, **40**:3, 299-314 (2020).

48 F. Datchi, A. Dewaele, P. Loubeyre, R. Letoullec, Y. Le Godec, B. Canny, Optical pressure sensors for high-pressure-high-temperature studies in a diamond anvil cell. *High Press. Res.*, **27**:4, 447-463 (2007).

49 A. Lacam, C. Chateau, High-pressure measurements at moderate temperatures in a diamond anvil cell with a new optical sensor: $SrB_4O_7:Sm^{2+}$. *J. Appl. Phys.*, **66**, 366-372 (1989).

50 J. M. Leger, C. Chateau, A. Lacam, $SrB_4O_7:Sm^{2+}$ pressure optical sensor: Investigations in the megabar range. *J. Appl. Phys.*, **68**, 2351-2354 (1990).

51 F. Datchi, R. LeToullec, P. Loubeyre, Improved calibration of the $SrB_4O_7:Sm^{2+}$ optical pressure gauge: Advantages at very high pressures and high temperatures. *J. Appl. Phys.*, **81**, 3333-3339 (1997).

52 F. Birch, Finite Elastic Strain of Cubic Crystals. *Phys. Rev.*, **71**, 809-824 (1947).

53 P. Vinet, J. H. Rose, J. Ferrante, J. R. Smith, Universal features of the equation of state of solids. J. Phys.: Condens. Matter, 1, 1941-1963 (1989).

54 P. I. Dorogokupets, A. Dewaele, Equations of state of MgO, Au, Pt, NaCl-B1, and NaCl-B2: Internally consistent high-temperature pressure scales. *High Press. Res.*, **27**, 431-446 (2007).

55 O. L. Anderson, D. G. Isaak, S. Yamamoto, Anharmonicity and the equation of state for gold. *J. Appl. Phys.*, **65**, 1534-1543 (1989).

56 S. Anzellini, A. Dewaele, F. Occelli, P. Loubeyre, M. Mezouar, Equation of state of rhenium and application for ultra high pressure calibration. *J. Appl. Phys.*, **115**, 043511 (2014).

57 W. A. Crichton, M. Mezouar, Noninvasive pressure and temperature estimation in large-volume apparatus by equation-of-state cross calibration. *High Temperatures – High Pressures*, **34**, 235-242 (2002).

Chapter 3:

In situ characterization under extreme conditions using synchrotron x-rays

In this chapter, we provide the essential information about the different probing techniques used in the framework of this thesis. We describe the principles of x-ray diffraction on crystals and liquids, x-ray absorption density measurements and viscosity measurements. Since all experiments have been performed at the ESRF synchrotron, and mostly at beamline ID27 which had just gone through a major upgrade, we also provide a description of this facility.

1. Synchrotron radiation

High pressure diffraction experiments can only be performed if an extremely bright radiation is used. The energy of the x-ray also must be high because of the limited x-ray aperture of high-pressure cells and the highly absorbing pressure windows at energies below 15 keV. The small size of the sample imposes the use of a highly collimated and extremely brilliant beam. Because of that, high pressure experiments are very difficult to perform with conventional laboratory x-ray sources. The European Synchrotron Radiation Facility (ESRF) is currently the only fourth generation high-energy synchrotron worldwide , having gone through a major upgrade of its accelerator and some of its beamlines since 2019.

Figure 3.1. Photograph of the ESRF [courtesy of ESRF].

1.1. The ESRF

The European Synchrotron Radiation Facility (ESRF) is a research center created in 1989 and initially funded by twelve European countries and later joined by nine additional ones. The ESRF was the first *third generation*, and now recently the first *fourth generation* facility in the world, making it the most intense x-ray synchrotron source.

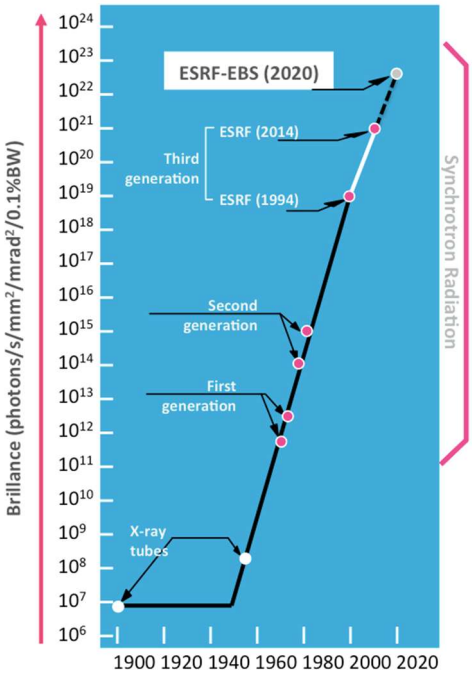

Figure 3.2. Historical evolution of the brilliance of x-ray sources [courtesy of ESRF].

The ESRF accelerator complex is composed of 3 parts: the linear accelerator, the booster synchrotron and the storage ring (see Figure 3.3.).

Electron are first injected from an electron gun into the linear accelerator or Linac. After only travelling 20 cm in the Linac, the electrons have already reached (almost) the speed of light, which is why it is preferred to speak of the “energy” of the electrons, rather than of their speed. At the end of the Linac, which is 20 m long, the energy of the electrons is 200 million electronvolts (200 MeV). The electrons are then injected into the booster synchrotron where their energy is ramped up thanks to accelerating cavities up to 6 GeV. When the electrons have reached this energy, they are sent to the storage ring, where they are maintained at constant energy.

The electrons are injected in bunches. Each bunch contains about 1 billion electrons and measures about 6 µm in height, 20 µm in width and about 1 cm in length. The electron bunches circulate inside a vacuum chamber in an ultra-high vacuum environment, 10^{-9} mbar, comparable to the level of vacuum found in space.

The electrons are kept on a circular trajectory by a series of magnets. When they pass through a bending magnet, the relativistic electrons are subjected to an acceleration perpendicular to their velocity, and emit light known as synchrotron radiation. In emitting this light, they lose about $1/1000^{th}$ of their energy at each turn in the storage ring. The latter is restored by using accelerating or radio-frequency (RF) cavities.

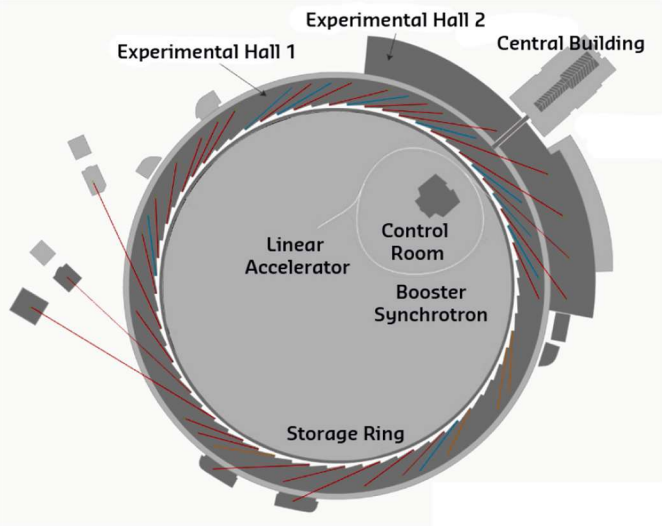

Figure 3.3. Schematic view of the ESRF. The location of the accelerators is indicated [courtesy of ESRF].

1.2. The ID27 High pressure beamline

Beamline ID27 is an x-ray station mostly designed for x-ray diffraction and fully dedicated to science at very high pressures[1]. The beamline accommodates complex sample environments such as the double-sided laser heating system for high T experiments in the diamond anvil cell (DAC)[2], the helium cryostat for low-T DAC experiments, and the Paris-Edinburgh press[3-5]. These techniques are powerful tools to explore a very wide pressure (1-300 GPa) and temperature (5-5000 K) range. All beamline components (source, optics and detectors) are entirely designed for these very demanding conditions.

1.2.1. The x-ray source

High pressure diffraction experiments require high photon flux at high x-ray energies because of the limited x-ray aperture of the high-pressure cells and the highly absorbing pressure windows at energies below 15 keV. Thanks to the upgrade of the ESRF to 4th generation, the extremely bright source (EBS) provides a significantly higher photon flux density and higher coherence. At photon energies above 30 keV, the energy range most relevant to diffraction and imaging at extreme conditions, the brilliance is increased by almost two orders of magnitude and the coherent fraction of the photon flux by a factor 10. Therefore, the choice of an optimized x-ray source is of primary importance to fully exploit the outstanding performance of the EBS. A U18 cryo-undulator (CPMU18), placed in the middle of the ID27 straight section, was selected as the best system in terms of photon flux and tunability. This undulator replaced the former two U23 in-vacuum undulators installed on ID27 prior to the upgrade. The performance of a U23 undulator is compared to a CPMU18 system installed on the EBS (Figure 3.4.). The numerical simulations show a substantial gain in photon flux and a much better tunability in the energy region between 15 and 25 keV.

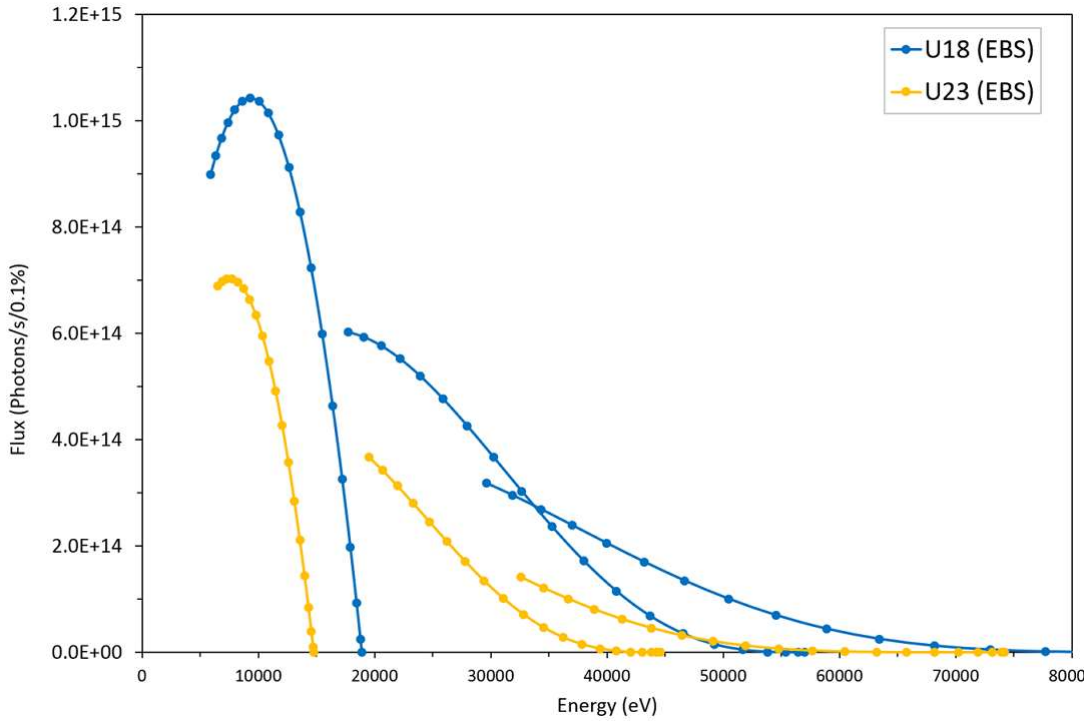

Figure 3.4. On axis brilliance for 2-meter long U23 and CPMU18 undulators installed on the EBS. [courtesy of M. Mezouar]

1.2.2. The hutches

ID27 is built up of three optics hutches (OH1, OH2 and OH3), one experimental hutch (EH), a control cabin, a laser heating high-pressure laboratory and a workshop.

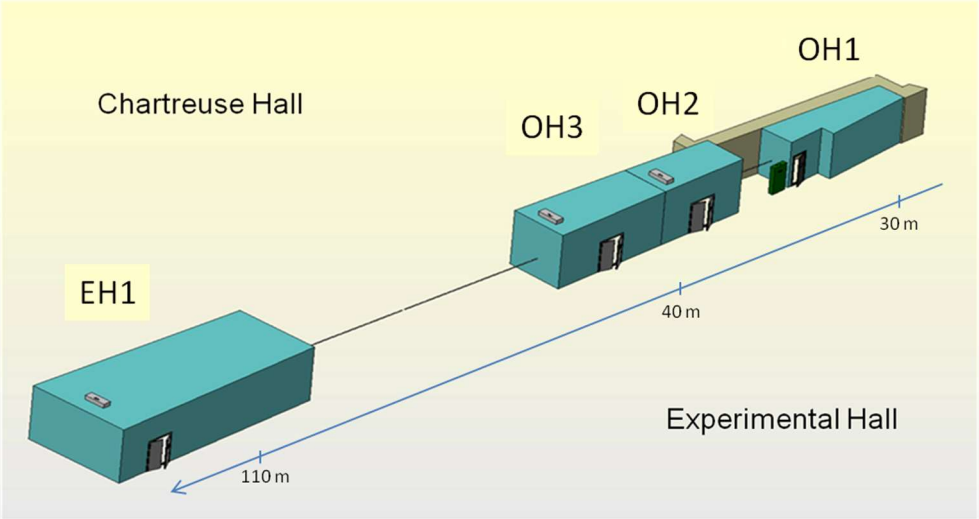

Figure 3.5. Representation of the ID27 beamline

OH1 houses the double multilayer mirror (DMM) and attenuators for the incoming synchrotron beam. The DMM is used to clean the beam after the undulator and produces a "pink" beam. The DMM is at a distance of 30 m from the source.

OH2 houses the double crystal monochromator (DCM) at a distance of 40 m from the source. OH3 is more or less empty and houses the absorber and beam shutter at the end of the optics hutches before the long tube to the experimental hutch.

Monochromatic or "pink" beam between 15 and 60 keV is produced and shaped in the three optic hutches.

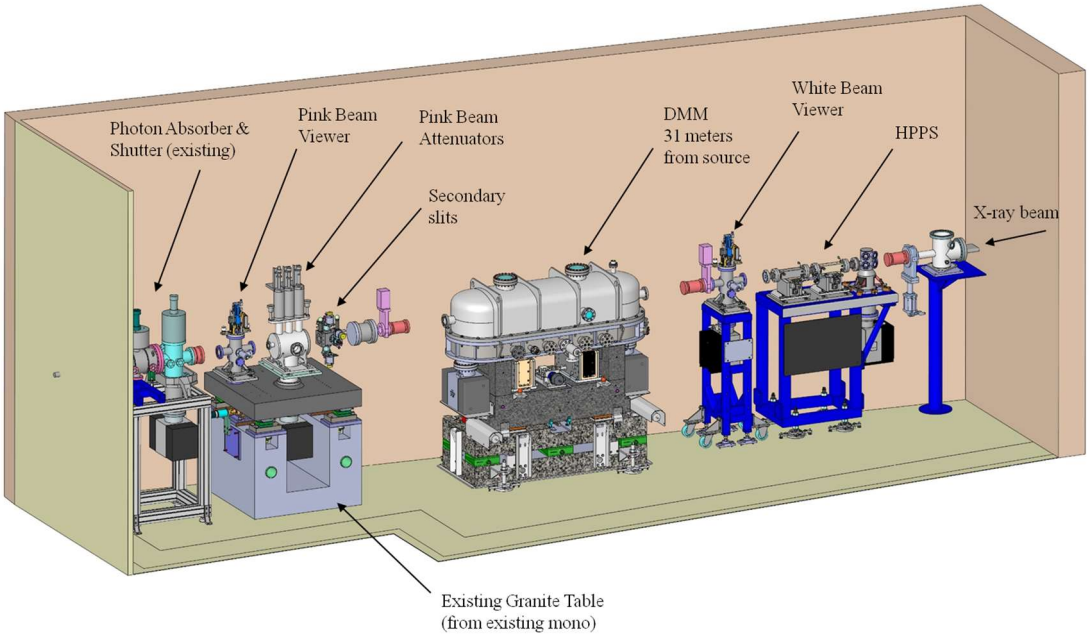

Figure 3.6. Principal optical elements in optics hutch OH1. [courtesy of M. Mezouar]

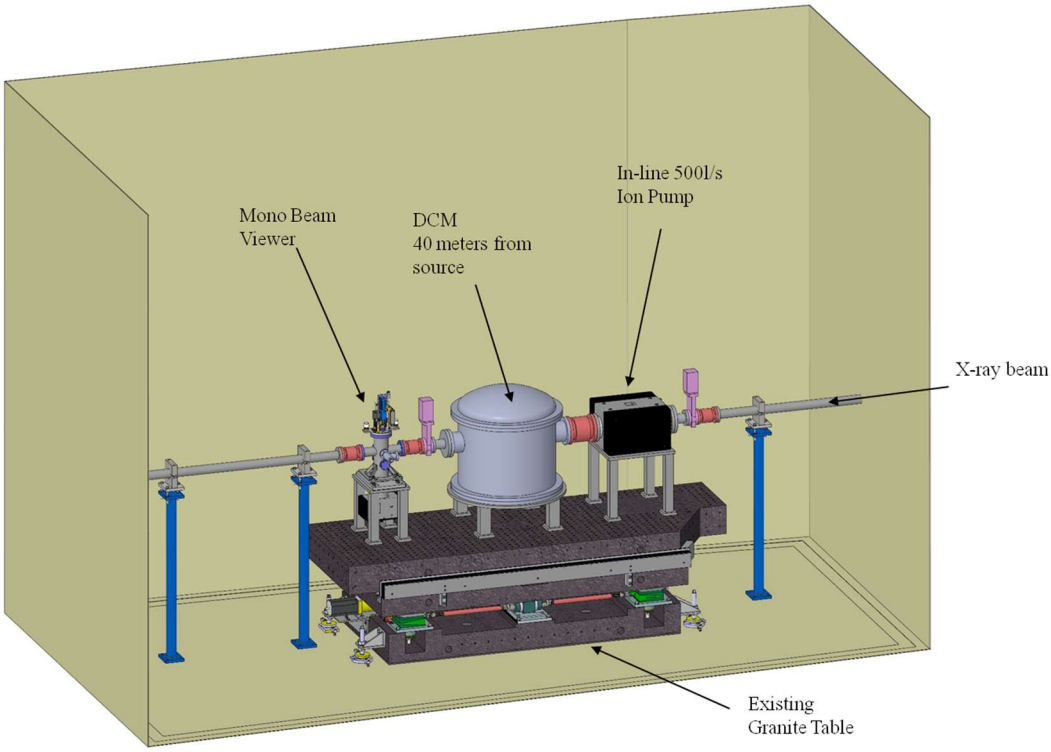

Figure 3.7. Principal optical elements in optics hutch OH2. [courtesy of M. Mezouar]

The experimental hutch is located at 110 meters from the X-ray source. This is essential for nano-focusing experiments while keeping the maximum space for complex sample environments (laser heating). The experimental hutch provides Kirkpatrick-Baez mirror for focusing, goniometers for sample positioning, further auxiliary equipment and the detectors. All these elements are mounted on high-stability granites and can be moved and put in place by high-precision translations.

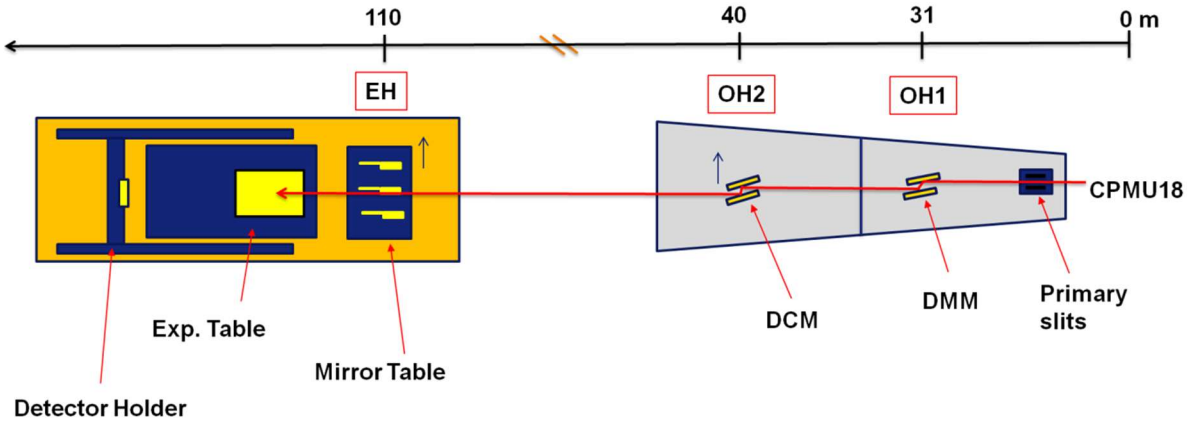

Figure 3.8. Optical configuration of the ID27 beamline. OH3 that does not contain any optical elements is not represented.

1.2.3. Monochromatic and "pink" beam

The double-multilayer mirror (DMM) is always in the white beam of the undulator. The DMM is used to suppress harmonics of the undulator. It produces a "pink" beam which can be further monochromatized by the monochromator. The pink beam produced by the DMM can be used for time-resolved x-ray diffraction, x-ray fluorescence and x-ray imaging down to the microsecond time scale.

The fixed-exit double-crystal monochromator (DCM) that accommodates two silicon crystals Si(111), scatters in the horizontal plane and is used for high resolution nano and micro x-ray diffraction applications.

1.2.4. Focusing options

The focusing options are covering the range of super-nano focus, nano-focus and micro-focus between 250 nm and 1.5 µm. The Kirkpatrick-Baez KB systems for focusing offer a large

working distance to accommodate complex sample environments. The KB3 is the default focusing device.

Table 3.1. Characteristics of the three available KB systems of the ID27 beamline.

	KB1 (super-nano)	KB2 (nano)	KB3 (micro)
Energy range [keV]	15 - 25	33	30 - 60
Focus (H x V) [nm]	270 x 220	350 x 500	2000 x 2000
Working distance [mm]	180	430	470
Flux [photons/s] Monochromatic beam, ray tracing 15 keV $\Delta E/E = 1.5 \times 10^{-4}$	7×10^{12}	1.1×10^{13}	2.2×10^{12}
Flux [photons/s] Pink beam, ray tracing 15 keV $\Delta E/E = 2$ %	5×10^{14}	7×10^{14}	1×10^{14}
	nano- and micro-LH-stage for DAC	nano- and micro-LH-stage for DAC / heavy duty stage	micro-LH-stage for DAC / heavy duty stage

1.2.5. Sample stages

There are three available sample stages at the ID27 high pressure beamline. The three sample stages are a nano-positioning system, a micro-positioning system for low and high temperature diamond anvil cell x-ray diffraction, x-ray fluorescence and x-ray imaging experiments (also called the "laser-heating stage"), and a heavy-duty goniometer for the Paris-Edinburgh press or other heavy equipment, with a maximum load of 200 kg.

- The nano-stage for DAC includes three high precision translations and one rotation for nano-diffraction and nano-fluorescence experiments in diamond anvil cells (DAC).
- The micro-stage for laser-heating stage double-sided YAG and CO_2, which is a modified version of the "former" ID27 laser-heating setup with Schwarzschild objectives for temperature measurements.
- The heavy-duty stage for Paris-Edinburgh press, resistively heated DAC or helium-flow cryostat.

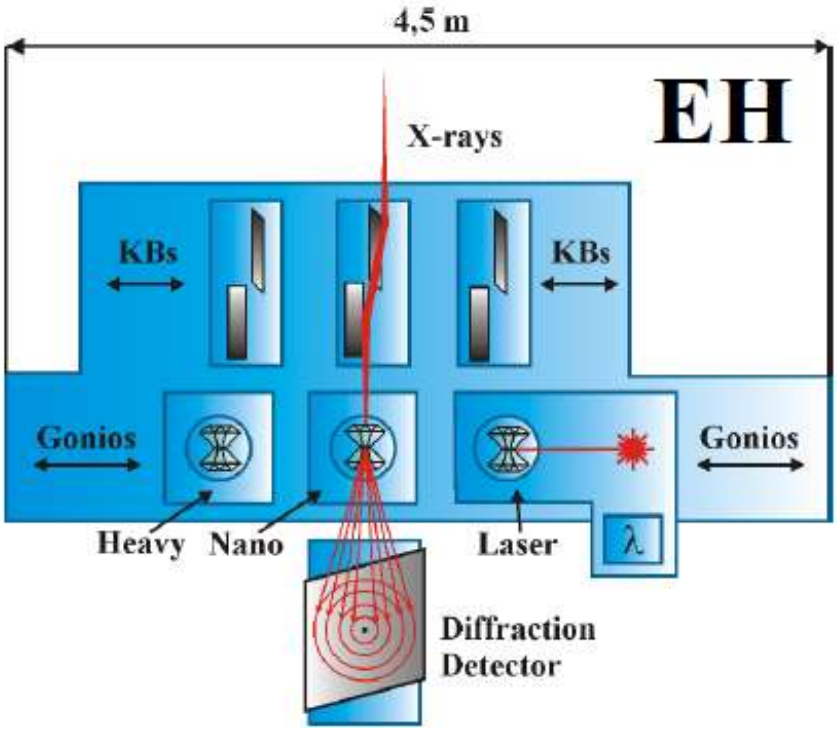

Figure 3.9. Sketch of the experimental hutch. The setup includes three movable KB systems, three specific goniometers and a large area detector. The KB-mirror systems are mounted on a high-stability granite table. A high-precision air pad lateral translation enables switching rapidly from the different pre-aligned focusing configurations.

1.2.6. Detectors

Since 2021, the detector used at ID27 for x-ray diffraction is the EIGER2 X CdTe 9M detector from DECTRIS. It is a large area detector optimized for high energy diffraction experiments. It covers a large field of view, with a 233.2 x 245.2 mm (H x V) sensitive area, in the form of 3110 x 3269 pixels (75 x 75 μm^2 pixel size). This photon-counting CdTe pixel based detector exhibits much higher performances than the previous Perkin-Elmer system. The photon-counting CdTe detector shows significantly less noise, resulting in improved visibility of weak diffraction rings. It also has a very small readout time (few ms), particularly convenient for time resolved experiments.

ID27 is also equipped with the fast PCO DIMAX for X-ray imaging which can record up to 7000 images per second.

Figure 3.10. Eiger2X CdTe photon-counting detector from DECTRIS on the right and rayonix MX170-HS detector on the left.

1.2.7. The multi-channel collimator (MCC)

When using the Paris-Edinburgh press setup, the sample is confined inside a complex environment (hBN capsule, graphite heater, boron-epoxy gasket). This environment, although

crucial to ensure efficient thermal insulation and to produce quasi-hydrostatic pressure conditions, generate a strong and non-negligible x-ray diffraction background. The oscillating slit system (Soller slits) also called multichannel collimator (MCC) is a setup that enables almost complete subtraction of the scattering signals from the sample environment in x-ray diffraction data collections. The MCC used on ID27 is a device optimized for Paris-Edinburgh press[6] and is inspired from the device proposed for multi-anvil presses[7]. The MCC allows the *in situ* collection of high quality x-ray diffraction data of liquids, amorphous and crystalline materials at both high pressure and high temperature conditions[8]. It is placed between the detector and the sample (see above Figure 3.10.).

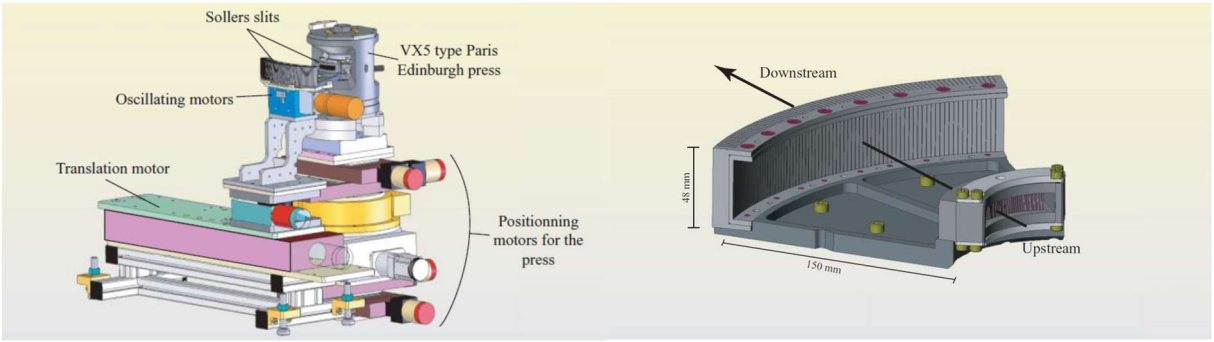

Figure 3.11. Left. Experimental setup installed on the high-pressure beamline ID27 at the ESRF. The Paris Edinburgh press VX5 type is installed on different positioning motors. The MCC system is mounted on positioning motors to center it on the incident x-ray beam, and on oscillating motors that rotate during the acquisition procedure. A translation motor is also present in order to remove the slits during x-ray absorption measurements. Right. Drawing of the MCC.[9]

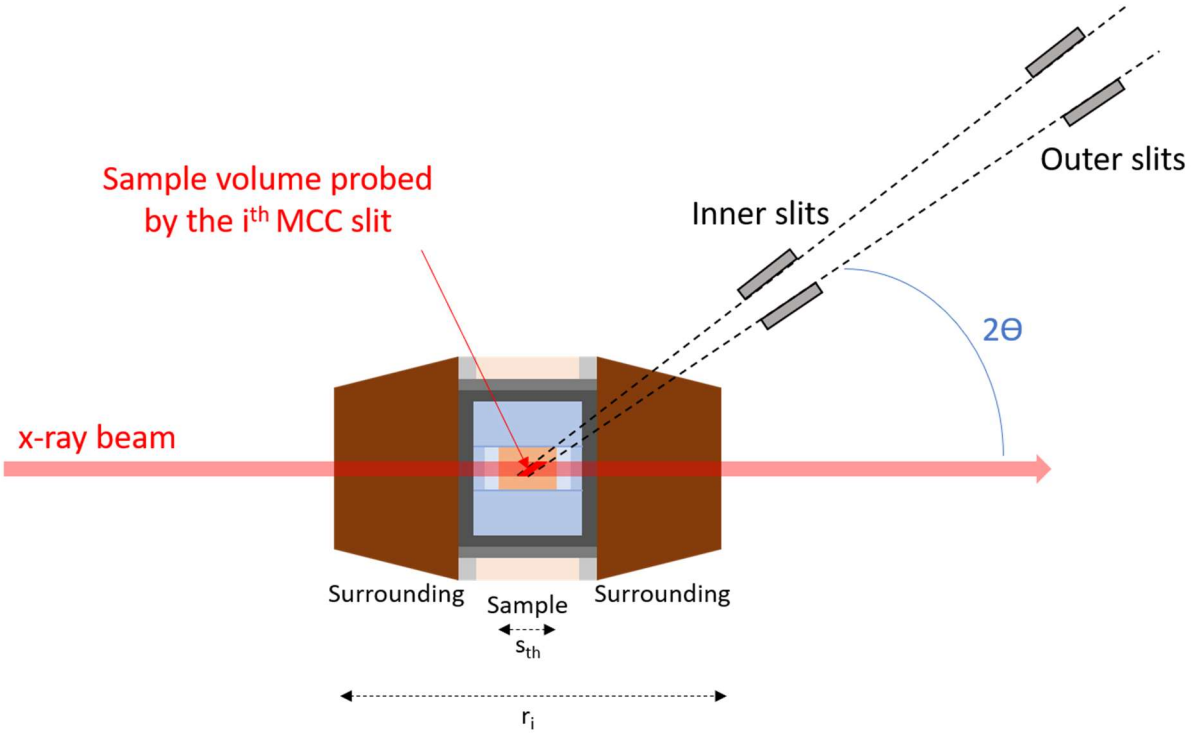

Figure 3.12. Schematic representation of the principle of the Soller slits for the ith slit, in the case of a PEP sample assembly

The basic principle of the MCC is illustrated in Figure 3.12. The volume seen by the detector is defined by the inner and the outer slit network. The diffracted intensities intercepted by the detector through the multi-channel collimator mostly come from the sample and the majority of the parasitic contribution coming from the PEP sample environment is eliminated. It is worth to mention that the background reduction through the MCC is optimal at higher angles. This is illustrated in Figure 3.13., where the diffraction pattern of an iron-sulfur liquid sample in the PEP cell, with the different contributions coming from the sample environment are shown. The theoretical maximum angle φ_i where a part i of the cell assembly is still diffracting may be geometrically calculated as follows:

$$\varphi_i = 2\sin^{-1}\left(\frac{\delta}{2r_i}\right)$$

where δ is the slit thickness and r_i is the radius of the considered part i of the cell assembly. The volume seen by the detector decreases with the angle 2θ and depends on the beam size and the dimensions of the inner and outer slits of the MCC. Both sets of slits are composed of 75 slits at 0.8° angle from each other to cover a total angle of 60° (i.e. 30° for the

2θ diffraction geometry). The inner slits block is located at 50 mm from the sample and composed of a set of 50 µm slits, while the outer block is located at 200 mm from the sample and composed of a set of 200 µm slits. This geometry insures a high spatial selectivity of the MCC. During an experiment, the sample is centered on the rotation axis of the MCC by maximizing the sample to noise ratio. During an acquisition, the MCC rotates around the sample at a constant speed, so that we obtain a homogeneous exposure of the 2D detector.

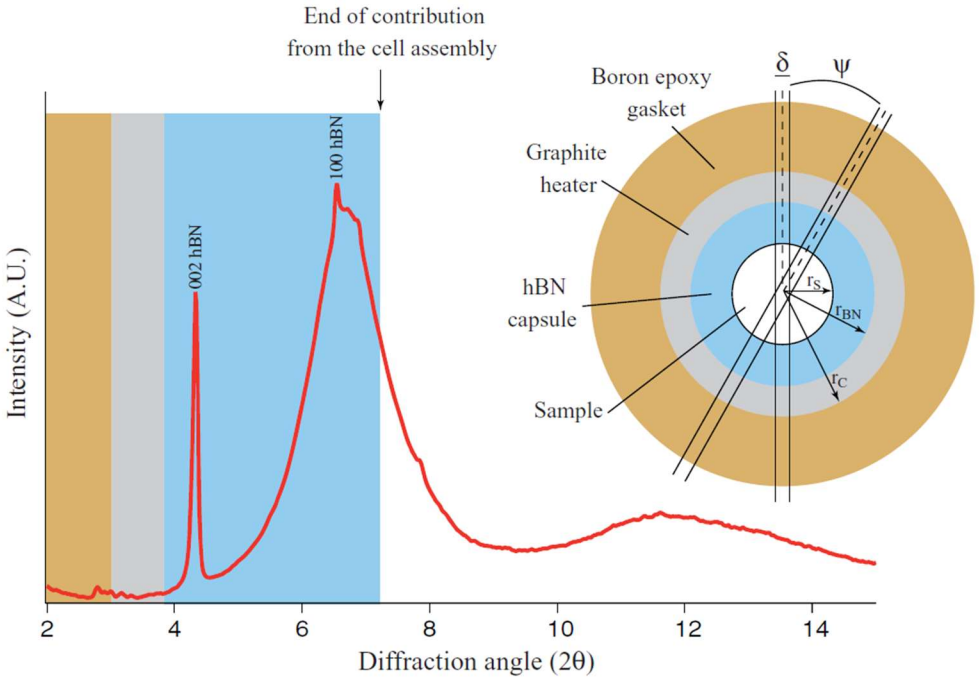

Figure 3.13. Diffraction signal from Fe-S liquid alloy with the different angle zone where each part of the cell assembly contributes to the signal, calculated following the equation $\varphi_i = 2\,sin^{-1}\,(\delta/2r_i)$. On the right, schematic drawing of the cell assembly indicating the principle of the MCC, where the diffracting zone at an angle φ correspond to the intersection of the incident x-ray beam and the zone defined by the slit positioned at this angle.[9]

2. X-ray diffraction

Knowledge about the structure of a material and how it evolves with pressure and temperature is essential for multiple scientific questions of fundamental or applied interest. The x-ray diffraction method is the most common technique used to determine the structure of a material under extreme conditions of pressure and temperature. The use of synchrotron sources, in particular of the fourth generation such as ESRF, has revolutionized the domain, providing a highly focused and extremely brilliant x-ray beam. This instrument enables to probe very

small samples as well as light elements. All x-ray diffraction experiments performed in the framework of this thesis have been made at ESRF (ID27, ID02 and ID22 beamline) or SOLEIL (SWING beamline). In the next subsections, we describe the principles of x-ray diffraction.

2.1. X-ray diffraction on crystals

The diffraction of x-rays by matter results from the elastic interaction of x-rays with the electrons of the material. In the case of a crystalline material, the diffracted waves will interfere constructively or destructively depending on the crystal symmetries, metrics and atomic contents. Therefore, the diffraction of x-rays by matter emerges as a powerful technique to retrieve the information about its structure, unit cell parameters and atomic positions.

The crystalline structure of a material comes from the repetition by translation of a primitive unit cell in the three direction of space **a**, **b** and **c**. The lattice structure is the regular periodic array of points defined by:

$$\boldsymbol{r} = u\boldsymbol{a} + v\boldsymbol{b} + w\boldsymbol{c}$$

where u, v and w are integers. In the three-dimensional space, there are 14 fundamental Bravais lattices, distributed in the 7 crystal systems: triclinic, monoclinic, orthorhombic, tetragonal, hexagonal, trigonal, and cubic. The crystal structure results from the association of an identical basis of atoms to every lattice point. Each atom j of the unit cell is labelled by its position vector $\boldsymbol{r}_j$:

$$\boldsymbol{r}_j = x_j\boldsymbol{a} + y_j\boldsymbol{b} + z_j\boldsymbol{c}$$

where x_j, y_j and z_j are the atomic coordinates which values are between 0 and 1.

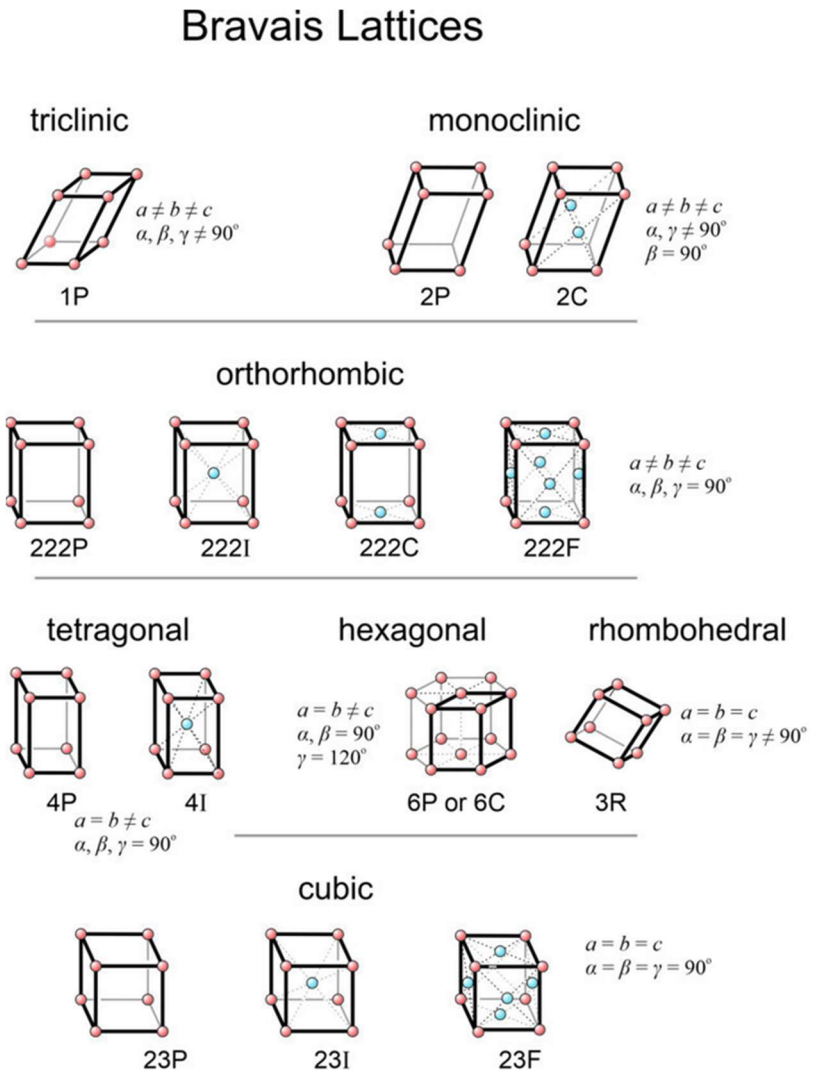

Figure 3.14. Representation of the 14 fundamental Bravais lattices for a three-dimensional crystal structure.

In crystallography, it is of common use to express the plane orientation in the reciprocal space defined as the Fourier transform of the Bravais lattice. It enables to simplify numerous crystallographic calculations and to easily formulate the diffraction theory (x-ray, neutrons, electrons). In the reciprocal space, the orientation of a crystallographic plane is expressed using the Miller indices (hkl). The (hkl) indices for a specific plane orientation are expressed in the reciprocal space $\boldsymbol{a}^*$, $\boldsymbol{b}^*$ and $\boldsymbol{c}^*$ expressed as:

$$\boldsymbol{a}^* = 2\pi \frac{\boldsymbol{b} \times \boldsymbol{c}}{\boldsymbol{a} \cdot (\boldsymbol{b} \times \boldsymbol{c})} \; ; \; \boldsymbol{b}^* = 2\pi \frac{\boldsymbol{c} \times \boldsymbol{a}}{\boldsymbol{b} \cdot (\boldsymbol{c} \times \boldsymbol{a})} \; ; \; \boldsymbol{c}^* = 2\pi \frac{\boldsymbol{a} \times \boldsymbol{b}}{\boldsymbol{c} \cdot (\boldsymbol{a} \times \boldsymbol{b})}$$

The lattice points in the reciprocal space are defined by a set of vector **G** in a similar way as in the direct space:

$$G = v_1 a^* + v_2 b^* + v_3 c^*$$

where v_i are integers.

The determination of the crystal structure is classically performed by means of x-ray, neutron or electron diffraction. In the framework of this thesis, x-ray diffraction was the only method employed, so we will restrict this introduction to this sole case. The wavelengths of the x-ray radiation must be comparable or smaller than the interatomic distances characteristic of the condensed matter. Figure 3.15. presents a simplified description of the interaction between an incident radiation at wavelength λ and a crystal plane with an incidence angle θ.

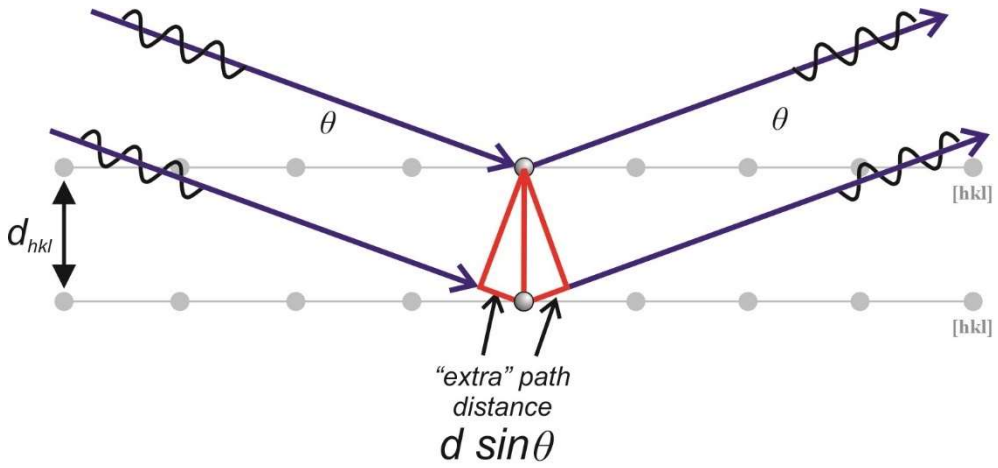

Figure 3.15. Interaction of the incident radiation with a set of parallel (hkl) planes, set apart of a distance d_{hkl}.

The distance between two consecutive planes is denoted d_{hkl}. The path difference between a radiation diffracted by the first plane and a radiation diffracted by the second plane is:

$$\delta = 2d_{hkl}\sin(\theta)$$

It is then possible to define the condition of constructive interferences, in which the phase shift between the two waves $\Delta\phi$ must be a multiple of 2π, i.e. $\Delta\phi = 2n\pi$ where n is an integer. Knowing that $\Delta\phi = 2\pi\delta/\lambda$, we obtain the Bragg law:

$$2d_{hkl}\sin(\theta) = n\lambda$$

Hence, for an incident radiation at wavelength λ, a set of planes defined by the Miller indices (hkl) will diffract the incident wave at an angle θ, and the measure of that angle enables to directly determine d_{hkl} for that set of planes.

$$K = k' - k = \Delta k = G$$

In the framework of this thesis, powders were studied using x-ray diffraction. In that case, the sample is composed of small crystallites with a random orientation. For a sufficiently large collection of crystallites, one will always find among these crystallites a certain amount that presents an incidence angle θ with the x-ray incident radiation satisfying the Bragg law. We can therefore consider that when a wave interacts with the sample, every [hkl] planes will diffract simultaneously, and that a single measure is sufficient to obtain the full set of Bragg peaks. In the ideal case, the resulting diagram is composed of homogeneous rings (called Debye-Scherrer rings) at a distance 2θ from the origin, depending on the [hkl] diffraction plane.

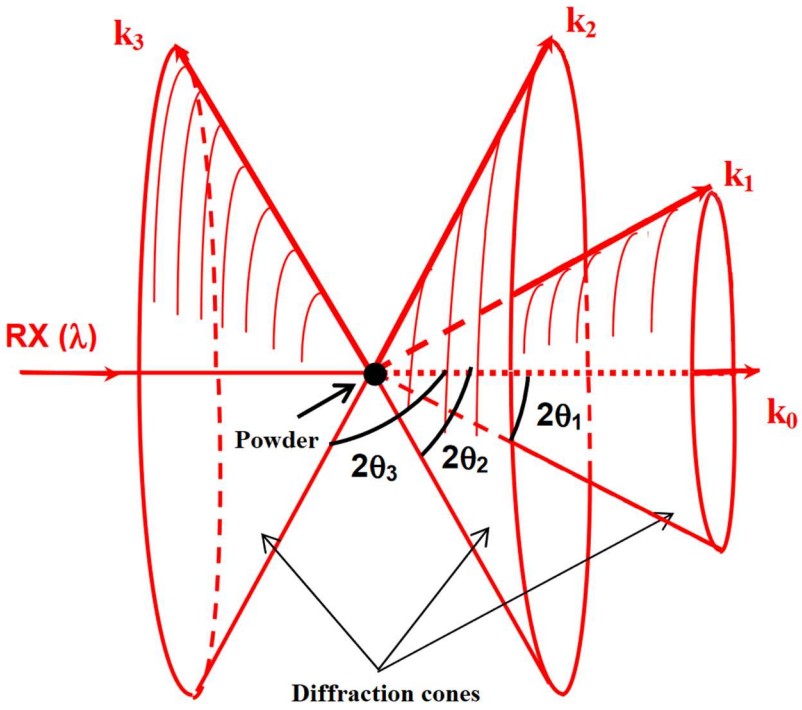

Figure 3.16. Configuration for the powder diffraction giving rise to Debye-Scherrer cones.

In addition to the position of the 2θ reflections, the diffractogram holds another information in the form of the relative intensity of the integrated peaks. The latter is related to the structure factor $\vec{F}_{hkl}$:

$$\vec{F}_{hkl} = \sum_{j=1}^{n} f_j(hkl) e^{-2i\pi(hx_j+ky_j+lz_j)}$$

where f_j is the form factor of the atom *j*:

$$f_j(\theta) = \int \rho_j(r) \exp(-2i\pi \boldsymbol{r}.\boldsymbol{r}^*) d\boldsymbol{r}$$

where $\rho_j(r)$the electronic density of the atom *j* is, $\boldsymbol{r}^*$ is the diffusion vector of amplitude $2\sin(\theta)/\lambda$. The scattered intensity is the product of the scattered amplitude by its complex conjugate:

$$I_{hkl} = F_{hkl} F_{hkl}^* = |F_{hkl}|^2$$

In the case of a perfect powder, the measure of the reflections relative intensities therefore enables to extract the nature of the diffracted materials, as well as their position in the lattice.

2.2. Powder diffraction – structural refinement

Prior to an experiment, the sample to detector distance, detector tilt angles and beam center must be accurately determined using a standard reference material such as LaB_6 or CeO_2 powder. In the framework of this thesis, the x-ray diffraction images were collected in transmission geometry on a two-dimensional detector and azimuthally integrated using the PyFAI software[10] as implemented in the DIOPTAS[11] suite. The resulting one-dimensional diffraction patterns were analyzed using the GSAS software[12] to refine the unit cell parameters and volume using a Le Bail[13] extraction of d-spacings using a pseudo-Voigt peak shape function. This method requires the knowledge of the space group and approximate unit cell parameters as input before starting the refinement. A typical pattern resulting from an experiment of this thesis and its corresponding Le Bail fit is shown in Figure 3.17.

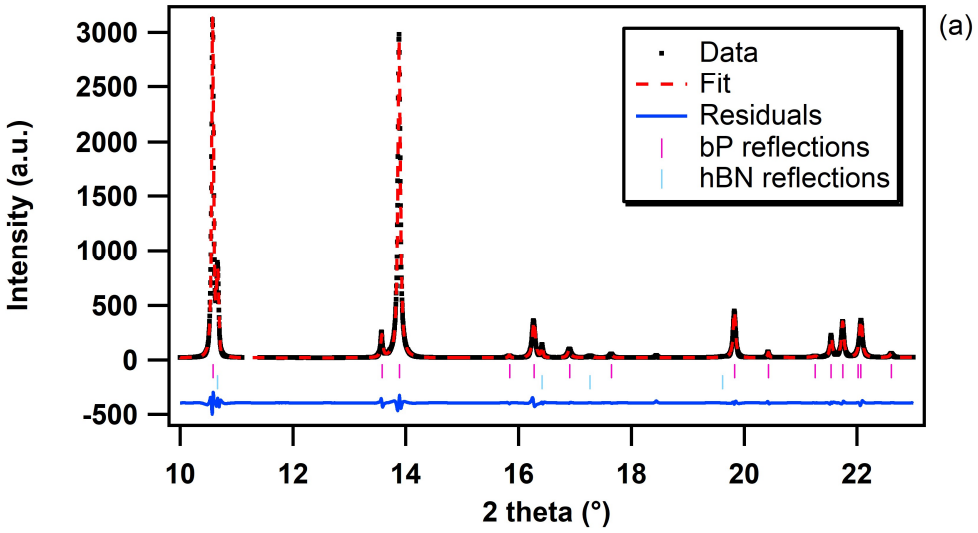

Figure 3.17. Diffraction pattern of powder black phosphorus at ambient conditions and its Le Bail fit.

2.3. X-ray diffraction on liquids

The liquid state is characterized by the lack of periodicity and therefore of long-range order. In a liquid, the distribution of atoms around a given atom or molecule at short distances is not uniform due to spatial and orientational correlations imposed by the molecular shape and intermolecular interactions. These correlations lie in the radial distribution function $g(r)$, which measures the deviation of the atomic density from its average value, by the presence of broad oscillations at definite distances, whose intensities decrease with r as $exp(-|r|/\xi)$, where ξ is the correlation length. X-ray diffraction of liquids makes possible to measure the structure factor $S(Q)$, which is related to the radial distribution function $g(r)$ by Fourier transform.

Since the diffuse scattering in a DAC experiment is dominated by background scattering, the analysis is necessarily different than for most liquid diffraction experiments where background scattering is minimized. In the framework of this thesis, we have used the well-established methodology and formalism developed by J. Eggert and collaborators[14] to analyze our x-ray diffraction data.

Theory

The Debye scattering equation gives the spherically averaged coherent x-ray scattering from N disordered atoms as:

$$I^{coh}(Q) = \sum_{m}^{N}\sum_{n}^{N} f_m(Q) f_n(Q) \frac{\sin Qr_{mn}}{Qr_{mn}}$$

where $Q = 4\pi \sin\theta/\lambda$ is the scattering momentum, $f_m(Q)$ is the atomic form factor for atom m, and r_{mn} is the distance between atoms m and n. For this thesis, only single element liquids were studied, so we can restrict ourselves to the case of a monoatomic liquid composed of identical atoms and separate the terms with $m = n$ to find:

$$I^{coh}(Q) = Nf^2(Q)\left(1 + \sum_{n\neq m} \frac{\sin Qr_{mn}}{Qr_{mn}}\right)$$

To develop this equation, we define the average atomic density function $\rho(r)$ such that:

$$\rho(r)dV \equiv \langle \rho_m(r_{mn}) dV_n \rangle_S$$

where $\rho(r)dV$ is the average number of atom centers in the volume element dV at distance r from a central atom, and S is the volume of liquid probed by the x-ray beam. We can rewrite the summation of the coherent scattering equation as an integral over the x-ray illuminated sample volume S:

$$I^{coh}(Q) = Nf^2(Q)\left\{1 + \int_S \rho(r) \frac{\sin Qr}{Qr} dV\right\}$$

Adding and subtracting an average atomic density ρ_0 (constant in S, and 0 elsewhere) to $\rho(r)$, we find:

$$I^{coh}(Q) = Nf^2(Q)\left\{1 + \int_S [\rho(r) - \rho_0] \frac{\sin Qr}{Qr} dV + \int_S \rho_0 \frac{\sin Qr}{Qr} dV\right\}$$

The last term in this equation represents the scattering from a hypothetical object which shares the same shape as the sample and a homogeneous density. This scattering would occur at such small angles close to the direct beam that it is generally not experimentally observable. Thus, we are left with the only experimentally observable coherent scattering of the N disordered atoms:

$$I^{co}\ (Q) = Nf^2(Q)\left\{1 + \int_0^{\infty} [\rho(r) - \rho_0] \frac{\sin Qr}{Qr} 4\pi r^2 dr\right\}$$

The structure factor is defined as:

$$S(Q) \equiv \frac{I^{coh}(Q)}{Nf^2(Q)} = 1 + \int_0^\infty [\rho(r) - \rho_0] \frac{\sin Qr}{Qr} 4\pi r^2 dr$$

And using the Fourier integral theorem, we can transform the previous equation to find:

$$F(r) \equiv 4\pi r[\rho(r) - \rho_0] = \frac{2}{\pi} \int_0^\infty Q\ i(Q) \sin(Qr)\ dQ$$

where $i(Q) = S(Q) - 1$. The radial distribution function or pair distribution function $g(r)$ is defined as $\rho(r)/\rho_0$ and is deduced from the previous equations as:

$$g(r) = 1 + \frac{F(r)}{4\pi r \rho_0}$$

X-ray diffraction of liquids in the DAC

For liquid samples in a DAC, the measured signal contains both the coherent and incoherent scattering of the sample and of the diamond anvils.

The experimentally measured scattered intensity $I^{meas}(Q)$ can be separated into the sample and background contributions terms modified by several factors:

$$I^{meas}(Q) = T(Q)I^{samp}(Q) + sI^{bkgd}(Q)$$

where $T(Q)$ and s are the DAC transmission and scale factor respectively, and $I^{bkgd}(Q)$ is the empty-cell background scattering. The total scattering from the sample is expressed as:

$$I^{samp}(Q) = \frac{1}{N\alpha} \left[I^{co}\ (Q) + N \sum_p I_p^{inco}\ (Q) \right]$$

where α is the normalization factor to transform the signal into atomic units and $I_p^{incoh}(Q)$ is the incoherent (Compton) scattering from atoms p in the sample. Therefore, the experimental determination of $I^{coh}(Q)$ is given by:

$$I^{co}\ (Q) = N\left[\alpha I^{samp}(Q) - \sum_{p} I_{p}^{inco}\ (Q)\right]$$

with:

$$I^{samp}(Q) = \frac{I^{meas}(Q) - sI^{bkgd}(Q)}{T(Q)}$$

Thus, the determination of the coherent signal highly depends on the quality of the background scattering measurement. In addition, the transmission of the diamond windows and of the multi-channel collimator must be included in the data analysis for a correct evaluation of the diffracted intensities. During an experiment, the background scattering is measured at the start or at the end of the experiment when the sample chamber of the DAC is empty. By orientating the DAC, we try to minimize Bragg peaks coming from the diamond anvils in the detector area where the liquid signal is collected. However, the thermal diffuse scattering (noted TDS) located near Bragg peaks giving each peak a broad temperature dependent footprint may interfere, thus, this empty cell background measurement should be performed at each temperature of the collected data set. When this empty cell measurement is not possible the signal from the solid sample collected near the melting line can be used as a reference background. This method of background subtraction relies on the fact that the coherent scattering in a crystalline solid is confined to narrow Bragg peaks and the associated TDS. Since the sample Bragg peaks are much sharper than any liquid information, they are easily removed by peak fitting. The incoherent Compton scattering is the same in the crystal and the liquid. When using this subtraction method, the TDS and incoherent scattering (Compton scattering) from the solid sample still need to be considered. The simplest description of TDS assumes that each molecular unit vibrates as a single unit independently of any other atoms. In this case the TDS is isotropic and proportional to a Debye-Waller factor:

$$I^{TDS}(Q) = NZ_{tot}^{2} f_{e}^{2}(Q)\left[1 - e^{-\langle \mu_{s}^{2} \rangle Q^{2}}\right]$$

where $\langle \mu_{s}^{2} \rangle$ is the mean-square component of the displacement of the molecular units in the scattering direction. In order to obtain an effective empty-cell background, the total diffuse scattering arising from Compton scattering (denoted $\sum_{p} I_{p}^{incoh}(Q)$) and TDS can be subtracted from the solid-sample background such as:

$$I^{bkgd}(Q) = I^{bkgd}_{solid}(Q) - \frac{NT(Q)}{\alpha'}\left\{\sum_p I_p^{incoh}(Q) - Z_{tot}^2 f_e^2(Q)\left[1 - e^{-\langle\mu_s^2\rangle Q^2}\right]\right\}$$

where α' is a normalization factor to convert from atomic units to experimental intensity.

The normalization factor α is determined using the Krogh-Moe and Norman method, which uses the properties of $\rho(r)$ and $\sin(Qr)$ when r goes to zero:

$$\lim_{r\to 0}[\rho(r)] = 0$$

$$\lim_{r\to 0}[\sin(Qr)] = Qr$$

To minimize the artificial oscillations in the PDF due to experimental errors in α and s and the truncation of $I^{meas}(Q)$ at a finite Q_{max}, we used the optimization procedure of J. Eggert and collaborators [14]. This procedure enables to determined $S(Q)$, $g(r)$, and the average number density ρ_0 and is based on a least-squares minimization of the artificial oscillations of $F(r) = 4\pi\rho_0[g(r) - 1]$ at small r (below the first intermolecular when $g(r)$ is expected null). The number density is directly related to the normalization coefficient α but is independent of the scale factor s. The determination of the number density is especially sensitive to the limited Q range over which $I(Q)$ is measured.

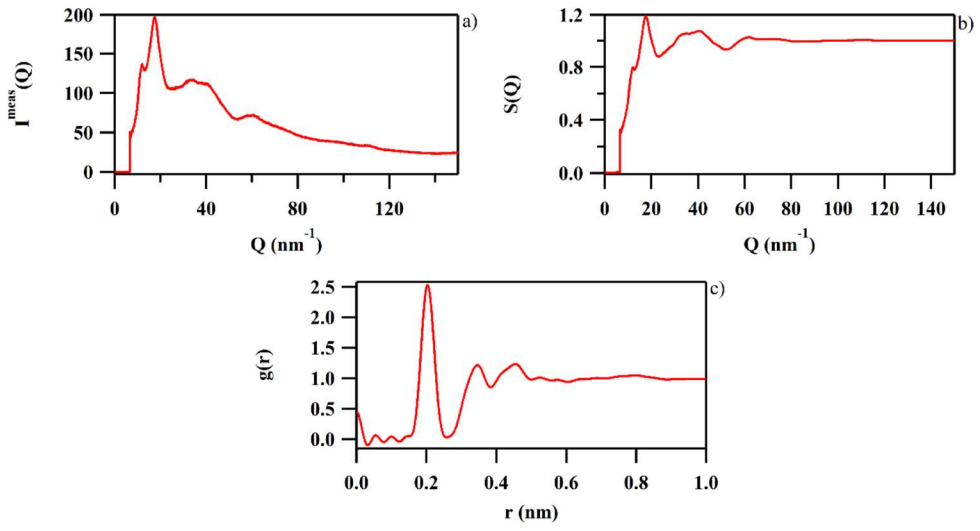

Figure 3.18. a) Raw integrated x-ray diffractogram of liquid sulfur. b) Associated structure factor $S(Q)$. c) Associated pair distribution function $g(r)$.

3. Density measurements by x-ray absorption in the PEP

In the framework of this thesis, the density of liquid phosphorus was determined by measuring the absorption of x-rays by the sample. The x-ray absorption was initially developed to measure the density of relatively heavy metallic melts such as tellurium using a large volume press[15-17], and was successfully applied by Katayama et al. on liquid phosphorus[18]. The x-ray absorption is related to the density of the sample through the Beer-Lambert law[19]:

$$\frac{I}{I_0} = e^{-\mu\rho l}$$

where I_0 and I are the intensity of the beam before and after the sample respectively, μ is the mass absorption coefficient, ρ is the density of the sample, and l is the length of the sample in the axis of the beam. In practice, the method consists in measuring the intensity of the x-ray beam that is absorbed by the sample while scanning the press perpendicularly to the x-ray beam. The beam intensity is recorded using photodiodes, or ionization chambers, before and after the sample. The principle is illustrated in Figure 3.19.

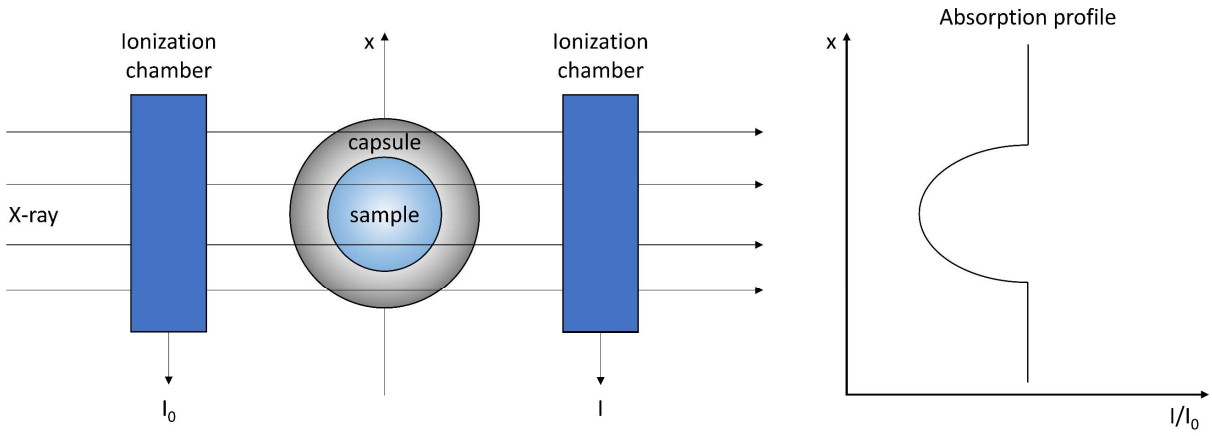

Figure 3.19. Principle of density measurement by x-ray absorption.

Ion chambers were used to record the incident and transmitted x-ray beam intensities I_0 and I. The two ion chambers were filled with one bar of argon. The absorption profiles I/I_0 were collected at constant P-T conditions by translating the press in the horizontal direction perpendicular to the X-ray beam, as previously stated. The full absorption profile contains contributions from the sample, diamond capsule, and surrounding material consisting of the

hBN capsule, the graphite furnace and the boron-epoxy gasket. Therefore, the absorbance of each media must be considered. The transmitted intensities of each media can be denoted as:

$$I_s(x) = I_0 e^{-\mu_s \rho_s t_s(x)}$$

$$I_d(x) = I_0 e^{-\mu_d \rho_d t_d(x)}$$

$$I_c(x) = I_0 e^{-\mu_c \rho_c t_c(x)}$$

where s, d and c refer to the sample, the diamond ring and the surrounding capsule respectively, μ are the mass absorption coefficients of given elements (tabulated for simple elements in the NIST standard reference database 126[20]), ρ are the densities and $t(x)$ are the thicknesses of the different component of the sample assembly probed by the x-ray beam as a function of the horizontal position x. The origin of the x-axis is taken at the center of the sample as shown in Figure 3.20.

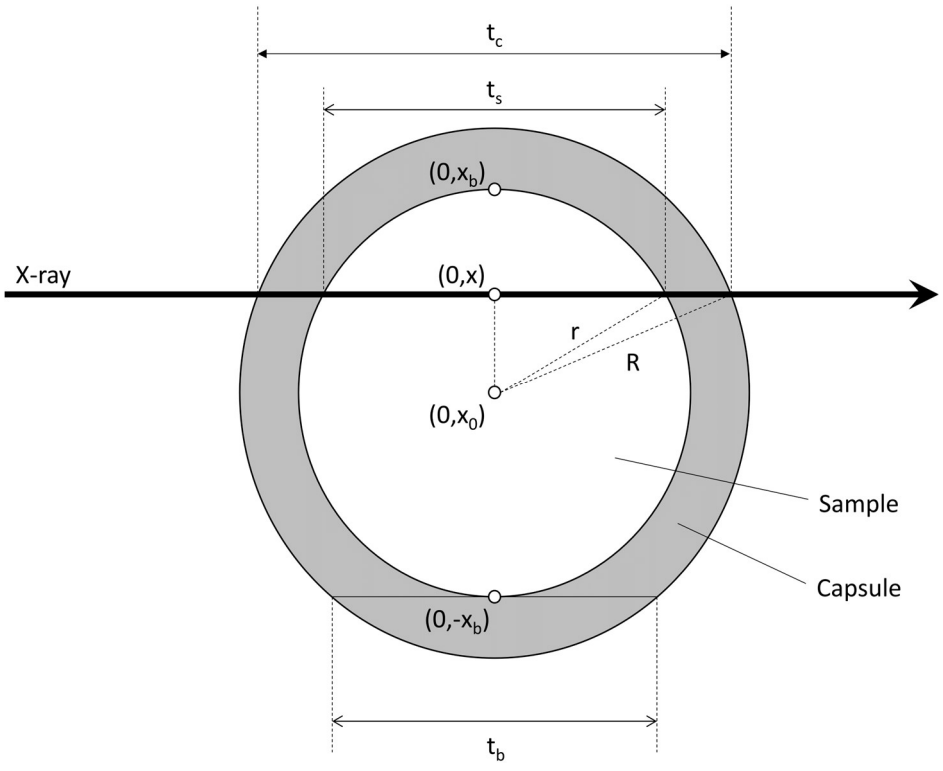

Figure 3.20. Capsule and sample geometries and shapes. Gray and white colors show the diamond capsule and the sample, respectively.

From geometrical considerations, $t(x)$ can be expressed as:

$$t_s(x) = 2\sqrt{r^2 - (x - x_0)^2} \quad \text{for } x < r$$

$$t_d(x) = 2\sqrt{R^2 - (x - x_0)^2} - 2\sqrt{r^2 - (x - x_0)^2} \quad \text{for } x < r$$

$$t_d(x) = 2\sqrt{R^2 - (x - x_0)^2} \quad \text{for } r < x < R$$

where r and R are the sample and diamond capsule radius respectively.

The absorbance A is defined following the Beer-Lambert law as follows:

$$A = -\ln\left(\frac{I}{I_0}\right) = \mu\rho t$$

Therefore, the total absorbance can be written as:

$$A_{tot}(x) = -\ln\left(\frac{I}{I_0}\right) = \mu_s\rho_s t_s(x) + \mu_d\rho_d t_d(x) + \mu_c\rho_c t_c(x)$$

The contribution from the surrounding material must be included in the data treatment. The standard method to solve this issue is detailed in the work of Terasaki and collaborators[21]. It consists in defining the absorbance at the boundary between the sample and the diamond capsule such as:

$$A_b = -\ln\left(\frac{I}{I_0}\Big|_{|x_b|}\right) = \mu_d\rho_d t_b + \mu_c\rho_c t_c(x_b)$$

And $t_c(x_b) \approx t_c(x) \approx t_c$ when x < R as the thickness variation of the outer elements of the assembly is quasi-negligible and remains constant when probing the center of the assembly in the horizontal direction. The relative thickness variation of the capsule with respect to the thickness at the boundaries between the sample and the diamond is comprised between 0 and 300 µm and lead to absolute errors of less than 1%.

Then, using the two previous equations:

$$A_{tot}(x) = A_b - \mu_d\rho_d t_b + \mu_s\rho_s t_s(x) + \mu_d\rho_d t_d(x)$$

$$A_{tot}(x) = A_b + \mu_s\rho_s t_s(x) + \mu_d\rho_d (t_d(x) - t_b)$$

where A_b is a constant. The geometrical considerations give:

$$t_d(x) - t_b = 2\sqrt{R^2 - (x - x_0)^2} - 2\sqrt{r^2 - (x - x_0)^2} - 2\sqrt{R^2 - r^2} \qquad \text{for } x < r$$

$$t_d(x) - t_b = 2\sqrt{R^2 - (x - x_0)^2} - 2\sqrt{R^2 - r^2} \qquad \text{for } r < x < R$$

Finally, the density ρ_s can be calculated from the relation:

$$\rho_s = -\frac{1}{\mu_s t_s(x)}\left\{\ln\left(\frac{I}{I_0}\right) + A_b + \mu_d \rho_d (t_d(x) - t_b)\right\}$$

where the constant A_b is experimentally determined at the boundary between the sample and the capsule, at point A or B of Figure 3.21., where the diamond absorption is maximal and the sample absorption is minimal. The validity of this approximation is justified by the use of low-Z materials as surrounding capsule assembly that ensure a good contrast between the sample and its environment.

In the 0 – 5 GPa pressure range where the x-ray absorption experiments were performed, the deformation of the diamond capsule is neglected, and we considered that the capsule shape remains circular. If we were to investigate higher pressure ranges, the sample part would be assumed to be deformed to ellipsoidal shape.

The very small density variation of diamond in the 0 – 5 GPa pressure range was neglected ($\Delta(I/I_0) \approx 4 \times 10^{-4}$ for a density variation of 1%). A typical absorbance profile is shown in figure 3.21. The sample density ρ_s is the average of $\rho_s(x)$ over the central part of the assembly where the thickness ratio of sample to diamond is the largest. The obtained density points are in excellent agreement with the data available in the literature and the absolute error in the density is estimated smaller than 1% using the standard deviation method.

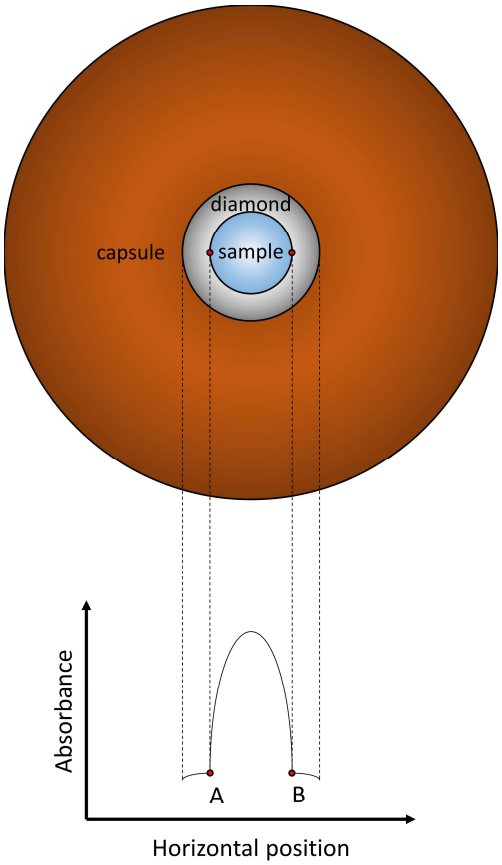

Figure 3.21. Schematic of the x-ray absorption method (inspired from Sanloup[22]).

4. X-ray viscosity measurements

We conducted in-situ x-ray radiographic imaging under high pressure-temperature (P,T) conditions to extract macroscopic insights from the liquid sample. Figure 3.22. illustrates a schematic representation of our x-ray imaging setup. This system consists of a PCO DIMAX fast camera, magnification optics capable of up to x10 magnification, resulting in an effective pixel size of approximately 1 µm, and a fluorescence screen that convert the transmitted x-rays into visible light via a single-crystal YAG scintillator.

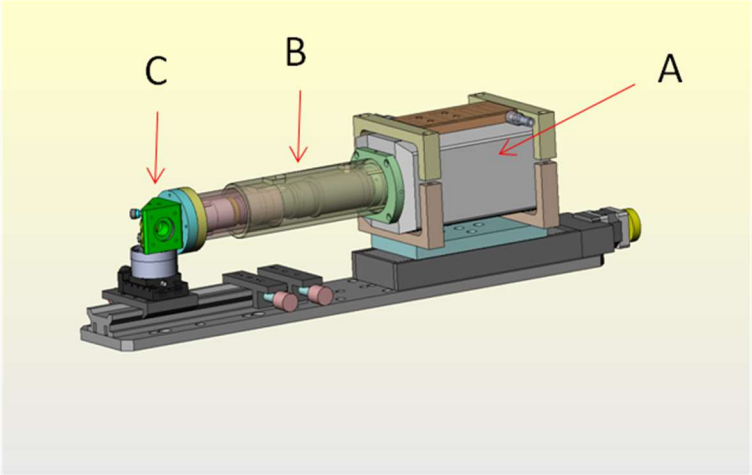

Figure 3.22. Full-field XRI detector. A. PCO DIMAX camera, B. Optics for zoom adjustment, C. X-ray fluorescence screen and mirror.

Viscosity represents a macroscopic property that reflects a fluid's inherent resistance to flow. Understanding viscosity under extreme pressure-temperature conditions holds primordial importance across various scientific domains. Notably, in the field of geosciences, viscosity plays a pivotal role in processes such as volcanic activity and plate tectonics. Consequently, there has been a concerted effort to develop in-situ viscometry techniques for high-pressure melts within the Paris-Edinburgh press, employing the falling sphere method[23-24]. In practice, this technique involves the placement of a dense sphere crafted from heavy metals (e.g. tungsten, rhenium or platinum) with precisely characterized density and diameter on top of the sample within the sample assembly. Subsequently, the sample is rapidly pressurized and heated within the PEP, a process detailed in Chapter 2. As the sample crosses its melting point, the sphere falls, and the viscosity (denoted as η) of the liquid is determined using the Stokes relation:

$$\eta = \frac{2gr_s^2(\rho_s - \rho_l)}{9V}\frac{F}{K}$$

where g represents the gravity constant, ρ_s stands for the density of the sphere, while ρ_l denotes the density of the dense liquid, r_s is the radius of the sphere, and V is the velocity of the sphere, determined by tracking its fall through radiographic imaging. The parameters F and K account for wall effects and finite length corrections[25]:

$$F = 1 - 2.104\left(\frac{r_s}{r_c}\right) + 2.109\left(\frac{r_s}{r_c}\right)^3 - 0.95\left(\frac{r_s}{r_c}\right)^5$$

$$K = 1 + 3.3\left(\frac{r_s}{h}\right)$$

where r_c is the internal diameter of the capsule, and h is the length taken to be the entire fall distance.

The sphere's displacement is continuously monitored through time-lapsed radiographic imaging, as depicted in Figure 3.23. To achieve this, we precisely determined the effective pixel size and subsequently employed the software ImageJ to track the center of the sphere's movement. This procedure enabled us to generate a distance-time plot, as presented in Figure 3.24., which exhibits a characteristic sigmoidal shape. The fall of the sphere unfolds in distinct phases: an initial acceleration phase, followed by a free-fall regime, culminating in a deceleration phase as it reaches the bottom of the sample capsule. The sphere's velocity is then deduced from the linear portion of the velocity curve corresponding to the free-fall regime.

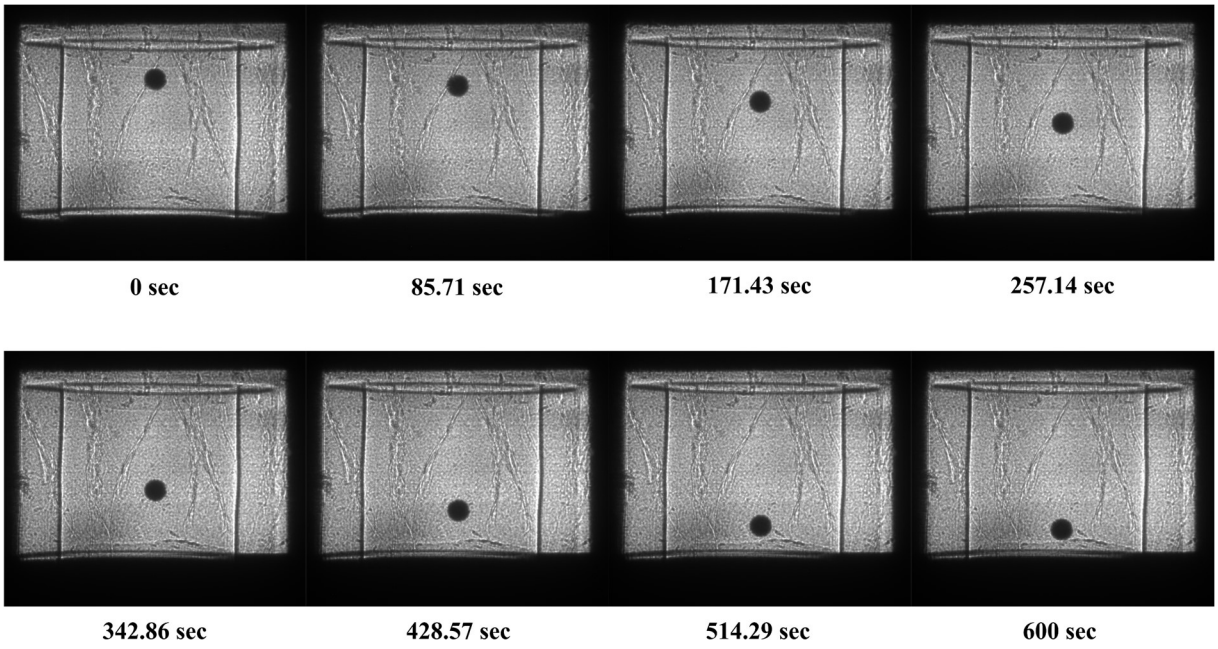

Figure 3.23. Radiograph images of a platinum falling sphere in liquid sulfur at 0.25 GPa and 420 K recorded with the PCO DIMAX camera.

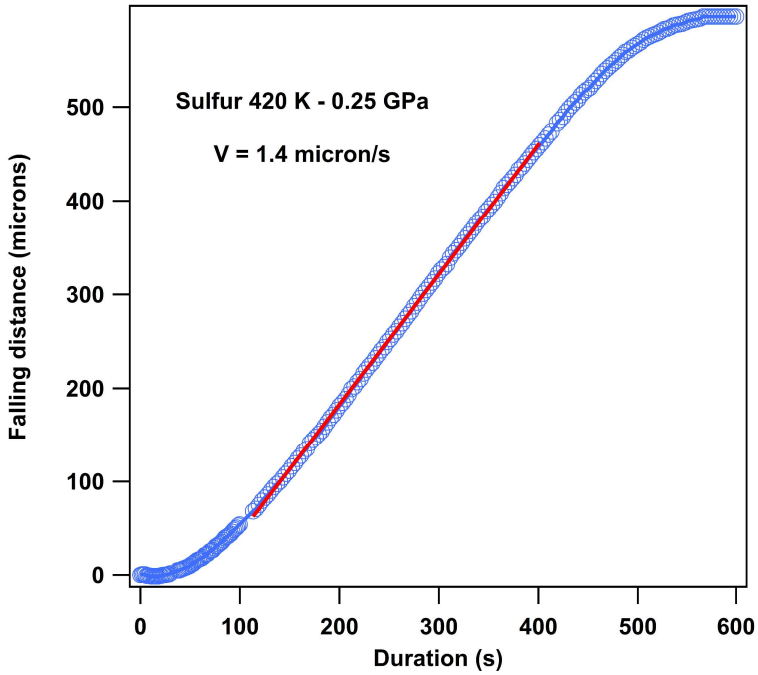

Figure 3.24. Distance vs time plot and derived velocity for a WC sphere falling in liquid S at 0.25 GPa and 420 K. The distance-time plot exhibits a sigmoid shape with nonlinear regions at the ends, reflecting acceleration and deceleration of the sphere as it approaches the bottom of the capsule. The slope of the least-squares, best-line through the region of constant velocity is the terminal velocity used to calculate viscosity.

The determination of viscosity requires consideration of several potential sources of error. Firstly, in the case of low-viscosity melts, an inadequate number of captured images may lead to an imprecise determination of the terminal velocity. It is widely accepted that a minimum of 10 images is necessary to accurately establish velocity. In our current study, the utilization of high-speed x-ray imaging has enabled us to determine the terminal velocity of the falling sphere with a typical standard deviation of maximum few percent. Another source of error comes from the precision in the determination of the sphere's diameter. The sphere's diameter is initially determined via optical microscopy prior to the experiment, achieving a typical precision of 2 μm. Subsequently, this value is cross-checked using pixel calibration on the PCO DIMAX images. This introduces an uncertainty of approximately 3 to 5% in the viscosity determination. Consequently, the cumulative uncertainty associated with the falling sphere viscosity measurements for low-viscosity melts, representing the worst-case scenario, is of the order of 10%.

References

1. T. Poręba, D. Comboni, M. Mezouar, G. Garbarino, M. Hanfland, Tracking structural phase transitions via single crystal x-ray diffraction at extreme conditions: advantages of extremely brilliant source. *J. Phys. Condens. Matter*, 2022, **35**, 054001.
2. T. Fedotenko, L. Dubrovinsky, G. Aprilis, E. Koemets, A. Snigirev, I. Snigireva, A. Barannikov, P. Ershov, F. Cova, M. Hanfland, N. Dubrovinskaia, Laser heating setup for diamond anvil cells for *in situ* synchrotron and in house high and ultra-high pressure studies, *Rev. Sci. Instrum.*, 2019, **90**, 104501.
3. J. M. Besson, G. Hamel, P. Grima, R. J. Nelmes, J. S. Loveday, S. Hull and D. Haüsermann, A Large Vokume Pressure Cell for High Temperatures. *High Press. Res.*, 1992, **8**, 625.
4. S. Klotz, Th. Strässle, G. Rousse, G. Hamel and V. Pomjakushin, Angle-dispersive neutron diffraction under high pressure to 10 GPa. *Appl. Phys Lett.*, 2005, **86**, 031917.
5. G. Morard, M. Mezouar, N. Rey, R. Poloni, A. Merlen, S. Le Floch, P. Toulemonde, S. Pascarelli, A. San Miguel, C. Sanloup and G. Fiquet, Optimization of Paris-Edinburgh press cell assemblies for *in situ* monochromatic X-ray diffraction and X-ray absorption. *High Press. Res.*, 2007, **27**, 223.
6. M. Mezouar, P. Faure, W. Crichton, N. Rambert, B. Sitaud, S. Bauchau, G. Blattmann, Multichannel collimator for structural investigation of liquids and amorphous materials at high pressures and temperatures. *Rev. Sci. Instrum.*, 2002, **73**, 3570-3574.
7. K. Yaoita, Y. Katayama, K. Tsuji, T. Kikegawa, O. Shimomura, Angle-dispersive diffraction measurement system for high-pressure experiments using a multichannel collimator. *Rev. Sci. Instrum.*, 1997, **68**, 2106-2110.
8. G. Weck, G. Garbarino, S. Ninet, D. Spaulding, F. Datchi, P. Loubeyre, M. Mezouar, Use of a multichannel collimator for structural investigation of low-Z dense liquids in a diamond anvil cell: validation on fluid H_2 up to 5 GPa. *Rev. Sci. Instrum.*, 2013, **84**, 063901.
9. G. Morard, M. Mezouar, S. Bauchau, M. Álvarez-Murga, J. -L. Hodeau, G. Garbarino, High efficiency multichannel collimator for structural studies of liquids and low-Z materials at high pressures and temperatures. *Rev. Sci. Instrum.*, 2011, **82**, 023904.
10. G. Ashiotis, A. Deschildre, Z. Nawaz, J. P. Wright, D. Karkoulis, F. E. Picca, J. Kieffer, The fast azimuthal integration Python library: pyFAI. *J. Appl. Crystallogr.*, 2015, **48**, 510-519.

11. C. Prescher, V. B. Prakapenka, DIOPTAS: A program for reduction of two-dimensional X-ray diffraction data and data exploration. *High Press. Res.*, 2015, **35**, 223-230.
12. B. H. Toby, EXPGUI, a graphical user interface for GSAS. *J. Appl. Crystallogr.*, 2001, **34**, 210-213.
13. A. Le Bail, H. Duroy, J. L. Fourquet, Ab-initio structure determination of LiSbWO6 by X-ray powder diffraction. *Materials Research Bulletin*, 1988, **23**, 447-452.
14. J. H. Eggert, G. Weck, P. Loubeyre, M. Mezouar, Quantitative structure factor and density measurements of high-pressure fluids in diamond anvil cells by x-ray diffraction: Argon and water. *Phys. Rev. B*, 2002, **65**, 174105.
15. Y. Katayama, Density measurements of non-crystalline materials under high pressure and high temperature. *High Press. Res.*, 1996, **14**, 383-391.
16. Y. Katayama, K. Tsuji, H. Kanda, H. Nosaka, K. Yaoita, T. Kikegawa, O. Shimomura, Density of liquid tellurium under pressure. *J. Non-Cryst. Solids*, 1996, **205**, 451-454.
17. Y. Katayama, K. Tsuji, O. Shimomura, T. Kikegawa, M. Mezouar, D. Martinez-Garcia, J. -M. Besson, D. Häusermann, M. Hanfland, Density measurements of liquid under high pressure and high temperature. *J. Synchrotron Radiat.*, 1998, **5**, 1023-1025.
18. Y. Katayama, Y. Inamura, T. Mizutani, M. Yamakata, W. Utsumi, O. Shimomura, Macroscopic separation of dense fluid phase and liquid phase of phosphorus. *Science*, 2004, **306**, 848-851.
19. D. F. Swinehart, The Beer-Lambert Law. *J. Chem. Educ.*, 1962, **39**, 7, 333-335.
20. J. H. Hubbell, S. M. Seltzer, Tables of X-ray Mass Attenuation Coefficients and Mass Energy-Absorption Coefficients from 1 keV to 20 MeV for Elements Z = 1 to 92 and 48 Additional Substances of Dosimetric Interest. *NIST Standard Reference Database 126*, 1996. **DOI : https://dx.doi.org/10.18434/T4D01F**
21. H. Terasaki, K. Nishida, Y. Shibazaki, T. Sakamaki, A. Suzuki, E. Ohtani, T. Kikegawa, Density measurement of Fe_3C liquid using X-ray absorption image up to 10 GPa and effect of light elements on compressibility of liquid iron. *J. Geophys. Res.*, 2010, **115**, B06207.
22. C. Sanloup, Density of magmas at depth. *Chemical Geology*, 2016, **429**, 51-59.
23. Y. Kono, C. Kenney-Benson, Y. Shibazaki, C. Park, G. Shen, Y. Wang, High-pressure viscosity of liquid Fe and FeS revisited by fallin sphere viscometry using ultrafast X-ray imaging. *Physics of the Earth and Planetary Interiors*, 2015, **241**, 57-64.

24. J. -P. Perillat, M. Mezouar, G. Garbarino, S. Bauchau, In situ viscometry of high-pressure melts in the Paris-Edinburgh cell: application to liquid FeS. *High Press. Res.*, 2010, **30**, 415-423.
25. W. D. Kingery, Property Measurements at High Temperatures: Factors Affecting and Methods of Measuring Material Properties at Temperatures Above 1400 C (2550 F). *John Wiley & Sons*, 1959.

Chapter 4:

Anisotropic thermo-mechanical response of layered hexagonal boron nitride and black phosphorus: application as a simultaneous pressure and temperature sensor

In this chapter, we re-examine the exceptional anisotropic thermo-mechanical properties of both hexagonal boron nitride (hBN) and black phosphorus (bP) using in situ high-resolution synchrotron X-ray diffraction. These measurements are of primordial importance as they are the internal calibrants which were used during most of this thesis work to determine the pressure and temperature conditions of the experiments. Besides providing an accurate description of the effects of pressure and temperature on the lattice parameters and volume of these two materials, our findings allow to highlight a novel pressure-temperature metrology taking advantage of the exceptional anisotropic properties of bP, which can be simultaneously used as pressure temperature sensor during XRD experiments in an extended P-T domain.

1. Introduction

Accurate determination of pressure and temperature conditions is a fundamental concern in high-pressure science, as it profoundly influences the reliability of experimental outcomes. To achieve precise measurements, we employed in-situ pressure sensors in both diamond anvil cell and Paris-Edinburgh press experiments throughout this thesis work. Our choice of internal calibrants primarily revolved around hexagonal boron nitride (hBN) and black phosphorus (bP), two materials of significant interest due to their layered structures. Understanding their thermal equations of state holds great important in the realm of two-dimensional materials, offering insights into anisotropic thermo-mechanical properties and exfoliation mechanisms.

As detailed in Chapter 2, the utilization of two calibrants with well-characterized equations of state is sufficient to comprehensively determine the pressure-temperature conditions within an experiment. Hence, it was imperative to initiate this research work by conducting a concise reevaluation of the thermo-mechanical behavior of hexagonal boron

nitride and black phosphorus, aiming to derive their equations of state. This groundwork was essential, considering the persistent discrepancies in the determination of the thermoelastic parameters of these materials, despite numerous theoretical and experimental investigations.

To validate the derived equations of state, we conducted three distinct experiments using three distinct setups, ensuring the reproducibility of the measured thermo-mechanical properties of these materials. Emphasis was placed on quantitatively assessing subtle variations of the in-plane thermo-mechanical parameters by acquiring a large dataset through small incremental changes in pressure and temperature.

2. Article

This article focuses on a comprehensive re-examination of the thermo-elastic characteristics of hexagonal boron nitride and black phosphorus. Our study reaffirmed the remarkable anisotropic properties inherent to bP and introduced an innovative metrology approach that takes full advantage of its intriguing thermo-elastic behavior. Subsequently, this pioneering metrology served as the foundation for conducting most of the experiments in this thesis work.

Anisotropic thermo-mechanical response of layered hexagonal boron nitride and black phosphorus: application as a simultaneous pressure and temperature sensor

Hermann Muhammad[1], Mohamed Mezouar[1], Gaston Garbarino[1], Tomasz Poreba[1], Giorgia Confalonieri[1], Matteo Ceppatelli[2,3], Manuel Serrano-Ruiz[3], Maurizio Peruzzini[3], Frédéric Datchi[4]

[1]*European Synchrotron Radiation Facility (ESRF), 71, Avenue des Martyrs, Grenoble, France*

[2]*LENS, European Laboratory for Non-linear Spectroscopy, Via N. Carrara 1, I-50019 Sesto Fiorentino, Firenze, Italy*

[3]*ICCOM-CNR, Institute of Chemistry of Organo Metallic Compounds, National Research Council of Italy Via Madonna del Piano 10, I-50019 Sesto Fiorentino, Firenze, Italy*

[4]*Institut de Minéralogie, de Physique des Milieux Condensés et de Cosmochimie (IMPMC), Sorbonne Université, CNRS UMR 7590, MNHN, 4 place Jussieu, F-75005 Paris, France*

Hexagonal boron nitride (hBN) and black phosphorus (bP) are crystalline materials which can be seen as an ordered stacking of two-dimensional layers, which leads to outstanding anisotropic physical properties. The knowledge of the thermal equations of state of hBN and bP is of great interest in the field of 2D materials for a better understanding of the anisotropic thermo-mechanical properties and exfoliation mechanism of these materials. Despite several theoretical and experimental studies, important uncertainties remain in the determination of the thermoelastic parameters of hBN and bP. Here, we report accurate thermal expansion and compressibility measurements along the individual crystallographic axes, using *in situ* high-temperature and high-pressure high-resolution synchrotron X-ray diffraction. In particular, we have quantitatively determined the subtle variations of the in-plane thermo-mechanical parameters by subjecting these materials to hydrostatic conditions and collecting a large number of data points in small pressure and temperature increments. Based on the anisotropic behavior of bP, we propose the use of this material as sensor for the simultaneous determination of pressure and temperature in the 0-5 GPa, 298-1700 K range.

I. Introduction

Thermal equations of state (EOS) are fundamental properties of condensed matter[1] which are of great relevance in a variety of research fields including solid state physics, materials science and chemistry. They are intimately linked to the materials atomic arrangement and provide invaluable information about the nature and amplitude of the microscopic interactions. As such, thermal EOS can be directly related to first-principles calculations based on density functional theory (DFT)[2,3]. In this regard, materials with strong spatial anisotropy are of particular interest because they often exhibit exceptional directional physicochemical properties. Among them, hexagonal boron nitride (hBN) and black phosphorus (bP) have attracted great attention from chemists, physicists and materials scientists since their discovery. HBN is a layered crystalline solid isostructural to graphite. It is formed of single-atom thick layers of alternating boron and nitrogen arranged in the same hexagonal lattice (Fig. 1 ab) while graphite is made of single-atom thick layers of carbon that give rise to graphene[4]. As such, these materials exhibit similar anisotropic properties. The hBN sheets present an AA' stacking pattern along the crystallographic *c*-axis, resulting in a crystalline structure with space group $P6_3/mmc$[5]. Despite being an electrical insulator with ~ 5.9 eV band gap, hBN is a good thermal conductor, which makes it one of the rare materials combining these two generally antagonistic physical properties. As hBN is commonly depicted as the insulating isostructure of graphene, it constitutes a material of choice in industrial applications such as coating[6] and dielectric material[7], and some devices applications[8]. HBN is also known for its chemical inertness[9-10], and tribological properties[11-12] that makes it interesting as solid lubricant[13-15] and high-temperature ceramic material[16].

Black phosphorus (bP) is the most stable allotrope of phosphorus at ambient conditions of pressure and temperature[17-18]. It has been first synthesized by subjecting white phosphorus to moderate pressure and temperature conditions (P>1.2 GPa and T>500 K)[19] and, since 2014 it has acquired increasing importance as the bulk material for the preparation of phosphorene by exfoliation techniques[20-21]. Indeed, bP exhibits a crystalline layered structure (A17 orthorhombic structure with space group *Cmce*) made by the ordered stacks of 2D puckered layers of P atoms, called phosphorene by analogy to graphene in the case of graphite (Fig. 1 cd). Similarly to hBN, and due to its puckered structure, few layers phosphorene exhibit an outstanding anisotropic mechanical behavior such as a negative Poisson's ratio[22] and very contrasting directional Youngs's modulus[23]. In contrast to graphene[24], which needs doping to

become semiconductor, and similarly to transition metal dichalcogenide (TMD) monolayers[25], such as MoS_2, phosphorene is a 2D semiconductor with a direct band gap value of 2 eV significantly larger than bP (0.3 eV)[20,26-27]. In addition, it presents a high carrier mobility (~1000 $cm^2V^{-1}s^{-1}$), good current on/off ratio (~10^4–10^5) and anisotropic in-plane properties, which makes phosphorene and phosphorene-based heterostructures very promising for future applications in nanophotonics, nanoelectronics[21,28-30], energy storage[31], sensing[32-33] and catalysis[34].

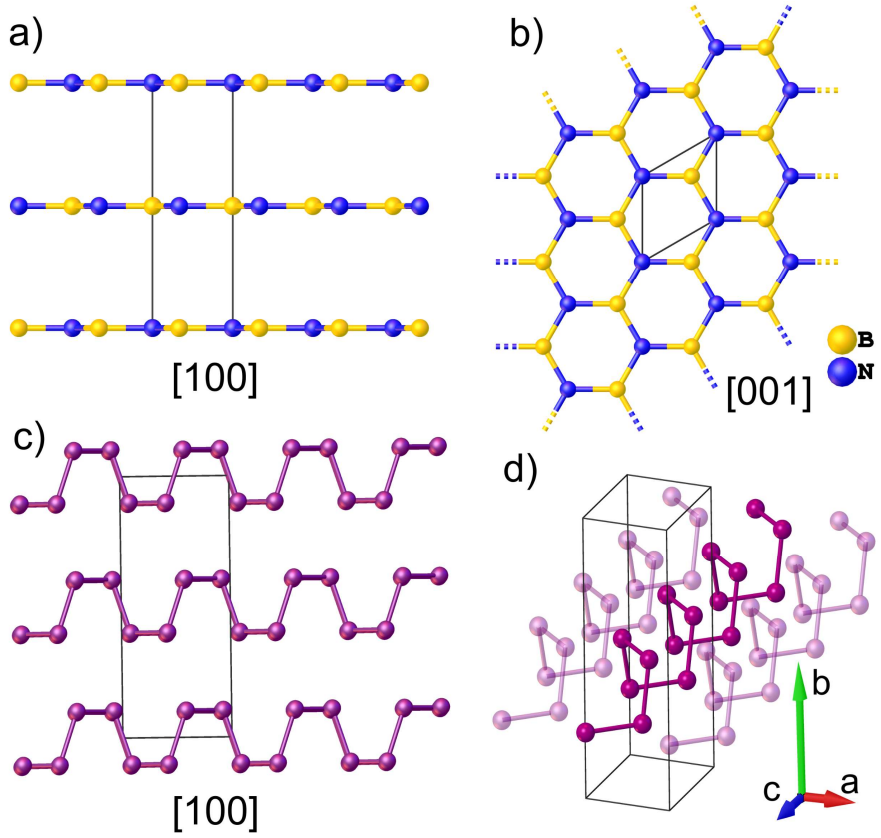

Fig. 4.1. *Molecular structures of hBN (a,b) and bP (c,d). HBN assumes planar conformation (a) while bP forms puckered bi-layers (c). Intra-layer differences between the regular, hexagonal layer in hBN (b) and screw-like hinged structure of bP extending in [001] (d), respectively.*

HBN and bP exhibit strong covalent intralayer bonds with sp^2 (hBN) and sp^3 (bP) hybridization and relatively weak van der Waals interlayer forces which leads to very contrasting directional thermal equations of state (EOS). The precise determination of the EOS parameters of these materials is made very difficult due to the weak pressure and temperature variations of the intra-plane inter-atomic distances. Indeed, for both materials, the intra-plane compressibility is 1 to 2 orders of magnitude lower than the inter-plane ones[35-41]. Additionally,

nonlinear pressure and temperature effects have also been reported[35-52], although not yet precisely quantified.

Here we report accurate directional thermal EOS of hBN and bP using *in situ* high-resolution synchrotron x-ray diffraction performed under perfect hydrostatic conditions using liquid He as pressure transmitting medium. Besides providing an accurate description of the effects of pressure and temperature on the lattice parameters and volume of these two materials, our findings allowed to highlight a new pressure-temperature metrology based on the exceptional anisotropic properties of bP, which can be simultaneously used as pressure and temperature sensor during XRD experiments in an extended P-T domain.

II. Experimental Method

High purity powders of hexagonal boron nitride (hBN) purchased from the company Goodfellow (product code: B-60-RD-000105), and black phosphorus (bP, 99.999+%) synthesized at ICCOM-CNR (Florence, Italy) from red phosphorus as described in reference[53] have been used as starting materials.

Three independent experimental runs (run 1 to 3) were carried out to determine precisely the thermal equations of state (EOS) of hBN and bP using *in situ* monochromatic X-ray diffraction. Run 1 and 2 were devoted to the determination of the ambient pressure thermal expansion coefficients of hBN and bP, while run 3 was focused on the low pressure (P<10 GPa) room temperature EOS of these materials. All the experimental work has been conducted at the European Synchrotron Radiation Facility (ESRF, Grenoble, France). Run 1 and 3 have been performed at the high-pressure XRD beamline ID27[54] while run 2 was carried out at the high-resolution powder XRD beamline ID22[55-56]. In the following, more details about the different runs are provided.

a. Run 1:

This high-temperature run was carried-out by increasing the temperature at ambient pressure using the resistive heating device of a Paris-Edinburgh (PE) press[57-59]. This system can generate stable and homogeneous temperatures over a wide range from 298 to 2500 K. A standard PE sample geometry was employed[59-60]. bP was confined inside a diamond capsule of 1 mm inner diameter, 1.5 mm outer diameter and 1 mm height to ensure good thermal conductivity and minimize the temperature gradients. This diamond capsule was inserted into a chemically inert hBN cylinder and closed using two hBN caps. No evidence of chemical

reactivity of bP was observed in any of the collected x-ray diffraction patterns. The sample container was placed inside a cylindrical graphite heater of 1.9 mm inner diameter, 2.4 mm outer diameter and 3.1 mm height that was sealed using two graphite caps in contact with 2 copper electrodes. To thermally insulate the graphite heater, it was contained in an x-ray transparent boron-epoxy gasket[60]. The temperature was measured with a precision of ± 1 K using a chromel-alumel thermocouple in contact with the diamond capsule. Monochromatic x-ray diffraction measurements were performed at the beamline ID27. The incident x-ray beam energy was fixed to 20 keV (λ=0.6199 Å), covering a large scattering angle from 3 to 25°. The two-dimensional XRD patterns were collected in transmission geometry using a MAR165 CCD detector. A high efficiency multichannel collimator[61] was used to remove most of the parasitic elastic and inelastic x-ray signal coming from the sample assembly (graphite heater and boron-epoxy gasket). The sample to detector distance, detector tilt angles and beam center were accurately determined using a LaB_6 powder standard. The two-dimensional XRD images were integrated using the PyFAI software[62] as implemented in the DIOPTAS[63] suite. The resulting one-dimensional XRD patterns have been analyzed using the GSAS software[64]. The unit-cell parameters and volume of hBN and bP have been obtained by Le Bail[65] extraction of d-spacings using a pseudo-Voigt peak shape function. As hBN and bP were contained in the same sample assembly, the XRD patterns contain contributions from both samples. A typical XRD pattern of hBN and bP obtained at ambient pressure and 300 K, and the corresponding Le Bail adjustment are presented in Fig. 2(a). The temperature was increased from room T to 760 K by small T increments of 10 K up to 470 K, and slightly larger ones (15 K) at higher T.

b. Run 2:

In order to cross-check the results obtained in run 1 for bP, run 2 has been performed using a different experimental set up. This high-T run 2 has been carried out at the high-resolution powder diffraction beamline ID22 (ESRF) using a heating device consisting of a hot gas blower from the company Cyberstar positioned at an optimum distance (~5 mm) from the sample. This device generates a smooth laminar flow of hot air that results in a homogeneous temperature distribution over a large volume of more than 10 mm^3. This homogeneously heated volume is much larger than the sample (~1 mm^3) ensuring very small temperature gradients. BP was contained in a 0.5 mm inner diameter quartz capillary. The incident energy was set to 35 keV (λ=0.3543 Å). The temperature interval covered in this run was from 298 to 715 K as it has been previously reported that bP starts to decompose at higher T[47]. The data have been collected

upon heating with a temperature interval of 60 K (± 1 K). High resolution XRD patterns were collected over the 2Θ range of 1° – 62° using a multi-analyzer stage of 13 Si(111) crystals coupled to a Dectris Eiger2 X 2M-W CdTe pixel detector. As for run 1, the structural parameters were derived by Le Bail[65] extraction of the d-spacings using a pseudo-Voigt peak shape function using the GSAS software[64]. A typical XRD pattern obtained at 300 K and ambient pressure and the corresponding Le Bail fitting are shown in Fig. 2(b).

c. Run 3:

Run 3 was dedicated to the accurate determination of the room T equation of state (EOS) of bP and hBN. As for run 1, the x-ray diffraction measurements were conducted at the ID27 high-pressure XRD beamline. Fine powder samples of bP and hBN were loaded together in a Le Toulec type membrane diamond anvil cell[66]. The high-pressure cavity consisted of a 300 µm hole drilled in a 50 µm thick rhenium foil. Helium, which remains liquid below 11 GPa and thus provides perfect hydrostatic conditions over the whole investigated pressure range, was used as pressure transmitting medium. The pressure was determined from the shift of the R_1 luminescence peak of a ruby chip placed in the pressure cavity, using the Ruby2020 calibration[67]. The pressure (P) was determined as the average of the pressures measured before and after XRD data collections. The maximum pressure difference was 0.1 GPa. P was increased in fine steps (0.15 GPa steps in the 0-4 GPa pressure range and 0.4 GPa steps in the 4-10.5 GPa pressure range) up to 10.5 GPa. This has been essential to accurately determine the very small in-plane cell parameters variation of hBN and bP. The incident x-ray beam energy was fixed to 33.169 keV (λ = 0.3738 Å) using a silicon (111) double-crystal monochromator. The two-dimensional diffraction images were collected in transmission geometry using a Dectris Eiger2 9M CdTe pixel detector. The sample to detector distance, detector tilt angles and beam center were accurately determined using a CeO_2 powder standard. The data were analyzed in a similar way as for run 1 and 2 (Le Bail fitting). Typical diffraction patterns of bP and hBN acquired during run 3 at room temperature and ambient pressure, respectively, and the corresponding Le Bail refinements are shown in Fig. 2(c) and Fig. 2(d), respectively.

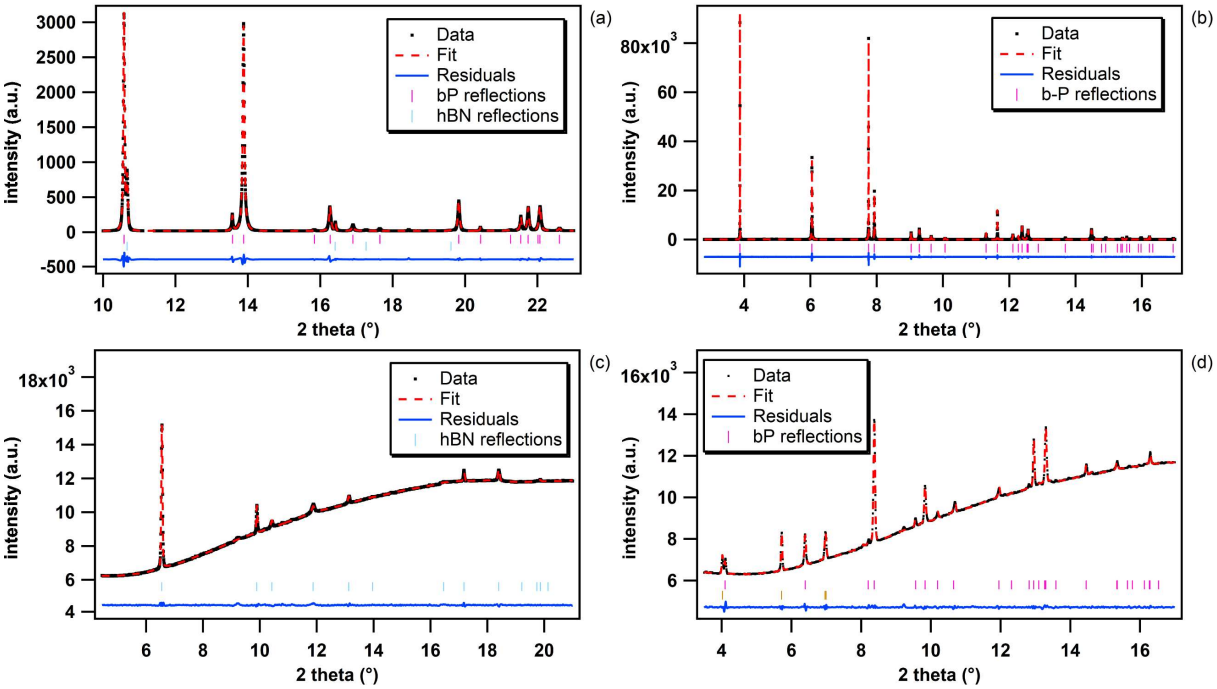

Fig. 4.2. *Integrated XRD patterns of hBN (panel a,c) and bP (panel b,d) in run 1 to -3 and their corresponding Le Bail fittings. (a) Run 1 (Ambient pressure, T=300 K; the XRD patterns were collected simultaneously), (b) Run 2 (Ambient pressure, T=300 K), (c) and (d) Run 3 (Ambient pressure, T=300K). The higher background in run 2 and 3 is due the small sample dimension and high x-ray Compton scattering signal from the diamond anvil cell.*

III. Thermal expansion of hBN and bP at ambient pressure

a. Hexagonal boron nitride

The temperature dependence of the unit-cell parameters and volume of hBN obtained in run 1 is presented in Fig. 3. The resulting linear and volumetric thermal expansion coefficients are listed in Table 1.

The *c* lattice parameter presents, within experimental error, a standard linear and positive temperature evolution up to 1280 K, the maximum temperature reached in this run (see Fig. 3b). A linear regression of the data gives:

$$c(T) = c_0[1 + \alpha_c(T - 300)] = 6.6706(7)[1 + 4.23(1) \times 10^{-5} \times (T - 300)] \qquad \text{Eq. 1}$$

where c_0 is the *c* lattice parameter at 300 K, α_c the corresponding linear thermal expansion coefficient, and T the temperature. Here and throughout the manuscript, the error bars refer to the standard deviation of the parameters as obtained from the mathematical refinement of the experimental data.

As previously reported[42,43], along the *a* crystallographic axis, we observe an unusual negative variation of the thermal expansion (Fig. 3a). Indeed, along this axis the network contracts in a non-linear way, at least up to 1280 K. It is worth noting, that the absolute temperature variation of the *a* lattice parameter is 2 orders of magnitude weaker than that of *c*. Its temperature dependence can be expressed as a third order polynomial expression:

$$\mathrm{a\,(T)} = \mathrm{a_0}[1 + \alpha_a(\mathrm{T} - 300) + \alpha'_a(T^2 - 300^2) + \alpha''_a(T^3 - 300^3)]$$

$$= 2.5069(2)[1 - 4.63(17) \times 10^{-6} \times (T - 300) + 3.07(23) \times 10^{-9} \times (T^2 - 300^2) \quad \text{Eq. 2}$$

$$-7.0(10) \times 10^{-1} \times (T^3 - 300^3)]$$

where a_0 is the *a* lattice parameter value at 300 K, α_a, α'_a and α''_a the corresponding thermal expansion coefficient, its first and second derivatives respectively, and *T* the temperature (Fig. 3a, Table 1).

Due to the weak effect along *a*, the evolution of the unit-cell volume of hBN is dominated by the temperature effect on the *c* lattice parameter and evolves linearly with T over the probed temperature range as expressed by:

$$\mathrm{V(T)} = \mathrm{V_0}[1 + \alpha_V(\mathrm{T} - 300)] = 36.290(3)[1 + 3.96(1) \times 10^{-5} \times (\mathrm{T} - 300)] \quad \text{Eq. 3}$$

where V_0 is volume at 300 K, α_V the corresponding volumetric thermal expansion coefficient and T the temperature (Fig 3c, Table 1).

The large contrast between the directional thermal expansion coefficients corresponding to the *a* and *c* lattice parameters is explained by the anisotropic structure of hBN, particularly by the striking difference in nature between the chemical bonds in the *ab* plane and along the *c* axis of the hexagonal lattice. As shown in Fig. 3a and Table 1, the negative thermal expansion along the *a*-axis has already been reported[42,43] although never precisely quantified in a wide temperature domain. This is explained by the low number of collected data points and narrower temperature interval probed in these former studies. As suggested by Pease[42], this unusual variation may be due to the fact that the strong in-plane chemical bonds oppose standard thermal expansion by layer puckering effects related to out-of-plane thermal motion. The much larger and positive thermal expansion along the *c* axis is resulting from the low van der Waals forces that are acting along this crystallographic direction.

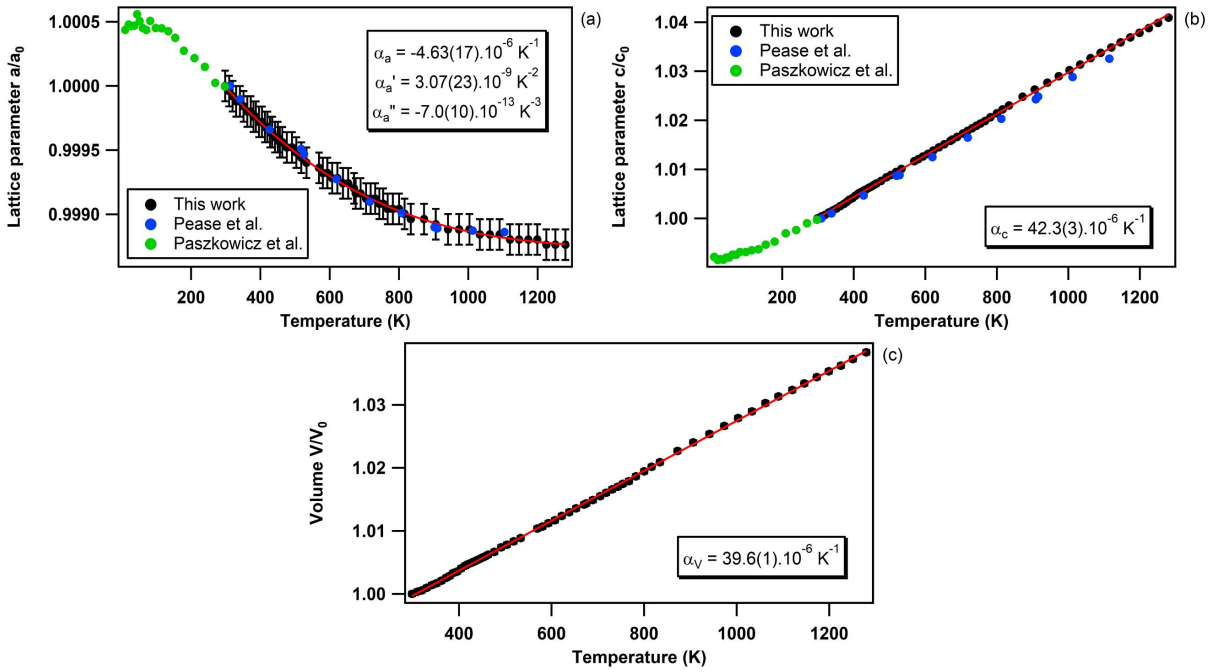

Fig. 4.3. *Relative thermal expansion of the a and c lattice parameters of hBN with respect to their ambient T values at ambient P, respectively along the [100] (panel a) and, [001] (panel b) directions. The volumetric thermal expansion of hBN at ambient P is displayed in panel c. Symbols correspond to the experimental data from this (black) and literature (color) studies, whereas the red curves are linear or polynomial fits of our data. Error bars in the last two panels are smaller than the size of the plotted points.*

Table 4.1 *Volumetric and linear thermal expansion coefficients of hBN at ambient pressure from this work and the literature.*

Exp	T range (K)	α_a (10^{-6} K^{-1})	α_a' (10^{-9} K^{-2})	α_a'' (10^{-13} K^{-3})	α_c (10^{-6} K^{-1})	α_V (10^{-6} K^{-1})	Technique
This work	298-1280	-4.63(17)	3.07(23)	-7.0(10)	42.3(1)	39.6(1)	Powder XRD
Pease[42]	273-1073	-2.9	1.9	-	40.5	-	Powder XRD
Zhao et al.[36]	300-1280	-0.0098	0.0102	-	51.6	49.1(19)	Powder XRD
Paszkowicz et al.[43]	128-297.5	-2.72	0	-	3.2	-	Powder XRD
Solozhenko et al.[44]	300-1800	-	-	-	-	40.9(8)	Powder XRD
Yates et al.[45]	80-780	-2.76	-	-	38.0	-	Interferometric measurements

b. Black phosphorus

The relative temperature dependence of the unit-cell parameters and volume of bP obtained from Le Bail fitting[65] are presented in Fig. 4. The evolution of the linear and volumetric thermal expansions from run 1 and 2, obtained using different experimental methods, are in excellent agreement. A linear regression is employed to determine the directional and volumetric thermal

expansions in the 298-750 K temperature range. As reported in previous studies[47], the sudden reduction of the Bragg reflections intensities, followed by their complete disappearance, attests for the decomposition of bP at higher temperature. The obtained directional and volumetric thermal expansion coefficients are listed and compared with the literature data in Table 2.

The volumetric thermal expansion obtained in this work is in excellent agreement with that reported by Henry et al.[47] and Rodrigues et al.[49] and in relatively good agreement with that reported by Faber et al.[48]. As for this study, the employed experimental method in[47-51] was *in situ* XRD. A good agreement is also found with the density-functional theory (DFT) calculations of Sansone et al.[52]. However, strong deviations emerge with respect to the papers by Keyes et al.[51] and Riedner et al.[50], likely due to a much smaller set of collected data points in these studies.

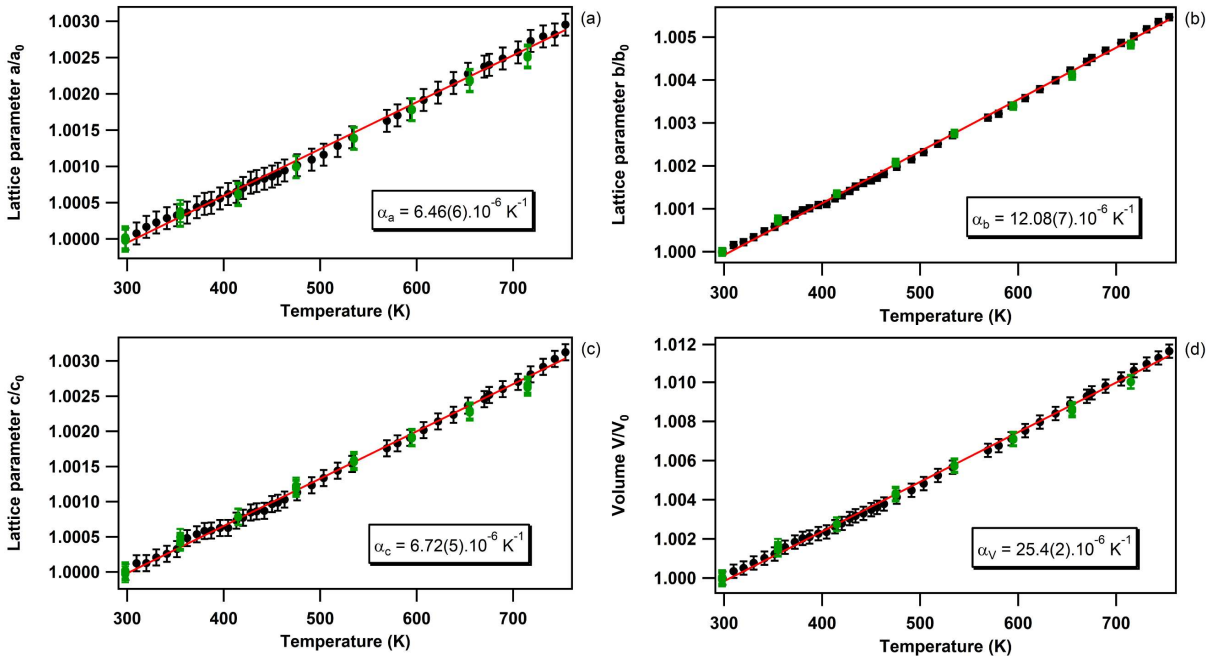

Fig. 4.4. *Thermal expansion of lattice parameters (a, b and c) and volume (V) of bP at ambient pressure with respect to the corresponding ambient T values (a_0, b_0, c_0, V_0). Decomposition of bP was observed above 750 K. Black and green circles correspond to data coming from run-1 and run-2 respectively.*

As expected, the smallest directional thermal expansion is found in the (010) plane, where the atoms form covalently-bonded puckered layers. By comparison, the crystallographic *b* direction, normal to the layers, presents a nearly twice as large thermal expansion value compared to the *a* and *c* directions (Table 2). This is consistent with the presence of weaker van der Waals-type interactions only along the crystallographic b direction. As previously reported by Henry et al.[47], we do not confirm the in-plane anisotropy suggested by the DFT calculations

of Sansone et al.[52]. In contrast with Henry et al.[47], we did not observe a discontinuity in the slope of the linear expansion coefficients for the *a* and *c* parameters above 706 K. This could be due to the smaller temperature increment used in the present study which resulted in better data sampling and smaller error bars.

Table 4.2. *Volumetric and lattice thermal expansion coefficients of bP at ambient pressure from this work and the literature.*

Exp	T range (K)	α_a (10^{-6} K^{-1})	α_b (10^{-6} K^{-1})	α_c (10^{-6} K^{-1})	α_V (10^{-6} K^{-1})	Technique
This work	298-750	6.46(6)	12.08(7)	6.72(5)	25.4(2)	Powder XRD
Henry et al.[47]	300-706	6.4(1)	11.8(1)	6.5(2)	24.8(2)	Powder XRD
Faber et al.[48]	300-575	8(5)	11(2)	5(5)	22(12)	Powder XRD
Rodrigues et al.[49]	170-250	4.9(3)	11.7(4)	7.7(2)	24.5(3)	Powder XRD
Riedner et al.[50]	300-475	53(5)	10(2)	0(5)	63(12)	Single Crystal XRD
Keyes et al.[51]	300-700	22(2)	38(4)	39(4)	99(10)	Powder XRD
Sansone et al.[52]	300-600	1	11	8	20	DFT

IV. Room temperature equations of state of hBN and bP

a. Hexagonal boron nitride

The pressure dependence of unit-cell parameters and hBN volume obtained from run 3 are shown in Fig. 5 with data from the literature.

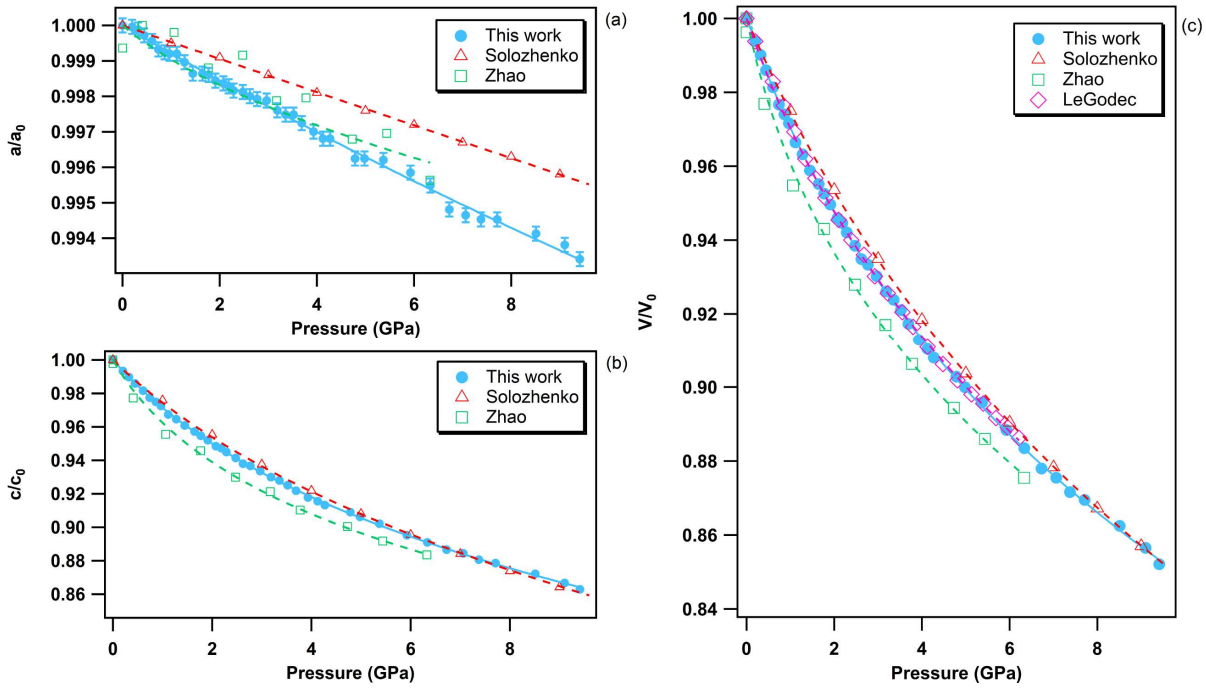

Fig. 4.5. *Evolution with pressure of the relative lattice parameters (a/a_0 and c/c_0) and volume of hBN in the 0-10 GPa pressure range at room temperature. The solid blue circles represent the data acquired in the present study upon compression. Empty symbols refer to the data reported in the literature. Red triangles: Solozhenko et al.[35]; green squares: Zhao et al.[36]; pink diamonds: Le Godec et al.[46]. The individual a and c-axis data were fitted using a polynomial equation and the volume data using the third order Birch-Murnaghan equation of state[68].*

As shown in Fig. 5a, the *a* lattice parameter of hBN presents a very small variation in the 0-10 GPa pressure range, only reducing by 0.7% of its initial value over the investigated pressure range. By contrast, we have measured a much larger variation of 14% along the *c* axis in the same pressure interval (Fig. 5b). The strong compressibility anisotropy can be clearly appreciated in Fig. 6a. This observation is consistent with the characteristic layered structure of the material, featuring strong intra-plane covalent bonds and weak van der Waals inter-plane interactions.

Table 4.3. *Refined EOS parameters of hBN at ambient temperature from this work and literature.*

Exp	P range (GPa)	V_0 (Å^3)	K_0(GPa)	K_0'	Technique	EOS type
This work	0 – 9.5	36.18 ± 0.06	27.4 ± 0.9	11.4 ± 0.8	Powder XRD	3rd order BM
Solozhenko et al.[35]	0 – 12	36.17	36.7 ± 0.5	5.6 ± 0.2	Powder XRD	Murnaghan
Zhao et al.[36]	0 – 9.0	-	17.6 ± 0.8	19.5 ± 3.4	Powder XRD	3rd order BM
Le Godec et al.[46]	0 – 6.7	-	27.6 ± 0.5	10.5 ± 0.5	Powder XRD	3rd order BM

Table 4.4. *3rd order polynomial adjustment of the directional variation of the individual a and c-axis of hBN. A, B, C, D are the polynomial coefficients obtained from the fit.*

Axis	P range (GPa)	A	B	C	D	Technique	Polynomial fit
a axis	0 – 9.5	2.504[9]	-0.00081[2]	0.000012[2]	-	Powder XRD	2nd order
c axis	0 – 9.5	6.661[5]	-0.0284[3]	0.0025[1]	0.000107[6]	Powder XRD	3rd order

The equation of state (EOS) parameters of hBN have been derived using the EoSFit program[69,70] by fitting the experimental data using a third-order Birch-Murnaghan EOS[68] with the following expression:

$$P = \frac{3}{2}K_0\left[\left(\frac{V}{V_0}\right)^{-7/3} - \left(\frac{V}{V_0}\right)^{-5/3}\right] \times \left\{1 + \frac{3}{4}(K_0' - 4)\left[\left(\frac{V}{V_0}\right)^{-2/3} - 1\right]\right\} \qquad \text{Eq. 4}$$

where P is the pressure, V_0 and V are the unit-cell volumes at ambient pressure and at pressure P, K_0 and K_0' are the bulk modulus and its first derivative at ambient pressure, respectively. The fitted EOS parameters are listed in Table 3 together with the available literature data. Polynomial regressions of the directional unit-cell parameters are presented in Table 4. The EOS parameters obtained in this study are in very good agreement with those reported in the study of Le Godec et al.[46], in which, however, only the volumetric variations are reported, thus not allowing a direct comparison with the directional variations obtained in the present study. On the other hand, significant differences with the work of Solozhenko et al.[35] and Zhao et al.[36] are highlighted in Fig. 5. Specifically, along the *a*-axis, the scatter of data points is more pronounced in Zhao et al.[36], while a smaller slope of the linear variation is observed in Solozhenko et al.[35]. This is explained by the very small variation of the parameter *a* (0.7% over the entire pressure range studied) which is at the sensitivity limit of the *in-situ* XRD method employed in these studies. Moreover, in these works, a non-hydrostatic solid medium was used, which could potentially induce large pressure gradients, which in turn can lead to unprecise pressure and cell parameters determination. In the current study, helium was employed as pressure-transmitting medium, thus ensuring perfect hydrostatic conditions. Along the *c*-axis, as the variations with pressure are much larger (14%), the relative difference between our data and those of the two studies in the literature is less pronounced.

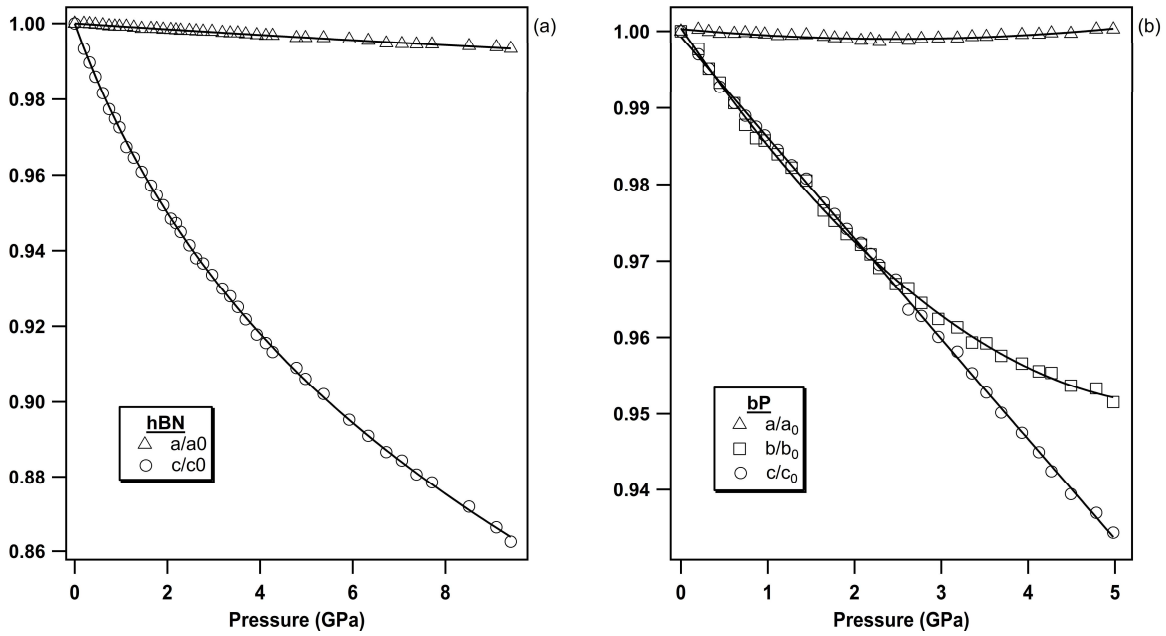

Fig. 4.6. *Evolution with pressure of the lattice parameters of (a) hBN and (b) bP, normalized to their ambient pressure values to highlight their anisotropic compressive behavior.*

b. Black Phosphorus

The pressure variation of the relative lattice parameters and unit-cell volume of bP at ambient temperature are presented together with the literature data in Fig. 7.

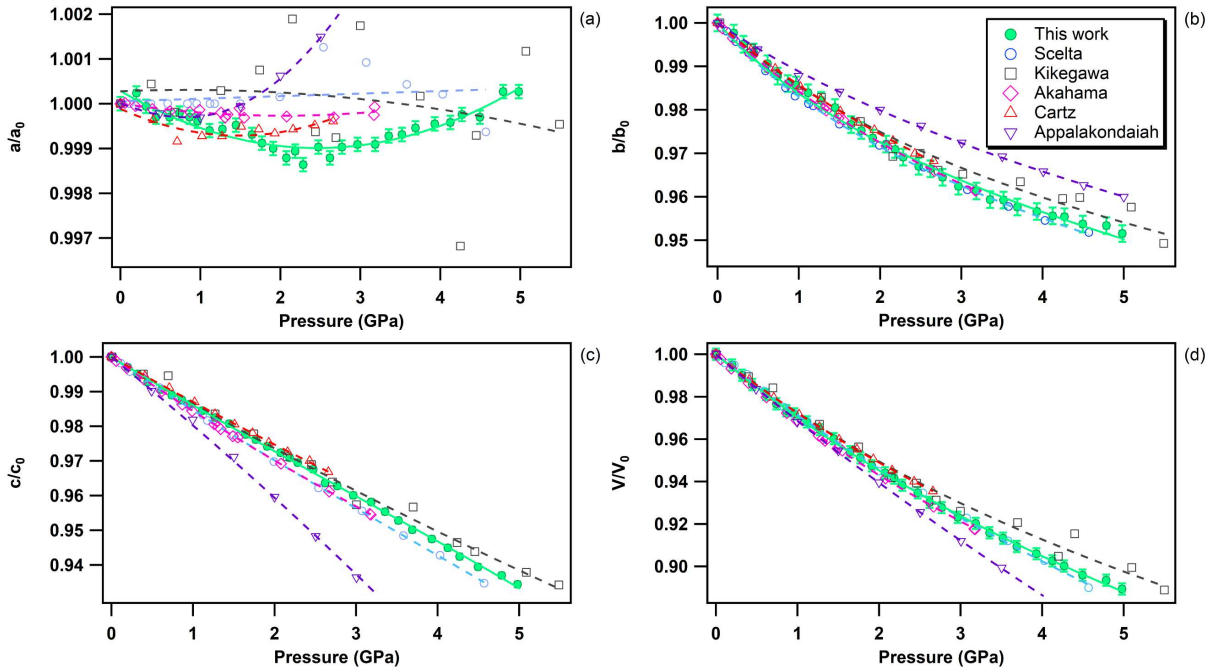

Fig. 4.7. *Relative lattice parameters and unit-cell volume variation of bP in the 0-5 GPa pressure range at room temperature. The solid green circles represent the data obtained in the present study. The empty symbols refer to the data reported in the literature. Blue circles : Scelta et al.[37]; black rectangles; Kikegawa et al.[38]; pink diamonds; Akahama et al.[39]; red up triangles; Cartz et al.[40]; and, violet down triangles; Appalakondaiah et al.[41]. The individual a, b and c-axis data were fitted using a polynomial equation and the volume data using a third order Birch-Murnaghan equation of state[68].*

As hBN, bP exhibits a strong anisotropic behavior (see Fig. 6b). The *b* and *c* axes of the orthorhombic lattice reduces by approximately 5% while the *a*-axis is nearly incompressible in the entire stability field of bP up to 5 GPa. Using *ab initio* DFT calculations, Appalakondaiah et al.[41] proposed an explanation for this mechanical behavior. Indeed, they showed that the elastic constant C_{11} is much larger than the C_{22} and C_{33} ones (see ref.[41] for C_{ii} index correspondence with the crystallographic directions), which implies that bP is stiffer against deformation along the *a*-axis than along the *b* and *c* axes. Owing to the very small volume change along *a*, very accurate XRD measurements and perfect hydrostatic conditions are required for quantitative analysis. We could observe a shallow relative *a*-axis contraction of 10^{-3} between 0 and ~2.4 GPa, followed by an expansion of the same amount at higher pressure up to 5 GPa. As shown in Fig. 7, such behavior was not reported in previous experimental studies[37-40] due to higher data points scattering, limited pressure range, or the presence of pressure gradients. It is also worth noting that, despite a significant difference in the absolute values, the DFT calculations in ref.[41] reproduce well the observed experimental trends under pressure. This behavior may be attributed to the competitive effects of the layer puckering of the sheets and of the atomic repulsion.

Table 4.5. *Volumetric EoS parameters of bP at ambient temperature from this work and literature. *These parameters have been calculated from the data provided in the literature.*

Exp	P range (GPa)	V_0 (Å^3)	K_0(GPa)	K_0'	Technique	EOS type
This work	0 – 5	152.06 ± 0.16	29.8 ± 0.7	5.7 ± 0.5	Powder XRD	3rd order BM
Scelta et al.[37]	0 – 5	151.28 ± 0.16	33.3 ± 1.3	3.1 ± 0.6	Powder XRD	Vinet
Kikegawa et al.[38]	0 – 5	151.2 ± 4.8	36 ± 2	4.5 ± 0.5	Powder XRD	Murnaghan
Akahama et al.[39]*	0 – 3.2	151.94 ± 0.02	29.1 ± 0.2	5.7 ± 0.2	Powder XRD	3rd order BM
Cartz et al.[40]*	0 – 2.7	151.80 ± 0.17	32.8 ± 2.3	5.8 ± 1.9	Powder XRD	3rd order BM
Appalakondaiah et al.[41]	0 – 5	151.3	30.7	-	DFT	-

Table 4.6. *Lattice parameters evolution of bP with pressure. A, B, C, D are the polynomial coefficients obtained in the linear (c axis) and third-order (a,b axis) adjustments.*

Axis	P range (GPa)	A	B	C	D	Technique	Polynomial fit
a-axis	0 – 5	3.314[1]	-0.0009[2]	0.00014[8]	0.000009[11]	Powder XRD	3rd order
b-axis	0 – 5	10.48[1]	-0.0163[6]	0.0012[3]	0.00003[4]	Powder XRD	3rd order
c-axis	0 – 5	4.375[2]	-0.01315[6]	-	-	Powder XRD	Linear

The volumetric EOS and directional 3rd order polynomial parameters of bP are listed in Table 5 and 6, respectively. Like for hBN, a third-order Birch-Murnaghan EOS[68] was employed to fit the experimental volume data. Due to the quasi-incompressible nature of the *a*-axis, the obtained polynomial coefficients B, C and D are close to zero. This unique feature can be exploited for accurate P, T metrology as detailed in section V. In agreement with previous studies[37-40], the *c* axis has the particularity to vary quasi-linearly with pressure, while the *b* axis presents a regular behaviour. With the exception of Kikegawa et al.[38], our volumetric EOS parameters V_0, K_0 and K'_0 are in good agreement with those reported in the literature.

c. A7 phase of phosphorus

BP displays a series of pressure-induced first-order phase transitions[37]. As shown in Fig. 8, upon compression orthorhombic bP undergoes a first-order phase transition to the A7 rhombohedral form (space group *R-3m*). As previously reported[37], the onset of this phase

transformation is observed at ~5 GPa and is associated with a large volume discontinuity of 13% which corresponds to a major atomic rearrangement. This leads to the partial loss of the structural anisotropy of bP. The EOS parameters of the A7 phase of P are listed in Table 7 together with the literature data. Our results are in excellent agreement with those of Scelta et al.[37], but strongly deviates from those reported by Kikegawa et al.[38] and Clark et al.[71]. This is again explained by the larger data point scatter and the potential presence of significant pressure gradients as non-hydrostatic solid pressure media have been employed in these two studies. As mentioned earlier, helium was used as pressure transmitting medium both in this study and that of Scelta et al.[37].

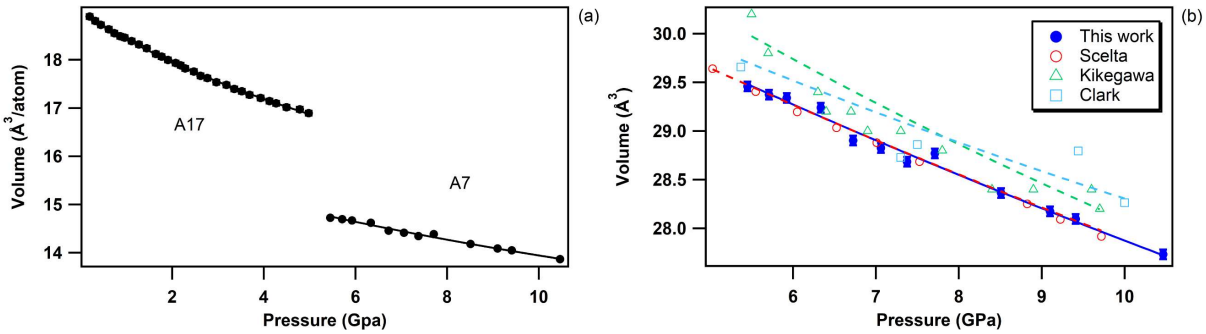

Fig. 4.8. *(left) Equation of state of bP at ambient temperature across the orthorhombic to rhombohedral (A7) first-order phase transition, observed at 5 GPa. (right) Unit-cell volume evolution of A7 rhombohedral P in the 5 – 10.5 GPa pressure range at room temperature. The solid blue circles represent the data acquired in the present study. The empty symbols refer to the data reported by Scelta et al.[37] (red circles), Kikegawa et al.[38] (green up triangles) and Clark et al.[71] (blue squares). The corresponding EoS fits are represented by lines.*

Table 4.7. *Volumetric EOS parameters of rhombohedral A7 phosphorus at ambient temperature from this work and literature.*

Exp	P range (GPa)	V_0 (Å³/atom)	K_0(GPa)	K_0'	Technique
This work	5 – 10.5	15.92 ± 0.06	64.8 ± 2.8	2.4 ± 0.4	Powder XRD
Scelta et al.[37]	5 – 10	15.88 ± 0.02	68 ± 2	1.9 ± 0.3	Powder XRD
Kikegawa et al.[38]	5.5 – 9.7	16.6 ± 0.2	46 ± 4	3.0 ± 0.6	Powder XRD
Clark et al.[71]	3 – 10	15.97 ± 0.02	65.0 ± 0.6	-	Powder XRD

V. Exploiting the anisotropic thermo-elastic properties of bP for simultaneous P,T determination

As shown by Crichton and Mezouar[72], it is possible to simultaneously determine the pressure and the temperature from the thermal equations of state of 2 materials subjected to the same P,T conditions. This method is commonly used for P,T metrology in large volume presses. The precision of this method depends on the contrast between the thermoelastic parameters (bulk modulus K_0 and thermal expansion α) of the two materials. For example, NaCl and Au constitute a good couple of materials because NaCl is much softer than Au, but expands much less upon heating. In principle, this method could be applied to a single material with highly anisotropic thermo-elastic properties used as sensor for both P and T variables. As shown in Fig. 9, bP is an excellent candidate material for this type of application. Indeed, as discussed above, it is quasi-incompressible in one direction and has a high linear thermal expansion coefficient (α_a= 6.46(6)·10^{-6} K^{-1}) along the *a*-axis (Fig. 4a, 7a and Table 2). This unique property allows the simultaneous determination of P and T with a good precision.

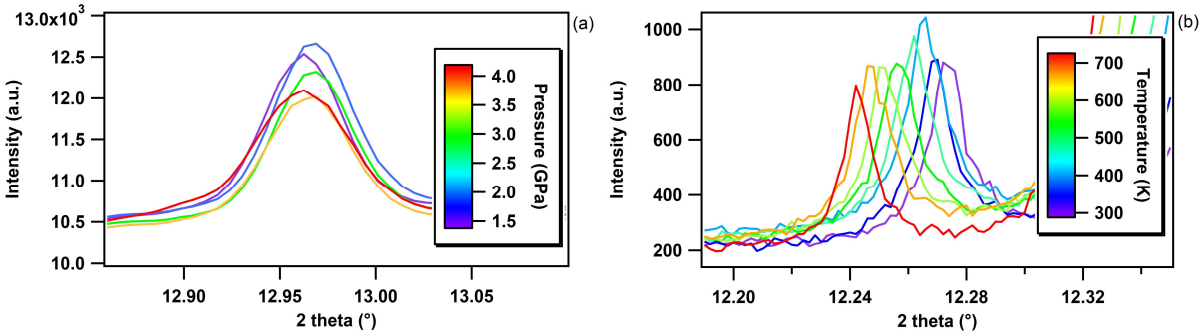

Fig. 4.9. *(panel a) Evolution of the position of the (200) reflection of bP with pressure at ambient temperature showing no pressure shift due to compression along the a-axis. (panel b) Evolution of the (200) reflection of bP with temperature at ambient pressure.*

Indeed, this remarkable feature makes orthorhombic bP the only known element that can be employed as simultaneous P,T sensor. In practice, its *a* lattice parameter can be determined, for instance, from the (200) Bragg reflection alone and the temperature can then be derived using the linear T dependence of *a* according to the following equation:

$$T(K) = \frac{a/a_0 - 1}{\alpha_a} + 300 = \frac{a/a_0 - 1}{6.46 \times 10^{-6}} + 300 \qquad \text{Eq. 5}$$

where a and a_0 are the values of the a lattice parameter at a given pressure and temperature, and at ambient condition, respectively and α_a is the directional thermal expansion coefficient of bP along *a* (Fig. 4a and Table 2).

The pressure can then be derived from the third-order Birch-Murnaghan equation of state[68] of bP (Eq. 4 and Table 5). The precision of this method is ± 15 K and 0.1 GPa, which is sufficient for the determination of phase diagrams in the P,T range up to 5 GPa and 1700 K.

An example of application which aimed at determining a melting point of bP under pressure using the Paris-Edinburgh (PE) press[57-59] is presented in Fig. 10. The PE press can generate pressures and temperatures in excess of 10 GPa and 2500 K and is ideally suited to determine P, T phase diagram using *in situ* XRD. The melting of bP is clearly evidenced by the disappearance of the XRD peaks and appearance of a broad diffuse x-ray scattering signal associated with the loss of the crystalline order. Thanks to the established metrology, the P,T pathway in the phase diagram of bP and position of a melting point have been determined with a precision of ± 15 K at 0.5 GPa. More details about this work will be presented in a future publication.

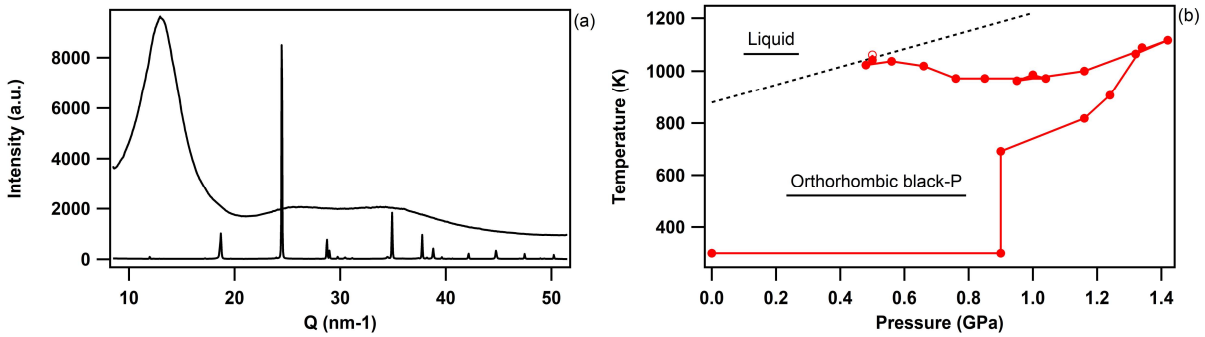

Fig. 4.10. *Determination of a melting point of bP using the anisotropic thermo-elastic properties of bP. (Left) Melting criteria: At the melting the Bragg reflections of bP disappear (bottom XRD pattern) and a liquid diffuse signal appears (upper XRD pattern). (Right) P,T pathway of the XRD data collection. Solid red circles indicate crystalline bP, while the empty red circle indicate the liquid state. The dotted line represents the melting line of bP.*

VI. Conclusion

In this study, we utilized in situ high-resolution x-ray diffraction to accurately determine the equations of state parameters, as well as the volumetric and linear thermal expansion coefficients, of hexagonal boron nitride (hBN) and black phosphorus (bP). Our investigation focused on precisely characterizing the non-linear variations of the unit-cell parameters of these 2D materials under different temperatures and pressures. These materials possess anisotropic properties due to their layered structure, making them relevant for various energy and

technology applications. Our findings offer detailed insights into the structural behavior of hBN and bP at the nanoscale level under high-pressure and temperature conditions achievable with current industrial technology. Consequently, this information contributes to a better understanding and enhancement of the synthesis, stability, and application of these 2D nanostructured materials. Moreover, our data serve as a valuable experimental reference to refine theoretical calculations and gain a deeper understanding of the two-dimensional interactions present in these materials. Lastly, we propose a novel method for high-pressure and high-temperature metrology, utilizing the highly anisotropic directional thermoelastic properties of bP. This innovative approach could be advantageous for large volume press or diamond anvil cell experiments conducted within the low-pressure, high-temperature regime. The exceptional characteristics of bP enable its utilization as a single sensor for simultaneous determination of pressure and temperature through XRD analysis.

References

1 P. Chaikin, & T. Lubensky, Principle of Condensed Matter Physics. *Cambridge University Press,* Cambridge, England, 1995.

2 P. Hohenberg, & W. Kohn, Inhomogeneous electron gas. *Phys. Rev.*, 1964, **136**, B864.

3 W. Kohn, Nobel lecture: Electronic structure of matter-wave functions and density functionals. *Rev. Mod. Phys.*, 1999, **71**, 1253.

4 J. D. Bernal, The Structure of Graphite, *Proc. R. Soc. Lond. A*, 1924, **106**, 749-773.

5 R. S. Pease, Crystal Structure of Boron Nitride. *Nature*, 1950, **165**, 722-723.

6 R. Nikbakht, & B. Jodoin, Thick Cu-hBN Coatings Using Pulsed Gas Dynamic Spray Process: Coating Formation Analysis and Characterization. *Journal of Thermal Spray Technology*, 2022, **31**, 609-622.

7 C. R. Dean, A. F. Young, I. Meric, C. Lee, L. Wang, S. Sorgenfrei, K. Watanabe, T. Taniguchi, P. Kim, K. L. Shepard, & J. Hone, Boron nitride substrates for high-quality graphene electronics. *Nature Nanotechnology*, 2010, **5**, 722-726.

8 A. S. Mayorov, R. V. Gorbachev, S. V. Morozov, L. Britnell, R. Jalil, L. A. Ponomarenko, P. Blake, K. S. Novoselov, K. Watanabe, T. Taniguchi, A. K. Geim, Micrometer-Scale Ballistic Transport in Encapsulated Graphene at Room Temperature. *Nano Lett.*, 2011, **11**, 6, 2396-2399.

9 A. K. Geim, & I. V. Grigorieva, Van der Waals heterostructures. *Nature*, 2013, **499**, 419-425.

10 L. H. Li, J, Cervenka, K Watanabe, T, Taniguchi, & Y. Chen, Strong oxidation resistance of atomically thin boron nitride nanosheets. *ACS Nano*, 2014, **8**, 1457-1462.

11 A. Kovalčíková, J. Balko, C. Balázsi, P. Hvizdoš, J. Dusza, Influence of hBN content on mechanical and tribological properties of Si_3N_4/BN ceramic composites. *Journal of the European Ceramic Society*, 2014, **34**(14), 3319-3328.

12 L. Wang, Y. Bai, Z. Ma, C. Ge, H. Guan, X. Zhang, Tribological performances of hexagonal boron nitride nanosheets via surface modification with silane coupling agent. *SN Applied Sciences*, 2021, **3**, 368.

13 P. Madhukar, N. Selvaraj, C. Rao, G. Veeresh Kumar, Tribological behavior of ultrasonic assisted double stir casted novel nano-composite material (AA7150-hBN) using Taguchi technique. *Composites Part B Engineering*, 2019, **175**, 107136.

14 D. Berman, A. Erdemir, & A. V. Sumant, Approaches for Achieving Superlubricity in Two-Dimensional Materials. *ACS Nano*, 2018, **12**, 3, 2122-2137.

15 R. Zhang, Q. Ding, S. Zhang, Q. Niu, J. Ye, L. Hu, Construction of a continuously layered structure of hBN nanosheets in the liquid phase via sonication-induced gelation to achieve low friction and wear. *Nanoscale*, 2019, **11**, 12553-12562.

16 O. Popov, V. Vishnyakov, L. Fleming, M. Podgurskiy, & L. Blunt, Reaction Sintering of Biocompatible Al_2O_3-hBN Ceramics. *ACS Omega*, 2022, **7**, 2, 2205-2209.

17 J. W. Mellor, A Comprehensive Treatise on Inorganic and Theoretical Chemistry, 1922, **Vol. VIII**, 744-754.

18 D. Corbridge, Phosphorus: Chemistry, Biochemistry and Technology, Sixth Edition, Taylor & Francis, New York, 2013.

19 P. W. Bridgman, Two new modifications of phosphorus, *J. Am. Chem. Soc.*, 1914, **36**, 7, 1344-1363.

20 L. Li, Y. Yu, G. J. Ye, Q. Ge, X. Ou, H. Wu, D. Feng, X.H. Chen and Y. Zhang, Black phosphorus field-effect transistors, *Nat. Nanotechnol.*, 2014, **9**, 372-377.

21 H. Liu, A. T. Neal, Z. Zhu, Z. Luo, X. Xu, D. Tománek, & P. D. Ye, Phosphorene: an unexplored 2D semiconductor with a high role mobility, *ACS Nano.*, 2014, **8**, 4033-4041.

22 Y. Du, J. Maassen, W. Wu, Z. Luo, X. Xu, & P. D. Ye, Auxetic black phosphorus: A 2D material with negative Poisson's ratio, *Nano Lett.*, 2016, **16**, 6701-6708.

23 L. Vaquero-Garzon, R. Frisenda, & A. Castellanos-Gomez, Anisotropic buckling of few-layer black phosphorus, *Nanoscale*, 2019, **11**, 12080-12086.

24 K. S. Novoselov, A. K. Geim, S. V. Morozov, D. Jiang, Y. Zhang, S. V. Dubonos, I. V. Grigorieva, & A. A. Firsov, Electric field effect in atomically thin carbon films, *Science*, Density-driven liquid-liquid phase separation in the system Al_2O_3-$Y_2O_3$2004, **306**, 666-669.

25 Q. H. Wang, K. Kalantar-Zadeh, A. Kis, J. N. Coleman, & M. S. Strano, Electronics and optoelectronics of two-dimensional transition metal dichalcogenides. *Nat. Nanotech.*, 2012, **7**, 699-712.

26 H. Asahina, & A. Morita, Band structure and optical properties of black phosphorus. *J. Phys. C Solid State Phys*, 1984, **17**, 1839-1852.

27 A. S. Rodin, A. Carvalho, & A. H. Castro Neto, Strain-Induced Gap Modification in Black Phosphorus, *Phys. Rev. Lett.*, 2014, **112**, 176801.

28 X. Ling, H. Wang, S. Huang, F. Xia, & M. S. Dresselhaus, The renaissance of black phosphorus, *Proc. Nat. Acad. Of Sci.*, 2015, **112**, 4523-4530.

29 M. Peruzzini, et al., A perspective on recent advances in Phosphorene functionalization and its applications in devices. *Eur. J. Inorg. Chem.*, 2019, **11**, 1476-1494.

30 J. Lu, J. Yang, A. Carvalho, H. Liu, Y. Lu, & C. H. Sow, Light-matter interactions in Phosphorene. *Acc. Chem. Res.*, 2016, **49**, 1806-1815.

31 D. Yuan, Y. Dou, Z. Wu, Y. Tian, K.-H. Ye, Z. Lin, S. X. Dou and S. Zhang, Atomically Thin Materials for Next-Generation Rechargeable Batteries. *Chem. Rev.*, 2022, **122**, 1, 957-999.

32 K. Khan, A. K. Tareen, M. Iqbal, Z. Ye, Z. Xie, A. Mahmood, N. Mahmood and H. Zhang, Recent Progress in Emerging Novel MXenes Based Materials and their Fascinating Sensing Applications. *Small*, 2023, **19**, 2206147.

33 A. Yang, D. Wang, X. Wang, D. Zhang, N. Koratkar and M. Rong, Recent advances in phosphorene as a sensing material, *Nano Today*, 2018, **20**, 13-32.

34 X. Yu, W. Liang, C. Xing, K. Chen, J. Chen, W. Huang, N. Xie, M. Qiu, X. Yan, Z. Xie and H. Zhang, Emerging 2D pnictogens for catalytic applications: status and challenges. *J. Mater. Chem. A*, 2020, **8**, 12887-12927.

35 V. L. Solozhenko, G. Will and F. Elf, Isothermal compression of hexagonal graphite-like boron nitride up to 12 GPa. *Solid State Communications*, 1995, **96**, 1-3.

36 Y. Zhao, R. B. Von Dreele, D. J. Weidner and D. Schiferl, P-V-T Data of hexagonal boron nitride h BN and determination of pressure and temperature using thermoelastic equations of state of multiple phases. *High Press. Res.*, 1997, **15**, 369-386.

37 D. Scelta, A, Baldassarre, M. Serrano-Ruiz, K. Dziubek, A. B. Cairns, M. Peruzzini, R. Bini and M. Ceppatelli, The p-sc structure in phosphorus: bringing order to the high pressure phases of group 15 elements. *Chem. Commun.*, 2018, **54**, 10554-10557.

38 T. Kikegawa and H. Iwasaki, An X-ray Diffraction Study of Lattice Compression and Phase Transition of Crystalline Phosphorus. *Acta Cryst.*, 1983, B**39**, 158-164.

39 Y. Akahama, M. Miyakawa, T. Taniguchi, A. Sano-Furukawa, S. Machida and T. Hattori, Structure refinement of black phosphorus under high pressure. *J. Chem. Phys.*, 2020, **153**, 014704.

40 L. Cartz, S. R. Srinivasa, R. J. Riedner, J. D. Jorgensen and T. G. Worlton, Effect of pressure on bonding in black phosphorus. *J. Chem. Phys.*, 1979, **71**, 1718.

41 S. Appalakondaiah, G. Vaitheeswaran, S. Lebègue, N. E. Christensen and A. Svane, Effect of van der Waals interactions on the structural and elastic properties of black phosphorus. *Phys. Rev. B*, 2012, **86**, 035105.

42 R. S. Pease, An X-ray study of boron nitride. *Acta Cryst.*, 1952, **5**, 356-361.

43 W. Paszkowicz, J. B. Pelka, M. Knapp, T. Szyszko and S. Podsiadlo, Lattice parameters and anisotropic thermal expansion of hexagonal boron nitride in the 10 – 297.5 K temperature range. *Applied Physics A*, 2002, **75**, 431-435.

44 V. L. Solozhenko and T. Peun, Compression and thermal expansion of hexagonal graphite-like boron nitride up to 7 GPa and 1800 K. *J. Phys. Chem Solids*, 1997, **58**, 9, 1321-1323.

45 B. Yates, M. J. Overy and O. Pirgon, The anisotropic thermal expansion of boron nitride. *Philos. Mag.*, 1975, **32**, 4, 847-857.

46 Y. Le Godec, D. Martinez-Garcia, M. Mezouar, G. Syfosse, J. -P. Itié and J. -M. Besson, Thermoelastic behavior of hexagonal graphite-like boron nitride. *High Press. Res.*, 2000, **17**, 1, 35-46.

47 L. Henry, V. Svitlyk, M. Mezouar, D. Sifré, G. Garbarino, M. Ceppatelli, M. Serrano-Ruiz, M. Peruzzini and F. Datchi, Anisotropic thermal expansion of black phosphorus from nanoscale dynamics of Phosphorene layers. *Nanoscale*, 2020, **12**, 4491-4497.

48 In ref. 50 this work is reported as “Private Communication” by J. Faber. To our knowledge, this study was never published.

49 J. E. F. S. Rodrigues, J. Gainza, F. Serrano-Sánchez, C. López, O. J. Dura, N. Nemes, J. L. Martinez, Y. Huttel, F. Fauth, M. T. Fernández-Diaz, N. Biškup and J. A. Alonso, Structural Features, Anisotropic Thermal Expansion, and Thermoelectric Performance in Bulk Black Phosphorus Synthesized under High Pressure. *Inorg. Chem.*, 2020, **59**, 20, 14932-14943.

50 R. Riedner, S. R. Srinivasa, L. Cartz, T. G. Worlton, R. Klinger and R. Beyerlein, Anisotropic thermal expansion and compressibility of black phosphorus, *AIP Conf. Proc.*, 1974, **17**, 8-20.

51 R. W. Keyes, The Electrical Properties of Black Phosphorus. *Phys. Rev.*, 1953, **92**, 580.

52 G. Sansone, A. J. Karttunen, D. Usvyat, M. Schütz, J. G. Brandenburg and L. Maschio, On the exfoliation and anisotropic thermal expansion of black phosphorus, *Chem. Commun.*, 2018, **54**, 70, 9793-9796.

53 M. Serrano-Ruiz, M. Caporali, A. Ienco, V. Piazza, S. Heun and M. Peruzzini, The role of water in the preparation and stabilization of high-quality Phosphorene flakes. *Adv. Mater. Interfaces*, 2016, **3**, 1500441.

54 T. Poręba, D. Comboni, M. Mezouar, G. Garbarino and M. Hanfland, Tracking structural phase transitions via single crystal x-ray diffraction at extreme conditions: advantages of extremely brilliant source. *J. Phys. Condens. Matter*, 2022, **35**, 054001.

55 A. N. Fitch, C. Dejoie, E. Covacci, G. Confalonieri, O. Grendal, L. Claustre, P. Guillou, J. Kieffer, W. de Nolf, S. Petitdemange, M. Ruat and Y. Watier, ID22, the high-resolution powder-diffraction beamline at ESRF. *Accepted for publication in J. Synchrotron Radiat.*, 2023.

56 C. Dejoie, M. Coduri, S. Petitdemange, C. Giacobbe, E. Covacci, O. Grimaldi, P.-O. Autran, M. W. Mogodi, D. Š. Jung and A. N. Fitch, Combining a nine-crystal multi-analyser stage with a two-dimensional detector for high-resolution powder X-ray diffraction. *J. Appl. Cryst.*, 2018, **51**, 1721-1733.

57 J. M. Besson, G. Hamel, P. Grima, R. J. Nelmes, J. S. Loveday, S. Hull and D. Häusermann, A Large Volume Pressure Cell for High Temperatures. *High Press. Res.*, 1992, **8**, 625.

58 S. Klotz, Th. Strässle, G. Rousse, G. Hamel and V. Pomjakushin, Angle-dispersive neutron diffraction under high pressure to 10 GPa. *Appl. Phys. Lett.*, 2005, **86**, 031917.

59 G. Morard, M. Mezouar, N. Rey, R. Poloni, A. Merlen, S. Le Floch, P. Toulemonde, S. Pascarelli, A. San Miguel, C. Sanloup and G. Fiquet, Optimization of Paris-Edinburgh press cell assemblies for *in situ* monochromatic X-ray diffraction and X-ray absorption. *High Press. Res.*, 2007, **27**, 223.

60 M. Mezouar, T. Le Bihan, H. Libotte, Y. Le Godec and D. Häusermann, Paris-Edinbugh large-volume cell coupled with a fast imaging-plate system for structural investigation at high pressure and high temperature. *J. Synchrotron Radiat.*, 1999, **6**, 1115.

61 G. Morard, M. Mezouar, S. Bauchau, M. Álvarez-Murga, J. -L. Hodeau and G. Garbarino, High efficiency multichannel collimator for structural studies of liquids and low-Z materials at high pressures and temperatures. *Review of Scientific Instruments*, 2011, **82**, 023904.

62 G. Ashiotis, A. Deschildre, Z. Nawaz, J. P. Wright, D. Karkoulis, F. E. Picca, J. Kieffer, The fast azimuthal integration Python library: pyFAI. *Journal of applied crystallography*, 2015, **48**, 510-519.

63 C. Prescher and V. B. Prakapenka, DIOPTAS: A program for reduction of two-dimensional X-ray diffraction data and data exploration. *High Press. Res.*, 2015, **35**, 223-230.

64 B. H. Toby, EXPGUI, a graphical user interface for GSAS. *Journal of applied crystallography*, 2001, **34**, 210-213.

65 A. Le Bail, H. Duroy, J. L. Fourquet, Ab-initio structure determination of $LiSbWO_6$ by X-ray powder diffraction. *Materials Research Bulletin*, 1988, **23**, 447-452.

66 R. Letoullec, J. P. Pinceaux, & P. Loubeyre, The membrane diamond anvil cell: A new device for generating continuous pressure and temperature variations. *High Pressure Research*, 1988, **1**, 77-90.

67 G. Shen, Y. Wang, A. Dewaele, C. Wu, D. E. Fratanduono, J. Eggert, S. Klotz, K. F. Dziuket, P. Loubeyre, O. V. Fat'yanov, P. D. Asimow, T. Mashimo, R. M. M. Wentzcovitch & other members of the IPPS task group, Toward an international practical pressure scale: A proposal for an IPPS ruby gauge (IPPS-Ruby2020). High Pressure Research, 2020, **40**:3, 299-314.

68 F. Birch, Finite Elastic Strain of Cubic Crystals. *Phys. Rev.*, 1947, **71**, 809-824.

69 R. J. Angel, J. Gonzalez-Platas and M. Alvaro, EosFit7c and a Fortran module (library) for equation of state calculations. *Zeitschrift für Kristallographie – Crystalline Materials*, 2014, **229**, 405-419.

70 J. Gonzalez-Platas, M. Alvaro, F. Nestola and R. J. Angel, EosFit7-GUI: A new graphical user interface for equation of state calculations, analyses and teaching. *Journal of applied crystallography*, 2016, **49**, 1377-1382.

71 S. M. Clark and J. M. Zaug, Compressibility of cubic white, orthorhombic black, rhombohedral black, and simple cubic black phosphorus. *Phys. Rev. B*, 2010, **82**, 134111.

72 W. A. Crichton, M. Mezouar, Noninvasive pressure and temperature estimation in large-volume apparatus by equation-of-state cross-calibration. *High Temperatures - High Pressures*, 2002, **34**, 235-242.

Chapter 5:

Melting curve of black phosphorus

In Chapter 1, we recalled the important controversies that remained concerning the melting curve of black phosphorus. We report in this Chapter our experiment investigations of the melting transition in black phosphorus. The first part deals with the determination of the melting curve. Using the novel metrology introduce in Chapter 4, we obtained accurate melting points measurements up to 5 GPa and 1700 K. This allowed us to determine the precise location of the triple point where the two liquids, LDL and HDL, and the solid bP meet on the melting line. Moreover, we discuss the reversibility of the transition below and above the LDL-HDL-solid triple point. In the second part, we present our measurements of the density discontinuity at the melting transition, for which no data existed previously. We found that the density jump increases sharply with decreasing pressure below the LDL-HDL-solid triple point and reaches 60 % at the lowest investigated pressure (0.1 GPa), which is the largest value ever observed for a melting transition. We then discuss the outstanding thermodynamics of the melting transition in phosphorus.

1. Melting curve of black phosphorus: evidence for a solid-liquid-liquid triple point

In this section, we present a detailed study of the melting curve of black phosphorus up to 5 GPa and 1700 K using in situ XRD. After a brief introduction, we provide some specific method and technical details, before presenting our experimental results.

1.1. Introduction

Phosphorus exhibits a very rich polymorphism[1-2]. The structure and physico-chemical properties of the numerous allotropes of phosphorus have been extensively studied using a variety of experimental and computational methods[2-14]. Three main allotropes are stable or metastable under ambient *P,T* conditions: white (wP), red (rP) and black phosphorus (bP). BP, the most stable allotrope[1], has been firstly prepared under high-pressure, high-temperature conditions using rP as starting material[15]. As graphite, it features a layered structure with strong covalent intralayer bonds and weak van der Waals interlayer interactions[14, 16-17]. The *P*-*T* phase diagram of bP exhibits unique features. At ambient *P* and high *T*, due to its exceptional

anisotropic crystalline structure[14, 18-22], bP begins to thermally decompose at 600 K[23-24] and, in contrast with most elemental solids, does not melt or sublimate. The lowest *P-T* conditions at which melting of bP has been reported are 0.3 GPa and 1123 K. Another fundamental peculiarity that bP only shares with orthorhombic sulfur[25] is that it exhibits a first-order phase transition in its liquid state[26] between a low-density liquid (LDL) supposedly composed of P_4 molecular units[26-27] and a high-density liquid (HDL) with a local atomic arrangement resembling that of bP[27]. The melting curve of bP has been investigated by several authors in the range 0.3-5 GPa using either electric resistivity[28] or *in situ* energy dispersive x-ray diffraction[29-31] in piston-cylinder apparatus[32] and multi-anvil presses[33]. However, the measured melting curves differ greatly between authors, especially above 1 GPa: while some have found a positive slope above this pressure[28], others have reported a negative one, resulting in a bell-shaped melting curve going through a maximum temperature[29-31]. In addition, the melting curve was found in some cases to exhibit a discontinuous slope around 1 GPa, supposedly as a result of the liquid-liquid transition[30-31], whereas a continuous evolution was reported in the other studies[28,29]. There is thus at present no consensus on the location and shape of the melting line of bP below 5 GPa, nor on the existence of a triple point where the melting line intersects the liquid-liquid transition line.

Here, using an original P,T metrology, we accurately determined the melting curve position and slope using in situ high-resolution synchrotron x-ray diffraction performed under high-pressure and -temperature conditions. We have also established the occurrence and position of the liquid-liquid-solid triple point (LLSTP) and characterized the irreversibility of the transformation of low-density liquid P into rP in the low-pressure regime below 1 GPa.

1.2. Additional experimental details

All experimental runs were carried out on the ID27 high-pressure x-ray diffraction beamline of the European Synchrotron Radiation Facility (Grenoble, France)[34]. A VX5 Paris-Edinburgh press[35-37] has been employed as compression device. The sample consisted of a high purity (99.999+%) powder of black phosphorus (bP) produced following the synthesis method described in[38]. It was confined in a sample assembly optimized for accurate melting point determination[37,39] as described in Chapter 2. A diamond cylinder of 1 mm inner diameter, 1.5 mm outer diameter and 1 mm height was used as inert sample container. The excellent thermal conductivity of diamond ensured very low temperature gradients within the x-ray probed volume. The diamond capsule was sealed using two chemically inert hexagonal boron nitride

caps that served as soft pressure medium. The high temperatures up to 1800 K were generated using a high resistivity cylindrical graphite heater supplied with direct current from a stabilized power supply. This heater was inserted in a x-ray transparent boron-epoxy gasket that served as thermal and electrical insulator[39]. *In situ* monochromatic x-ray diffraction have been carried out in transmission geometry either at 20.0 keV (λ=0.6199 Å) or at 33.169 keV (λ=0.3738 Å) to cover a large 2 theta scattering angle from 3 to 25 degrees. Two-dimensional diffraction patterns were collected using a MAR165 CCD detector from MAR Research or an EIGER2 9M pixel detector from DECTRIS. Typical exposure time of 10 seconds was sufficient to collect high-quality XRD patterns. A high efficiency multichannel collimator (MCC)[40] was used to remove most of the parasitic elastic and inelastic x-ray signal coming from the sample environment (graphite heater and boron-epoxy gasket). The sample to detector distance, detector tilt angles and beam center were accurately determined using LaB_6 powder as standard. The two-dimensional XRD images were integrated using the PyFAI software[41] as implemented in the DIOPTAS suite[42]. The resulting one-dimensional diffraction patterns were analysed using the GSAS software[43] to refine the unit-cell parameters and volume of bP by Le Bail[44] extraction of d-spacings using a pseudo-Voigt peak shape function.

The main objective of this study is to accurately establish the position and slope of the melting curve of bP. Therefore, it is of crucial importance to accurately determine the pressure *P* and temperature *T* at which the XRD measurements have been performed. Here, we have established an original and accurate *P,T* metrology that is detailed in[22]. In short, it is based on exploiting the highly anisotropic character of bP due to its layered structure. Indeed, in its *P,T* stability field, bP is quasi-incompressible along the crystallographic *a*-axis and exhibits a small but finite linear thermal expansion with coefficient $\alpha_a = 6.46(6)\cdot10^{-6}$ K^{-1}. This remarkable feature makes it the only element that can be employed as simultaneous *P,T* sensor. In practice, the *a* lattice parameter of bP can be determined, from the (h00) type Bragg reflections, the temperature can then be derived using its linear T dependence established in ref.[22]:

$$T(K) = \frac{a - a_0}{\alpha_a} + 300$$

where *a* and a_0 = 3.3150 Å are the values of the *a* lattice parameter at a given pressure and temperature, and ambient conditions, respectively. The pressure can then be derived from the volume of bP using the refined third-order Birch-Murnaghan equation of state[45] parameters

obtained in[22]. This method enables the determination of *P* and *T* with a precision of ± 25-45 K and 0.1-0.3 GPa in the entire *P,T* stability field of bP up to 5 GPa and 1700 K.

Another fundamental aspect for this type of studies resides in the use of an unambiguous melting criterion. Here we have employed a standard and well-established criterion[46-48]: the x-ray signature associated with the loss of crystalline order that occurs at melting. As shown in Figure 5.1., through the use of a multi-channel collimator (MCC)[40], high quality diffraction patterns were obtained for solid and liquid phosphorus. The transition between these two states is evidenced by the disappearance of the Bragg reflections of bP and the appearance of a diffuse x-ray signal from the liquid phase when the melting line is crossed. This happens during melting either towards the low-density liquid (LDL) when the pressure is reduced at constant temperature (Figure 5.1.a) or towards the high-density liquid (HDL) when the temperature is increased at constant pressure (Figure 5.1.b).

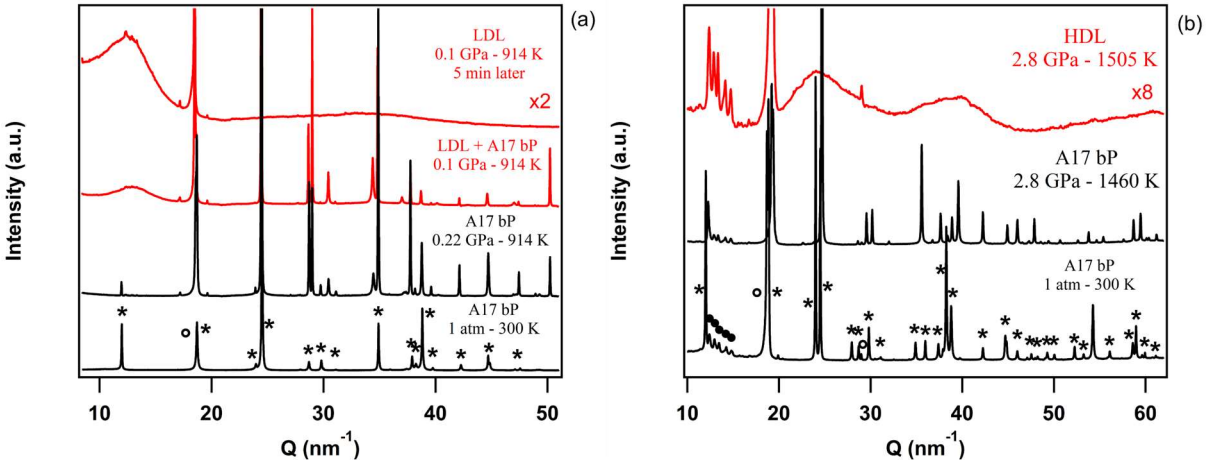

Figure 5.1. Melting of bP observed by XRD at two different P below and above the solid-LDL-HDL triple point, respectively. XRD patterns collected on (a) decompression at constant temperature (914 K) toward the low-density liquid, and (b) increasing temperature at constant pressure (2.8 GPa) toward the high-density liquid. The black asterisks, black filled circles, and empty white circles indicate the Bragg reflections of bP, the boron-epoxy gasket, and the hexagonal boron nitride container, respectively.

1.3. Results and discussion

Typical *P,T* pathways in the phase diagram of bP in the range 0.1-5.3 GPa and 300-1800 K are shown in Figure 5.2., and the determined melting points are listed in Table 1.

A freshly loaded sample was employed for each of them to ensure the high quality of the collected datasets and control their reproducibility. XRD patterns were systematically collected along 19 distinct *P,T* pathways leading to the determination of 19 points on the melting curve of bP. It is worth nothing that we were able to collect data points at very low pressure down to 0.10 (± 0.03) GPa, where solid-liquid coexistence has been observed. Low pressure melting points determination is challenging due to the mechanical instability of bP near ambient pressure[23-24]. In practice, to reach the melting curve, the temperature was increased by small increments of approximately 30 K at constant pressure or the pressure was finely reduced at constant temperature by steps of 0.1 GPa to bracket the melting temperatures and pressures with accuracies of 25-45 K and 0.03-0.35 GPa. At pressures below 1.2 GPa, the melting of bP towards the LDL can be clearly assessed by the appearance of a strong diffuse x-ray signal which exhibits a first sharp diffraction peak (FSDP) at a Q value of 13 nm^{-1} (Figure 5.1.a). As reported elsewhere[26-27], this FSDP is associated to the medium-range correlations between the P_4 tetrahedra that are present in the LDL. At higher pressures (P > 1.2 GPa), the melting occurs toward the HDL which exhibits two distinct maxima in the diffracted intensity I(Q) at 2.3 and 4.0 $Å^{-1}$ (Figure 5.1.b) that are unambiguous signatures of the HDL[27]. This enabled the accurate location of the liquid-liquid-solid triple point (LLSTP). It is worth noting that the remaining Bragg reflections present at low Q (Q < 30 nm^{-1}) are assigned to the sample container material (boron-epoxy gasket, graphite heater and h-BN capsule) that are not fully filtered by the MCC[40].

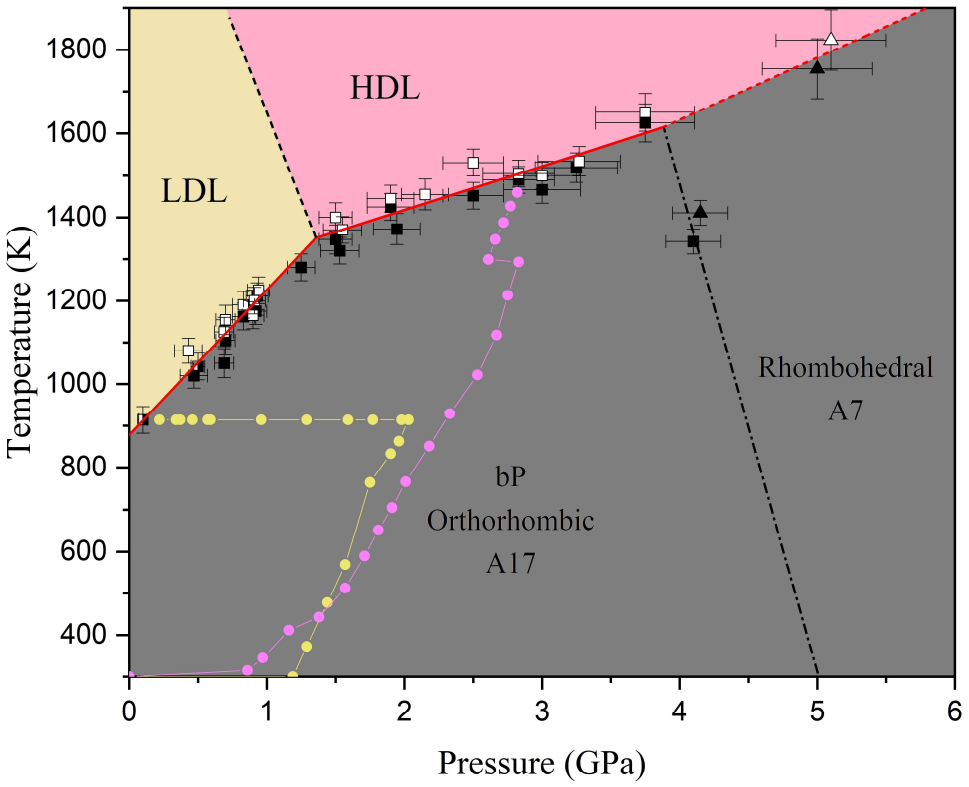

Figure 5.2. Melting curve of bP. Black and white symbols denote respectively the solid and liquid state. Black squares are for the A17 bP solid and black triangles are for the A7 solid. Two typical P-T pathways are represented by line-connected yellow and pink filled circles, where each symbol indicates a P-T point where a XRD measurement was performed.

We note that, in agreement with previous works[28-31], no structural phase transition is observed in solid P below melting, and thus A17 bP directly melts into either LDL or HDL. As shown in Figure 5.1.a, we could also observe the coexistence of A17 bP and LDL at 0.1 GPa, 914 K. This gives further support to the fact that bP is the thermodynamic stable phase from 0 to 4 GPa along the melting line. An additional melting point was obtained at 5.05 GPa, 1780 K that corresponds to the melting of the A7 solid phase. Using the A17-A7 transition point obtained here at 4.12 GPa, 1375 K, and that previously reported at 5 GPa at 300 K[2], we can infer the position of the A17-A7-HDL triple point at 3.88 GPa, 1615 K. There seems to be a slight increase in the slope of the melting line above this triple point, although this is weakly constrained by our unique melting point.

Table 5.1. Measured melting points of A17 bP, except for the point indicated by * which corresponds to the melting of the A7 solid.

Pressure (GPa)	Temperature (K)	Pressure (GPa)	Temperature (K)
0.10 (3)	914 (25)	1.54 (12)	1355 (30)
0.45 (10)	1050 (25)	1.90 (15)	1435 (30)
0.50 (5)	1042 (25)	2.05 (15)	1414 (35)
0.69 (7)	1088 (30)	2.50 (20)	1492 (30)
0.70 (7)	1129 (30)	2.83 (25)	1498 (30)
0.83 (8)	1176 (30)	3.00 (28)	1483 (30)
0.92 (8)	1205 (30)	3.26 (30)	1527 (35)
0.93 (8)	1200 (30)	3.75 (35)	1637 (45)
1.25 (10)	1330 (30)	5.05 (40)*	1788 (70)*
1.50 (12)	1374 (30)		

The measured melting points of bP are shown in Figure 5.2., and are listed in Table 5.1. The lowest pressure melting point has been observed at 0.1 GPa and 914 K. From the linear extrapolation of our melting curve below 0.1 GPa, the ambient pressure melting point is estimated at 880 ± 15 K in good agreement with the extrapolation to zero of ref[28,30-31]. Within present uncertainties, the melting temperature increases linearly with pressure and exhibits two distinct pressure regimes. Indeed, the slope of the melting curve is suddenly and significantly modified at the LLSTP, changing from 348 ± 21 K·GPa^{-1} to 105 ± 12 K·GPa^{-1} below and above the LLSTP respectively. This abrupt reduction by a factor ~3.3 is likely due to the large local atomic order difference between the LDL and HDL From the Clausius-Clapeyron relation[49,50], significant differences in the associated melting entropy and volume between the low- and high-pressure regimes (below and above the LLSTP, respectively) may thus be expected. The LLSTP is located at the intersection of the low- and high-pressure melting lines at 1.35 ± 0.15 GPa and 1350 ± 75 K. We note that these P-T coordinates of the LLSTP differ from those that can be inferred from the intersection of the LLT line and the present melting line, which is due to the difference in P-T metrology used in the two studies. In Figure 5.2., the LLT line was thus constructed using the presently determined position of the LLSTP, and the slope of the LLT line we report in the next Chapter.

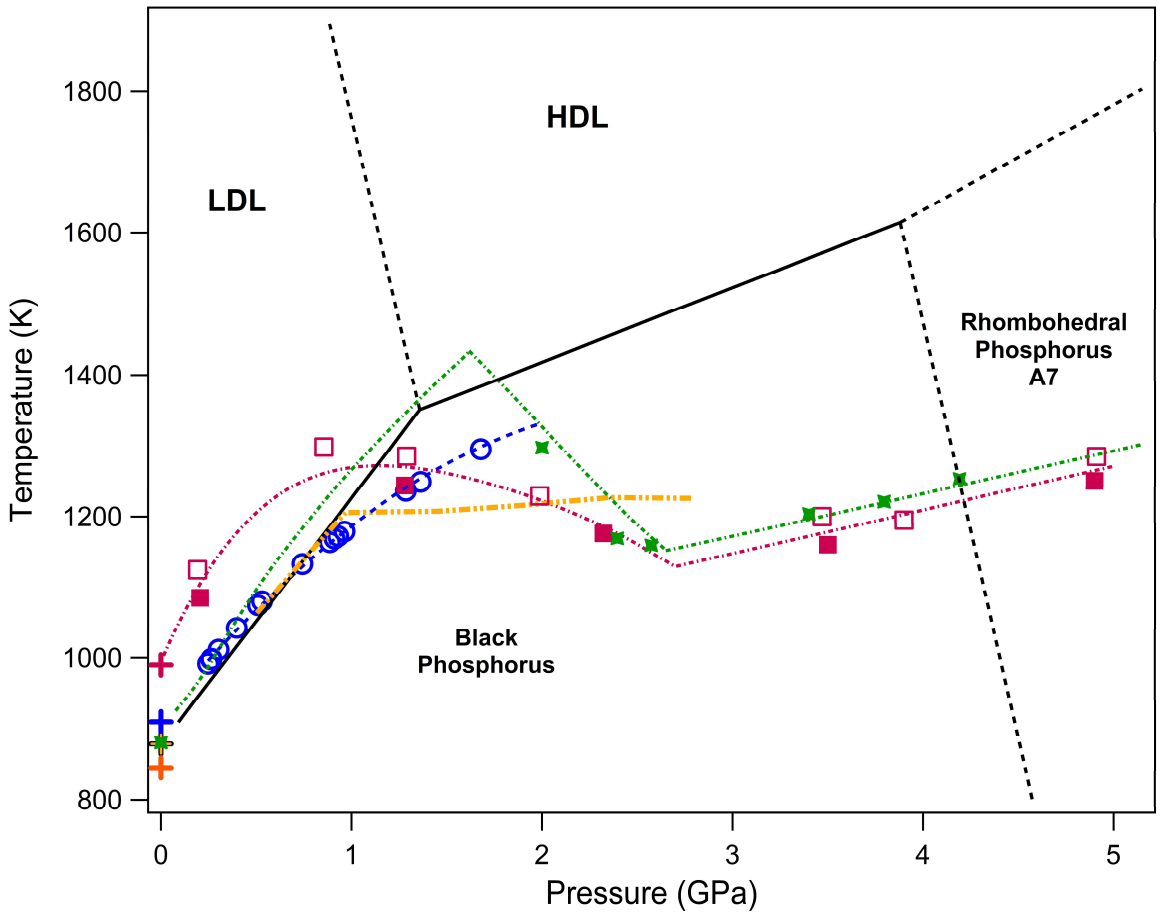

Figure 5.3. Comparison between the melting curve of bP from this work (black line) and the melting curve from Akahama et al[29] (red dashed line and symbols), Marani and Guarise[28] (blue dashed line and symbols), Mizutani et al[30] (yellow dashed line) and Solozhenko et al[31] (green dashed line and symbols). Plain and empty squares denote respectively the solid and liquid state. The colored crosses indicate the melting temperatures obtained by extrapolation of the various melting curves to ambient pressure.

A comparison of the bP melting curve determined in this study with literature data is shown in Figure 5.3. Large disagreements appear between these different works and the one presented here. These are most probably due to a variety of experimental problems which are discussed in the following. The melting curve reported by Marani and Guarise[28] was determined by electric resistivity measurements. It agrees fairly well with our results up to ~1 GPa but deviates from them at higher pressures. Indeed, no break in slope is highlighted and the melting curve of Marani and Guarise appears to follow a monotonous quadratic variation. Moreover, no data was collected above 1.6 GPa, which does not allow for a complete comparison. The deviation observed above 1 GPa is probably due to the inaccuracy of the temperature

measurement of the electric resistivity method at high pressure. Indeed, this technique does not consider the effects of pressures on the temperature probe (thermocouple) which are nevertheless significant[52]. The three other reported works[29-31] were carried out by the same method using *in situ* energy dispersive x-ray diffraction in multi-anvil presses[33]. However, these studies have led to widely divergent results. Akahama et al.[29] reported a maximum of the melting curve around 1 GPa, followed by a reduction of the melting temperature toward the triple point between the HDL, orthorhombic bP and the rhombohedral A7 phase located around 2.7 GPa and 1100 K. In a more recent work, Solozhenko et al.[31], have obtained qualitatively similar results but with a much sharper slope of the melting curve in the low-and high-pressure regimes despite the absence of data points near the LLSTP. In Mizutani et al.[30], in agreement with the current work, a break in the slope of the melting curve is observed around 1 GPa. However, the reported slope in the high-pressure regime differs from our result by one order of magnitude ($dT/dP = 105 \pm 12$ K·GPa^{-1} and $dT/dP = 15$ K·GPa^{-1}, in this work and Mizutani et al.[30], respectively). The diverging results could be explained by 3 main reasons. As for the work of Marani and Guarise[28] a thermocouple was employed as temperature sensor and the significant pressure effect was neglected. The second potential source of imprecision originates from the employed melting criterion based on the energy dispersive x-ray diffraction (EDX) method. Indeed, in the EDX method, the x-ray detection is carried out using a single point detector[53] that intercepts only a very small fraction of the photons diffracted by the sample. At high temperature and more particularly near the melting point, it is well known[54-55] that materials undergo strong recrystallization effects. This, in turn, transform a randomly oriented x-ray powder patterns into highly oriented diffraction spots that occupy a much smaller fraction of the Debye-Scherrer rings. Contrary to the present work, the employed melting criterion in[31] is solely based on the disappearance of the Bragg reflections. This could lead to an incorrect determination of melting as it can be confused with recrystallization. The third problem resides the low number of collected data in the previous studies. For example, in the references[29],[31] less than 5 melting points are determined while 19 data points are reported here. Another fundamental advantage of the current study is related to the employed metrology. As explained in the method section and detailed in ref[22], we used the anisotropic properties of the sample itself to simultaneously extract *P* and *T* with very good precision. As the bP sample is used as *P,T* sensor, this method also guarantees the absence of pressure and temperature gradients, which is not the case with the other methods mentioned above. Indeed, in multi-anvil presses[33], the pressure calibrant and the temperature probe is located at a finite distance (typically 1 mm) from the sample, which inevitably results in larger systematic errors.

In complement to determining the melting curve, we have studied the reversibility of the transition by *in situ* characterization of the crystal structure of the solids recovered after temperature quenching of the melt. As shown in Figure 5.4.b, on quenching the HDL from P-T conditions above the LLSTP, the Bragg reflections of the orthorhombic bP solid are recovered, thus confirming that HDL crystallizes into bP in agreement with previous reports[29, 56]. By contrast, starting from the LDL at pressures below the LLSTP, the recovered solid phase at ambient conditions displays a XRD pattern which is different and much more complex from the one of bP, as briefly reported in[29]. The Le Bail refinement of this XRD pattern (see Fig. 4a) shows that the structure of the recovered solid is compatible with the aP42 structure of fibrous red phosphorus (rP)[57]. The large texture of the quenched solids, observable in the middle panels of Figure 5.4., prohibits any Rietveld refinement. The refined unit-cell parameters for aP42 rP are listed in Table 5.2. and compared with the literature data[57]. The 1-3 % mismatch in the lattice parameters and volume may either indicate residual temperature in the solid after quenching or that the structure is different from aP42. We also attempted to fit the XRD pattern using the monoclinic structure of Hittorf's violet phosphorus (see Chapter 1) but they did not match. The reversibility of melting above the LLSTP suggests a proximity of the local order in HDL and bP, while its irreversibility below the LLSTP shows that the local atomic arrangement in LDL differs strongly from that in bP. Indeed, in such case we may expect a large surface energy between LDL and bP, which makes the nucleation of bP unfavored compared to red P. A similar case has been reported in water: when it is supercompressed at 1.7 GPa, it crystallizes into the metastable ice VII rather than the stable ice VI due to a smaller liquid/ice VII surface energy[58]. A more detailed study of the quenched solid and of its melting line should however be undertaken to better understand the irreversible character of the melting of bP below the triple point and will be the subject of future works. The different nature of the quenched products of LDL and HDL indirectly confirms that the local atomic arrangement in these two liquid phases is substantially different.

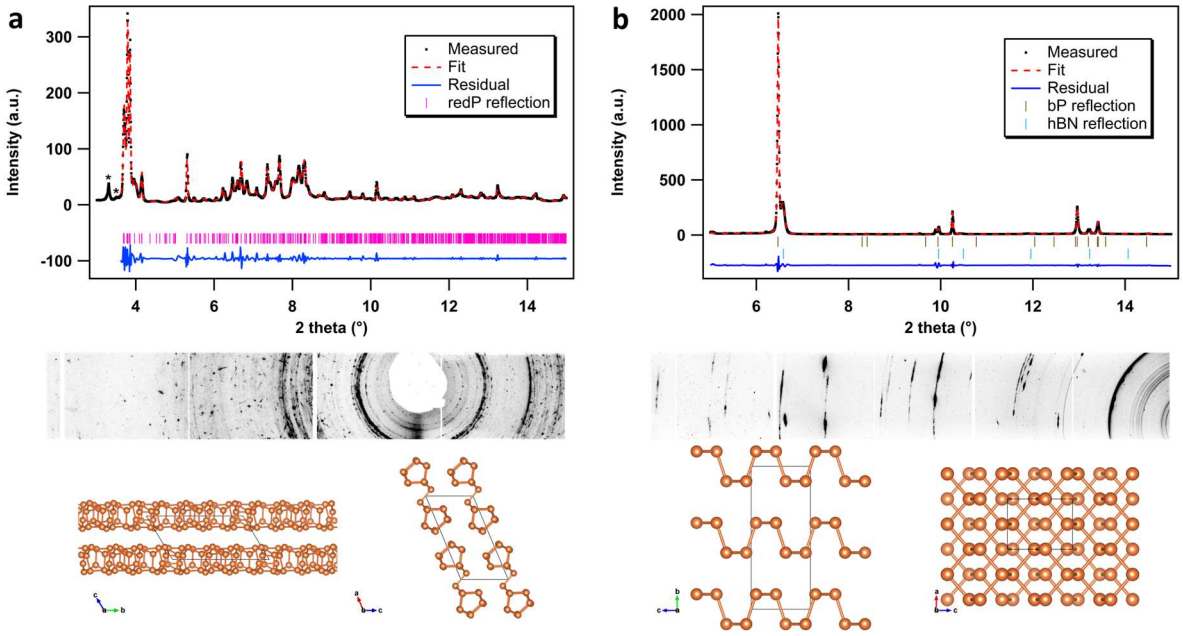

Figure 5.4. *Upper panels*: XRD patterns of the solid phases obtained by temperature quenching (a) the LDL from 0.5 GPa and 1060 K to ambient P-T conditions, and (b) the HDL from 2.25 GPa and 1455 K to 1 GPa and 400 K. The x-ray wavelength is 0.3738 Å. The red curves are Le Bail refinement of the patterns using the (a) aP42 rP and (b) A17 bP structures. The blue line is the fit residual and ticks indicate the position of the Bragg reflections. *Middle panels*: respective XRD images. *Lower panels*: crystalline structures of (a) aP42 rP and (b) A17 bP viewed along two different crystallographic directions.

Table 5.2. Refined unit cell parameters of aP42 red phosphorus and A17 black phosphorus from this study and from the literature.

Phase	**a (Å)**	**b (Å)**	**c (Å)**	**α (°)**	**β (°)**	**γ (°)**	**V (Å^3)**	**Conditions**
aP42 - This work	12.291(10)	13.043(6)	7.168(7)	117.42(4)	108.60(7)	95.04(6)	928.4(13)	P_{atm} / 400 K
aP42 - Ruck et al.[56]	12.198(8)	12.986(8)	7.075(7)	116.99(7)	106.31(7)	97.91(7)	911.25	Ambient
A17 – This work	3.3180(10)	10.323(2)	4.312(1)	90	90	90	147.7(1)	1 GPa / 400 K
A17 – Akahama et al.[19]	3.31408(6)	10.3146(2)	4.30779(8)	90	90	90	147.26(1)	0.99 GPa / 300 K

2. Thermodynamics of melting

Phase transitions are fascinating phenomena at the heart of condensed matter physics. Among them, melting is a very common and intuitive first-order transformation that is associated with a change in density and enthalpy. Despite this apparent simplicity, melting is an extremely complex many body and multiscale problem for which the exact microscopic mechanisms are still largely elusive[59]. For most materials, the density change at melting is negative (expansion) and ranges from 2 to 6 %. A few materials, such as silicon, exhibit slightly larger values up to 12 % and an increase in density at melting[60]. Here we report combined *in situ* x-ray diffraction and density measurements along the melting line of black phosphorus.

As shown in Figure 5.5., we have established that the large structural difference and the existence of a first-order phase transition between the two liquids give rise to a strong discontinuity in the slope of melting line. Below the liquid-liquid-solid triple point (LLSTP) which is located at 1.35 GPa and 1350 K, this slope is very steep (348 $K \cdot GPa^{-1}$) while beyond the LLSTP, it is reduced by a factor of ~3 (105 $K \cdot GPa^{-1}$). This suggests a peculiar melting behavior of bP, but so far no *in situ* density measurements have been conducted along the melting line of bP to determine the density jump at melting, and through the Clausius-Clapeyron relation[49-50], the associated melting entropy and enthalpy.

We performed *in situ* x-ray diffraction and absorption measurements at the beamline ID27[34] of the European Synchrotron Radiation Facility (ESRF) to accurately determine the density, entropy and enthalpy discontinuity at melting in bP in the *P–T* range 0–5 GPa and 800–1,700 K. The *P–T* pathways are presented in the experimental phase diagram of phosphorus in Figure 5.5.

The solid and molten states of bP were characterized *in situ* in a Paris–Edinburgh press[35-37]. The concomitant disappearance of the Bragg reflections from solid bP and appearance of a strong diffuse x-ray scattering signal from liquid P was employed as unambiguous melting criteria[46-48]. Density measurements were performed at pressures below and above the LLSTP, respectively. The accuracy of the density measured by this method ranging from 1 to 5%[25], depending on the sample, a value that is much smaller than the density jumps observed in this work. X-Ray diffraction patterns of solid and liquid phosphorus were also collected at each *P–T* point to characterize the nature of the liquid (LDL or HDL). The

XRD patterns of solid bP were also employed to extract the pressure and temperature with an accuracy of ±25 K and ±0.1 GPa following the procedure detailed in Chapter 3.

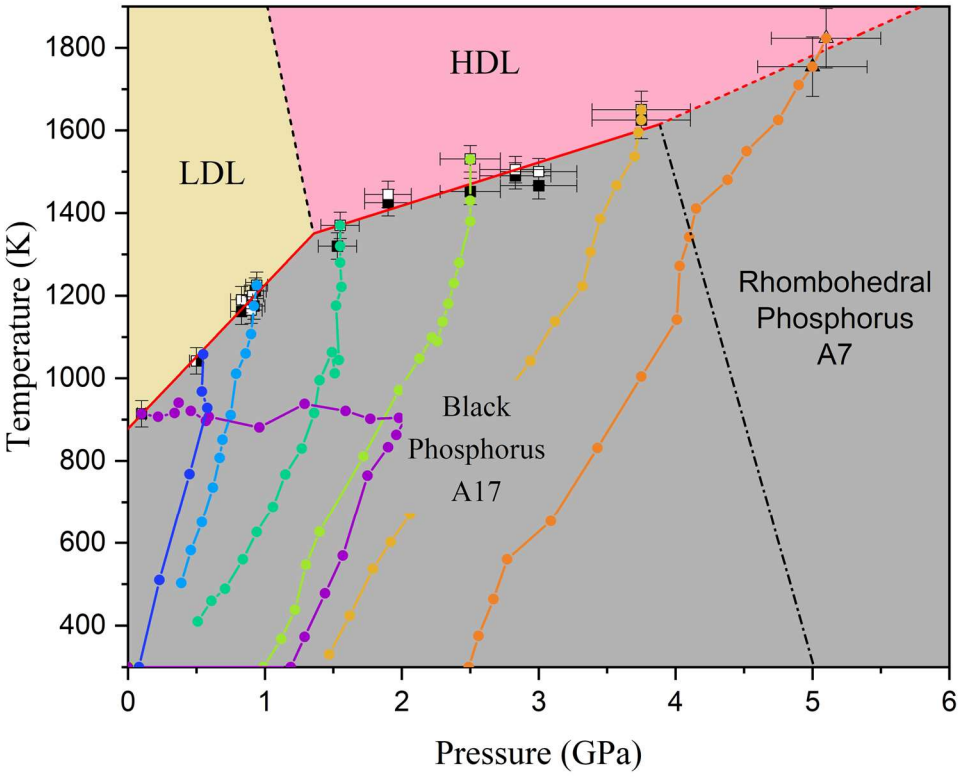

Figure 5.5. Melting line and pressure-temperature locations of the collected x-ray absorption data points in the phase diagram of phosphorus. The white and black symbols correspond to the liquid and solid states, respectively.

Examples of x-ray absorption profiles (XAPs) and corresponding XRD patterns at pressures below and above the LLSTP are presented in Figure 5.6. From the XAPs, we have accurately determined the relative density discontinuity at melting ($\Delta\rho/\rho=\rho_l-\rho_s/\rho_s$, where the indices *s* and *l* stand for the solid and liquid state, respectively). As presented in Figure 5.7. and Table 5.3., a colossal density jump $\Delta\rho/\rho$ of up to 60 % is observed when the melting line is crossed towards the stability field of the LDL at 0.1 GPa and 914 K. This colossal $\Delta\rho/\rho$ at melting and the weakness of van der Waals type inter-plane interactions are likely to induce mechanical instabilities in the crystal structure of bP at pressures below 0.1 GPa. These are probably responsible for the reported decomposition of this material[23-24] at ambient pressure and high temperature (T > 600 K). As shown in Figure 5.6., the measured structure factors *S(Q)*

in the low- and high-pressure regimes exhibit strong short-range correlations typical of a liquid. The calculated liquid densities are close to that of water (ρ_l=1.22 (10) g.cm^{-3} at 0.1 GPa and 914 K), thus ruling out a direct transformation to a gas state. In addition, the density reduction involved in a sublimation process is normally much larger, typically 5.10^4 %, i.e. 3 orders of magnitude greater than what we have measured. When increasing pressure, the amplitude of the density discontinuity decreases substantially but remains very large. At P=0.92 GPa and T=1205 K, bP still undergoes a density jump of more than 37 %. The reduction of the density jumps with pressure is likely due to the high compressibility of liquid phosphorus relatively to that of the solid in the low-pressure regime. In contrast, beyond the LLSTP, a normal melting behaviour was observed. Indeed, standard density changes of less than 7 % were measured when the melting line was crossed towards the HDL.

Table 5.3. Pressure and temperature locations of the density measurements, and corresponding density, entropy and enthalpy jumps at melting. The P-T marked with an asterisk correspond to the melt from the A7 phase.

P (GPa) / T (K)	ρ solid (g.cm^{-3})	ρ liquid (g.cm^{-3})	Δρ/ρ (%)	ΔS (J.K^{-1}.mol^{-1})	L (kJ.mol^{-1})
0.1 / 914	2.61 (6)	1.04 (3)	60 (2)	52 (7)	47 (9)
0.545 / 1013	2.59 (6)	1.31 (4)	49 (3)	34 (5)	34 (7)
0.92 / 1205	2.68 (10)	1.55 (7)	42 (3)	24 (6)	29 (8)
0.93 / 1200	2.52 (7)	1.59 (5)	37 (4)	21 (4)	25 (6)
1.54 / 1355	2.78 (5)	2.59 (5)	7 (4)	8 (6)	11 (8)
1.9 / 1445	2.67 (7)	2.66 (6)	1 (7)	1 (6)	1 (9)
2.5 / 1491	2.81 (6)	2.73 (5)	3 (5)	3 (5)	5 (8)
2.83 / 1497	2.87 (5)	2.81 (5)	2 (4)	2 (5)	3 (7)
2.945 / 1516	2.89 (6)	2.85 (4)	1 (4)	1 (4)	2 (7)
3 / 1483	2.95 (6)	2.90 (6)	2 (4)	2 (5)	3 (8)
3.75 / 1637	2.95 (6)	2.89 (6)	2 (4)	2 (5)	3 (8)
5.05 / 1788*	3.28 (11)	2.98 (9)	9 (5)	-	-

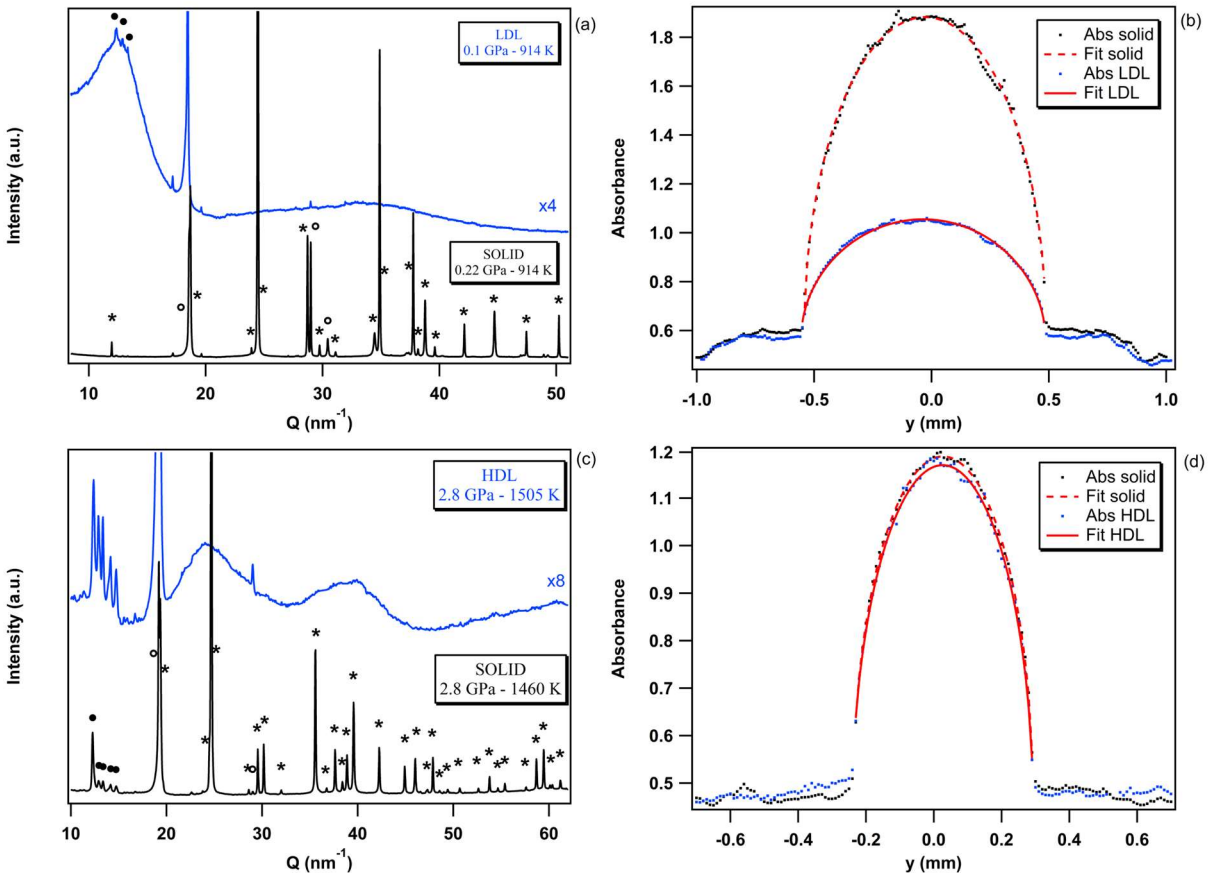

Figure 5.6. XRD patterns of solid and liquid phosphorus and corresponding x-ray absorption profiles at pressures below and above the liquid-liquid-solid triple point. (a) and (c) x-ray diffraction patterns of solid and liquid phosphorus below and above the LLSTP, respectively. (b) and (d) x-ray absorption profiles of solid and liquid phosphorus below and above the LLSTP, respectively.

Using the Clausius-Clapeyron relation[49-50] and the melting slopes accurately established in the previous section, we have determined the melting entropy ΔS and latent heat L associated to the transformation. Here again, very large values of ΔS and L have been obtained for melting below the triple point, whereas standard values of ΔS and L are reached for melting beyond the triple point (Figure 5.7. and Table 5.3.). It is also worth noting the strong effect of pressure on these quantities in the low-pressure regime. Indeed, ΔS and L are reduced by a factor of ~2 by applying a moderate pressure of ~1 GPa. This suggests a direct and strong effect of density on the entropy of the LDL by reducing the number of accessible micro-states in its thermodynamic partition function.

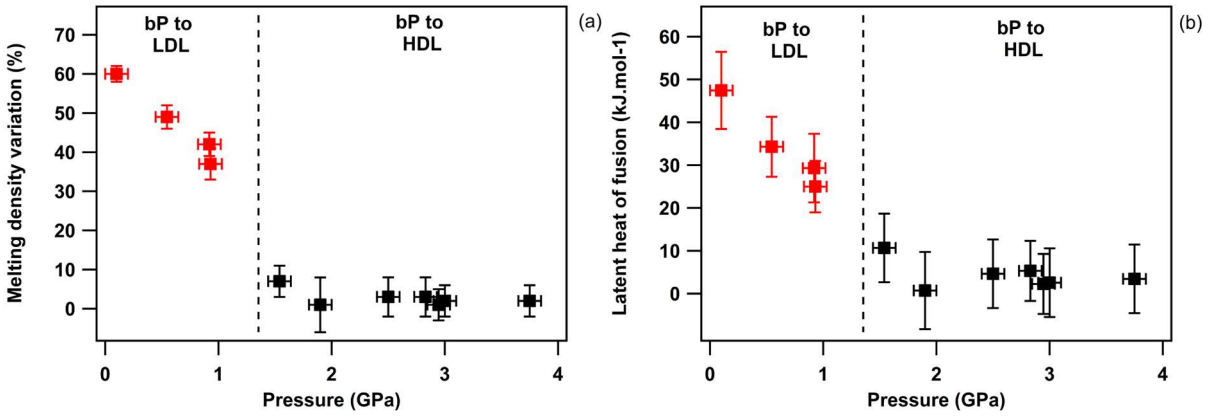

Figure 5.7. Density jump and latent heat variation at melting in the low- and high-pressure regimes.

The comparison between the density and enthalpy jumps at melting for a representative selection of elements and phosphorus is presented in Figure 5.8. The majority of the elements exhibits a negative density variation while few show a density increase at melting. Independently of its sign, this density variation ranges between 1 and 15 % for all the elements. As presented in Figure 5.8, the exceptionally large density discontinuity of more than 60 % observed in phosphorus is a unique case in the periodic table of the elements and, more generally, among all known compounds. The melting of bP is also associated with a very large latent heat variation of up to 48 kJ.mol^{-1} only slightly exceeded by silicon (50.55 kJ.mol^{-1})[61]. For example, the latent heat of melting of ice is 6 kJ.mol^{-1}.[62] This attests to the highly endothermic nature of this reconstructive transformation which consumes a considerable amount of energy. The anomalous behaviour of bP is certainly related to the striking difference in the local atomic arrangement of solid bP and the LDL. In agreement with previous works[26,51], we have observed sharp structural differences between the low- and high-density liquids. In the low-pressure regime below the LLSTP, the structure of liquid P is very similar to that of molecular white-P liquid[26]. As shown in Figure 5.6., it exhibits a first sharp diffraction peak (FSDP) at 14 nm^{-1}, which is a manifestation of intermediate-range order on length scales larger than those typical of nearest-neighbour distances[63]. In phosphorus, it is related to medium range order correlations of the tetrahedral P_4 units present in the liquid state at low pressure[26]. As reported by Katayama et al.[26] and Monaco et al.[51], the associated pair distribution function (PDF) exhibits one well defined peak at 2.14 Å corresponding to the first neighbor distance of the P_4 molecules. A sudden and drastic reduction of the intensity of the FSDP is observed in the structure factor of the HDL phase, in full agreement with earlier reports[26,51]. The PDF of

the HDL exhibits more extended correlations than the LDL and displays four distinct peaks at distances of 2.23 Å, 3.49 Å, 5.26 Å and 6.52 Å with 3.6 and 13 atoms in the first and second coordination shell[26,64], respectively. From *ab initio* molecular dynamics simulations, Zhao et al.[65] have suggested that the local structure of the HDL is similar to that of bP. This would explain the standard and relatively low density change at melting in the P-T regime beyond the LLSTP.

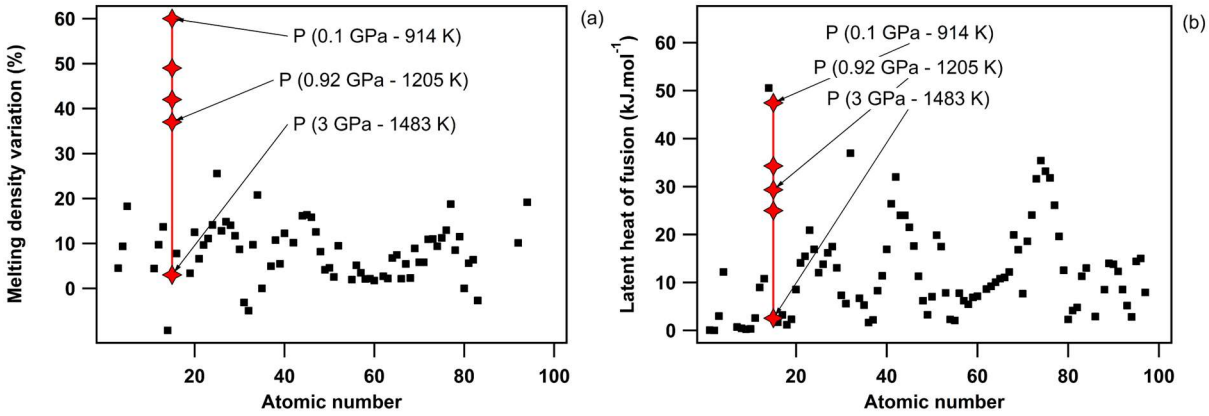

Figure 5.8. (a) Comparison of the density jumps and (b) latent heat at melting of selected elements (black squares) and phosphorus (red symbols).

Conclusion

In this Chapter, we employed *in situ* high-resolution x-ray diffraction to accurately determine the melting curve of bP in an extended *P,T* range up to 5 GPa and 1700 K, and to characterize the reversibility of the liquid to solid transformation. The melting curve was determined with unparalleled accuracy using an original metrology which takes full advantage of the exceptional anisotropic properties of bP[2,22]. This enabled the simultaneous and accurate measurement of *P* and *T* using the sample itself as *P,T* sensor, ensuring the absence of significant *P,T* gradients in the sample volume probed by the x-ray beam. Based on this experimental approach, two distinct regimes of melting, corresponding to the low- and high-density liquid were observed, allowing the precise determination of the triple point between the LDL, HDL and crystalline bP in the *P,T* phase diagram of P. The very contrasting slope of the melting curve indirectly confirms the striking difference in the local atomic arrangement of the LDL and HDL, as evidenced by the irreversible nature of the transformation in the low-pressure regime, where the low-density liquid obtained by melting bP irreversibly crystallizes into rP. This suggests that the local order in the LDL, currently considered as composed of isolated and

weakly bound P_4 molecular units, could have instead a much more complex structure, stimulating further systematic structural studies of the LDL and of the transition line between the LDL and HDL. At pressures below the LLSTP, we found a colossal jump in density at melting in phosphorus that exceeds by one or two orders of magnitude that measured in any other material. In the high-pressure regime above the LLSTP, a standard melting behaviour is recovered, supporting the idea that solid bP and the HDL are structurally close at short scale. The colossal density jump at low pressure is associated to a very large enthalpy modification, signature of a strongly endothermic reconstructive transformation. The large amplitude of the first-order phase transition may explain the observed instability and subsequent decomposition of bP at ambient pressure and high temperature that was for a long time interpreted as sublimation. We have evidenced a direct effect of density on the entropy of the LDL suggesting a significant reduction of the accessible micro-states with pressure. As phosphorus also exhibits a strongly first-order LDL to HDL transition with a 40% volume change[66], a direct comparison with the thermodynamics of melting could yield significant insights into the intimate nature of the two transformations.

References

1. D. E. C. Corbridge, *Phosphorus: Chemistry, Biochemistry and Technology*, Sixth Edition, Taylor & Francis, New York, 2013.
2. D., Scelta, A. Baldassarre, M. Serrano-Ruiz, K. Dziubek, A. B. Cairns, M. Peruzzini, R. Bini and M. Ceppatelli, The p-sc structure in phosphorus: bringing order to the high pressure phases of group 15 elements. *Chem. Commun.*, 2018, **54**, 10554-10557.
3. D. Corbridge and E. Lowe, Structure of white phosphorus: Single crystal X-ray examination. *Nature*, 1952, **170**, 629.
4. A. Simon, H. Borrmann and H. Craubner, Crystal structure of Ordered White Phosphorus (β-P). *Sulfur Relat. Elem.*, 1987, **30**, 1-2, 507-510.
5. H. Okudera, R. E. Dinnebier and A. Simon, The crystal structure of γ-P4, a low temperature modification of white phosphorus. *Z. Kristallogr.*, 2005, **220**, 259-264.
6. B. V. Shanabrook and J. S. Lannin, Structural and vibrational properties of amorphous phosphorus. *Phys. Rev. B*, 1981, **24**, 4771-4780.
7. S. Elliott, J. Dore and E. Marseglia, The structure of amorphous phosphorus. *J. Phys. Colloques*, 1985, **46**, C8349-C8353.
8. P. Jóvári and L. Pusztai, On the structure of amorphous red phosphorus. *Appl. Phys. A*, 2002, **74**, S1092-S1094.
9. J. M. Zaug, A. K. Soper and S. M. Clark, Pressure-dependent structures of amorphous red phosphorus and the origin of the first sharp diffraction peaks. *Nat. Mater.*, 2008, **7**, 890-899.
10. E. N. Rissi, E. Soignard, K. A. McKiernan, C. J. Benmore and J. L. Yarger, Pressure-induced crystallization of amorphous red phosphorus. *Solid State Comm.*, 2012, **152**, 390-394.
11. Y. Zhou, W. Kirkpatrick and V. L. Deringer, Cluster fragments in amorphous phosphorus and their evolution under pressure. *Adv. Mater.*, 2022, **34**, 2107515.
12. J. C. Jamieson, Crystal structures adopted by black phosphorus at high pressures, *Science*, 1963, **139**, 1291-1292.
13. W. Crichton, M. Mezouar and G. Monaco, Phosphorus: New in situ powder data from large-volume apparatus. *Cambridge Univ. Press. Power Diffr.*, 2003, **18**, 155-158.
14. D. Scelta, A. Baldassarre, M. Serrano-Ruiz, K. Dziubek, A. B. Cairns, M. Peruzzini, R. Bini and M. Ceppatelli, Interlayer bond formation in black phosphorus at high pressure. *Angew. Chem. Int. Ed.*, 2017, **56**, 14135-14140.

15. P. W. Bridgman, Two new modifications of phosphorus. *J. Am. Chem. Soc.*, 1914, **36**, 7, 1344-1363.
16. R. Hultgren, N. S. Gingrich and B. E. Warren, The atomic distribution in red and black phosphorus and the crystal structure of black phosphorus. *J. Chem. Phys.*, 1935, **3**, 351-355.
17. A. Brown and S. Rundqvist, Refinement of the crystal structure of black phosphorus. *Acta. Crystallogr.*, 1965, **19**, 684-685.
18. T. Kikegawa and H. Iwasaki, An X-ray diffraction study of lattice compression and phase transition of crystalline phosphorus. *Acta Cryst.*, 1983, B**39**, 158-164.
19. Y. Akahama, M. Miyakawa, T. Taniguchi, A. Sano-Furukawa, S. Machida and T. Hattori, Structure refinement of black phosphorus under high pressure. *J. Chem. Phys.*, 2020, **153**, 014704.
20. L. Cartz, S. R. Srinivasa, R. J. Riedner, J. D. Jorgensen and T. G. Worlton, Effect of pressure on bonding in black phosphorus. *J. Chem. Phys.*, 1979, **71**, 1718.
21. S. Appalakondaiah, G. Vaitheeswaran, S. Lebègue, N. E. Christensen and A. Svane, Effect of van der Waals interactions on the structural and elastic properties of black phosphorus. *Phys. Rev. B*, 2012, **86**, 035105.
22. H. Muhammad, M. Mezouar, G. Garbarino, T. Poręba, G. Confalonieri, M. Ceppatelli, M. Serrano-Ruiz, M. Peruzzini and F. Datchi, Anisotropic thermo-mechanical response of layered hexagonal boron nitride and black phosphorus: application as a simultaneous pressure and temperature sensor. arXiv:2307.07533 , 2023**.**
23. W. Luo, R. Yang, J. Liu, Y. Zhao, W. Zhu and G. M. Xia, Thermal sublimation: a scalable and controllable thinning method for the fabrication of few-layer black phosphorus. *Nanotechnology*, 2017, **28**, 285301.
24. L. Henry, V. Svitlyk, M. Mezouar, D. Sifré, G. Garbarino, M. Ceppatelli, M. Serrano-Ruiz, M. Peruzzini and F. Datchi, Anisotropic thermal expansion of black phosphorus from nanoscale dynamics of Phosphorene layers. *Nanoscale*, 2020, **12**, 4491-4497.
25. L. Henry, M. Mezouar, G. Garbarino, D. Sifré, G. Weck and F. Datchi, Liquid-liquid transition and critical point in sulfur. Nature, 2020, 584, 382-386.
26. Y. Katayama, T. Mizutani, W. Utsumi, O. Shimomura, M. Yamakata and K. Funakoshi, A first-order liquid-liquid phase transition in phosphorus. *Nature*, 2000, **403**, 170-173.
27. Y. Senda, F. Shimojo and K. Hoshino, The metal-nonmetal transition of liquid phosphorus by ab initio molecular dynamics simulations. *J. Phys.: Condens. Matter*, 2002, **14**, 3715-3723.

28. A. Marani and G. B. Guarise, Fusione del fosforo nero fino a 16.000 atm. *Chim. Ind.*, 1968, **50**, 663-665.
29. Y. Akahama, W. Utsumi, S. Endo, T. Kikegawa, H. Iwasaki, O. Shimomura, T. Yagi and S. Akimoto, Melting curve of black phosphorus, *Phys. Let. A*, 1987, **122**, 129-131.
30. T. Mizutani, Y. Katayama, W. Utsumi, K. Funakoshi, M. Yamakata and O. Shimomura, Anomaly in the melting curve of black phosphorus associated with a liquid-liquid transition. *Science Technol. High Press. (Proceedings of AIRAPT-17)*, 2000, 525-528.
31. V. L. Solozhenko and V. Turkevich, P-T phase diagram of phosphorus revisited. *J. Phys. Chem. C*, 2023, **127**, 12, 6088-6092.
32. P. W. Bridgman, The technique of high pressure experimenting, *Proc. Am. Acad. Arts Sci.*, 1914, **49**, 11, 627-643.
33. N. Kawai, M. Togaya and A. Onodera, A new device for pressure vessels. *Proc. Jpn. Acad.*, 1973, **49**, 8, 623-626.
34. T. Poręba, D. Comboni, M. Mezouar, G. Garbarino and M. Hanfland, Tracking structural phase transitions via single crystal x-ray diffraction at extreme conditions: advantages of extremely brilliant source. *J. Phys. Condens. Matter*, 2022, **35**, 054001.
35. J. M. Besson, G. Hamel, P. Grima, R. J. Nelmes, J. S. Loveday, S. Hull and D. Häusermann, A large volume pressure cell for high temperatures. *High Press. Res.*, 1992, **8**, 625.
36. S. Klotz, Th. Strässle, G. Rousse, G. Hamel and V. Pomjakushin, Angle-dispersive neutron diffraction under high pressure to 10 GPa. *Appl. Phys. Lett.*, 2005, **86**, 031917.
37. G. Morard, M. Mezouar, N. Rey, R. Poloni, A. Merlen, S. Le Floch, P. Toulemonde, S. Pascarelli, A. San Miguel, C. Sanloup and G. Fiquet, Optimization of Paris-Edinburgh press cell assemblies for *in situ* monochromatic X-ray diffraction and X-ray absorption. *High Press. Res.*, 2007, **27**, 223.
38. M. Serrano-Ruiz, M. Caporali, A. Ienco, V. Piazza, S. Heun and M. Peruzzini, The role of water in the preparation and stabilization of high-quality Phosphorene flakes. *Adv. Mater. Interfaces*, 2016, **3**, 1500441.
39. M. Mezouar, T. Le Bihan, H. Libotte, Y. Le Godec and D. Häusermann, Paris-Edinburgh large-volume cell coupled with a fast imaging-plate system for structural investigation at high pressure and high temperature. *J. Synchrotron Radiat.*, 1999, **6**, 1115.
40. G. Morard, M. Mezouar, S. Bauchau, M. Álvarez-Murga, J. -L Hodeau and G. Garbarino, High efficiency multichannel collimator for structural studies of liquids and low-Z materials at high pressures and temperatures. *Review of Scientific Instruments*, 2011, **82**, 023904.

41. G. Ashiotis, A. Deschildre, Z. Nawaz, J. P. Wright, D. Karkoulis, F. E. Picca and J. Kieffer, The fast azimuthal integration Python library: pyFAI. *Journal of applied crystallography*, 2015, **48**, 510-519.
42. C. Prescher and V. B. Prakapenka, DIOPTAS: A program for reduction of two-dimensional X-ray diffraction data and data exploration. *High. Press. Res.*, 2015, **35**, 223-230.
43. B. H. Toby, EXPGUI, a graphical user interface for GSAS. *Journal of applied crystallography*, 2001, **34**, 210-213.
44. A. Le Bail, H. Duroy and J. L. Fourquet, *Ab-initio* structure determination of $LiSbWO_6$ by X-ray powder diffraction. *Materials Research Bulletin*, 1988, **23**, 447-452.
45. F. Birch, Finite elastic strain of cubic crystals, *Phys. Rev.*, 1947, **71**, 809-824.
46. J. -A Queyroux, S. Ninet, G. Weck, G. Garbarino, T. Plisson, M. Mezouar and F. Datchi, Melting curve and chemical stability of ammonia at high pressure: a combined X-ray diffraction and Raman study. *Phys. Rev. B*, 2019, **99**, 134107.
47. A. Dewaele, M. Mezouar, N. Guignot and Paul Loubeyre, Melting of lead under high pressure studied using second-scale time-resolved X-ray diffraction. *Phys. Rev. B*, 2007, **76**, 144106.
48. S. Anzelline, D. Alfé, M. Pozzo and D. Errandonea, Melting line of calcium characterized by *in situ* LH-DAC XRD and first-principles calculations. *Sci. Rep.*, 2021, **11**, 15025.
49. R. Clausius, Ueber die bewegende Kraft der Wärme und die Gesetze, welche sich daraus für die Wärmelehre selbst ableiten lassen. *Annalen der Physik* (in German), 1850, **155**, 368-397.
50. M. C. Clapeyron, Mémoire sur la puissance motrice de la chaleur. *Journal de l'École polytechnique* (in French), 1834, **23**, 153-190.
51. G. Monaco, S. Falconi, W. A. Crichton and M. Mezouar, Nature of the First-Order Phase Transition in Fluid Phosphorus at High Temperature and Pressure. *Phys. Rev. Lett.*, 2003, **90**, 255701.
52. G. C. Kennedy and R. C. Newton, The effect of pressure on the electromotive force of a platinum-bismuth thermocouple. *J. Geophys. Res.*, 1961, **66**, 1491-1493.
53. A. J. Dicken, J. P. O. Evans, K. D. Rogers, C. Greenwood, S. X. Godber, D. Prokopiou, N. Stone, J. G. Clement, I. Lyburn, R. M. Martin and P. Zioupos, Energy-dispersive X-ray diffraction using an annular beam. *Opt. Express*, 2015, 23, 13443-13454.
54. S. Anzellini, A. Dewaele, M. Mezouar, P. Loubeyre and G. Morard, Melting of iron at Earth's inner core boundary based on X-ray diffraction, *Science*, 2013, **340**, 464-466.

55. A. Dewaele, M. Mezouar, N. Guignot and P. Loubeyre, High Melting Points of Tantalum in a Laser-Heated Diamond Anvil Cell, *Phys. Rev. Lett.*, 2010, **104**, 255701.
56. S. Endo, Y. Akahama, S. Terada and S. Narita, Growth of large single crystals of black phosphorus under high pressure. *Jpn. J. Appl. Phys.*, 1982, **21**, L482.
57. M. Ruck, D. Hoppe, B. Wahl, P. Simon, Y. Wang and G. Seifert, Fibrous red phosphorus. *Angew. Chem. Int. Ed.*, 2005, **44**, 7616-7619.
58. G. W. Lee, W. J. Evans and C. -S. Yoo, Crystallization of water in a dynamic diamond-anvil cell: Evidence for ice VII-like local order in supercompressed water. *Phys. Rev. B*, 2006, **74**, 134112.
59. A. Samanta, M. E. Tuckerman, T. -Q. Yu and E. Weinan, Microscopic mechanisms of equilibrium melting of a solid, *Science*, 2014, **346**, 729–732.
60. V. M. Glazov and O. D. Shchelikov, Volume Changes during Melting and Heating of Silicon and Germanium Melts., *High Temperature*, 2000, **38**, 405-412.
61. C. Zhou and S. Wu, Medium- and high-temperature latent heat thermal energy storage: Material database, system review and corrosivity assessment. *Int. J. Energy Res.*, 2019, **43**, 621-661.
62. H. Kumano, T. Asaoka, A. Saito and S. Okawa, Study on latent heat of fusion of ice in aqueous solutions. *Int. J. Refrig.*, 2007, **30**, 267-273.
63. C. Massobrio and A. Pasquarello, Origin of the first sharp diffraction peak in the structure factor of disordered network-forming systems: Layers or voids? *J. Chem. Phys.*, 2001, **114**, 7976-7979.
64. S. Falconi, W. A. Crichton, M. Mezouar, G. Monaco and M. Nardone, Structure of fluid phosphorus at high temperature and pressure: An x-ray diffraction study. *Phys. Rev. B*, 2004, **70**, 144109.
65. G. Zhao, H. Wang, D. M. Hu, M. C. Ding, X. G. Zhao and J. L. Yan, Anomalous phase behavior of first-order fluid-liquid phase transition in phosphorus. *J. Chem. Phys.*, 2017, **147**, 204501.
66. Y. Katayama, Y. Inamura, T. Mizutani, M. Yamakata, W. Utsumi, O. Shimomura, Macroscopic separation of dense fluid phase and liquid phase of phosphorus. *Science*, 2004, **306**, 848-851.

Chapter 6:
Liquid-liquid transition in phosphorus

This Chapter reports on our experimental exploration of liquid phosphorus within the pressure-temperature range of 0 – 4 GPa and 800 – 2500 K, focusing on the liquid-liquid transition.

In Chapter 1, we outlined some unresolved questions regarding the liquid-liquid transition (LLT) in phosphorus. In particular, theoretical investigations have suggested that the density variation across the transition initially increases with rising temperature and decreasing pressure and then decreases to ultimately converge to zero, indicative of the presence of a liquid-liquid critical point (LLCP) concluding the transition boundary. Prior to this work, only one measurement of density variation across this transition had been conducted at 1 GPa and 1300 K. Here, we report new measurements of both the transition line and of the associated density jump, extending from 1500 to 2550 K. These do not show the expected downturn of the density change, thus questioning the existence of the LLCP. Furthermore, we find that the energetics of the transition is very similar to that of the melting of bP, which suggests a similarity in the nature of the two transformations. In a second part, we present viscosity measurements for both liquid phases that bring further insights into the nature and behaviors of the two liquids.

1. Thermodynamics of the liquid-liquid transition in phosphorus

1.1. Introduction

Liquid-liquid transition (LLT) is an intriguing phenomenon in which a pure liquid transforms into another via a first-order phase transition[1]. Due to their counterintuitive nature, LLTs have puzzled scientists for decades and challenged our perception of the liquid state, for which the notion of polymorphism has long been considered impossible. LLTs have been predicted from computer simulations of several systems[2-7] and have been the subject of much debate in the case of water[8-12]. So far however, experimental evidence remains scarce and often controversial because it mainly concerns supercooled, i.e. metastable, liquids in which LLT occurs simultaneously with crystallization, making it difficult to separate the two phenomena. A liquid-liquid critical point (LLCP), similar to the well-known gas-liquid critical point, has

been predicted at the end of the LLT line in some cases[8,13-14], but until the recent work on sulfur[15] it has never been observed in any material. In the case of water, this putative LLCP has been invoked to understand thermodynamic anomalies in the supercooled regime[10].

Among the few systems for which a LLT transition has been reported in their pressure-temperature (*P,T*) stability domain, phosphorus has been one of the most theoretically and experimentally investigated[13-14,16-20]. This is certainly due to the spectacular nature of the strongly first-order LLT in this compound that is accompanied by a very clear change in its atomic structure factor[16] and a very significant change in density[17]. This transition occurs in a relatively easily accessible *P,T* region, which makes it an ideal object of study. The position and slope of the LLT line, the structure of low- (LDL) and high-density liquid (HDL) have been reported experimentally[20] and through molecular dynamics *ab initio* simulations[14]. The existence of a liquid-liquid critical point similar to the one experimentally observed in sulfur has also been predicted[13-14]. In addition, in Chapter 5, we have evidenced a colossal density discontinuity of up to 60 % at melting resulting from the striking difference between the local atomic arrangements in the solid and liquid phase. This value is 1 order of magnitude larger than that observed at melting for any materials. Despite all these works, important uncertainties remain regarding the thermodynamics and driving forces of this transition. In addition, no systematic density measurements have been performed along the LLT line. Another important trigger for this study resides in the possibility to carry-out a direct comparison between the thermodynamics of the LLT and melting. Here, we performed combined *in situ* x-ray diffraction and absorption experiments to determine accurately the evolution of the density discontinuity and latent heat associated to the transformation over an extended pressure-temperature region and search for the predicted liquid-liquid critical point. In turn, all this information will be exploited to better understand the intimate nature of the LLT in phosphorus.

1.2. Additional experimental details

All experimental runs were carried out using the Paris-Edinburgh press[21-23] and the sample was confined in the same sample assembly as described in Chapter 5. The XRD and x-ray absorption experiments (density measurements) were conducted in transmission geometry. A multi-channel collimator[24] positioned between the sample and the XRD detector enabled the collection of high-quality XRD patterns by almost complete eliminating the elastic and inelastic background from the sample container. The incident x-ray beam wavelength was set to 0.3738 Å using a silicon(111) double-crystal monochromator. The use of a high-energy x-ray

beam ensured a low-absorption by the sample surrounding material and a large angular coverage up to 30 degrees (2Θ angle). The XRD data have been collected on a 2-dimensional EIGER2 9M pixel detector from DECTRIS with small pixel size (75x75 μm^2) and high quantum efficiency (E > 80 %). An important goal of this work is to establish the position and slope of the LDL to HDL transition line. Therefore, particular care was taken in the accurate determination of the pressure *P* and temperature *T*. In its stability field, we have directly exploited the anisotropic thermal and compressional behaviour of bP to simultaneously and accurately obtain *P* and *T*. This method was employed in the stability range of solid bP up to 5 GPa and 1700 K. In the stability of the LDL and HDL *T* was determined with and accuracy of ± 75 K by extrapolating the relation between the electrical power and the temperature obtained in the domain of existence of bP. The pressure with an accuracy of 0.1 GPa was obtained using the equation of state of hexagonal boron nitride determined in Chapter 4. Another fundamental aspect in the current work resides in the use of clear criterion to unambiguously distinguish the LDL from the HDL. Here we have employed the strong x-ray signature associated with the drastic local atomic arrangement that is associated to the LDL-HDL transformation. As presented in Figure 6.2., through the use of a multi-channel collimator (MCC)[24], high quality diffraction patterns were obtained for the LDL and HDL.

1.3. Construction of the liquid-liquid transition line in phosphorus

We have carried out a systematic investigation of the structure and density of liquid phosphorus in the vicinity of the LDL-HDL transition line. Typical *P,T* pathways in the experimental phase diagram of phosphorus in the range 0.1 – 4 GPa and 1300 – 2500 K are presented in Figure 6.1. In order to avoid the colossal jump in density (up to 60%) associated with melting that we reported in Chapter 5 and the high risk of blow-out associated with it, particular pathways in the *P,T* plane have been followed. The sample was first pressurized at room temperature and, as shown in Figure 6.1., then heated to cross the melting line at pressures beyond the liquid-liquid-solid triple point (LLSTP). In this pressure regime, the density discontinuity at melting is modest and safe for the sample assembly. In the liquid state, the data have been systematically collected on decompression along 7 isotherms at temperatures from 1500 to 2550 K. A fresh sample loading was used for each of them to ensure the high quality of the collected datasets and control their reproducibility. In practice, the pressure was finely reduced at constant temperature by steps of ~0.1 GPa to bracket the HDL to LDL transition temperatures and pressures with an accuracy of ± 75 K and ± 0.1 GPa.

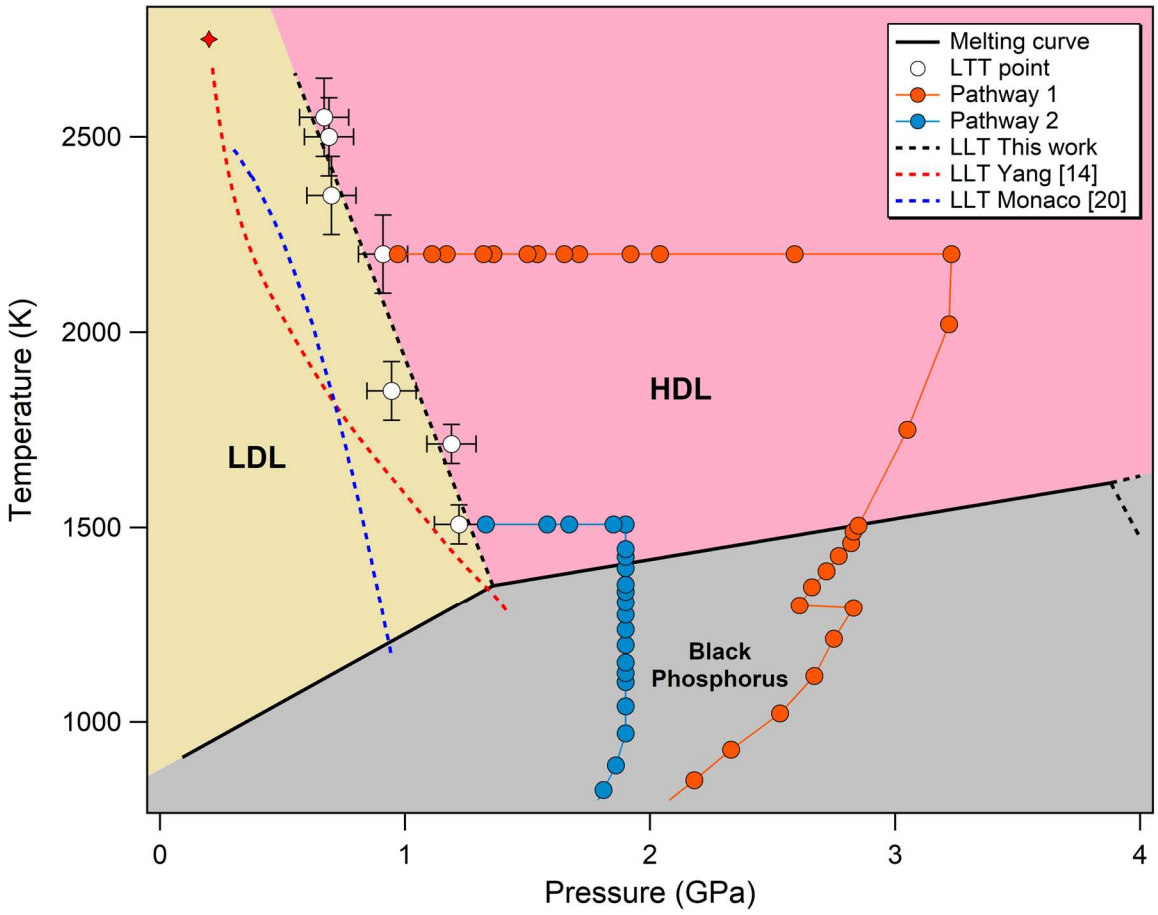

Figure 6.1. P,T location of the measured LDL-HDL transition points and associated density jumps in the phase diagram of phosphorus (white disks). Orange and blue disks: 2 examples of P,T pathways followed in this study. Black line: melting curve of phosphorus as reported in Chapter 5, dashed black, blue and orange lines: LDL-HDL transition line, from this work and from ref.[20] and[14], respectively.

The transition between LDL and HDL has been assessed using 2 unambiguous criteria. As shown in Figure. 6.2., the strong increase of the FSDP intensity at a Q value of ~13 nm^{-1} and the modification of the position and intensity of the higher Q oscillations that are associated to the LDL-HDL transformation have been employed as first criterion. As reported in refs[16,19], this FSDP is associated to the medium-range correlations between the P_4 tetrahedral molecular units that are present in the LDL. In agreement with previous studies[16-17,20], pure LDL and HDL phases (Figure 6.2.) have been clearly evidenced in a small pressure interval attesting of a sudden, strongly first-order transformation. As presented in Figure 6.3., the drastic reduction of the x-ray absorption due to the density collapse occurring when the HDL transforms to the LDL has been used as second criterion. The simultaneous use of these 2 criteria enabled the

determination of the position and slope of LDL-HDL transition line with an accuracy of 0.1 GPa and 75 K. Within uncertainties, we observe a linear variation of the transition temperature with pressure, with a negative slope of -1634 ± 200 $K.GPa^{-1}$. These results are consistent with our melting curve reported in Chapter 5. Indeed, the linear extrapolation of the LLT line established in this work intersects the melting curve of bP at the liquid-liquid-solid triple point determined from change of slope of the melting line. Furthermore, as shown in Figure 6.1., our results are in good agreement with those reported in[20] that also employed *in situ* XRD at high-pressure and high-temperature in the Paris-Edinburgh press. In both studies, below 2200 K, a linear variation of the transition and a similarly negative slope (-2400 $K.GPa^{-1}$ in ref[20]) has been obtained. Only a slight systematic pressure shift of ~0.2 GPa has been observed that is near the accuracy limit of the methodology employed in these 2 experimental works. At temperatures above 2200 K, in contrast with Monaco et al., we did not observe a non-linear evolution of the LDL-HDL transition line. Such non-linear behavior has been also reported in a recent *ab initio* molecular dynamics simulation[14] but in a much wider temperature domain (Figure 6.1.).

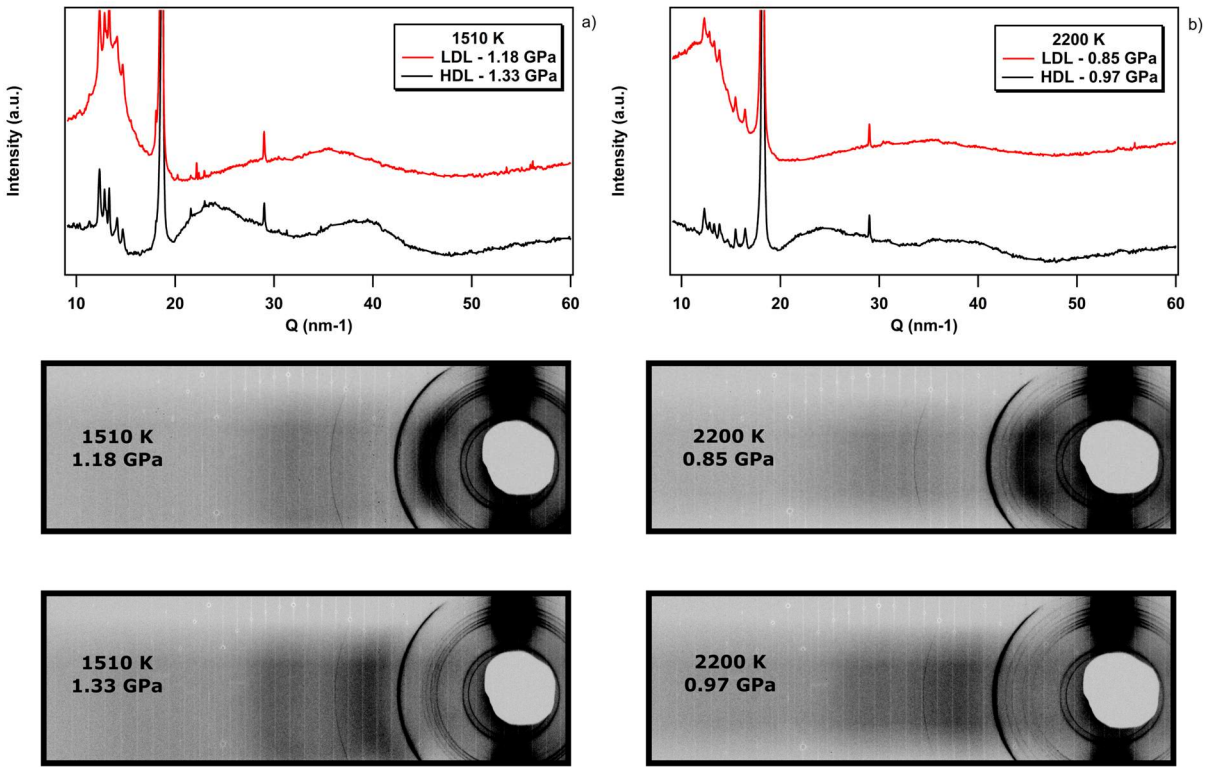

Figure 6.2. 2-dimensionnal XRD images (bottom panels) and corresponding 1-dimensionnal XRD patterns highlighting the phase transformation from the LDL to the HDL. XRD patterns in red, pure LDL at 1.18 GPa and 1510 K and, 0.85 GPa and 2200 K. XRD patterns in black: pure HDL 1.33 GPa and 1510 K and, 0.97 GPa and 2200 K. The remaining Bragg reflections at low Q (below 30 nm^{-1}) originate from the sample container (boron-epoxy gasket, hBN capsule). The vertical white lines in the 2D XRD images come from the imperfect rotation of the MCC during acquisition.[24]

1.4. Colossal density variation of the liquid-liquid transition in phosphorus

In addition to the new determination of the transition line, we have accurately determined the associated density discontinuity ($\Delta\rho/\rho=\rho_L-\rho_H/\rho_H$, where the indices H and L stand for the HDL and LDL state, respectively) in an extended temperature domain (up to 2500 K) using the well-established x-ray contrast absorption method developed by Katayama et al.[15,17] and detailed in Chapter 3. This method has an accuracy of ~1 % to 5 %, a value that is much smaller than the observed density jumps. Examples of x-ray absorption profiles determined at the same P,T conditions as the diffractograms of Figure 6.2. are presented in Figure 6.3. When the LDL-HDL line is crossed, extraordinarily large density variations $\Delta\rho/\rho$ of up to 63% are observed. This value is even larger than the reported colossal density

discontinuity (of up to 60 %) associated to the melting of bP towards the LDL in Chapter 5. it is indeed 1 to 2 orders of magnitude larger than those observed at melting (or associated to solid-solid phase transitions) for any materials and are likely related to the striking difference in the local atomic arrangements of the LDL and HDL. As shown in Figure 6.2., the structure factors *S(Q)* in the LDL and HDL exhibit strong short-range correlations typical of a liquid. In particular, for the LDL, the calculated densities are close to that of water (e.g. ρ_L=1.18 (10) g.cm^{-3} at 0.91 GPa and 2200 K), therefore excluding a direct transformation to a gas.

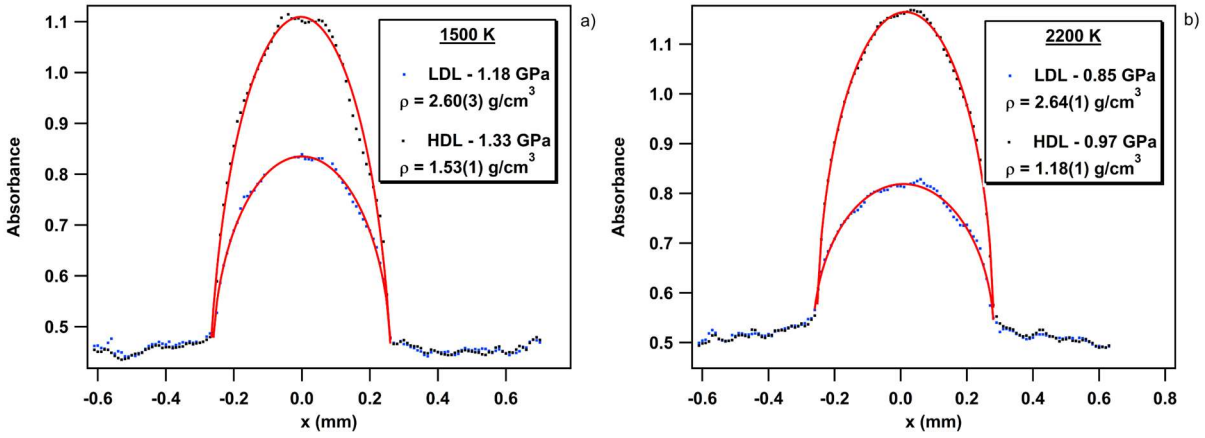

Figure 6.3. X-ray absorption profiles obtained across the LDL-HDL transition and measured at the same P,T conditions as the XRD data presented in Fig. 2. Top profiles: LDL. Bottom profiles: HDL.

In order to better understand the thermodynamics of the LLT transition, the entropy jumps (ΔS) and the latent heat (ΔH) associated with it were determined using the Clausius-Clapeyron relation[25-26] and, the slope of the LLT and density jumps determined experimentally. All of these results are listed in Table 6.1. As for melting, very large values of ΔH up to 30 kJ.mol^{-1} have been obtained (for water the latent heat of melting is 6 kJ.mol^{-1}, a value considered as large). This is a direct consequence of the strong changes in the local atomic arrangement involved in the LDL-HDL transformation. The temperature variation of $\Delta\rho$ and ΔH are compared to literature data in Figure 6.4. Only one experimental data point has been previously reported by Katayama et al.[17] at low *P,T* conditions (1 GPa and 1300 K) that is in nice agreement with this study although the transition pressure is lower than observed here at 1300 K. Two recent theoretical studies[13,14] have been devoted to the study of the LDL-HDL transition over an extended *P,T* range. They have been carried out using either pure *ab initio* molecular dynamics (AIMD) simulations[13] or molecular dynamics using machine-learning

trained potential on AIMD trajectories[14]. Although different in absolute values, they both report the existence of a maximum in the temperature variation of the density jump and latent heat. In addition, they provided evidence for the existence of a liquid-liquid critical point at the endpoint of the LLT line. As shown in Figure 6.4., these simulation results contradict our experimental measurements in several aspects. Indeed, we did not observe a maximum but rather a monotonic increase of the density jumps and latent heat with temperature. Furthermore, due to the rapid increase of these quantities with temperature and the strong negative slope of the LLT, it is clear that there is no liquid-liquid critical point in the *P,T* domain studied. These discrepancies can be linked to the initial structural model used in the simulations which considers that the LDL is composed only of free P_4 tetrahedral molecules[13] or to the choice of the collective variable (or order parameter, here the FSDP of the structure factor S (Q)) linked to this structural model[14]. Indeed, we have shown in Chapter 5 that the local structure of the LDL could be much more complex than previously thought. In agreement with Akahama et al.[27] and Brazhkin et al.[28], we have observed that the solid recovered after temperature quenching of the LDL is red phosphorus (rP), a complex allotrope of phosphorus (monoclinic structure) made of tubes with pentagonal cross sections[29]. This strongly suggests that the LDL contains large structural assemblies that are more challenging to simulate. This scenario is also supported by earlier *ab initio* molecular dynamics simulations that predicted that the P_4 molecules in LDL were unstable and polymerized at high temperatures[18,30].

Table 6.1. Pressure and temperature locations of the density measurements, and corresponding density, entropy and enthalpy jumps at the LDL-HDL transition.

P (GPa) / T (K)	ρ HDL ($g.cm^{-3}$)	ρ LDL ($g.cm^{-3}$)	Δρ/ρ (%)	ΔS ($J.K^{-1}.mol^{-1}$)	ΔH ($kJ.mol^{-1}$)
0.67 / 2550	2.59 (8)	0.97 (4)	63 (2)	12.3 (29)	31 (9)
0.69 / 2500	2.59 (5)	0.96 (4)	63 (2)	12.5 (29)	32 (9)
0.70 / 2350	2.78 (7)	1.15 (3)	59 (2)	9.8 (20)	23 (6)
0.91 / 2200	2.64 (1)	1.18 (1)	55 (1)	9.0 (14)	20 (4)
0.95 / 1850	2.79 (5)	1.43 (2)	48 (2)	6.5 (12)	12 (3)
1.19 / 1714	2.72 (6)	1.40 (3)	48 (2)	6.6 (14)	11 (3)
1.22 / 1508	2.60 (3)	1.53 (1)	41 (1)	5.1 (9)	8 (2)

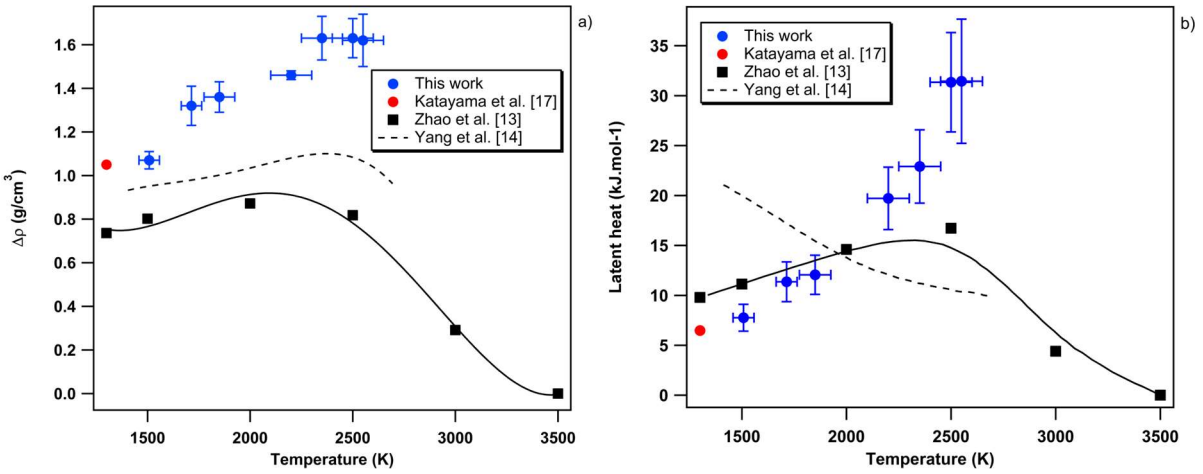

Figure 6.4. Temperature evolution of the density jumps and latent heat along the LLT from this work (blue disks), from ref[17] (red disk), from ref[14] (dashed black line) and ref[13] (black curve and filled squares).

To get deeper insights on the nature of the LDL-HDL transformation, we have made a direct comparison with the thermodynamics of melting that we have reported in Chapter 5. As shown in Figure 6.5., there is a striking similarity between the pressure variation and amplitude of the density discontinuity and latent heat for these 2 apparently distinct phase transitions. Indeed, a linear variation of the jumps in density $\Delta\rho/\rho$ and latent heat L with pressure was obtained for the LLT which almost overlaps with the melting data. As for melting, for the LLT the amplitude of $\Delta\rho/\rho$ (and L) drops significantly from 63% to 41% (and from 31 to 8 kJ.mol^{-1}) in the small pressure range included between 0.7 and 1.2 GPa. This suggests that the driving forces of these 2 phenomena are of the same nature and may be related to the interplay between entropy and density in the LDL and HDL.

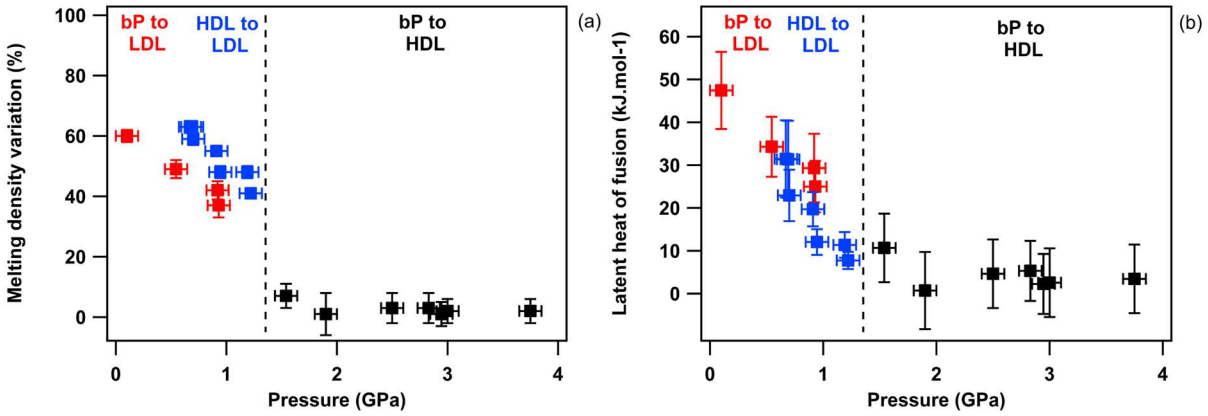

Figure 6.5. Pressure variation of the density jumps and latent heat in the LDL and HDL stability fields and comparison to melting. Blue squares: LDL to HDL transition, red and black squares: crystalline bP to LDL and HDL, respectively.

2. Viscosity of the two liquids

To gain a deeper understanding of the LDL and HDL structures, we conducted viscosity measurements using the "falling sphere" technique, as described in Chapter 3 of this thesis, with a monochromatic incident X-ray beam (λ = 0.3738 Å). It is noteworthy to highlight the enhanced quality of the X-ray radiographic images subsequent to the recent upgrade (EBS) of the European Synchrotron Radiation Facility from a third-generation to a fourth-generation synchrotron source. This advancement, coupled with the utilization of an improved imaging setup at the new ID27 beamline, featuring the PCO DIMAX camera as opposed to the CoolSNAP HQ2 CCD camera used before the EBS, has significantly enhanced our ability to capture high quality X-ray radiographic images, as illustrated in Figure 6.6

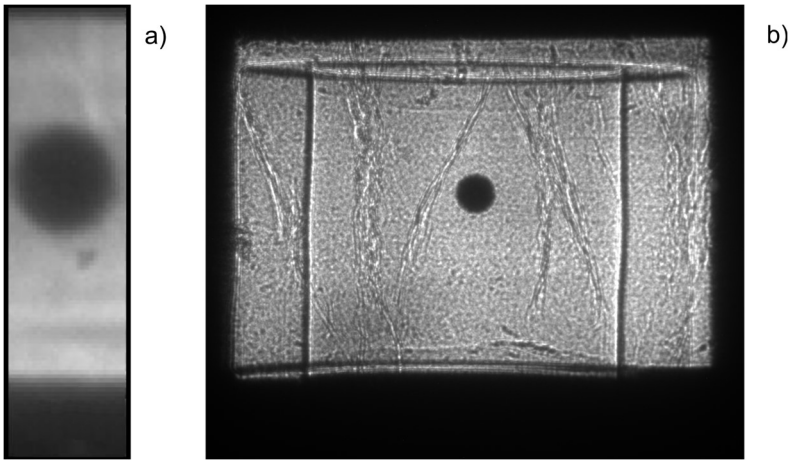

Figure 6.6. Comparison between X-ray images obtain (a) before and (b) after the EBS upgrade in 2020 and ID27 reconstruction in 2021. The recent developments considerably increased the data precision.

Figure 6.7. illustrates the typical pressure-temperature (P,T) pathways within the phase diagram of black phosphorus over the range of 0.1 – 3 GPa and temperatures spanning 700 to 1700 K. The specific P,T conditions employed in this study are itemized in Table 6.2. These P,T conditions were ascertained through the innovative metrology method presented in Chapter 4, using X-ray diffraction patterns systematically collected along the five distinct P,T pathways. These pathways lead to the determination of five viscosity points within the stability regions of LDL and HDL. A freshly loaded sample was employed for each of them to ensure the high quality of the collected datasets and control their reproducibility.

Notably, three of the five pathways were originally explored in L. Henry's thesis[31] on the former ID27 beamline and have been re-analyzed in the context of this present research work. The remaining two pathways were specifically investigated during the course of this thesis.

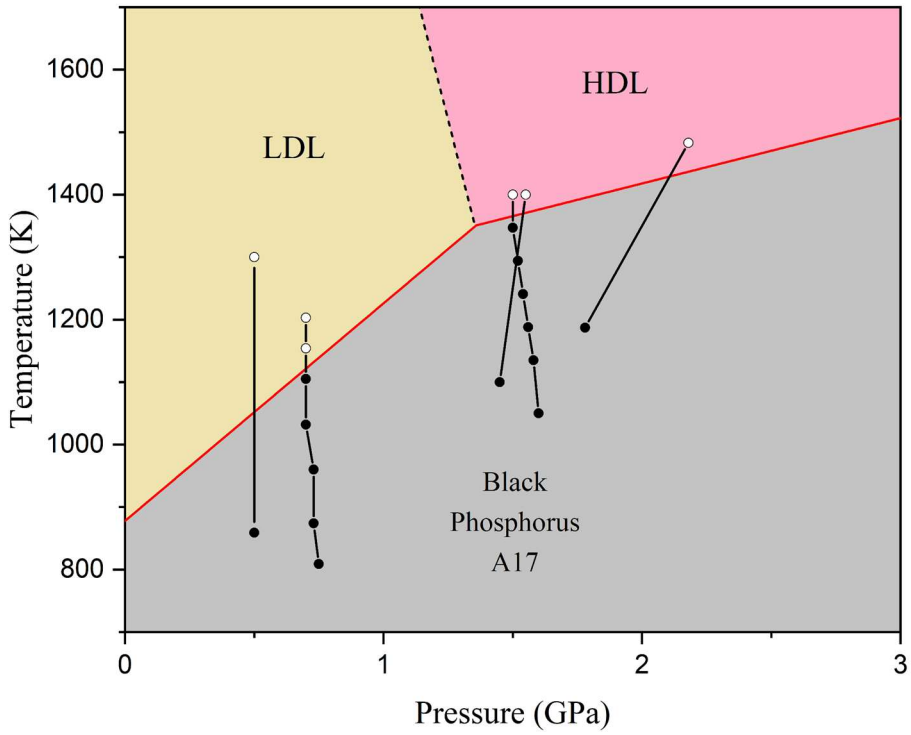

Figure 6.7. Phase diagram of bP. Black and white symbols denote respectively the solid and liquid state. The five P,T pathways are represented by line-connected circles, where each symbol indicates a P-T point where XRD and XRI measurement was performed.

For the two pathways that were pursued in our investigation, a practical approach was employed to cross the melting curve. The involved incremental temperature increases of approximately 40 K while maintaining a constant pressure. At the point where sample recrystallization started, X-ray radiographic images were systematically captured with each successive temperature increment to monitor the sphere's fall. After radiographic observations, P,T conditions were held constant, and diffraction patterns of the sample and P-T calibrants were collected (Figure 6.8.). It is worth to point out that the resulting measured melting points were implemented when constructing the black phosphorus melting curve presented in Chapter 5.

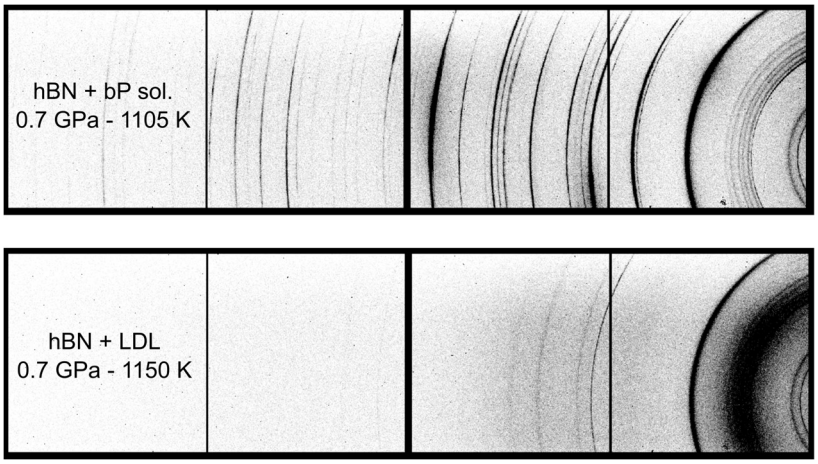

Figure 6.8. XRD image of solid bP at 0.7 GPa and 1105 K, and its subsequent melting with temperature increase up to 1150 K. The liquid displays a large band of diffuse X-ray scattering located at approximately 4.51° (2Θ angle), which corresponds to a distance of 4.751 Å (Q value of 1.323 $Å^{-1}$).

Figure 6.9. presents a series of X-ray radiographic images captured over time, illustrating the vertical displacement of a rhenium sphere within the HDL phase at conditions of 1.5 GPa and 1400 K. Subsequently, in Figure 6.10., we present a profile depicting the sphere's fall over time, which was constructed by tracking the sphere's position in each frame using the ImageJ software. This distance-time plot exhibits a sigmoidal shape, characterized by nonlinear regions at its extremes, reflecting both the acceleration and deceleration phases as the sphere approaches the bottom of the sample volume.

Within the region of constant velocity, a least-squares best-fit line is determined, and the slope of this line corresponds to the terminal velocity. The terminal velocity is then employed in accordance with Stokes' relation, presented in Chapter 3, to calculate the viscosity of the sample.

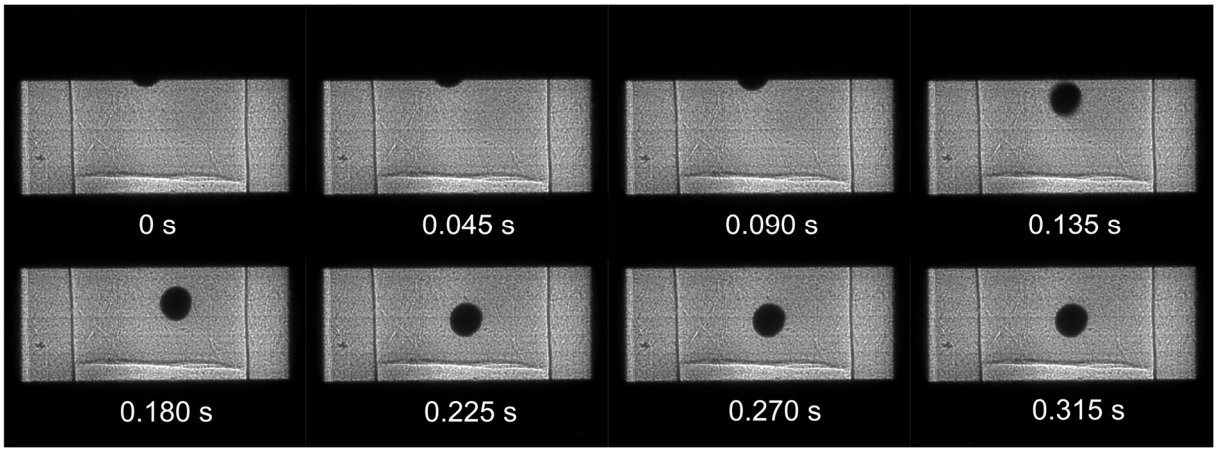

Figure 6.9. Sequence of X-ray radiographic images showing the displacement of a rhenium sphere in the HDL at 1.5 GPa and 1400 K. The frame time is indicated in the individual frames.

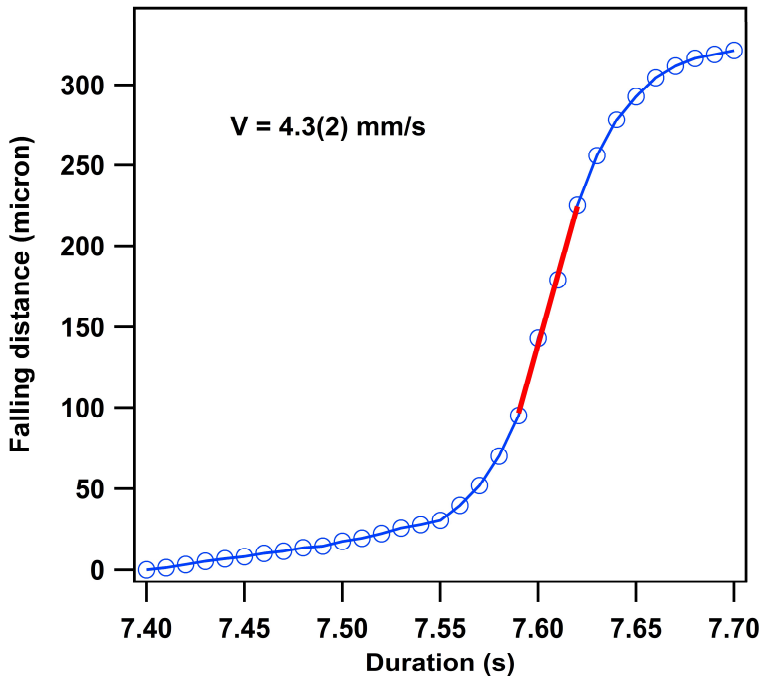

Figure 6.10. Distance-time plot for a rhenium sphere falling in liquid P at 1.5 GPa and 1400 K. The distance-time plot exhibits a sigmoid shape with nonlinear regions at the ends, reflecting acceleration and deceleration of the sphere when it approaches the bottom of the capsule.

We conducted a series of five viscosity measurements within the pressure range of 0.5 to 2.16 GPa, focusing on the vicinity of the liquid-liquid-solid triple point of black phosphorus. Key experimental parameters, including sphere diameters, terminal velocities, and the resultant calculated viscosities, are succinctly presented in Table 6.2. Furthermore, in

Figure 6.11., we have depicted a graphical representation illustrating the large viscosity discontinuity with respect to pressure.

Table 6.2. Experimental conditions and results.

Sample	P (GPa)	T (K)	r_s(μm)	V (mm/s)	F/K	η (Pa.s)
Henry_1	0.50	1300	184	0.0265	0.39	21 (2)
Henry_2	1.55	1400	177	19.5	0.40	0.026 (3)
Henry_3	2.16	1440	180	9	0.40	0.057 (6)
This work_1	0.70	1150	82	0.000508	0.52	291 (29)
This work_2	1.50	1400	93	4.3	0.47	0.039 (4)

For the HDL phase, our viscosity measurements agree well with those previously reported by L. Henry[31], underscoring the reproducibility of these measurements. However, a notable difference exists for the LDL phase, as our viscosity value being more than ten times larger. This discrepancy could be due to the different temperatures at which the data was measured, L. Henry's data being collected approximately 250 K higher than the melting. This would mean that the viscosity of the LDL is strongly temperature dependent, dropping by approximately one order of magnitude in 250 K.

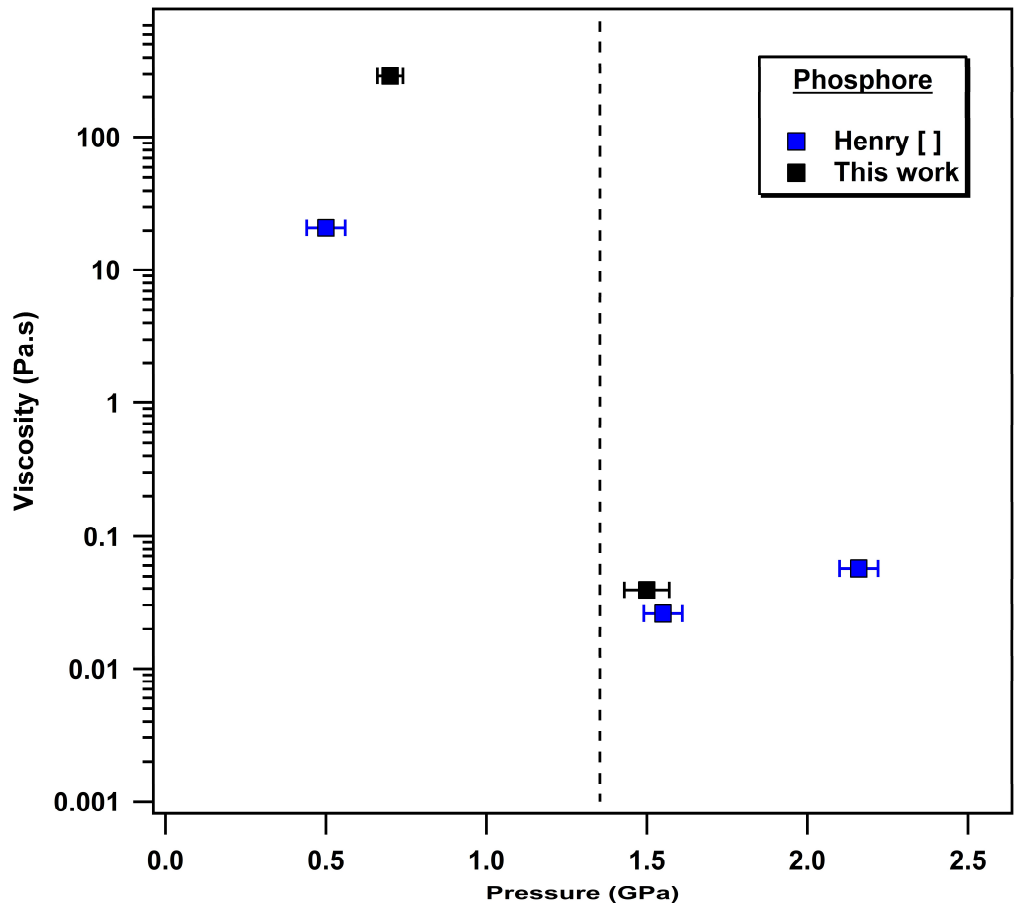

Figure 6.11. Viscosity of liquid P at different P, T conditions, coming from this work, or measured during L. Henry's thesis and re-analyzed in the framework of this thesis.

Remarkably, the viscosity of the HDL is 3 to 4 orders of magnitude less than that of the LDL. This observation matches well the computational simulations conducted by Senda et al.[32] using ab-initio Molecular Dynamics (MD), which propose the occurrence of chemical bond breaking and rearrangement at the picosecond timescale within the HDL. These processes contribute to a more intricate and dynamic local structure.

Conversely, the LDL exhibits an exceptionally high viscosity in comparison to other molecular liquids such as water[33] and CO_2[34], which typically have viscosities in the range of a few millipascal-seconds. The viscosity of molten white P of 2 mPa.s was measured by Campbell et al.[35] and Dobinski[36] in the 300 – 420 K temperature range. To provide perspective, the LDL viscosity of phosphorus surpasses that of polymeric sulfur, with 0.69 Pa.s at conditions of 3.2 GPa and 788 K.[37] This suggests that the LDL structure differs significantly from the prevailing consensus, which categorized the LDL as a molecular liquid closely resembling molten white P, composed of isolated and weakly bound P_4 molecules. Contrary to this accepted

view, the viscosity measurements indicate a behavior closer to that of a polymeric liquid, potentially composed of interconnected P_4 units, bearing resemblance to the subunit structure proposed for amorphous red phosphorus by Zaug et al.[38] This assumption could very well explain why, when quenching the LDL, black phosphorus is not recovered, but a crystalline phase of red phosphorus instead (see Chapter 4). Our findings suggest that the LDL is a much more interconnected liquid than previously assumed, and that the HDL, in agreement with Senda et al.[32] is a much more dynamic liquid that initially thought.

Conclusion

In this Chapter, we performed combined in situ high-resolution x-ray diffraction and density measurements to accurately determine the position and slope of the LDL-HDL transition line to temperatures in excess of 2500 K, and the density jumps associated with it. As for melting below the liquid-liquid-solid triple point, we found a colossal jump in density at melting in phosphorus that exceeds by one to two orders of magnitude that measured in any other material and for any type of first-order phase transitions (e.g. melting or solid-solid phase transitions). The colossal density jump of the LLT is associated to a very large latent heat, signature of a strongly endothermic reconstructive transformation. In contrast with the ab initio molecular dynamics simulations, we observed a rapid and monotonic increase of the density jumps and latent heat with temperature which suggests the absence of a liquid-liquid critical point and a much more complex atomic structure of the LDL. We have also evidenced a striking similarity between the thermodynamics of melting and of the LDL-HDL transformation. This suggests that the interplay between entropy and density may play a key role in driving these apparently distinct first-order phase transitions. We have also conducted an analysis of the viscosities of the two liquid phases, revealing a striking disparity: the low-density liquid exhibits a viscosity that is 3 to 4 orders of magnitude greater than that of the high-density liquid. This unexpected result contradicts prevailing theoretical studies suggesting that the LDL consists of P_4 molecules and instead suggests that the LDL may resemble more of a polymeric liquid, potentially comprised of interconnected P_4 units, a local structure proposed by Zaug et al.[38]. Our findings pose a significant challenge to existing interpretations regarding the nature and local structure of phosphorus's liquid phases and calls for new experimental and theoretical investigations of this complex system.

References

1. H. Tanaka, Liquid-liquid transition and polyamorphism. *J. Chem. Phys.*, 2020, **153**, 130901.
2. J. N. Glosli and F. H. Ree, Liquid-Liquid Phase Transformation in Carbon. *Phys. Rev. Lett.*, 1999, **82**, 4659-4662.
3. S. Sastry and C. A. Angell, Liquid-liquid phase transition in supercooled silicon. *Nat. Mater.*, 2003, **2**, 739-743.
4. M. A. Morales, C. Pierleoni, E. Schwegler and D. M. Ceperley, Evidence for a first-order liquid-liquid transition in high-pressure hydrogen from ab initio simulations. *Proc. Natl. Acad. Sci. USA*, 2010, **107**, 12799-12803.
5. B. Boates, A. M. Teweldeberhan and S. A. Bonev, Stability of dense liquid carbon dioxide. *PNAS*, 2012, **109**, 14808-14812.
6. B. Boates and S. A. Bonev, First-order liquid-liquid phase transition in compressed nitrogen. *Phys. Rev. Lett.*, 2009, **102**, 015701.
7. J. -Y. Raty, E. Schwegler and S. A. Bonev, Electronic and structural transitions in dense liquid sodium. *Nature*, 2007, **449**, 448-451.
8. P. H. Poole, F. Sciortino, U. Essmann and H. E. Stanley, Phase behavior of metastable water. *Nature*, 1992, **360**, 324-328.
9. S. Harrington, R. Zhang, P. H. Poole, F. Sciortino and H. E. Stanley, Liquid-liquid phase transition: evidence from simulations. *Phys. Rev. Lett.*, 1997, **78**, 2409-2412.
10. O. Mishima and H. E. Stanley, The relationship between liquid, supercooled and glassy water. *Nature*, 1998, **396**, 329-335.
11. S. Woutersen, B. Ensing, M. Hilbers, Z. Zhao and C. A. Angell, A liquid-liquid transition in supercooled aqueous solution related to the HAD-LDA transition. *Science*, 2018, **359**, 1127-1131.
12. R. Kurita and H. Tanaka, One the abundance and general nature of the liquid-liquid phase transition in molecular systems. *J. Phys. Condens. Matter*, 2005, **17**, 293-302.
13. G. Zhao, H. Wang, D. M. Hu, M. C. Ding, X. G. Zhao and J. L. Yan, Anomalous phase behavior of first-order fluid-liquid phase transition in phosphorus. *J. Chem. Phys.*, 2017, **147**, 204501.
14. M. Yang, T. Karmakar and M. Parrinello, Liquid-liquid critical point in phosphorus. *Phys. Rev. Lett.*, 2021, **127**, 080603.

15. L. Henry, M. Mezouar, G. Garbarino, D. Sifré, G. Weck and F. Datchi, Liquid-liquid transition and critical point in sulfur. *Nature*, 2020, **584**, 382-386.
16. Y. Katayama, T. Mizutani, W. Utsumi, O. Shimomura, M. Yamakata and K. Funakoshi, A first-order liquid-liquid phase transition in phosphorus. *Nature*, 2000, **403**, 170-173.
17. Y. Katayama, Y. Inamura, T. Mizutani, M. Yamakata, W. Utsumi, O. Shimomura, Macroscopic separation of dense fluid phase and liquid phase of phosphorus. *Science*, 2004, **306**, 848-851.
18. D. Hohl and R. O. Jones, Polymerization in liquid phosphorus: Simulation of a phase transition. *Phys. Rev. B*, 1994, **50**, 17047-17053.
19. Y. Senda, F. Shimojo and K. Hoshino, The metal-nonmetal transition of liquid phosphorus by ab initio molecular-dynamics simulations. *J. Phys.: Condens. Matter*, 2002, **14**, 3715-3723.
20. G. Monaco, S. Falconi, W. Crichton and M. Mezouar, Nature of the first-order phase transition in fluid phosphorus at high temperature and pressure. *Phys. Rev. Lett.*, 2003, **90**, 2557011-2557014.
21. J. M. Besson, G. Hamel, P. Grima, R. J. Nelmes, J. S. Loveday, S. Hull and D. Häusermann, A Large Volume Pressure Cell for High Temperatures. *High Press. Res.*, 1992, **8**, 625.
22. S. Klotz, Th. Strässle, G. Rousse, G. Hamel and V. Pomjakushin, Angle-dispersive neutron diffraction under high pressure to 10 GPa. *Appl. Phys. Lett.*, 2005, **86**, 031917.
23. G. Morard, M. Mezouar, N. Rey, R. Poloni, A. Merlen, S. Le Floch, P. Toulemonde, S. Pascarelli, A. San Miguel, C. Sanloup and G. Fiquet, Optimization of Paris-Edinburgh press cell assemblies for *in situ* monochromatic X-ray diffraction and X-ray absorption. *High Press. Res.*, 2007, **27**, 223.
24. G. Morard, M. Mezouar, S. Bauchau, M. Álvarez-Murga, J. -L Hodeau and G. Garbarino, High efficiency multichannel collimator for structural studies of liquids and low-Z materials at high pressures and temperatures. *Rev. Sci. Instrum*., 2011, **82**, 023904.
25. R. Clausius, Ueber die bewegende Kraft der Wärme und die Gesetze, welche sich daraus für die Wärmelehre selbst ableiten lassen. *Annalen der Physik*, 1850, **155**, 368-397.
26. M. C. Clapeyron, Mémoire sur la puissance motrice de la chaleur. *Journal de l'École polytechnique*, 1834, **23**, 153-190.
27. Y. Akahama, W. Utsumi, S. Endo, T. Kikegawa, H. Iwasaki, O. Shimomura, T. Yagi and S. Akimoto, Melting curve of black phosphorus, *Phys. Lett. A*, 1987, **122**, 123-131.

28. V. V. Brazhkin and A. J. Zerr, Relative stability of red and black phosphorus at P < 1 GPa. *J. Mater. Science*, 1992, **27**, 2677-2681.
29. M. Ruck, D. Hoppe, B. Wahl, P. Simon, Y. Wang and G. Seifert, Fibrous red phosphorus. *Angew. Chem. Int. Ed.*, 2005, **44**, 7616-7619.
30. T. Morishita, Liquid-Liquid Phase Transitions of Phosphorus via Constant-Pressure First-Principles Molecular Dynamics Simulations. *Phys. Rev. Lett.*, 2001, **87**, 105701.
31. L. Henry, Liquid-liquid transitions in elemental liquids. *PhD thesis*, 2019.
32. Y. Senda, F. Shimojo and K. Hoshino, The metal-nonmetal transition of liquid phosphorus by *ab initio* molecular-dynamics simulations. *J. Phys.: Condens. Matter*, 2002, **14**, 3715-3723.
33. E. H. Abramson, Viscosity of water measured to pressures of 6 GPa and temperatures of 300 C. *Phys. Rev. E*, 2007, **76**, 051203.
34. E. H. Abramson, Viscosity of carbon dioxide measured to a pressure of 8 GPa and temperatures of 673 K. *Phys. Rev. E*, 2009, **80**, 021201.
35. A. N. Campbell and S. Katz, The Viscosity of Liquid Phosphorus. *J. Am. Chem. Soc.*, 1935, **57**, 11, 2051-2055.
36. Dobinski, *Acad. Polonaise Sci. et Lettres*, Ser. A., p 103, March-April, 1934. Figures reproduced in ref [35].
37. H. Terasaki, T. Kato, K. Funakoshi, A. Suzuki and S. Urakawa, Viscosity of liquid sulfur under high pressure. *J. Phys.: Condens. Matt.*, 2004, **16**, 1707.
38. J. M. Zaug, A. K. Soper and S. M. Clark, Pressure-dependent structures of amorphous red phosphorus and the origin of the first sharp diffraction peaks. *Nat. Mater.*, 2008, **7**, 890-899.

Conclusion and perspectives

The primary objective of this thesis was to gain a deeper knowledge of the liquid-liquid transition (LLT) in phosphorus. Since the discovery of this phase transition by Katayama et al.[1] in 2000, there has been several theoretical studies devoted to this peculiar and surprising phenomenon, but comparatively less experimental investigations. Some of the predictions made by the ab initio molecular dynamics (AIMD) simulations thus remained non-confronted to experiments. In particular, AIMD simulations predicted a non-monotonous variation of the density and entropy variation along the transition line, initially increasing and then decreasing down to zero. This implied that the LLT line ends at a liquid-liquid critical point (LLCP) that the simulations have located either around 2800 K[2] or 3500 K[3]. The existence of the LLCP has been highly debated in the literature, especially in the case of supercooled water, making its confirmation in the case of phosphorus an important issue. Another incompletely resolved matter regarded the nature of the low-density and high-density liquid, which had been only characterized by x-ray diffraction. Besides the LLT, but related to it, large differences existed between the melting curves of bP reported in the literature, such that the existence of a liquid-liquid-solid triple point remained disputed. Furthermore, no data existed for the density and entropy variation at melting, and how they vary whether bP melts into LDL or HDL.

A first stage of the present work has been to establish a P-T metrology that would improve the accuracy of P-T measurements in the Paris-Edinburgh press at high temperature in the P-T range of interest for the present work. Accurate measurements of P and T are indeed a cornerstone of HP-HT experiments and may be at the origin of controversies, such as the diverging melting curves of bP. To this aim, we meticulously re-determined the room-temperature P-V equation of state, and the ambient pressure volumetric and linear thermal expansion coefficients of hexagonal boron nitride (hBN) and black phosphorus (bP). The HP measurements up to 10 GPa at 300 K were done in liquid He, ensuring perfect hydrostatic compression. The HT experiments at ambient P were done in the range 300-750 K and in two different experimental setups in order to check their reproducibility. The large number and high quality of the collected data points enabled to extract accurate values for the bulk modulus and its first-pressure derivative, and for the linear and volumetric thermal expansion coefficients. An original P-T metrology, based on the strongly anisotropic thermoelastic behavior of bP was deduced from this work, and was then systematically used in the experiments carried out during this thesis. Its originality and practicality reside in the fact that a single measurement of the

lattice parameters of bP suffices to determine both P and T, thanks to the quasi-incompressible character of the crystallographic a axis in the range 0 – 5 GPa. This new metrology thus holds promises for applications in large-volume press or diamond anvil cell experiments conducted up to 5 GPa and 1700 K. Since hBN and bP have relevance in diverse energy and technology applications, both in bulk and 2D forms, our results may also be useful to other fields.

In a second stage, we precisely determined the melting curve of black phosphorus using our newly established metrology. We observed that the melting temperature increases linearly with pressure in two distinct melting P-T domains, which correspond to the melting transition towards the low- and high-density liquids respectively. This enable the location of the triple point where the LDL, HDL and crystalline bP meet in the P-T phase diagram of phosphorus at 1.35 GPa and 1350 K. We found that the slope of the melting line reduces by a factor of ~3.3 from LDL to HDL, going from 348 to 105 $K.GPa^{-1}$ which indirectly confirmed the strong structural differences between the LDL and the HDL. The present melting curve significantly differs from previous reports. In particular, we found no maximum melting temperature unlike reported by some authors. The P-T determination of the melting transition was complemented by direct density measurements of the solid and liquid phase just below and above the transition, providing the first experimental data for the density difference between the two phases along the melting line. In the high-pressure regime above the liquid-liquid solid triple point (LLSTP), a standard melting behavior is observed, with a density change around 2-3%. At variance, for pressures below the LLSTP, the density jump increases rapidly with decreasing pressure and temperature, going from 37 % at 0.93 GPa – 1200 K to 60 % at 0.1 GPa and 914 K. Such values exceed by one to two orders of magnitude the density change at melting observed in any other material. From the Clausius-Clapeyron relation, we determined that the entropy and latent heat variation across melting below the LLSTP also reach remarkably high values, up to 47 $kJ.mol^{-1}$ for the latent heat at 0.1 GPa – 914 K. This attests that the melting of bP to LDL is a highly endothermic reconstructive transformation. This may explain the observed instability and subsequent decomposition of bP at ambient pressure and high temperature[4-5], incorrectly interpreted as a sublimation in the past. Our findings also revealed a direct effect of density on the entropy of the LDL suggesting a significant reduction of the accessible micro-states with increasing pressure.

In the third and final part of this work, we re-visited the determination of the LDL-HDL transition line and measured the associated density and entropy variation at various point from

1500 to 2550 K, noting that only one measurement of the density jump had been previously reported[6]. Below the LLSTP, we observed colossal density jumps upon crossing the LLT, going from 41 % to 63 %, and thus even surpassing those measured at melting. These dramatic density jumps during the LLT are also associated with a considerable latent heat. In contrast to ab initio molecular dynamics simulations, our experimental observations revealed a rapid and monotonic increase in the density jump and latent heat with temperature. Although the variation of the density jump with temperature seems to saturate at the highest investigated temperatures, no decrease is observed. These results are at odds with the predictions of AIMD simulations of a liquid-liquid critical point (LLCP) at 0.2 GPa,[2] at which the density variation becomes null, and shows that if such a LLCP exists, it must be located below 0.1 GPa. We also noted a remarkable resemblance between the thermodynamics of melting and of the LDL-HDL transformation. We suggest that the interplay between entropy and density may play a pivotal role in driving these seemingly distinct first-order phase transitions.

Moreover, we measured the viscosities of the two liquid phases and discovered a startling contrast: the LDL is unexpectedly 3 to 4 orders of magnitude more viscous than the HDL. This unconventional finding challenges the predominant hypothesis that the LDL is composed of isolated and weakly bound P_4 molecules, suggesting instead that the LDL exhibits characteristics closer to that of a polymeric liquid, potentially composed of interconnected P_4 and P_3 units, in a similar fashion as amorphous red P.[7]

Our findings fundamentally challenge current interpretations regarding the nature and local structure of phosphorus liquid phases. The extreme viscosities observed in the LDL, the irreversible nature of melting below the LLSTP, and the substantial disparity in density jumps and latent heats compared to ab-initio simulations collectively imply a much more complex atomic structure for the LDL than previously assumed. Systematic theoretical and experimental investigations of the melting and LLT in phosphorus hold the potential to yield more insights into the underlying nature of these transitions.

We anticipate that this thesis will invigorate renewed interest in the study of molecular systems in their liquid state. Numerous questions regarding phosphorus remain unanswered, including the behavior of density variations at the LLT as temperatures exceeding 2500 K, or, as we approach the LLSTP. The nature of the LDL and its potential relationship with other phosphorus allotropes (e.g. red or white forms) is still not completely understood. Techniques such as small angle X-ray scattering, capable of probing large polymeric chains, could be

employed to obtain more detailed structural information. Additionally, we underscore the significance of the interplay between entropy and density in driving the LDL-HDL transition and melting, which may involve a complex order parameter combining contributions from both entropy and density. However, a formal description of this underlying order parameter requires further theoretical development and may provide a generalized understanding of LLTs in molecular systems.

References

1. Y. Katayama, T. Mizutani, W. Utsumi, O. Shimomura, M. Yamakata and K. Funakoshi, A first-order liquid-liquid phase transition in phosphorus. *Nature*, 2000, **403**, 170-173.
2. M. Yang, T. Karmakar and M. Parrinello, Liquid-liquid critical point in phosphorus. *Phys. Rev. Lett.*, 20021, **127**, 080603.
3. G. Zhao, H. Wang, D. M. Hu, M. C. Ding, X. G. Zhao and J. L. Yan, Anomalous phase behavior of first-order fluid-liquid phase transition in phosphorus. *J. Chem. Phys.*, 2017, **147**, 204501.
4. Luo, W.; Yang, R.; Liu, J.; Zhao, Y.; Zhu, W.; Xia, G. M. Thermal sublimation: a scalable and controllable thinning method for the fabrication of few-layer black phosphorus. *Nanotechnology*, 2017, **28**, 285301.
5. Henry, L.; Svitlyk, V.; Mezouar, M.; Sifré, D.; Garbarino, G.; Ceppatalli, M.; Serrano-Ruiz, M.; Peruzzini, M.; Datchi, F. Anisotropic thermal expansion of black phosphorus from nanoscale dynamics of Phosphorene layers. *Nanoscale*, 2020, **12**, 4491-4497.
6. Y. Katayama, Y. Inamura, T. Mizutani, M. Yamakata, W. Utsumi, O. Shimomura, Macroscopic separation of dense fluid phase and liquid phase of phosphorus. *Science*, 2004, **306**, 848-851.
7. J. M. Zaug, A. K. Soper and S. M. Clark, Pressure-dependent structures of amorphous red phosphorus and the origin of the first sharp diffraction peaks. *Nat. Mater.*, 2008, **7**, 890-899.

List of Figures

List of Tables

Résumé :
Une transition liquide-liquide (LLT) est un phénomène particulier dans lequel un liquide mono-composant se transforme en un autre via une transition de phase du premier ordre. Une telle LLT a été découverte en 2000 dans le phosphore liquide à haute pression [Katayama et al, Nature 403 (2000)]. Les preuves expérimentales des LLT restent rares et contestées, et jusqu'à très récemment, un seul autre cas sans à été identifié sans ambiguïté dans le soufre [L. Henry et al, Nature, 584 (2020)]. De nombreuses questions demeurent ouvertes concernant le diagramme de phase du phosphorue et la thermodynamique des transitions de premier ordre qui y sont présentes. L'objectif de cette thèse est d'acquérir une compréhension plus approfondie des LLTs dans les systèmes moléculaires, avec un accent particulier sur le comportement enigmatique du phosphore. Pour atteindre cet objectif, nous avons mené une série d'expériences à haute pression et haute température pour examiner diverses facettes des transitions de phase et des propriétés structurelles du phosphore. Nous avons établi une nouvelle métrologie tirant plein potentiel des fascinantes propriétés thermo-élastique du phosphore. Grâce à cette métrologie, nous avons redéterminer la courbes de fusion et la LLT du phosphore, étudier leur réversibilités, et avons mesuré les sauts de densité colossaux associés à chacune de ces transitions. Nous avons également mesuré les viscosités des deux liquides et mis en évidence que le liquide de basse densité (LDL) est 3 à 4 ordres de grandeur plus visqueux que le liquide de haute densité (HDL). Nos résultats remettent fondamentalement en question les interprétations actuelles concernant la nature et la structure locale des phases liquides du phosphore. Les viscosités extrêmes observées dans le LDL, la nature irréversible de la fusion en dessous du point triple et la colossale disparité des sauts de densité et des chaleurs latentes par rapport aux simulation ab-initio impliquent collectivement une structure atomique beaucoup plus complexe du liquide que ce que l'on supposait auparavant.

Mots clés : [Phosphore, Transition liquide-liquide, Diagramme de phase, Hautes pressions, Métrologie, Thermodynamique, Viscosité]

[Melting curve and liquid-liquid transition in phosphorus]

Abstract :
A liquid-liquid transition (LLT) is a specific phenomenon in which a single-component liquid transforms into another through a first-order phase transition. Such an LLT was discovered in high-pressure liquid phosphorus in 2000 [Katayama et al, Nature, 403 (2000)]. Experimental evidence for LLTs remains scarce and debated, and until very recently, only one other unambiguous case had been identified in sulfur [L. Henry et al, Nature, 584 (2020)]. Many questions remain open regarding the phase diagram of phosphorus and the thermodynamics of the first-order transitions it undergoes. The aim of this thesis is to gain a deeper understanding of the LLTs in molecular systems, with a particular focus on the enigmatic behaviour of phosphorus. To achieve this goal, we conducted a series of high-pressure and high-temperature experiments to investigate various aspects of phase transitions and structural properties of phosphorus. We developed a new metrology that fully utilized the fascinating thermo-elastic properties of phosphorus. Thanks to this metrology, we redetermined the melting curve and LLT of phosphorus, studied their reversibility, and measured the colossal density jumps associated with each of these transitions. We also measured the viscosities of both liquids and found that the low-density liquid (LDL) is 3 to 4 orders of magnitude more viscous than the high-density liquid (HDL). Our results fundamentally challenge current interpretations regarding the nature and local structure of phosphorus liquid phases. The extreme viscosities observed in the LDL, the irreversible nature of melting below the triple point, and the colossal density jumps and latent heats compared to ab-initio simulations collectively imply a much more complex local structure of the liquid than previously assumed.

Keywords : [Phosphorus, Liquid-liquid transition, phase diagram, High pressure, Metrology, Thermodynamics, Viscosity]